In compliance with the
Canadian Privacy Legislation
some supporting forms
may have been removed from
this dissertation.

While these forms may be included
in the document page count,
their removal does not represent
any loss of content from the dissertation.

DAMAGE IN HETEROGENEOUS ALUMINUM ALLOYS

By

JUSTIN GAMMAGE, B.A.Sc., M.A.Sc.

A Thesis

Submitted to the School of Graduate Studies

in Partial Fulfillment of the Requirements

for the Degree of

Doctor of Philosophy

McMaster University

DOCTOR OF PHILOSOPHY
(Materials Science and Engineering)

McMASTER UNIVERSITY
Hamilton, Ontario

TITLE:	Damage in Heterogeneous Aluminum Alloys
AUTHOR:	Justin J. Gammage B.A.Sc., M.A.Sc. (University of Windsor)
SUPERVISORS:	Professors D.S. Wilkinson and J.D. Embury
NUMBER OF PAGES:	xvi, 254

ABSTRACT

The role of damage on the mechanical response of a heterogeneous material was investigated through both mechanical testing and x-ray tomography. X-ray tomography was used to obtain quantitative information on the evolution of damage through processes occurring at both the local and global scale. The results indicate that heterogeneity in the spatial distribution of particles does influence the damage process. However, the influence of having one particle or more interacting with another is limited to reducing the tensile deformation required to initiate damage. The rate at which damage evolves is similar for both isolated and non-isolated particles and increasing the number of neighbors around a non-isolated particle was determined to have no additional influence on the evolution of damage.

These results, coupled with mechanical testing measurements of both global and local properties, were used to develop models describing the flow response of composite materials as damage accumulates. Models were developed to predict the effects of both particle multiple cracking and micro-crack linkage on the composite flow response. The models predict that both damage processes reduce the load bearing capability of the material over that of an undamaged composite, however the loss in load bearing capability is much more severe when micro-crack linkage occurs. Micro-crack linkage rapidly leads to a loss in global stability so that the strain at which the composite fails is significantly less than previous models suggest.

The experimental behavior of the composite materials investigated in the modelling work favors that predicted by the micro-crack linkage model. Ductility predictions resulting from the micro-crack linkage model were sensitive to both the volume fraction and the matrix work hardening exponent. By varying the matrix work hardening exponent the micro-crack linkage model captured the experimentally observed range of ductility values present in literature.

ACKNOWLEDGEMENTS

First and foremost both Prof. D.S. Wilkinson and Prof. J.D. Embury must be acknowledged. Their support, guidance and friendship through my entire time at McMaster kept me focused and ensured that the years I spent working on this thesis will be remembered as some of the most interesting and enjoyable I have experienced. I would also like to thank Prof. D. Metzger for his valuable suggestions and guidance as a member of my supervisory committee.

The tomography work presented in this thesis was possible largely through the efforts of E. Maire (INSA de Lyon, Fr). His efforts in arranging for beamtime at the ESRF and help with both the tomography experiments and data processing ensured the success of the experiments. Both he and L.Babout also guaranteed that my time in France with his group included great times outside of the lab. I would also like to thank J-Y Buffière and all the other researchers at INSA de Lyon and the ESRF for their assistance with the tomography work.

Prof. Y. Brechet (I.N.P.G.Grenoble, Fr) has provided valuable input into the modelling work and other aspects of the research presented in this thesis. I was fortunate to have the opportunity to work with him on the model presented in this thesis a number of times throughout my research. This combined with the lectures he presented while at McMaster provided a large contribution to the knowledge I gained throughout my studies.

D.J. Lloyd and M.Gallernault (Alcan Int. KRDC) have provided useful suggestions and ideas for the tomography and instrumented indentation work presented in this thesis. Both they and CAMM also provided the opportunity to work in the KRDC research laboratories. This also included interacting with a number of Alcan personnel including W.Clapp who was a tremendous help with developing a polishing procedure for the experimental material.

A number of other individuals must be acknowledged. These include Prof. Hani Hanien for the experimental material produced via his impulse atomization technique. I would also like to extend my gratitude to C.Barry and D.Culley for all their assistance with my experimental work, particularly for the hot pressing and

mechanical testing. I would also like to acknowledge the financial support from both the Alcan Fellowship program and NSERC.

My time at McMaster was great largely due to the people I had the opportunity to interact with. Through these interactions many friendships, to numerous to mention, have developed. I would like to thank everyone from the Department of Materials Science and Engineering, in particular A206, for the great times.

Finally I would like to acknowledge the support of my family. The encouragement from my family was instrumental in my successful completion of the degree. Most especially, I would like to acknowledge my wife Angela for her love, friendship, support and encouragement, and my daughter, Alina, for giving me that extra bit of motivation to complete this thesis in a timely manner.

TABLE OF CONTENTS

LIST OF FIGURES

List of Tables

List of Symbols

A-area
a- average particle diameter
b- magnitude of the burgers vector
C- stiffness tensor
C^T- tangent modulus
C^S- secant modulus
C^*- effective stiffness
D- volume fraction of damaged material
d- particle diameter
ϵ- strain
E- stiffness or photon energy
f- volume fraction of phase in composite
g- Brokenbrough and Zok's damage parameter
G- Hashim and Strickman shear modulus
ξ- volume distribution function
λ- edge to edge spacing between particles
I- Identity matrix
K- Hashim and Strickman bulk modulus
L- distance between impenetrable obstacles
m- Wiebull modulus
n- work hardening exponent
n- number of cracks in cracked particles
N- number of photons
p- probability
α- proportionality constant
δ_{ij}- Kronecker Delta
ρ- density
r- particle radius
R- void radius
RA-reduction in area
S- Eshelby Tensor
S^*- compliance tensor
σ- stress
τ- shear stress
μ- shear modulus or attenuation coefficient
ν- Poisson's ratio
V- volume fraction of particles
W- Wiebull function
WHR- work hardening rate
Z- atomic number

CHAPTER 1

INTRODUCTION

The need for lightweight, high performance structural materials has led to the emergence of metal matrix composite materials (MMCs). By the addition of a stiff reinforcement to a ductile matrix, the resulting composite materials yield improvements in strength and stiffness.

Although the modulus and strength of a composite are significantly increased over that of the host matrix, ductility is often sacrificed as a consequence of the second phase addition. This loss of ductility is attributed to premature nucleation and accumulation of damage. The damage mechanisms depend on a number of factors such as interfacial strength, particle volume fraction, shape, size and distribution. These factors are often interrelated and understanding how they affect damage processes, and how they are affected by the flow properties of the matrix, will provide insight into ways of increasing the ductility of these dual phase systems.

Investigation of damage in the form of particle cracking has been limited primarily due to the experimental difficulty in observing the damage process. Particle fracture occurs immediately after the fracture strength of the particle is exceeded making the process difficult to observe experimentally. The final process of micro-crack linkage through the matrix between cracked particles is even more difficult to observe experimentally because the process occurs very rapidly.

While models have been developed to describe the loss of a material's stiffness and strength resulting from particle fracture [Wilkinson *et al.* (2001)], they significantly over-predict the experimentally observed ductility. This is because the models lack a description of the micro-crack linkage process that occurs at the local

scale that leads to fracture. Existing models for the coalescence of damage at the local scale [Brown and Embury (1973)] are typically based on damage involving the growth of voids to a critical length and assume that the distribution of the second phase is uniform. Heterogeneous materials like the AA6111/ Al_2O_3 composite used in this thesis, and most other metal matrix composites, do not have uniform distributions of the second phase, and it will be shown that this significantly effects the strain at which damage nucleastes and the conditions required for damage coalescence.

This thesis is aimed at providing the information necessary to develop a complete description of damage processes involving particle cracking. This includes:

1) Quantifying the effects of damage on the mechanical response.

2) Measuring the local properties of the matrix phase so that an understanding of its role in the damage process can be gained.

3) Quantitative analysis of the damage process in three-dimensions within the bulk of the sample.

4) Investigating the role of damage processes occurring at both the global and local scales.

5) Development of a model that will provide a more complete description of the role of damage on the mechanical response from the point at which deformation begins, until macroscopic instability is reached.

Mechanical testing was used to quantify the effects of damage on the mechanical response of a heterogeneous material. The mechanical testing results presented also

include information on the local matrix properties. This was obtained through the application of a new approach used to predict the elasto-plastic response through instrumented indentation tests.

Quantification of damage itself and its relationship to the overall deformation history was obtained through x-ray computed tomography coupled with in-situ tensile testing. While this technique has been applied in the field of medicine for nearly 30 years at resolution limits of roughly 300 μm, high-resolution (~ 1 μm) imaging of metallic matrix based material has only recently been made possible through the use of synchrotron radiation sources. Use of this technique to study the damage occurring with the experimental material used in this research has yielded new information on damage processes occurring at both the local and global scales. This includes new information on the evolution of damage including multiple cracking of particles and the influence of heterogeneity in the particle distribution on the damage processes. The experiments also provided new information relating the evolution of damage occurring within the bulk to the global level of stress and strain. Other quantitative information obtained includes the sensitivity of damage to particle shape, and aspect ratio.

The information generated through the experimental work was used to develop a comprehensive model for continuum-scale heterogeneous materials that damage through particle cracking. A new model that describes the coalescence of damage that occurs just prior to the onset of tensile instability was developed. Utilizing the model with a self-consistent effective medium analysis that incorporates the reduction in work hardening associated with particle fracture provides good predictions of the overall flow response of one of the materials studied in the current

work. The model also provides a good correlation with the experimentally observed ductility of a number of composite systems [Clyne and Withers (1993)] and indicates how both the volume fraction of the second phase and the work hardening of the matrix influence the composite ductility.

Following this introduction, the work will follow the outline presented in Table 1.1.

Table 1.1. Outline of work presented within the thesis.

Chapter 2	-Review of current methods of modelling the deformation of heterogeneous materials. -Review of models describing damage in heterogeneous materials. -Review of the application of computer aided x-ray computed tomography to study the evolution of damage within a heterogeneous material.
Chapter 3	-Description of experimental materials and manufacturing technique employed to produce the material.
Chapter 4	-Mechanical testing results
Chapter 5	-X-ray tomography results.
Chapter 6	-Presentation of new models developed to describe the damage occurring within heterogeneous materials and the resulting effects of damage on the mechanical response.
Chapter 7	-Discussion
Chapter 8	-Conclusions

CHAPTER 2

LITERATURE REVIEW

2.1 Introduction

Damage in ductile materials containing high modulus, second phase particles, often nucleates through particle/matrix decohesion or particle fracture. Both forms of damage reduce ductility, limiting the commercial application of a broad class of lightweight, high strength materials. The common form of damage nucleation through particle/matrix decohesion has received significant attention [Needleman (1992), Brown and Stobbs (1976), Goods and Brown (1979)], however, investigation of damage in the form of particle cracking has been limited [Brockenbrough and Zok (1994), Llorca and Gonzalez (1997), Wilkinson *et al.* (2001)].

Investigations of damage in the form of particle cracking have been limited primarily due to the experimental difficulty in observing this damage process. As a result, models describing the evolution of damage have been difficult to validate experimentally. Current models also do not include descriptions of the final damage process that lead to failure, and therefore over-estimate the experimentally observed ductilities [Wilkinson *et al.* (2001)].

This review will focus on existing approaches used to model the deformation behaviour of ductile metals containing a reinforcing second phase. In addition, experimental observations of damage evolution and accumulation will be examined in an attempt to distinguish modes of failure most favourable to the model alumina-reinforced aluminum composite proposed for use in this research. Finally, a relatively new

experimental technique used to characterize damage in heterogeneous microstructures- X-ray tomography- will be described.

2.2 Analytical Approaches to Modelling Multi-phase Plasticity

In this section, existing approaches of modelling plasticity in two-phase materials will be investigated. The first is based on discrete dislocation mechanics, while the second is based on continuum mechanics methodology. While the first method is sensitive to scale, the second is not. However, it does allow for the interpretation of some scale dependent effects. Finally, other models including finite element and hybrid finite element schemes will be discussed and compared to results from self-consistent methods.

2.2.1 The Dislocation Plasticity Approach

Mechanisms that examine the interaction of dislocations with the reinforcing phases are often referred to as Orowan type processes. While dislocations can bypass particles through particle shearing, when incoherent particles $\geq$10 nm exist the Orowan processes, described as dislocations bowing between particles, dominate. These mechanisms are based on interactions that occur at the sub-micron scale, and are quite sensitive to particle size and spacing. In general, Orowan processes are most suited to modelling deformation at the submicron length scale [Nan and Clark, 1996].

Deformation in two-phase systems is described with the dislocation plasticity approach based on four distinct contributions to the increase in flow stress. The first, and most significant contribution is based on the Orowan stress. This is the stress required to

move a dislocation along a glide plane containing impenetrable obstacles spaced a distance L apart

$$\Delta\tau = \alpha \frac{\mu b}{L} \tag{2.1}$$

where b is the magnitude of the Burgers vector of the metal matrix, μ is the shear modulus and α is a proportionality constant in the order of 1 to 1.2.

Further contributions arise from differences in coefficients of thermal expansion between the matrix and the reinforcement and interactions based on the scale of the reinforcing particles. Nan and Clarke (1996) report that the sum of the contributions for the increase in yield stress is of the form

$$\left(\Delta\sigma^m\right)^2 = \left(\Delta\sigma^m_{OR} + \Delta\sigma^m_{KIN}\right)^2 + \left(\Delta\sigma^m_{ISO}\right)^2 + \left(\Delta\sigma^m_{CTE}\right)^2 \tag{2.2}$$

where the subscripts OR, KIN, ISO and CTE represent the Orowan stress contribution, the kinematic and isotropic forms of the strain gradient contributions and the contribution arising from differences in the coefficients of thermal expansion. A comprehensive discussion of the micro-mechanical contributions to the increase in flow stress is given by Kelly and Nicholson (1971).

2.2.2 Effects of Scale

The approaches just discussed are generally most suited for description of micromechanics at the sub-micron length scale. When the scale exceeds a micron or so, the modelling work of Nan and Clark (1996) indicates that the size dependency diminishes, as illustrated presented in Figure 2.1. In their work, they modelled an Al alloy (A356, T4 condition) containing 13 vol.% SiC in a hypothetical size range of 10 nm

to 50 μm. The results show that the strength degrades rapidly with increased particle size up to a few microns. Once the particle size exceeds this, further increasing the particle size has a small effect on changing the strength level. At these larger length scales continuum based models become more suitable for the modelling of heterogeneous materials because of their size independence. There exists a scale in the range of 1 to 10 μm where neither continuum nor micro-mechanical models are individually adequate. In recent years, numerous authors [Lipkin *et al.*(1996), Fleck *et al.*(1994)] have developed theories to account for the mechanical behavior of materials at this intermediate length scale. A full description of this field of study, often referred to as strain gradient plasticity, is beyond the scope of this work because the reinforcing particles used in this research exceed this length scale. A good review of this field of research is given by Hutchinson (1998).

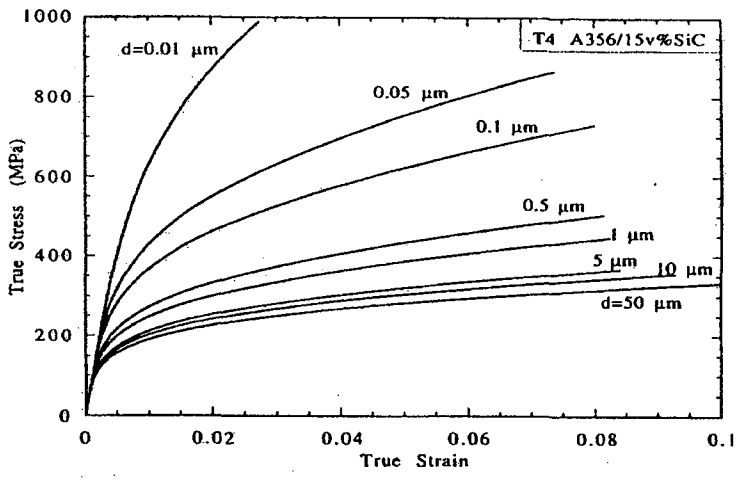

Figure 2.1. Dependence of flow stress on particle scale for a SiC/Al356 composite. After Nan and Clark (1996).

2.2.3 The Continuum Approach to Dual Phase Plasticity

As previously mentioned, continuum approaches to dual phase plasticity are most suited to modelling materials at a characteristic length scale greater than 10 μm. The

classical models are founded on the early works of Eshelby (1957) and Hill (1963). The models, although independent of scale, have been modified to incorporate some scale dependent contributions.

2.2.4 Linear Elastic Theory

To describe the linear elastic theory for a dual phase composite one must consider an ideal material, i.e., one with phases that are simply connected, with ideal perfect bonding and differing elastic constants. A solution describing the average properties of the composite, knowing only the volume fraction and the properties of the bulk phases, is given as follows

$$\langle \sigma \rangle = V_1 \langle \sigma_1 \rangle + (1 - V_1) \langle \sigma_2 \rangle \tag{2.3}$$

$$\langle \varepsilon \rangle = V_1 \langle \varepsilon_1 \rangle + (1 - V_1) \langle \varepsilon_2 \rangle \tag{2.4}$$

where the subscripts represent the stress and strain tensors for the ith phase. The volume fraction of phase 1 is represented by V_1, and that for phase 2 is represented by $(1\text{-}V_1)$. Assuming that both phases are linear elastic, (2.3) and (2.4) may be written in terms of the compliance and stiffness, C_i and S_i^* tensors respectively,

$$\langle \sigma \rangle = V_1 C_1 \langle \varepsilon_1 \rangle + (1 - V_1) C_2 \langle \varepsilon_2 \rangle \tag{2.5}$$

$$\langle \varepsilon \rangle = V_1 S_1^* \langle \sigma_1 \rangle + (1 - V_1) S_2^* \langle \sigma_2 \rangle \tag{2.6}$$

Following Conlon [1998], the strain in each phase may be written in terms of the average composite strain, $\langle \varepsilon \rangle$, multiplied by an arbitrary tensor **A**

$$\langle \sigma \rangle = V_1 C_1 A_1 \langle \varepsilon \rangle + (1 - V_1) C_2 A_2 \langle \varepsilon \rangle \tag{2.7}$$

Defining C^* as the effective stiffness tensor, the average stress may be written in terms of the average strain as

$$\langle \sigma \rangle = C^* \langle \varepsilon \rangle \tag{2.8}$$

By combining (2.7) and (2.8) an expression relating the effective composite stiffness to those of the individual phases may be obtained.

$$C^* = V_1 C_1 A_1 + (1 - V_1) C_2 A_2 \tag{2.9}$$

If the strain distribution between the phases is known, the effective stiffness reduces to,

$$C^* = C_2 + V_1 (C_1 - C_2) A_1 \tag{2.10}$$

A similar expression may be written to yield an expression for the effective compliance tensor if the stress distribution is known.

$$S^* = S_2^* + V_1 \left(S_1^* - S_2^* \right) B_1 \tag{2.11}$$

where B_1 is the tensor representing the stress distribution between phases Consider a continuous fiber reinforced composite loaded along a direction parallel to the fibers. The

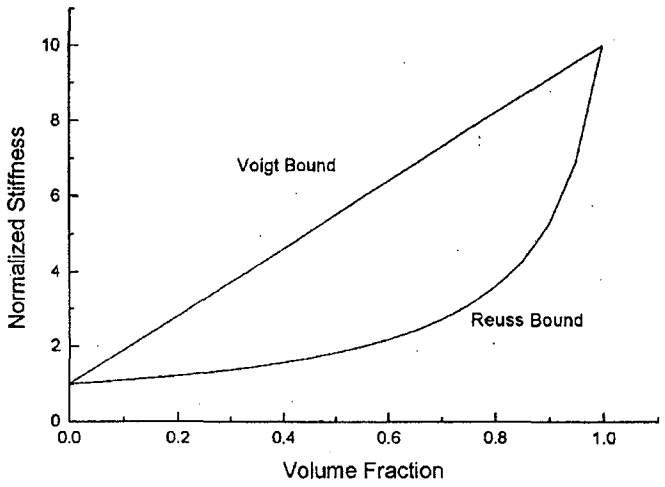

Figure 2.2. Graphical representation of the upper, "Voight" and lower, "Reuss" stiffness bounds as a function of second phase concentration. The normalized relative stiffness of the two phases, C_1/C_2 is ten. After Conlon, (1998).

loading dictates equal strain partitioning in each phase, reducing the value of A_1 to the identity matrix. This equal strain partitioning case is known as the "Voight" upper bound. A lower bound is established by considering equal stress partitioning, as would be the case of a continuous fiber composite loaded perpendicular to the fibers. The equal stress partitioning, or "Reuss" lower bound on composite stiffness is obtained by setting B_1 equal to the identity matrix in eq. (2.11). A graphical representation of the Voight and Reuss bounds is given in Figure 2.2.

Although the Voight and Ruess bounds do define the upper and lower limits of composite stiffness, the results are based entirely on satisfying either one of two boundary conditions. As a consequence, the boundary conditions defined at the interface consider either the strain compatibility or mechanical equilibrium, but not both. Further, the models assume ideal interfacial strength, resulting in predictions of the maximum extremes of the stress or strain within the composite.

Hashim and Strikman (1963) introduced a variational procedure to estimate the stiffness of statistically isotropic microstructures containing spherical second phase particles. The rigorous solution, based on elastic strain energy relationships, provides upper and lower bounds of the effective modulus. The method requires that the elastic modulus of the reference material medium be equal to the maximum and minimum tensor values of the participating phases. A full derivation is provided by Hashim and Strickman (1963). Their results provided expressions of the upper and lower bounds, K_U, G_U and K_L, G_L respectively, of the following form

Bulk Modulus Bounds

$$K_L^* = K_1 + \frac{V_2}{\frac{1}{K_2 - K_1} + \frac{3V_1}{3K_1 + 4G_1}} \quad (2.12)$$

$$K_U^* = K_2 + \frac{V_1}{\frac{1}{K_1 - K_2} + \frac{3V_2}{3K_2 + 4G_2}} \quad (2.13)$$

Shear Modulus Bounds

$$G_L^* = G_1 + \frac{V_2}{\frac{1}{G_2 - G_1} + \frac{6(K_1 + 2G_1)V_1}{5G_1(3K_1 + 4G_1)}} \quad (2.14)$$

$$G_U^* = G_2 + \frac{V_1}{\frac{1}{G_1 - G_2} + \frac{6(K_2 + 2G_2)V_2}{5G_2(3K_2 + 4G_2)}} \quad (2.15)$$

where V_j represents the volume fraction for each phase, K_j and G_j are the bulk and shear modulus of each phase and phase 2 is the reinforcement. The Hashin-Strikman bounds provide much better estimates of the upper and lower limits of bounds for spherically reinforced composites over those predicted by the Ruess and Voight models. Other authors [Talbot and Willis (1985)] have developed models based on the original Hashin-Strikman bounds, further improving the bound estimates for both linear and non-linear composites.

2.2.5 Eshelby Model

A finite prediction of a composite's mechanical response was significantly improved through the seminal work of Eshelby (1957). The Eshelby model accounts for internal stresses resulting from differences in mechanical or physical properties. An analytical technique to account for the *misfit* in properties between two phases has been developed for an ellipsoidal inclusion of any aspect ratio. The key requirement for the analytical solution is based on the fact that the stress at any point within an ellipsoid is constant.

Following the imaginary cutting and welding exercises described by Clyne and Withers (1993), consider an ellipsoidal region of homogeneous medium (an inclusion) removed from the matrix as shown in Figure 2.3. Now imagine that the region undergoes a transformation in shape (ε^T), so that it no longer freely fits back into the location in the matrix from which it came. To fit the inclusion back into the hole, surface tractions must be applied. Once the inclusion is placed in the region from which it came, the inclusion and matrix are welded together at the interface. Tractions are removed and the inclusion reaches equilibrium with the matrix at a constrained strain, ε^C.

The stress in the inclusion may be calculated based on Hooke's Law in terms of the elastic strain, ($\varepsilon^C - \varepsilon^T$) and the stiffness E_M.

$$\sigma_I = E_M(\varepsilon^C - \varepsilon^T) \tag{2.12}$$

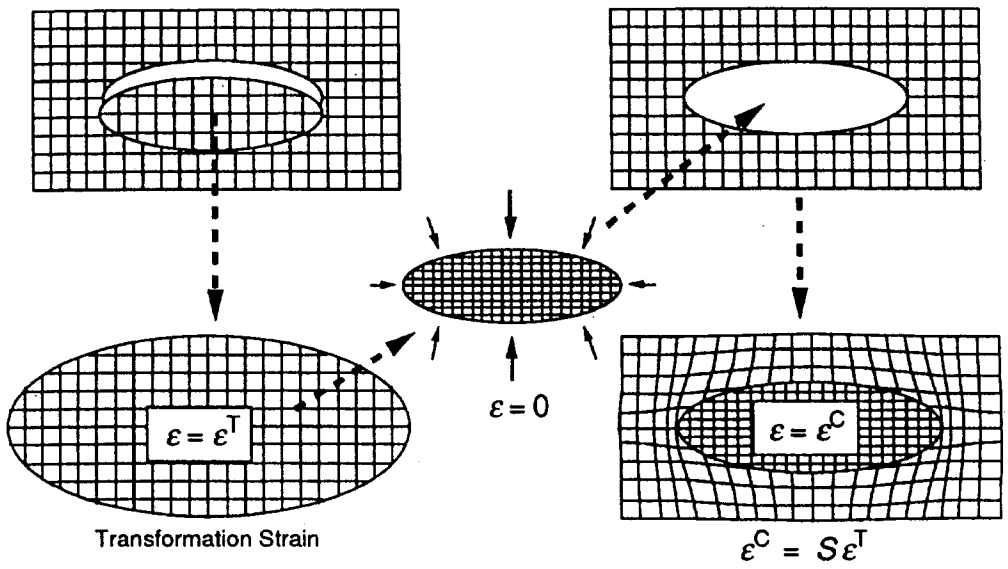

Figure 2.3 Illustration of Eshelby's imaginary cutting and welding exercises. After Clyne and Withers (1993).

The constrained strain may be written in terms of the transformation strain by the Eshelby tensor, *S*, based on the aspect ratio and Poisson's ratio of the inclusion material. As a result, the stress in the inclusion can be calculated through

$$\sigma_I = E_M (S - I)\varepsilon_T \tag{2.13}$$

where I is the identity matrix. The Eshelby tensor for a spherical inclusion is of the form

$$S = \frac{5\nu - 1}{15(1-\nu)}\delta_{ij}\delta_{kl} + \frac{4 - 5\nu}{15(1-\nu)}(\delta_{ik}\delta_{jl} + \delta_{il}\delta_{jk}) \tag{2.14}$$

where ν is Poisson's ratio and the δ_{ij} is the Kronecker delta. Calculation of the inclusion stress can be shown to reduce to [Clyne and Withers, (1993)],

$$\sigma_i = \frac{E_M (S - I)}{(E_i - E_M)S + E_M} E_i \varepsilon^{T^*} \tag{2.15}$$

where E_M and E_I represent the stiffness of the matrix and inclusion respectively, and ε^{T*} is the stress free transformation strain. Corbin and Wilkinson (1994) have shown that ε^{T*} is a function of applied strain and can be found using equation (2.15).

2.2.6 Self-Consistent Models

Although Eshelby's model provides useful predictions on the stress partitioning between phases, the model is limited to modelling dilute concentrations (f<1%) of the second phase. Numerous authors have attempted to extend the solution to account for higher concentrations of the second phase [Withers *et al.* (1989), Taya and Chou (1980), Auriault (1991)].

A successful approach to determining the effective elastic modulus of a composite originated from the early work of Hill (1963). The approach, called the self-consistent method, was based on a method first proposed by Hershey (1954) in studies of polycyrstalline materials. Numerous authors have since developed several variants of the original model proposed by Hill. The mathematical formulations of the self-consistent models vary and are mathematically complex. Although a full description of all models is beyond the scope of this work, the review will focus on a successful derivative of the earlier models. A good review of existing self-consistent models is given by Molinari et al (1997).

Two distinct approaches have emerged as the preferred methods for analytically modelling deformation. These approaches are known as the "Self-Consistent Effective Medium Approximation" (SCEMA), and the "Self Consistent Effective Field Approximation" (SCEFA). The two approaches are illustrated in Figure 2.4. In the SCEMA (Figure 2.4(b))

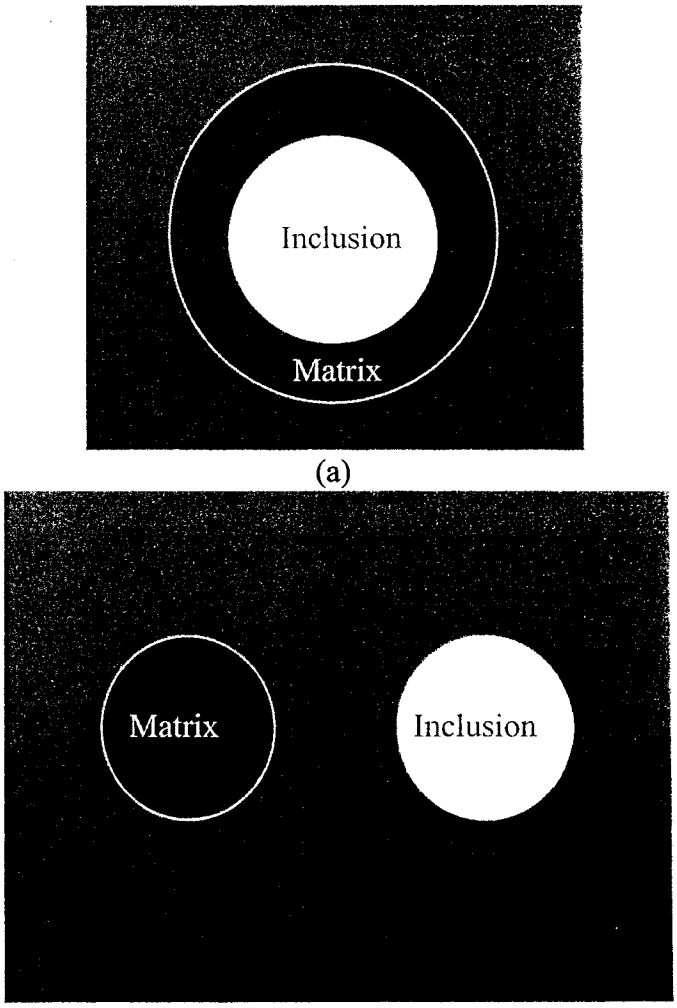

Figure 2.4. Graphical representation of the SCEFA, (a), and the SCEMA, (b), for a dual phase composite consisting of inclusions and a matrix.

both the hard phase and the soft phase are treated as randomly distributed inclusions embedded within the composite phase whose properties are initially unknown. An advantage of the SCEMA model is that the model does not require additional geometrical information (i.e. a definition of the matrix phase is not required), with exception to the average shape of the grains, for solution of the effective properties. The SCEFA (Figure 2.4 (a)), also termed the "Three Phase Model" by Christensen and Lo (1979), surrounds the hard phase by a uniform layer of the softer phase. The two phases are then further embedded in the composite, an effective medium possessing the average properties of both phases.

At low volume fractions of the second phase, both models yield similar results. As volume fraction increases, predictions of the overall effective properties diverge. The soft layer surrounding the harder phase in the SCEFA is assumed to remain connected even at high volume fractions. As a result, the effects of an elastic network of the hard phase are not included throughout the concentration spectrum, providing a "softer" response to changes in second phase concentration. In the SCEMA, each phase is treated separately, resulting in a more significant dependence on concentration, and an increase in strengthening over the SCEFA.

The SCEMA method is founded on Eshelby's equivalent inclusion method described earlier. However, in the case of the SCEMA formulation, the particle samples the average properties of the composite it is embedded in, rather than that of the matrix as in the equivalent inclusion method. Following Hill's (1963) original work, Corbin and Wilkinson (1994) show that the stress in the particle can be related to the applied load, σ^A, by

$$\sigma_{11}^{p} = \left[\frac{E_p}{SE_p + (1-S)E_c}\right]\sigma_{11}^{A} \tag{2.15}$$

where E_p and E_c are the modulus of the particle and the composite respectively. In the SCEMA method the matrix is modelled as a soft inclusion embedded in a uniform composite. As a result, the stress in the matrix phase can be approximated in the same manner as the particle by replacing the elastic modulus of the particle in (2.15) with that of the matrix. Through this approach the average stress in both the matrix and particle within the composite can be calculated.

As load is applied to a two-phase composite, each phase constrains the other. The total applied stress is carried by both phases, the degree to which will depend on the volume fraction and misfit stress. In loading, misfit or internal stresses arise from differences in the elastic modulus. To maintain equilibrium, these internal stresses must sum to zero

$$V_m\langle\sigma_m\rangle + V_p\langle\sigma_p\rangle = 0 \tag{2.16}$$

where V_m and V_p are the volume fractions of each phase and $\langle\sigma_m\rangle$ and $\langle\sigma_p\rangle$ are the internal stresses. Through superimposing the applied stress, σ_A, this may be expressed as

$$V_m\left(\langle\sigma\rangle_m + \sigma_A\right) + V_p\left(\langle\sigma\rangle_p + \sigma_A\right) = \sigma_A \tag{2.17}$$

Since the total stress within each phase is a sum of the internal stress and the applied load

$$\langle\sigma\rangle_m + \sigma_A = \left[\frac{E_m}{SE_p + (1-S)E_c}\right]\sigma_A \tag{2.18}$$

$$\langle\sigma\rangle_p + \sigma_A = \left[\frac{E_p}{SE_p + (1-S)E_C}\right]\sigma_A \tag{2.19}$$

The solution is self-consistent because the only knowledge needed to calculate the properties of the overall composite is the internal constraint between two phases. Through substitution of the matrix and particle stress, as given by eqs. (2.18) and (2.19), into eq. (2.17), the equation may be rearranged to yield an expression of the form (for S=7/15, Poisson's ratio of 1/3 and a single component of applied stress)

$$8E_C^2 + \left[(7-15V_p)E_p + (7-15V_m)E_m\right]E_c - 7E_pE_m = 0 \qquad (2.20)$$

where E_c, E_p and E_m are the elastic modulii of the composite, particle and matrix respectively. Christensen (1990) shows that a similar form holds for the SCEFA. Therefore, through solution of eq. (2.20) it is always possible to solve for the elastic modulus of the composite by knowing the elastic modulii of the particles and matrix.

2.2.7 Non-Linear Self-Consistent Models.

In the previous section, the SCEMA method was developed under the assumption that the composite deforms as a linear-elastic solid. However, for plastically deforming or creeping solids, the constitutive relation used in place of the elastic modulus is generally non-linear.

As a result, continuum approaches of modelling plastic deformation in two phase materials are treated incrementally. That is, the flow curve of either one, or both phases, are derived at small increments so that the instantaneous properties of the solid are assumed constant. At each increment of deformation, the properties of each phase are updated, using the physically appropriate constitutive law, to account for the change in mechanical response of each phase. These properties are then fed back into the global

constitutive relation (as an example eq. (2.20)) to calculate the effective response of the composite at each increment of strain.

Hutchinson (1970) approached this problem by defining the instantaneous tangent modulus C^T as the slope of the flow curve at an instantaneous strain, ε.

$$C^T = \frac{\partial \sigma}{\partial \varepsilon} \tag{2.21}$$

where σ is a function of flow stress dependent on strain rate, strain history, temperature etc. Budianski (1959) used a similar function of stress to define the secant modulus C^S. The secant modulus is defined as the ratio of flow stress to instantaneous strain.

$$C^S = \frac{\sigma}{\varepsilon} \tag{2.22}$$

A comparison of the two approaches is represented graphically for a strain hardening solid in Figure 2.5. In this representation, the solid is assumed to obey the Ramberg-Osgood relation for a power-law hardening solid.

$$\varepsilon = \frac{\sigma}{E} + \alpha \frac{\sigma_o}{E} \left(\frac{\sigma}{\sigma_o} \right)^{1/n} \tag{2.23}$$

where σ_o is a "reference stress", α is a proportionality constant and n is the hardening exponent. Through rearrangement of (2.23) the tangent modulus of a Ramberg-Osgood solid may be defined as

$$C^T = \left[\frac{1}{E} + \frac{\alpha}{E} \left(\frac{\sigma}{\sigma_o} \right)^{(1/n)-1} \right]^{-1} \tag{2.24}$$

In the elastic regime the secant and tangent moduli are identical. However, in the plastic regime the values of each differ. The degree at which the two values differ is

dependent on the magnitude of the hardening exponent. As n increases, values of the tangent and secant modulus converge. At lower values of n, the difference between the two moduli becomes considerable as shown graphically in Figure 2.5.

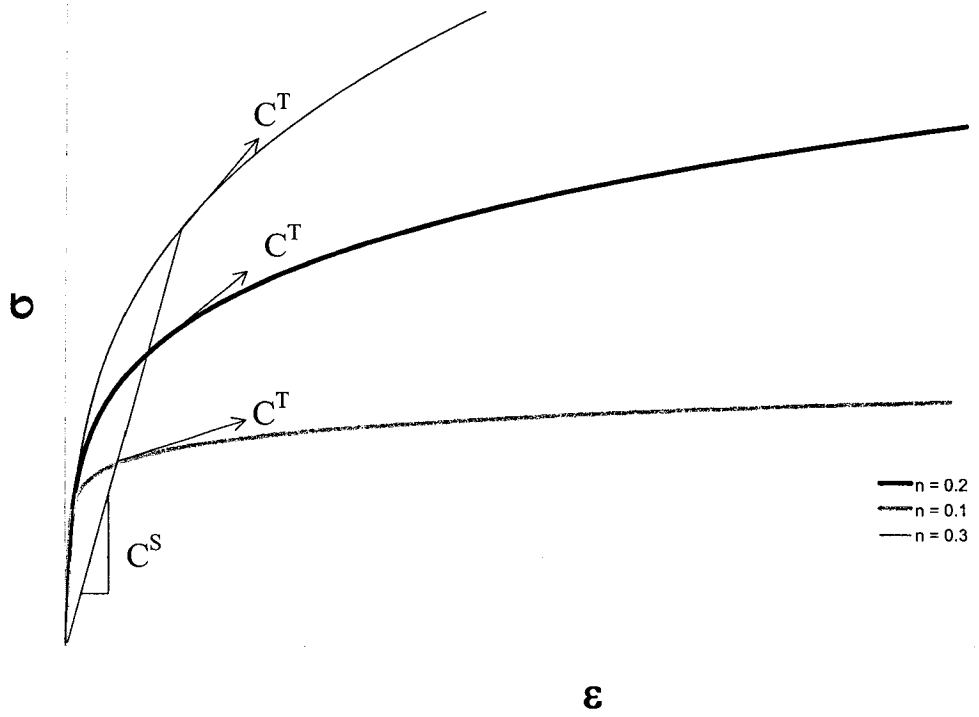

Figure 2.5. Graphical representation of the secant and tangent modulus construction for a power-law hardening solid, with σ_0= 70 MPa and E=70 GPa, at low plastic strain. As the hardening exponent, n, increases the values of the secant and tangent modulus converge.

The correct choice of either the tangent or secant modulus construction has not received significant discussion in literature. Wilkinson *et al.*(1997) used each construction in their SCEMA models to predict the deformation behaviour of a SiC particulate reinforced Al alloy. Their results indicate that the secant modulus approach predicts higher strengthening than that using the tangent modulus. Experimental results indicate that the softer response of the tangent modulus construction predicts the flow

curves more accurately. Molinari *et al.*(1997) have examined both approaches in the self-consistent modelling of grain-matrix interaction of polycrystals. Their results indicate that the tangent modulus provides too soft a response for rate independent materials and that the secant modulus provides a result that is too stiff. Their discussion indicates that the real interaction law should be softer than the secant formulation and stronger than the tangent formulation.

The self-consistent method of modelling plasticity in dual phase alloys provides a good approximation of the composite flow curves as shown in Figure 2.6. One of the greatest strengths of this method is the ability to model a heterogeneous distribution of the second phase reinforcement. By embedding high and low volume fraction regions in the composite medium, the averaging effects of interactions between the phases during plastic deformation are captured. As a result, these models provide better approximations

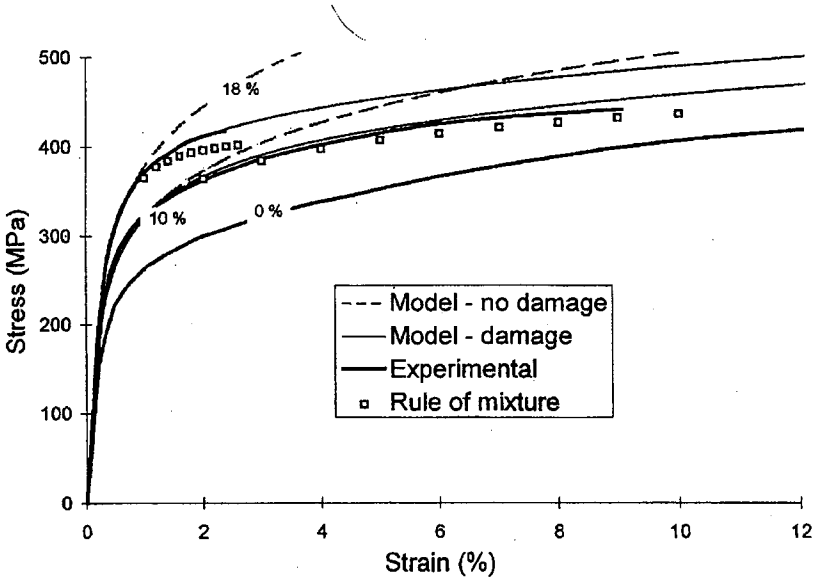

Figure 2.6. Comparison of SCEMA models developed by Wilkinson and coworkers with experimental results. The model also includes a damage calculation discussed in detail in sections 2.5.3 and 6.1. [Wilkinson *et al.*, 1996.]

to the global effects of heterogeneity than the finite element models discussed in the following section. Although some accuracy in results is lost at the local scale in the self-consistent models, the models provide good estimates of the global response of a plastically deforming composite.

2.3 Numerical Approaches to Continuum Plasticity

The finite element method (FEM) has also been used to model the mechanical response of dual phase materials. This method is based on either implicit or explicit piecewise descretization of a variational method. Solutions provide accurate, detailed information of deformation at the local scale with the advantage of being able to deal with complex geometry.

Two approaches have emerged in the recent FEM modelling of the mechanical response of dual phase materials. One is the elastic-plastic analysis [Argon *et al.* (1975), Watt *et al.* (1997)] used for modelling time independent small scale plastic deformation. A second method is that of the elastic-viscoplastic analysis used to model time dependent plastic behaviour[Christensen *et al.* (1989), Needleman *et al.* (1989)]. Provided that the work hardening is fairly insensitive to strain rate, the elastic plastic analysis is usually a more efficient method of modelling.

As commercial FEM packages evolve, the implementation of material dependent constitutive relations has become a much more straightforward task. Automatic mesh generators have simplified the task of creating appropriate meshes to model deformation. Further improvements in processing efficiency including adaptive meshing techniques have reduced computing time [(Mavriplis (1997)]. However, even with these

improvements, limitations do exist. FEM is based on the solution of governing differential equations at individual nodes of a mesh. For accuracy, the mesh size must be fine to capture local interactions dependent on shape and scale. As the mesh is refined the number of differential equations requiring solution expand, increasing the solution time exponentially. As a result, models are usually based on a local representative element, often referred to as a unit cell, to model the global response of the material. The unit cells often consist of usually only one representative reinforcing particle in a ductile matrix. Even though the models provide very accurate results at the local scale, their effectiveness in describing global behaviour is of concern. Further, the method does not possess the flexibility to efficiently vary the concentration or distribution of the second phase. Essentially, a new mesh, or model, is required each time the second phase concentration or distribution is modified.

An additional weakness with the use of FEM calculations used to model composite flow behavior, is the limitation to modelling the effects of second phase distribution. When the distribution is uniform, the global plastic response is satisfactorily modelled using the unit cell approximation. The effects of volume fraction on the flow curve are considered by scaling the ratio of the size of the reinforcing particle to that of the surrounding matrix. However, when the distribution is not homogeneous, the unit cell approach is quite sensitive to scale. The unit cells used to model clusters of particles are usually limited to containing two to three representative reinforcing particles. Results of these calculations are very sensitive to particle size, spacing and orientation. To accurately model the high volume fraction (clustered) regions, the unit cells must provide an accurate scale representation of the physical microstructure. When the effects of two

or more particle distributions within the cell are desired, the models are more prone to error because the interaction between unit cells will depend on the scale of each cell and the averaging effects of the distributions are not considered. As a consequence, it is difficult to create models that will accurately capture the effects of high and low volume fraction regions on the composites global plastic response. Although the FEM approach provides detailed information at the local scale, the models are not well suited to treatment of heterogeneity in the spatial distribution of the reinforcing particles.

2.4 Finite Element Embedded Cell Methods

Two notable models have been developed in an attempt to bridge the gap between the accuracy of the FEM and the efficiency of self-consistent based models. The first of these models is called the 3D axisymmetric model developed by Bao (1992) following the work of Needlemen *et al.* (1989). The cell model is a finite element model designed to represent a uniform distribution of particles in a ductile matrix. Spherical inclusions are embedded in the center of hexagonal cells, possessing the properties of the matrix. To reduce the computational complexity, the hexagonal cells are approximated as cylinders. The composite is made up from an array of these cells each possessing the appropriate boundary conditions. During loading, the cylindrical surfaces are constrained to remain cylindrical, however, they are permitted to dilate with zero average normal stress. Faces perpendicular to the loading direction must remain planar with zero average shear stress and an average normal stress of σ. In Bao's work, the ABAQUS finite element package was used to solve the boundary value problems at small strain increments.

A second model, called the embedded cell model [Dong and Schmauder (1996)] uses a somewhat different approach. In this case, the embedded cell is a finite element model of a spherical inclusion surrounded by a spherical coating of matrix, embedded in a rectangular "equivalent composite medium". This method imposes the mechanical response of the matrix and inclusion on the entire composite. Solution of the effective composite properties is achieved through an iterative process. The composite material is initially assigned an arbitrary stress-strain response. A comparison is then made between the material response and that of the embedded cell (say that of the matrix). If the responses differ, the material is then assigned the response of the embedded cell. The process repeats until the two results converge. Boundary conditions assigned to the rectangular embedding medium are similar to those of the 3D axisymmetric model. The overall shape is constrained to remain rectangular with zero normal and shear stress acting on the lateral surfaces. Surfaces perpendicular to loading are constrained to zero shear stress and a normal stress equivalent to σ. In the embedded cell method, the equivalent medium must be significantly larger than the embedded cell to represent an infinite medium.

Recently the embedded cell method has been revised to include the microstructural matricity [Dong *et al.* (1999)]. Phases in the structure are reduced to skeletal lines as shown in Figure 2.7. In the unique case of a sphere, the length of the skeletal lines reduces to a point. In the next step, the lengths of the skeletal lines S_α and S_β in the matrices are represented by the circumference of a circle with a diameter obtained through an average of the diameter of the embedding cell and the inclusion phase. Through this approach it is possible to define the matricity as the fraction of

length of the skeletal lines of one phase and the length of the skeleton lines of the participating phases.

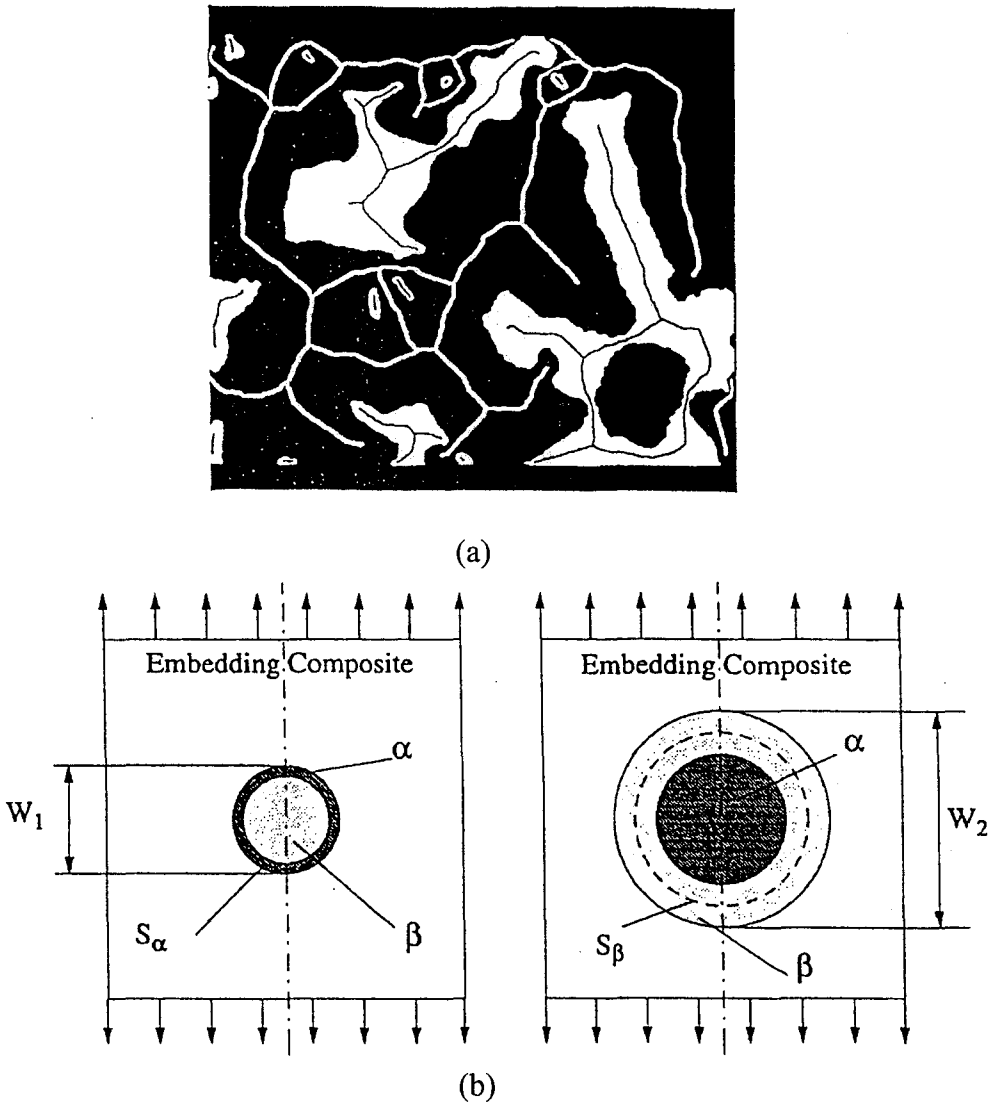

Figure 2.7. Illustration of embedded cell used by Dong *et. al.* (1999) with the incorporation of the matricity calculation of the represented microstructure. Skeletal lines (S_α and S_β) shown on phase α (white phase in Figure 7 (a)) and β (dark phase in Figure (a)). The skeletal lines are then used in embedded cell model where in one part the α phase is treated as the inclusion and another part where the β phase is treated as the inclusion.

A solution for the mechanical response follows the same approach as that for the embedded cell model described earlier with the addition of a matricity calculation. The diameters of the embedded cells are given as W_1 and W_2 that, along with the volume fraction of inclusions, dictate the diameter of the inclusion in the embedded cell. The unique advantage of this model is that it includes the effects of reinforcement shape, in addition to volume fraction, in the calculation of the composite's mechanical response. Experimental results indicate that the self-consistent embedded cell model provides a slightly better prediction than the SCEMA method. However, differences between the two models do not rule out the use of the SCEMA models for good estimates of the composite properties. The self-consistent embedded cell model, although powerful and more efficient than the pure FEM based method, requires significantly longer processing times than the self-consistent models and are best suited for modelling when local scale accuracy is critical.

2.5 Damage in Heterogeneous Materials

Ductile materials containing a second phase often suffer from lower ductility, when compared to their monolithic counterparts. The poor ductility results from the increased susceptibility to damage during the deformation process. Although, the deformation process contributes to the overall damage in ductile materials, the inhomogeneity of deformation is the controlling factor in dual phase materials. In ductile materials containing second phases, damage nucleates at the second phase either through particle cracking and/or cavitation due to the plastic constraint imposed by the particles.

The void growth and coalescence mode of failure has been reported by Whitehouse and Clyne (1992) in Al_2O_3 reinforced commercially pure aluminum. Their research studied the effects of two processing routes and particulate shape on damage nucleation. Results indicate that cavitation occurred preferentially for spherical particle reinforced aluminum processed through the powder metallurgy route. This may be attributed to the uniform stress distributions existing in the spherical powders and the weaker interfacial strengths provided by the powder metallurgy route over molten metal processes. Composites manufactured with angular particles using a squeeze casting process favoured particle fracture as the mode of failure. Failure of composites through void growth and coalescence is a common mode of failure in this class of materials and has been reported by authors for several dual phase systems [Guillemer-Neel *et al.* (2000), Thomson *et al.* (1998)]

Others have reported that particle fracture, followed by inter-void matrix cracking, as the favoured mode of failure in many composite systems. This mode is a dominant form of failure in particulate reinforced composites, particularly when particle sizes are large and the interfacial strength is high. Failure through particle fracture has been experimentally observed by Lorca and Gonzalez (1998), Whitehouse and Clyne (1992), and Srivastan (1996) in Al_20_3 reinforced Al alloys. Other authors have studied failure by particle cracking in SiC reinforced Al alloys. [Maire *et al.*(1997), Brechet *et al.*(1991), Kiser *et al.*, (1996)].

2.5.1 Void Nucleation, Growth and Coalescence

In some ductile materials, damage results from void nucleation, growth and coalescence of voids. When particle sizes exceed 1 μm a continuum plasticity approach is employed to model the propagation of damage [Thomason (1990), Giulliemer-Neel *et al.*(2000)]. The inclusion is usually assumed to have a higher modulus and much higher yield strength than the plastically deforming matrix. In many models, the inhomogeneity of deformation is calculated through an approach based on Eshelby's equivalent inclusion method described earlier. In the models, and experimental evidence reported in literature, there exists a critical state of strain or stress at which cavity nucleation occurs.

As stress is applied to a dual phase material, the matrix undergoes plastic deformation while the particle remains elastic. The modulus mismatch causes preferential stress partitioning to the particles, creating particle stresses that are often much higher than the far field matrix values. Many of the void nucleation models predict that a cavity will form at a critical strain based on an energy balance calculation. Both the micromechanical approach of Brown and Stobbs (1976) and Tanaka *et al.'s* (1970) continuum approach for spherically shaped inclusions, estimate that cavitation will occur if the elastic strain energy released is greater than or equal to the surface energy created. However, Goods and Brown (1977) report that the model proposed by Tanaka *et al.* is in poor agreement with experimental results and is strictly only appropriate when plastic relaxation is suppressed by particle shape effects associated with unrelaxed spherical particles. Argon *et al.* (1975) have proposed a continuum based model, including the incorporation of a dislocation punching mechanism, predicting cavitation to occur at a far field shear strain value at which the threshold of the interfacial stress is exceeded. The

main difference between the models is that Argon *et al.'s* model is a continuum based model, while the model of Brown and Stobbs reflects the increase in flow stress around a particle due to the increased rate of dislocation storage in that region.

In most materials, the shape, orientation and particle distribution influence the macroscopic strain at which local damage occurs. Since these factors modify the state of stress around the particle, the process of nucleation becomes much more difficult to predict. To incorporate these factors, Chu and Needlmen (1980) have adopted a statistical approach, based on a normal distribution of stress about the mean, to estimate the mean critical stress required for void nucleation.

Numerous studies have been conducted on the phenomenon of void growth. These studies have provided analytical laws based on single void growth [Rice and Tracy (1969)] for different void geometries and matrix mechanical behaviour. These single void analyses established the strong effect of hydrostatic tension on the growth of voids in a ductile metal. The models all tend to follow the classic growth law and are highly dependent on the stress triaxility

$$\frac{dR}{R} \propto f(\sigma_{Tr})d\varepsilon_p \qquad (2.25)$$

where R is the void radius, σ_{Tr} is the stress triaxility and ε_p is the plastic strain.

The phenomenon of void coalescence is the least understood of the three processes since it is a process of instability. Different modes of coalescence have been reported based on inter-void matrix necking or shear instability [Clyne and Withers (1992)]. The models describe a critical criteria growth parameter, for example that used in the model proposed by Brown and Embury (1973) or critical void volume fraction at

which nearly instantaneous coalescence of voids occurs. Others like Thomason (1968) proposed a model based on a load-limit failure of the inter-void matrix.

2.5.2 Particle Cracking and Crack Propagation

Significantly less literature is available on the phenomenon of damage initiation through particle cracking. Some authors [Brokenbrough and Zok (1994)] have developed quantitative measures of damage accumulation through particle cracking. Although models for particle fracture, often based on a statistical approach, have been developed, few if any analytical models describing the phenomenon of crack linkage through the inter-particle matrix have been proposed.

As a composite material is strained, an amplification of stress carried by the particles results from the increased stiffness over that of the matrix. In some cases, especially when the particles are large and the interfacial strength is high, the stress may exceed the fracture strength causing the particles to break. The percentage of particles fractured at a given strain depends on many factors including the matrix flow stress, particle shape, size and flaw size distribution.

Numerous authors have accounted for damage accumulation through particle fracture in continuum models. Mochida *et al.* (1991) have used an effective medium approach to model the experimentally observed progressive reduction in elastic modulus that occurs with the evolution of damage, in the from of cracked particles, in a metal matrix composite. Their continuum model required the calculation of the full stiffness tensor for each phase. When particles fractured, their approach to cracked particles was to replace them with an equivalent volume of matrix containing a penny shaped crack

across the diameter. Their study did not consider the aspect ratio and the method used to calculate local relaxation was not clear. Zhong *et al* (1999) modified their model to incorporate the effects of either particle shattering or particle cracking, where some load could still be carried by the particles, on the composite's mechanical response. The approach was essentially similar to Mochida's work with the exception that modified Eshelby tensors were used. The tensors were calculated through the use of FEM calculations for a cracked particle and a shattered particle, resulting in a value similar to Mochida's. Although the models predicted a reduction in the average composite elastic modulus, the work was based on elastic deformation, so no information on the effects of plastic deformation and the rate of particle fracture were considered.

One particularly useful model for describing the role of particle fracture on the plastic deformation and fracture of metal matrix composites was developed by Bockenbrough and Zok (1994). Their work extended an original FEM study performed by Bao (1992) that investigated the effects of both intact and cracked particles on the flow response of composites comprised of elasti-perfectly plastic matrixes and spherical particles. In Brockenbrough and Zok's work, the role of matrix work hardening and the elastic mismatch between the particles and the matrix were added to the study. By varying both the elastic mismatch and work-hardening exponent, they determined that apart from the initial transient, the flow response of a composite containing cracked particles was proportional to the matrix flow stress. They expressed this through a simple relationship of the form:

$$\sigma_{damaged}^{composite} = g_{damage}\sigma^{matrix} \qquad (2.26)$$

where g_{damage} is a function of work hardening exponent only and σ^{matrix} is the matrix flow stress. More recently Llorca and Gonzalez (1998) have shown that similar, but more complex polynomial expressions, can be used to describe how particle geometry effects this relationship.

Experimental work provides evidence that the reduction in work hardening as damage evolves is due largely to the loss of constraint associated with particle fracture. This was shown most elegantly by Kiser *et al.* (1996). In their work they pre-strained an Al-20% Si alloy in the T4 condition to a point just prior to instability defined by the Considére criterion. This deformation caused the material to become highly damaged. The sample was then heat treated to the T6 condition and retested. Upon reloading the highly pre-damaged sample exhibited ductility almost 2.5 times that of pristine material. This resulted from the fact that the pre-damaged sample did not nucleate any new damage and therefore the loss in composite work hardening was much lower than that of a damaging material. This therefore delayed the onset of instability over that of the damaging material. It is therefore evident that fracture is more strongly governed by the damage accumulation than the total level of damage existing in a composite before deformation.

The linkage of damage between cracked particles that results in the final fracture has been difficult to investigate experimentally. This is largely attributed to the process occurring very rapidly with the resulting failure almost immediately after it begins. Thomason (1968) and Brown and Embury (1973) have proposed models of the coalescence of damage between neighboring voids, but, to date no adequate models that

describe the micro-crack linkage process that leads to fracture in material that damage through particle cracking have been developed.

2.5.3 Particle Size Effects on Particle Fracture

Brechet *et al.*(1991) have studied the effects of particle size and aspect ratio on particle fracture. Their results indicate that both increased particle size and aspect ratio increase the probability of fracture at a given strain, as illustrated in Figures 2.8 and 2.9. Probability of particle fracture with increased size follows the common Wiebull statistic (d^3~volume) form. Aspect ratio effects have also been included in their model to predict the probability of particle fracture in the following form

$$p = 1 - \exp(-1.6\times10^{-4} \times d^3 \times \alpha\varepsilon) \qquad (2.27)$$

where d is the particle diameter in microns, α is the particle aspect ratio and ε is the applied strain. Their work provides a good qualitative description of the role of particle physical properties. However, since the work is based on results from a SiC reinforced

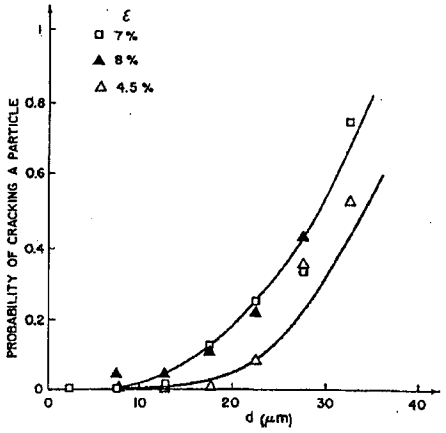

Figure 2.8. Graphical representation of relationship between particle size and probability of fracuture for SiC reinforced Al alloy. After Brechet *et al.* (1991).

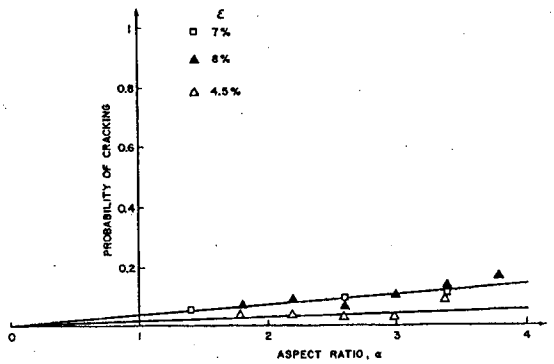

Figure 2.9. Probability of particle fracture dependence on aspect ratio for SiC reinforced Al alloys. After Brechet *et al.* (1991).

Al 356 alloy at three levels of strain, an accurate assessment of the influence Weibull modulus could not be quantified.

Other authors, [Kiser *et al.* (1996), Wilkinson *et al.* (1999)] have used models that predict probability of particle fracture based on the classical form of the Wiebull function

$$p = 1 - \exp(-(\sigma_p / \sigma_o)^m) \qquad (2.28)$$

where σ_p is the particle stress, σ_o is the particle threshold stress and m is the Wiebull modulus. Experimental measurements of the Weibull parameters specific to a particular from of particulate reinforcement were then used in the function to predict particle fracture in the SCEMA models used to predict the experimental flow curves.

2.5.4 Distribution Effects

Experimental evidence suggests that the spatial distribution of the second phase particles plays a significant role in the evolution of damage during deformation. The distribution of particles is often heterogeneous, that is, regions of high and low volume fraction co-exist in the same sample. This clustering effect further amplifies the inhomogeneity of the deformation, where regions of clustered particles carry a higher degree of the load.

When the second phase particles are closely spaced, the strain fields of the individual particles overlap, increasing the degree of plastic constraint of the inter-particle matrix. Some authors have used FEM calculations to investigate the effects of particle clustering. Both Watt *et al.*(1997) and Guillemer-Neel *et al.* (2000), indicate that a critical ratio of d/R, were d is the inter-particle spacing and R is the particle radius, for interaction exists. In clustered regions, particle spacing is reduced, resulting in the

overlap of stress fields, magnifying the local stress. As a result, higher work hardening rates exist in regions of high particle volume fraction due to the high degree of plastic constraint.

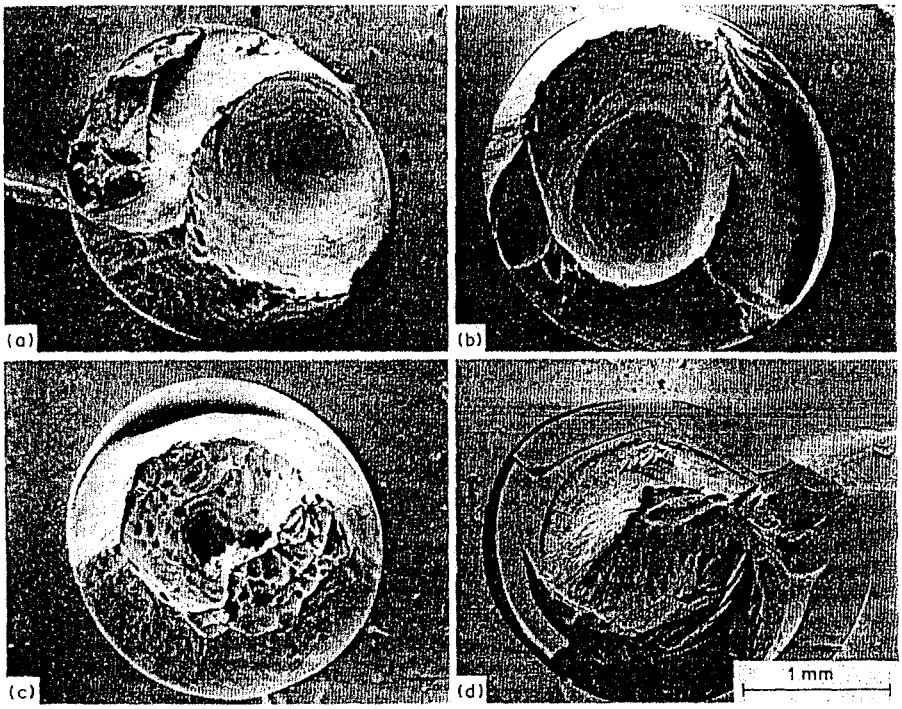

Figure 2.10. (a) Failure by growth of a single internal void. The lead/glass junction remained intact maintaining plastic constraint. (b) Failure involving some decohesion of the lead/glass junction, some constraint lost. (c) Failure involving an increased amount of decohesion resulting in decreased plastic constraint. (d) The lead/glass junction remained intact but concentric cracks formed in surrounding glass. Fracture surface is cavity free. After Ashby *et al.* (1989)

The failure of otherwise ductile materials, in the presence of plastic constraint, was studied in a series of novel experiments by Ashby *et al.* [1989]. In the first set of experiments, the authors manufactured a coaxial composite structure by pouring molten lead into a thick walled pyrex tube. A sharp crack was introduced in the glass tube and the composite was subsequently tested in tension. When the lead remained well bonded to pyrex, ie. the lead core was highly constrained, the lead reached a stress of up to 6

times that of lead deformed in the absence of plastic constraint and fractured at low plastic strain. In these samples, fractography showed that almost always, the lead core had developed a single, large, volcano like crater, as shown if Figure 2.10a. When debonding of the lead/pyrex junction increased, the deformation increasingly transformed to the more typical ductile fracture, ie. thinned down to a point, as the degree of debonding increased Fig 2.10 (b-d).

A second set of experiments utilized a sandwich type composite consisting of lead sandwiched between two pyrex plates. The sandwich specimens allowed a degree of control over the debond length and the angle of shear, θ. The debond angle was controlled by placing thin bands of carbon onto the glass prior to assembly of the sandwich specimens. The bands reduced the cohesion of the lead to the glass allowing

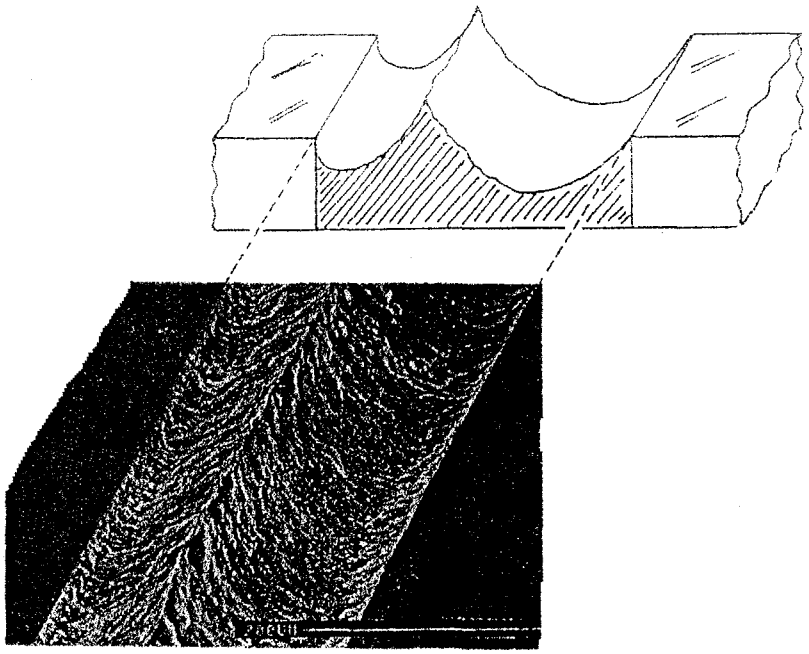

Figure 2.11. Illustration of the constrained necking mode present in samples with θ=0 and debond length =0. After Bannister and Ashby (1991).

manipulation of the debond length. The angle of shear was controlled by the relative position of cracks on either side of lead core. In this way, the effects of shear angle in highly constrained lead could be examined.

As in the first set of experiments, the plastically contrained lead reached a stress of 6 times, or more, that of unconstrained sheets when both the shear angle, θ, and the debond length was zero. Failure occurred at low plastic strains via necking to a ridge as illustrated in Figure 2.11. As the debond length increased, the plastic constraint decreased, allowing the lead cores to progressively neck down to a point typical of unconstrained deformation in this material.

The angle of shear with zero debond affects the peak stress in the following way. When the shear angle exceeds 25^0, the lead fails by shear. The intense plastic deformation is confined to a narrow shear band in which large plastic shear strain quickly work hardens the material. As the shear continues, the area under the shear plane decreases steadily to zero, and then the stress fall. When the angle is less than 25^0 deformation through the easier constrained necking mode is favoured which occurs at a lower applied load. The results of normalized peak stress vs. shear angle are summarized in Figure 2.12.

These well-controlled and repeatable series of experiments provide some insight into parameters controlling the fracture behaviour of composite materials containing either high volume fraction or clustered distribution of the second phase. When the particle spacing is small, in the order of the particle radius or less, the effects of the plastic constraint on the deformation behaviour becomes appreciable. In the three

dimensional microstructure of these materials, all the factors affecting fracture that were present in Ashby's experiments are present.

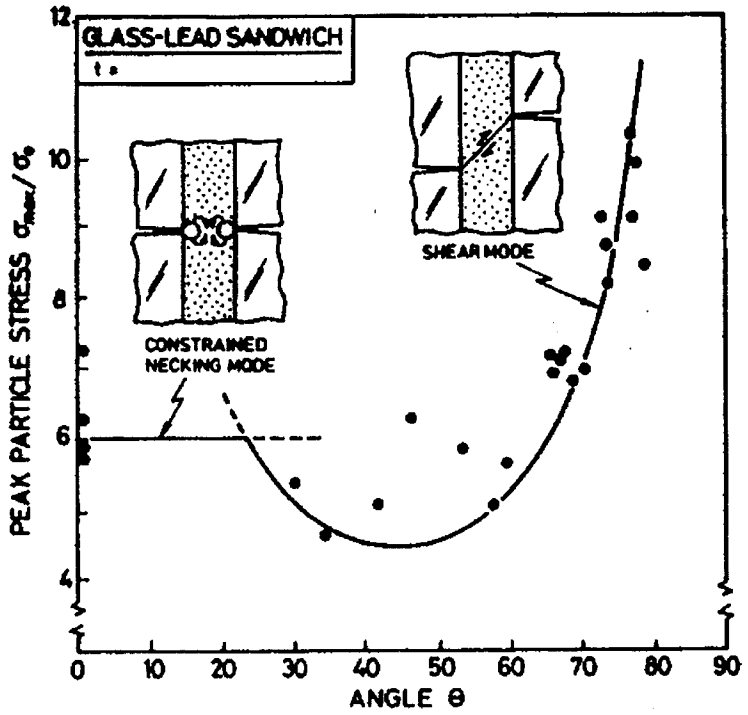

Figure 2.12. Peak stress in the lead-glass specimens as a function of shear angle at zero debond length. After Bannister and Ashby (1991).

In real microstructures, variations of the degree of plastic constraint, measured in Ashby's experiments by controlling the debond length, are caused through differences in the particle/matrix interfacial strength and the cracked particle spacing. The angle of shear is an additional factor of importance based on the relative position of adjacent cracked particles in the crack particle field. However, due to the very irregular nature of the particle field surrounding an individual cracked particle, it is difficult to assign a specific criterion for fracture based on say shear angle, crack particle spacing, the degree of debonding etc. An appropriate model for fracture in these materials would have to

include some form of statistical dependence on fracture based on both the crack particle spacing and an average limit criterion for fracture.

The clear picture is that the spatial distribution plays a significant role in damage processes. The plastic constraint, present in regions of high volume fraction, will cause significant changes in the damage processes commonly observed in the absence of constrained deformation. When the distribution is heterogeneous, Wilkinson et al (1997) have further shown that clustered regions experience higher levels of stress than other regions of a composite. This result, caused in part by the high plastic constraint in the clusters, will lead to preferential damage nucleation in these regions thereby further reducing the composite ductility.

2.6 Damage Accumulation Modelling

Damage accumulation models for fracture through MVC have received significant attention in literature. In particular these models have developed considerably with the use of somewhat complex accumulation algorithms based on coupling some of the introductory growth and coalescence laws with Dirichellet tessellations of the real microstructures. To date, few models address the accumulation of damage through consideration of particle cracking initiated damage accumulation.

2.6.1 Geometric Models

The earliest attempts at modelling damage accumulation were geometrically based models utilizing uniform distribution approximations. Several of these models

characterize the attainment of a critical state at which failure occurs. The main weaknesses in these exist mainly when failures of non-uniform microstructures are predicted using the following models as the sole failure criteria. Prediction of the fracture strain or stress are almost always over predicted, the degree to which depends on the real distribution, and therefore these models used in this form at best serve as upper estimates of composite ductility.

The simplest model was that of McClintock (1968). In this work, linkage of adjacent voids was assumed to occur when the growing voids physically came into contact. McClintock also included the important feature of the dependence of void growth on the stress triaxility in the accumulation model. However, both the localization processes between voids prior to contact and the stress field interaction between closely spaced particles are ignored, leading to large over estimates of the composite fracture strain.

Brown and Embury (1973) developed a relatively straightforward approach to describe the macroscopic strain required for coalescence. In their model, the linkage of voids was assumed to occur when adjacent voids grew to the point at which the void length equaled the intervoid spacing. When this condition was met, a 45^0 slip field could be drawn between the voids, and the lateral plastic constraint would be relaxed such that linkage could occur via localized necking. In this model the composite far field strain, ε_{ff}, required for fracture, or microvoid coalescence was estimated to be

$$\varepsilon_{ff} = \left[\sqrt{\frac{\pi}{6V_f}} - \sqrt{\frac{2}{3}}\right] - 1 \qquad (2.29)$$

where V_f is the volume fraction of the second phase. The model assumed a single nucleation strain and void growth proportional to the macroscopic strain which is not strictly valid for real materials. Nonetheless, the model has been shown to be accurate for several systems including spheroidized steels and copper-silica alloys. Another advantage of the model is the relative ease with which the model can be compared with readily measured experimental quantities. Several authours have extended the original Brown and Embury model to remove some of the original assumptions in question. For example, LeRoy modified the Brown and Embury model by replacing macroscopic strain dependent void growth with the Rice-Tracey void growth model (1969), thereby including the well-established effect of stress triaxility in the failure model.

An alternative model is Thomason's plastic limit-load failure model. The incipient limit-load condition can be represented in terms of the critical value of the mean stress, σ_n, required to initiate localized plastic flow in the intervoid matrix. The critical condition for limit-load failure is written as

$$\frac{\sigma_n}{2\tau_n(1-\sqrt{V_f})} = \frac{1}{2} + \frac{\sigma_m}{2\tau} \qquad (2.30)$$

where k, and k_n are the far field and intervoid yield shear stress and σ_m is the mean normal stress. Thomason suggests that when the voids are nucleated at large incoherent particles, that the intervoid and far field shear stress can be related via a simple rule of mixtures, $\tau=(1-V_f)\tau_n$. Thomason's model is essentially similar to that of Brown and Embury's with the additional incorporation of the important effects of stress triaxility on coalescence. In cases of high stress triaxility, σ_m is high, this model predicts that

coalescence can occur when the void length over particle spacing is much less than one, thereby providing a lower ductility estimate than that proposed by Brown and Embury.

Berg (1970) proposed a fundamentally different model that was later developed in the work of Gurson (1977), Yamoto (1978) and Tvergard (1981). This model of ductile fracture differs from the previous ones in that it assumes that the void-growth and coalescence can be fully described by the dilational plastic response of an elastic-plastic continuum containing an imaginary distribution of spherical microvoids. Gurson developed the matrix-softening model using a unit spherical cell with a single central void. This lead to an estimate of the dilational-yield surface of the form

$$\phi = \left(\frac{\sigma_n^2}{\sigma_{ys}^2}\right) + 2f\cosh\left(\frac{3\sigma_m}{2\sigma_{ys}}\right) - \left(1 - V_f\right)^2 \qquad (2.31)$$

where σ_n, σ_{ys} and σ_m are the mean, yield and mean normal stress respectively. As in the von Mises Yield criterion, the condition for plastic flow is met when ϕ=0.

The Gurson model provides a soft dilational response to the ductile fracture model. In particular, the model tends to neglect the strong dilational [Thomason (1990)] flow associated with internal necking. It considers this a secondary effect that can only occur following the formation of a localized shear-band or local softening. However, Tevegards (1981) revision to the model, by introducing arbitrary paramters q_1 and q_2, has provided fairly good fit to the experimental materials the he studied. Gurson's model, sometimes referred to as the Berg-Gurson model, is widely used in damage accumulation modelling. Often this model is used in conjunction with a coalescence model when both a primary and secondary void population exist [Bandstra and Koss (2000)]. In these models the fracture is governed by coalescence of the larger primary voids. The material

between the primary voids, which contains the population of the smaller secondary voids, is then assumed to behave as a "Gurson" material. The plastic softening predicted using the Gurson model in this population contributes to fracture by reducing the strain required for coalescence of the primary voids. The Gurson model is currently frequently employed, in a similar manner to that just discussed, in a number of the hybrid damage accumulation models.

2.6.2 Extensions of The Geometric Models

Multi-phase microstructures, particularly dispersion-strengthened systems, typically do not contain uniform or regular distributions of the second phase. As previously mentioned, the role of microstructural heterogeneity in the mechanical behaviour, in particular damage evolution, is significant. A considerable effort has been placed in obtaining quantitative descriptions of the second phase distribution. Typically characterization of the distributions involves the use of mathematical tessellation techniques such as the Dirichlet, Vornoi and Delaunay Triangulation techniques.

2.6.2.1 Tessellation Techniques

The basic approach to using all the tessellation techniques begins by considering all particles as points in the structure. A simple description of the point pattern distribution could be written in terms of the nearest neighbor distances of each of the particles. This however, provides information on only a very local scale and therefore fails to capture any aspects of particle clustering of three or more particles.

A better alternative, and more comprehensive, treatment than the nearest neighbor distance method involves the subdivision of the structure into cells constructed around each point in the structure. The cells formed around each point (typically a particle) have specific geometries that can then be used to characterize the distribution. Either a physically or geometry based criteria may be employed to subdivide the cells.

Construction of the Voronoi cell is based on geometrical criteria. For any three dimensional particle or point pattern it is possible to divide the region into cells, the Voronoi polyhedra [Burger (1986)], such that each cell pattern contains that part of the region closer to its point than to any other. The cell boundaries are constructed from planes which perpendicularly bisect the lines joining a particular particle to those around it.

The construction of the two-dimensional Dirichelet cells uses an approach similar to that employed for the construction of Voronoi polyhedra in three dimensions. In this

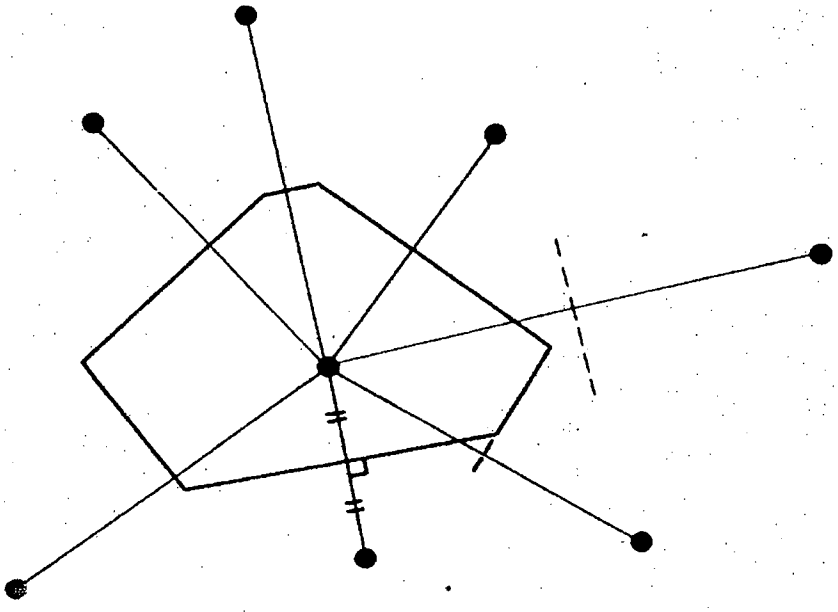

Figure 2.13. Construction of a Dirichlet cell about a given point. The cell is given by the inner envelope of lines which perpendicularly bisect the lines joining the given point to others in the dispersion.

case planes are subdivided into regions about each particle as illustrated in Figure 2.13. Each cell consists of that region in the plane closer to its point than to any other. By using a Dirichelet distribution to characterize the two dimensional material structure, it is possible to not only uniquely define near neighbors but will also enable clustering to be dealt with in a systematic fashion [Wray et al. (1983)].

It is important to reiterate the fact that both the Veronoi and Dirichlet tessellation techniques are both purely geometrically based and are well suited to continuum-based models. However, it is important to note that by definition, boundaries, whether they are real or imaginary, separate regions of some specific differing property. A property that may be of prime importance in the problem considered, particularly when the length scale involved involves dislocation mechanics. When slip systems or slip mechanisms differ from cell to cell, it is clear that some physically based criteria must be introduced into the construction of tessellation cells.

The Delaunay Triangulation technique for dispersion-strengthened systems is better suited in capturing the effects of the spatial distribution of particles when Orowan type processes are involved. This technique, while leading to similar topological features to the Voronoi tessellation technique, provides a better physically based description of the dislocation slip interactions between neighboring cells. As a result, the Delaunay Triangulation better accentuates the softening effects of particle clustering [Lépinoux and Estrin (2000)]. A full description of Daunay Triangulation is beyond the scope of this work due to the length scales involved (this work is well within the continuum range). However, those working at length scales below the continuum level, ie. $<1\mu m$, are

encouraged to review the work of Lépinoux and Estrin (2000) for a good description of the Delaunay Triangulation technique applied to dispersion-strengthened systems.

2.6.2.2 Damage Percolation Models

Recent work by Pilkey *et al.*(1998) and Worswick *et al.*(1998) has examined the nature of second phase clustering and its effect on damage accumulation through damage percolation modelling. Models of this type are of particular interest because they typically use the real particle distribution of the experimental microstructure to study damage evolution.

The particle fields of an experimental microstructure are first tessellated using a matrix erosion tessellation algorithm on the pixilated image [Pilkey *et al.* (1998)]. Through the use of the algorithm, relevant particle and clustering characteristics can be extracted for use as input into the percolation model. The algorithm also provides the inter-particle dilational spacing data [Pilkey *et al.* (1998)] used to identify the characteristic length scales of clustering within the particle field. Data from the tessellation algorithm is then read directly into the damage percolation model.

The software developed for the percolation model reconstructs the experimental microstructure using the tessellation output to define particle centroid coordinates, particle principle axis, nearest neighbor lists and a list of particles comprising each cluster. Each particle within the microstructure is represented by an ellipse with the principle axis orientated either perpendicular or parallel to the rolling direction. The percolation model treats damage evolution in three distinct stages: void nucleation, growth and finally coalescence.

Void nucleation is treated as being strain controlled following the model suggested by Embury (1985). Larger particles are assumed to nucleate voids preferentially and the fraction of nucleated voids increases with strain. These models are well suited to modelling void growth using the classical Rice Tracey model [Rice and Tracey (1969)], however, Worswick *et al.*(2000) use unit cell calculations by Thomson *et al.* (1999) to model void growth in their most recent model. This is largely due to the fact that this treatment considers void aspect ratio and strain state. The void growth rate is determined on isolated void, unit cell calculation and neglects growth rate changes resulting from particle clustering. Growth models also assume that once nucleated, the particle and the void can be treated as a single ellipsoidal void and therefore ignore any contributions from partial debonding. Coalescence is then treated using a modified version of Brown and Embury's (1973) ligament to void size ratio criteria. Modifications to Brown and Embury's (1973) were introduced to account for the relative position and orientation of the elongated voids with respect to the loading axis, illustrated in Figure 13, in the calculation of the coalescence criterion. Coalesced voids are then treated as single larger voids with growth of these larger, in addition to the smaller preexisting voids being consumed, in a multi stage coalescence process until a large catastrophic void forms as illustrated in Figure 2.14

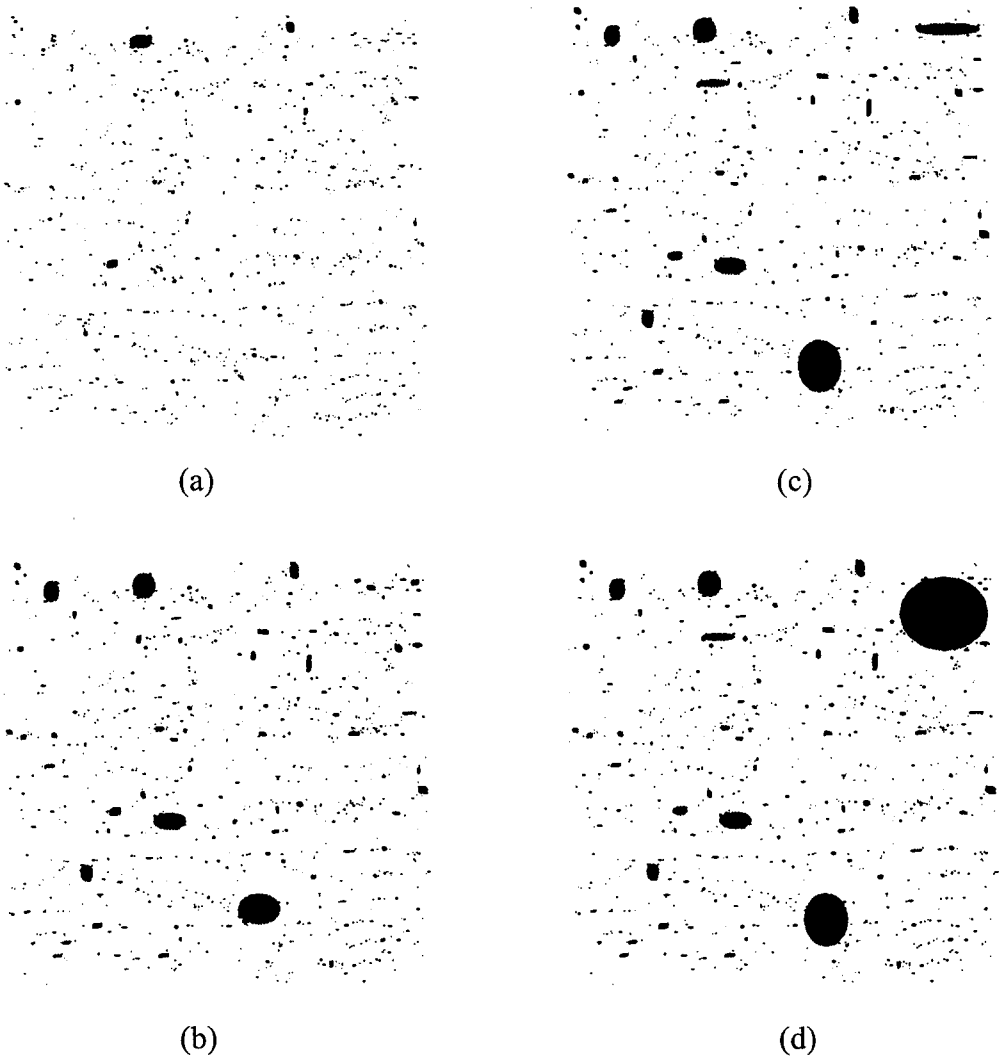

Figure 2.14. Illustration of results from the damage percolation models of Worswick and coworkers [Worswick *et al.*(1998)]. Damage percolation sequence for an Al-2% Si unrefined alloy under equi-biaxial strech conditions. The void coalescence sequence is visible with increased straining. (a) $\varepsilon_I = 18\%$, (b) $\varepsilon_I = 33.25\%$, (c) $\varepsilon_I = 33.75\%$ and (d) $\varepsilon_I = 34\%$.

These models provide a good qualitative and illustrative description of the damage process on a specific sample cross-section. The choice of the critical nucleation, growth and coalescence are somewhat subjective and since these models are very sensitive to these parameters, caution must be exercised when using the models as predictions. The authors themselves Worswick *et al.* (2000) state that while the models

are beneficial in interpreting the effect of particle distribution on formability, the simulations should not be viewed as predictive. In addition, the damage predictions are somewhat sensitive to a specific section of the microstructure experimentally examined and the damage evolution models can only be expected to predict damage on a small (approximately 1μm-1μm [Worswick *et al.* (1999)]), 2 dimensional sample of the real material. Improvements to these models will be forthcoming with the relatively new ability to experimentally observe the particle distribution in three-dimensions using high-resolution x-ray computed tomography. Three dimensional percolation models will provide a better and more quantitative description of damage evolution in a specific microstructure investigated.

2.6.3 Modelling the Mechanical Response of a Damaging Heterogeneous Material

Other authors [Wilkinson *et al.* (1998)] predict the effects of damage accumulation, through particle cracking, on the tensile flow curve in a more comprehensive manner. The continuum-based models, involving the self-consistent effective medium approximation described in detail earlier, consider how the evolution of damage, in the form of particle fracture, affects the composite flow response through incorporation of Brockenbrough and Zok's (1994) FEM calculation.

The self-consistent effective medium analysis damage model developed by Wilkinson and coworkers, referred to the SCEMA-damage model in the sections 6 and 7, is described in detail within section 6.1. Therefore only the essential features of the model will be outlined here. The SCEMA-damage model is particularly powerful in that

it allows for treatment of heterogeneity in the particle spatial distribution and uses experimentally determined values as input parameters to the model.

Modelling requires two steps. The first is determination of the undamaged flow response of each phase within the composite. Each phase within the composite is defined based on a given local volume fraction within the composite. For example a composite possessing a bimodal distribution of 10% and 20% local volume fraction regions would be represented by a 10% phase and 20% phase. The mechanical response of each phase is determined by running tangent-modulus self-consistent effective medium analysis (described in section 2.2.7) for composites of uniform distribution and the same volume fraction of each phase. These results are then fit to the Ramberg-Osgood relationship (see eq. (2.24)) so that the elasto-plastic response of each phase can be represented in the SCEMA-damage model.

Within the SCEMA-damage model, each phase is further subdivided into two regions. One region represents undamaged regions of the given phase, with behavior governed by the results generated in the first modelling step, and the other represents the damaged regions. The response of these "damaged" regions is governed by the results of the unit cell FEM work of Brokenbrough and Zok (1994), described in section 2.4.2., that relates the behavior of the damaged material to that of the matrix. The composite response is then calculated through Kreher and Pompe's (1989) self consistent formulation that consider the contributions, weighted by volume fraction, of the phases including the damaged and undamaged regions within each phase of the composite.

Prior to deformation the fraction of the phase comprised of the damaged region is zero because damage has not yet occurred. As deformation proceeds and damage

evolved an increasing fraction of a given phase is consumed by the damaged region. The fraction of damaged material at a given value of strain is calculated directly from Weibull statistics. At each increment of strain, the model estimates the value of the average particle stress within a given phase. This value of stress is then used to determine the fraction of damaged material based on the Weibull distribution of the experimentally determined particle fracture strength distribution.

The SCEMA-damage model provides good predictions of the composite flow response. The agreement is exceptionally good for the 2618 Al (T4) SiC composite used as an experimental comparison at both the 10% and 18% volume fractions studied as shown earlier in Figure 2.6. The evolution of damage defined in terms of the fraction of cracked particles coupled with Brokenbrough and Zok's calculation describing the behavior of the damage material result in modelling predictions that are virtually indistinguishable with the experimental material. The model captures the additional loss in work hardening apparent in the experimental material. This is particularly evident when the results of the original SCEMA model that excluded damage is compared with the SCEMA-damage model.

While this continuum-based model provides good estimates on the effects of particle cracking on the overall mechanical response, the model significantly overestimates the ductility of the two composite materials studied. Even though the effects of spatial distribution on the work hardening and increased rate of damage have been considered, the models do not consider the potentially important effect of crack initiation and propagation through the inter-particle matrix. As a result, the role of

particle fracture on the initiation and propagation of inter-void cracking and the resulting composite response remains largely unknown.

2.7 X-Ray Tomography

Developing models that describe damage evolution and its relationship to the flow response of a heterogeneous material clearly requires experimental observation. A number of methods that allow for a global measure of damage exist. These include measurements of damage through acoustic emission or changes in density. These methods however, fail to provide quantitative measures of features such as the sensitivity of damage to particle size, shape and heterogeneity in the spatial distribution of the second phase. Some of these local measurements can be obtained through optical or scanning electron microscopy on sections of interrupted tensile samples, the process is tedious, and unless serial section is employed, is limited to 2-dimensional characterization. Relating local events to the global state of stress is also difficult.

While existing methods of characterizing damage and damage evolution provide insight into the damage process, the field of materials characterization has recently been advanced through the efforts of members of the CNRS research federation in the Rhône alpes region of France . By taking advantage of the synchrotron x-ray source located at the European Synchrotron Radiation Facility in Grenoble, France, the research federation has been able to apply a technique used in medicine for the last 30 years, to materials characterization. While the computer aided tomography scans employed in medicine have a typical resolution of 300 um, the high energy x-rays provided by synchrotron

sources have allowed the current resolution limits to improve to the micron level in several metallic systems [Babout et al (2001), Maire et al (2002)].

Characterization through X-ray tomography has a number of advantages over conventional methods. The primary of these include the fact that it is a non-destructive characterization techique and allows quantitative damage observations to be taken of the bulk during in-situ testing. In particular, the technique allow for these observations to take place both on the global scale, and perhaps more importantly, on the local scale within the bulk of the three dimensional volumes. X-ray tomography affords the opportunity to evaluate the damage accumulation rate, the sensitivity of this rate to particle distribution, the sensitivity to particle size and shape and if the volume fraction of reinforcement is sufficient, the damage coalescence mechanism and rate.

While other methods such as scanning electron surface microscopy with in-situ mechanical testing does allow for observation of damage evolution on a polished surface of a sample, a direct correlation of damage based on the surface observations is not likely directly representative of the bulk behavior. Babout *et al.* (2001), suggest that the level of damage within the bulk of the sample can be twice that observed on the surface. This is attributed partially due to the difference in stress state on the surface over that of the bulk and the plugging of damage in the form of pores as a result of metallographic polishing. X-ray tomography eradicates these problems by allowing for three-dimensional, non-destructive observation of damage occurring within the sample bulk during deformation.

2.7.1 X-ray Radiography

The physics for X-ray radiography is based on the Beer-Lambert law [Felkamp et al (1984)] that provides an expression for the ratio of the number of transmitted photons, N_1 over the incident photons N_0 for a given ray of energy E, passing through a material with an attenuation coefficient of $\mu(s)$

$$\frac{N_1}{N_0} = \exp\left[- \int_{s \in ray} \mu(s) ds \right] \tag{2.32}$$

where the attenuation coefficient is integrated over the ray surface. The attenuation coefficient for a given material is based on the atomic number Z, the photon energy, E, and the material density, ρ. The expression for the attenuation coefficient in three dimensions is

$$\mu(x,y,z) = K\rho\frac{Z^4}{E^3} \tag{2.33}$$

where K is a constant. The attenuation is the basic law governing the change in contrast observed in a x-ray radiograph of a bulky material. This is because each point of the detector collects photons from the material that have experienced differing amounts of attenuation based on the material they have passed through. These differing amounts of attenuation allow for the visualization of the phase present in the microstructure.

2.7.2 X-ray Tomography.

The radiographic image generated on a two dimensional plane contains a large amount of information. Information collected at a given point of the detector is governed by the attenuation of the beam through a specific path though the sample. If the microstructure of the sample is complex, for example heterogeneity in the second phase distribution, the information from a single radiograph can be difficult to interpret. This can be overcome by combining the information in a series of radiographs taken at a number of sample rotation increments. If the rotation increments between each radiograph of the sample are sufficiently small, it is possible to calculate the local attenuation coefficient at each point in the three-dimensional sample [Maire et al. (2002)]. Through this it is possible to generated a three-dimensional image of the sample being investigated.

2.7.3 High Resolution Microtomography

Synchrotron radiation sources provide the x-rays possessing the high energy and high coherence required for high-resolution imaging. Ultra-relativistic electrons in a storage ring produce synchrotron radiation when they are accelerated by the magnetic field of bending magnets. By bending the path of the electrons, hard X-rays (λ=0.5 A) are emitted tangent to the trajectory of the electrons within the storage ring.

One of the features of the European Synchrotron Radiation Facility ID 19 beam line is the large source to sample distance and the small source size (100μm). The large source to sample distance in conjunction with slits produces a x-ray beam with high-lateral coherence (in the order of 100μm). This coupled with the double monochamater produce intense, monochromatic, highly collimated beams. The experimental set-up is illustrated in Figure 2.15.

X-ray beams from synchrotron radiation sources can penetrate through metallic samples over 2mm in thickness [Buffiére et al. (1999)]. When the phases present have significantly different attenuation coefficients, the resolution of the tomographic images resulting from the reconstruction of the individual radiographs approaches 1um. [Maire (2002)]. However, when the attenuation coefficient differences are small, as in the case of SiC and Al, the resolution of the technique using this conventional approach suffers.

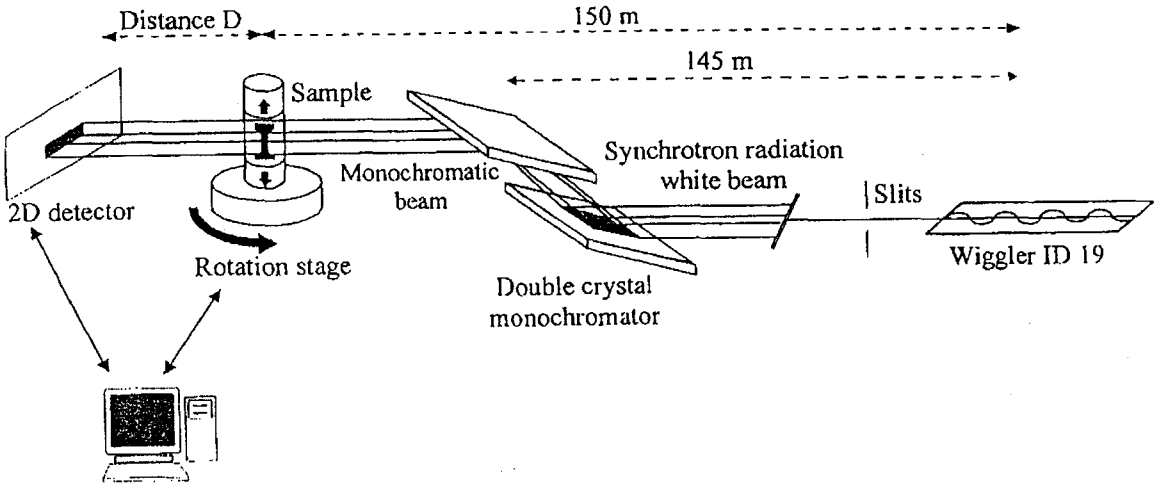

Figure 2.15. Schematic of the set-up used on the ID19 beam-line at the ESRF to record the radiographs during an in-situ tensile test. After Maire *et al.* (2001)

To alleviate resolution limitations, the research group in France, have developed the Phase Contrast Technique. This technique takes advantage of the fact that the refractive index for x-rays is slightly different than unity. As a result a slight difference in phase can be introduced between two parallel x-rays passing on each side of the interface between two different constituents in a material. When these waves propagate a sufficient distance, they interfere and provide a phase contrast at the interface between the two constituents. Application of this technique to x-ray tomography essentially involves placing the detector at a distance farther away than would typically be used for absorption contrast imaging. This added distance, allows for the phase contrast to be developed so that materials with small difference in x-ray attenuation can be imaged. This technique has also been successfully applied to imaging cracks in the early stages of development [Buffiére *et al.* (1999)].

2.7.4 Quantitative Damage Measurement Using X-ray Tomography

The use of x-ray tomography to provide quantitative measurements of damage in continuum scale heterogeneous metallic matrix based systems is an emerging field. To date the bulk of the high-resolution micro-tomography research has been performed at Beamline ID19 at the European Synchrotron Radiation Facility. X-ray tomography has been used to investigate metallic foams, semi-solid forming, superplasticity, grain boundaries and damage evolution during tensile tests.

The results obtained through these experiments have provided information on each of the above topics that would have otherwise been difficult or impossible to obtain to a high degree of accuracy using two-dimensional techniques. Application to

investigating damage evolution has recently been performed on both SiC/Al [Buffiére *et al.* (1999)] and ZrO_4/Al [Babout *et al.* (2001)]composites. The results in the SiC reinforce particles metal matrix composites indicate that the evolution of damage, though qualitatively similar, was much different than that at the surface. Babout *et al.*(2001) used tomography to study the evolution of damage in the form of the growth in porosity and have shown that the level predicted by classical models strongly over-predicts the level of global porosity. The technique has yet to be employed to study the evolution in damage in the form of particle cracking within the bulk. Based on the results so far, application of the technique to study this form of damage will clearly provide useful information on the damage process occurring both locally and globally within the sample bulk.

CHAPTER 3

MATERIALS AND EXPERIMENTAL METHODS

3.1 Introduction

The previous chapter outlined the current state of understanding on how damage processes occurring at second phase particles influence the deformation behavior of heterogeneous metallic matrix based materials. A reasonably good understanding of damage evolution in the form of particle matrix decohesion followed by void growth and microvoid coalescence exists. However in the case when the damage mechanism is one that involves particle cracking the understanding is less clear.

The aim of the work undertaken in this thesis was to investigate damage in the form of particle cracking in heterogeneous aluminum alloys so that a better understanding of this damage process could be gained. This limited the material selection to an aluminum matrix reinforced with well-bonded stiff particles. Both the high stiffness mismatch between the particles and the matrix, which promote a high level of stress partitioning, and a good bond with the surrounding matrix encourage damage in the form of particle cracking over a mechanism involving particle matrix decohesion [Llorca (2000)].

One of the factors limiting the development of a better understanding of damage occurring through particle cracking is the experimental difficulty in observing the final stages of the damage process. The use of X-ray tomography to observe damage alleviates many of the problems associated with the observation or measurements made using conventional techniques. The technique is limited to a

resolution of ~1 μm, therefore only damage occurring at length scales greater than this can be observed. Use of high resolution x-ray tomography in this work therefore dictated the use of reinforcing particles significantly larger than the resolution limits of the technique so that cracking of the particles could be clearly observed.

The final constraint placed on the material selection process was more processing than material related. Control over the spatial distribution of reinforcing particles within the composite was desired so that the effects of heterogeneity in the distribution could be investigated.

An AA 6111 matrix reinforced with spherical 40-50μm Al_2O_3 was a material that met all the above experimental requirements. Manufacturing the materials via a three-step process utilizing the impulse atomization technique, followed by hot pressing and extrusion provided a means of custom tailoring the spatial distribution of Al_2O_3. The high modulus mismatch (390 GPa for Al_2O_3 versus 70 GPa for Al) ensured a high level of stress partitioning. The impulse atomization technique, involving direct infusion of the Al_2O_3 into the AA6111 melt, improves the interfacial strength over the powder metallurgy route [Whitehouse *et al.* (1992)] and therefore provided a damage mechanism involving particle cracking. The large particle size was much greater than the resolution limits of the x-ray computed tomography technique thereby providing a means of viewing damage processes occurring at length scales suitable for the technique.

3.2 Composite Manufacturing Procedure

3.2.1 Matrix and Reinforcement

The matrix material selected for this study was commercial AA6111 supplied by Alcan International in Kingston, Ont. The chemical analysis results of the ingot used to manufacture of the composite material are presented in Table 3.1. The Alcan Research and Development Center in Kingston, Ontario performed the chemical analysis using a standard ICP analysis.

The reinforcing particles used for the composite material in this study were provided by CONDEA, Hamburg, Germany. The manufacturing process began with the hydrolysis of aluminum alkoxide that resulted in a high purity alumina slurry. The resulting raw alumina slurry was then spray-dried to form round particles of AlOOH (Boehmite). These spray-dried particles were then calcined at 650^0C to form gamma phase Al_2O_3.

Table 3.1. Chemical composition of AA6111 ingot prior to impulse atomization. All measurements are in terms of wt% and were determined through ICP analysis performed by Pierre Marois at Alcan's Kingston Research and Development Center

Mg	Fe	Cu	Mn	Si	Ti
0.67	0.26	0.75	0.22	0.64	0.073
Zn	**Cr**	**V**	**Zr**	**Ni**	
0.002	0.04	0.009	0.001	0.002	

The Al_2O_3 particles were then subsequently sieved using a 38 and 53 um mesh to obtain a narrow particle size distribution. A scanning electron microscope image of a sample of particles after sieving is presented in Figure 3.1. Particle density was measured on a 0.5 gram sample of particles using a pictometer. The measured density varied with the amount of time used to evacuate the pictometer chamber. Density measurements made on samples evacuated at times of 24 hours or greater produced a repeatable density measurement of 3.90 grams/cm^3, or approximately 99% that of the theoretical density.

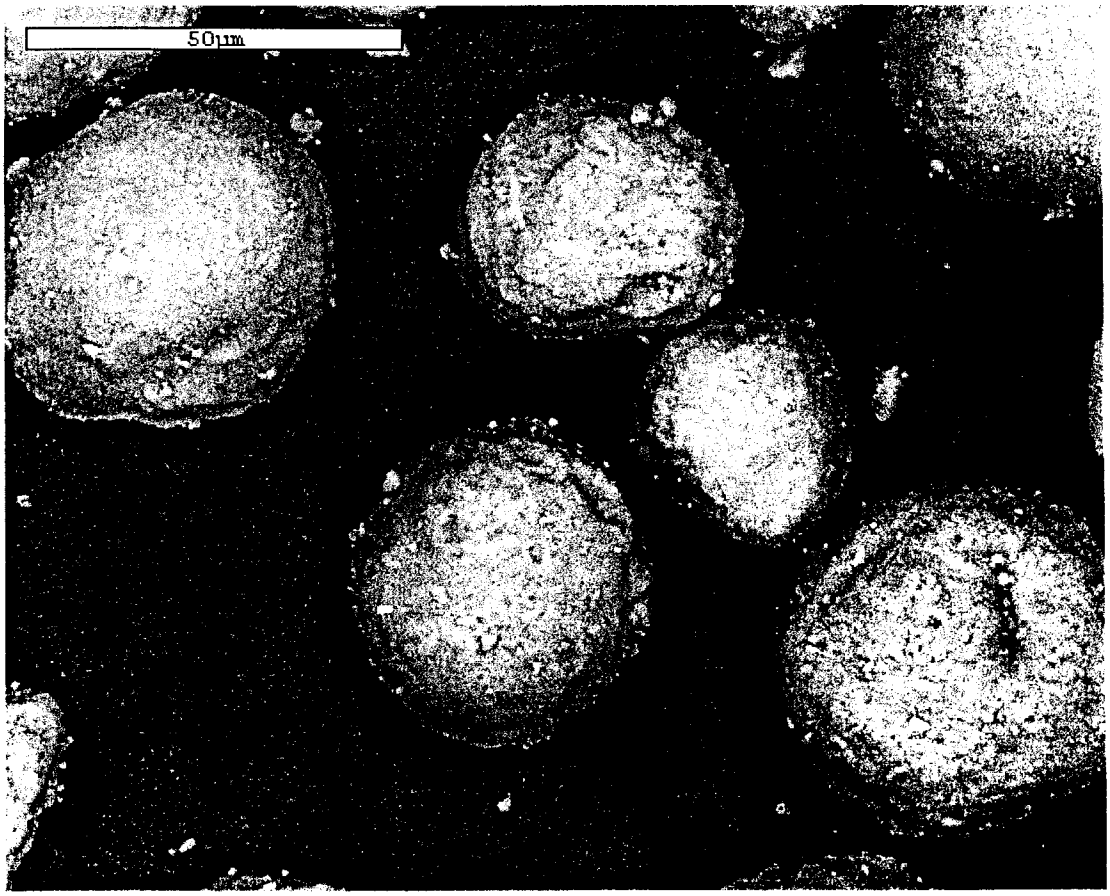

Figure 3.1. Scanning electron micrograph of a sample of spherically-shaped and sieved γ-Al_2O_3 particles supplied by CONDEA.

The high modulus mismatch, 390 GPa vs. 70 GPa, ensured a high degree of stress partitioning to the particles. Aluminum composites utilizing Al_2O_3 particles as reinforcement have also been successfully used by numerous researchers (Clyne and Withers, etc,) and manufactured commercially by Duralcan, a subsidiary of Alcan Int. Many composites that use Al_2O_3 particles as reinforcement typically employ angular particles of smaller size. In general, Al_2O_3/Aluminum composites manufactured by a powder metallurgy route typically failed through particle-matrix interface decohesion. In contrast, those manufactured by introducing the Al_2O_3 particles directly into the melt possessed stronger interfaces and typically failed through a mechanism involving cracking of the reinforcing particles [Whitehouse and Clyne (1992)].

3.2.2 Impulse Atomization[1]

The impulse atomization technique is a technique that provides a means of improving the particle matrix interfacial strength by direct infusion of the reinforcement into molten melt of the metal matrix. Additionally, consolidation of composite granules possessing different volume fractions of reinforcement allows for custom tailoring the spatial distribution of the reinforcing particles. The impulse atomization technique has been developed, and patented, by Prof. Hani Henein at the University of Alberta. Exact details of the technique are described in greater detail elsewhere [Yuan, Henein and Fallavollita, 1997] and will only be briefly outlined here.

---

[1] All of the composite granules were produced courtesy of Prof. Hani Henein, Advanced Materials and Processes Lab, University of Alberta, Edmonton, Alberta.

The first stage of the process involved melting the raw AA6111 into a crucible. Once the alloy was melted, a measured amount, depending on the desired volume fraction, of the sieved Al_2O_3 was added to the melt. Both phases were then mixed by both manual stirring with a ceramic rod and through the motion of the atomizing plunger. Initial atomizing runs indicated that the wettability of the Al_2O_3 was poor at temperatures below 1000^0C. Below this temperature the maximum volume fraction of Al_2O_3 incorporated into the composite granules was less than 1%. Raising the melt to a temperature range of 1000^0C-1200^0C significantly improved the wettability of the Al_2O_3 with the AA6111 melt. To further ensure that the reinforcing particles were well incorporated into the melt, the mixture was stirred for 30 minutes prior to atomization. All of the higher volume fraction (>1%) composites used in this study were mixed at a temperature range of 1000^0C-1200^0C for more than 30 minutes.

The physical process of impulse atomization followed the mixing of the Al_2O_3 particles into the melt. Once stirring was complete, a cap placed across the bottom of the crucible was removed, exposing milled holes in the bottom of the crucible. When the melt was still, the surface tension of the aluminum prevented any of the melt from dripping through the holes, thus preventing premature atomizing of the melt. A plunger submersed in the melt then applied a periodic pulse that forced pulses of the composite mixture out through the crucible holes. These pulses of composite mixture are forced out as streams that fall down a tower containing either an Argon or Nitrogen atmosphere. The liquid streams spherodize in flight due to the Raleigh instability, forming spherically shaped granules of composite material. The granules

were then collected from the bottom of the collection chamber. In all cases the granules fell onto a dry collection tray (ie. they were not collected in an oil or water bath). After every atomization run that involved the incorporation of Al_2O_3, varying amounts of unmixed Al_2O_3 particles remained in the crucible. It was therefore expected that the actual volume fraction would be less than the nominal volume fractions intended based on mixing the appropriate amounts of AA6111 and Al_2O_3 in the crucible prior to atomizing.

The size of the granules was controlled by a number of parameters in the atomization process. The plunger frequency, diameter of the milled holes in the bottom of the crucible and tower height and atmosphere all influence the final granule diameter. In this work, the composite granules typically were 400-700 um in diameter. Granules larger than this failed to freeze in flight and consequently splattered into pancake like shapes when they hit the bottom of the collection chamber and were rejected.

3.2.3 Consolidation

The composite granules were consolidated at 525^0C into cylindrical 2.25 cm (~1") diameter billets by uniaxial vacuum hot pressing in a closed graphite die. Since carbon is virtually insoluble in aluminum at 525^0C no precautions to prevent the diffusion of carbon into the composite granules were taken. Every composite billet was manufactured using the same process parameters described in what follows.

Each atomization run produced composite granules of a specific volume fraction. When a uniform distribution of a given volume fraction was desired,

granules possessing the desired volume fraction from a specific atomization run were consolidated to create spatially uniform distributions of Al_2O_3. When bimodal distributions were desired, granules with the desired volume fraction from different atomizing runs were combined to produce the final consolidated composite. For example, when a bimodal distribution of regions with 10% and 20% volume fraction was desired, granules from an atomizing run that produced nominal 10% volume fraction Al_2O_3 composite granules were combined with those from a run consisting of a nominal 20% volume fraction. In this way it was possible to custom tailor the distribution of the second phase distribution. Prior to insertion into the die, all bimodal distribution granule mixtures were milled for 30 minutes.

Following measuring and mixing the desired quantities, the graphite die and granules contained within it were placed within the furnace chamber of the isostatic hot pressing apparatus. The chamber was then evacuated to approximately 0.1 torr. Following the evacuation, the hot pressing process was initiated. This involved first heating up the chamber to 525^0 C using a ramp rate of approximately 5.5^0C per minute. Once the chamber reached the target temperature, the die was soaked at temperature for an additional 60 minutes. The two plungers of the graphite die were then loaded by the hydraulically actuated rams of the hot press machine to a consolidation pressure of 75 MPa for 100 minutes at 525^0C. Following this, the load was removed and the sample slowly cooled down to room temperature at a rate of approximately 1-2^0C per minute within the evacuated furnace chamber of the isostatic hot pressing apparatus.

3.2.4. Extrusion

Following consolidation into billets, the samples were then hot extruded into a cylindrical rod at an extrusion ratio of 16.1. Extrusion served two purposes. The first was that the extrusion yielded a product of a shape and dimension much more suitable for machining tensile test specimens. A second function of the extrusion was to break up the thin surface oxide on the granule surfaces. This ensured that each composite granule was well bonded to the next, resulting in an essentially continuous structure between granules in the extruded sample.

Initial attempts at extruding the billets were performed at a temperature of 400^0C. At this temperature a significant amount (more than 80% of the reinforcing particles were cracked) of damage in the form of particle cracking occurred. Optical microscopy revealed that raising the extrusion temperature to 500^0C and extruding at a slow 1-2mm/second extrusion rate reduced the level of damage so that less than 1% of the particles were damaged after the extrusion process. All composites used in this study were therefore extruded at this temperature and extrusion rate.

Extrusion elongated each of the prior spherically shaped granules into long, slender stringers as shown in Figure 3.2. This elongation of the extruded granules was particularly evident in the samples possessing bimodal distributions of regions of both high and low volume fraction. When the volume fraction of Al_2O_3 particles was low it was more difficult to distinguish the outline of the individual extruded granules because no visible boundaries between granules existed at optical magnifications of up to 200x.

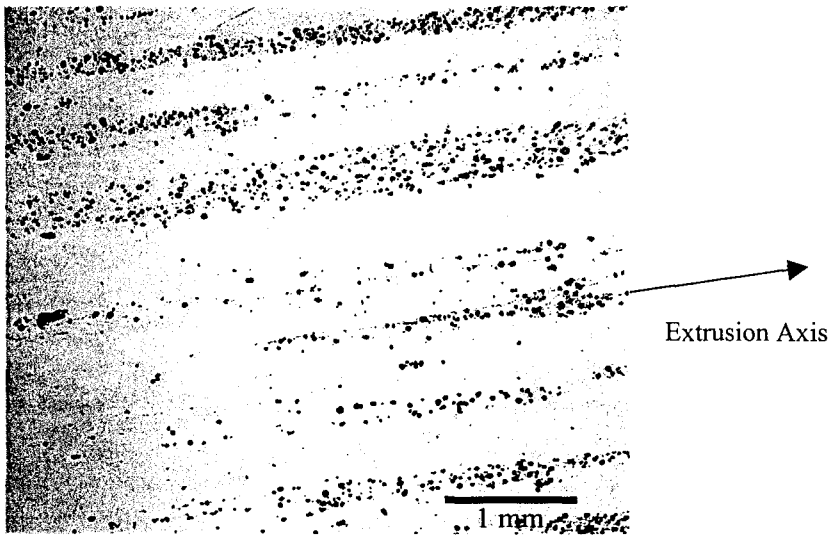

Figure 3.2. Low magnification image of extruded bimodal 0-20% volume fraction composite.

3.2.4 Heat Treatment

All samples machined from the composite extrusions underwent the same T4 heat treatment following machining. This heat treatment involved first inserting the samples into a preheated air furnace at 560^0C. Samples were then soaked at this temperature for 20 minutes, removed and immediately quenched into a room temperature water bath. All samples were then allowed to naturally age for 14 days.

3.3 Chemical Analysis

Preliminary tensile tests provided the first indications that the Mg levels in the AA6111 matrix had been depleted during the atomization process. In all cases, samples with the lowest nominal volume fractions of Al_2O_3 (5%) possessed flow curves with significantly higher values of stress at all values of plastic strain when compared to the higher nominal volume fraction (>10%) composites. This was true

for 6 different composite batches examined: two composites batches with <5% Al_2O_3, two with 10%, one with 20% and a final composite with a bimodal distribution of 10% and 20% Al_2O_3.

Since AA6111 is an age hardenable alloy correct proportions of the elements responsible for the primary precipitation strengthening, in this case Mg and Si, are necessary. As a first step, the chemical composition of composite granules from each atomizing run was analyzed to verify that the chemical composition of the matrix was the same as the starting AA6111 ingot. All elements, with the exception of Mg, were present at approximately the same concentrations. The ICP analysis of the matrix Mg content, measured in terms of matrix Mg wt%, was performed by Bodycote Ltd. in Burlington, Ontario. A second analysis was arranged through Prof. Hani Henen's group at the University of Alberta to validate the measurements provided by Bodycote Ltd. Results, presented in Table 3.2, generated by both facilities were in good agreement and revealed that the levels of matrix Mg were less than that of the AA6111 ingot used to produce the composite material. The Mg depletion, with Mg wt% approaching 1/10 the 0.6-0.7 wt% Mg range typical for AA6111, was most severe in composites possessing nominal volume fractions of 10% Al_2O_3 or greater. While the amount of Mg depletion in the nominal 5% Al_2O_3 composites was not as severe, the levels of Mg were still significantly less than those of the starting AA6111 ingot.

Table 3.2. Analysis of the Mg wt% present in the composite granules manufactured on different atomizing dates with varying atomizing parameters and nominal Al_2O_3 (alumina) volume fractions.

Run Number (yy/mm/dd)	ICP Analysis	Atomization Parameters			Nominal Alumina (vol%)	Comments
	Mg wt%	Mix Temp (C)	Mix Time (min)	Atomizing Temp (C)		
AA6111 ingot	0.6700					
001201	0.5000	770-780	not recorded	770-780	0	
001205	0.4700	968	20	710	2	
001207	0.1700	1000	20	710	5	
001215	0.1600	1100	not recorded	950	5	
010110	0.0380	1000	30	1000	10	
010115	0.0890	1000	60	1000	20	nozzle plate leaked
010116	0.0720	1000	30	1000	20	
010129	0.0580	1000	70	1050-1200	10	

The chemical analysis provided an explanation as to why the flow curves of the higher volume fraction reinforced composites were less than those of the low volume fraction composites. The results suggest that the precipitation strengthening likely did not occur to the same extent as it would have in AA6111 because the Mg required to form the precipitate existed at a concentration roughly $1/10^{th}$ of that in AA6111. This initial hypothesis was later confirmed through both micro-hardness measurements and transmission electron microscopy on the matrix material.

3.4 **Microhardness Testing**

Micro-hardness measurements were used to estimate changes in the matrix flow stress with natural aging time. Once a plateau in micro-hardness readings versus aging time was reached it was assumed that additional aging would not appreciably effect the matrix strength.

Previous studies on AA6111 performed at McMaster indicated that a natural aging time of 14 days (Gimple (2001)) was more than sufficient to reach the plateau

in precipitation strengthening process. In the composites studied in this thesis a 14-day aging time also proved to be more than sufficient in reaching this plateau in strengthening in all composites. In composites with nominal Al_2O_3 volume fractions of 10% or greater, aging had little or no affect on the measured Vickers hardness as illustrated in Figure 3.3. Samples with nominal volume fractions of 5% or lower reached a plateau in the measured hardness after 5 days of aging.

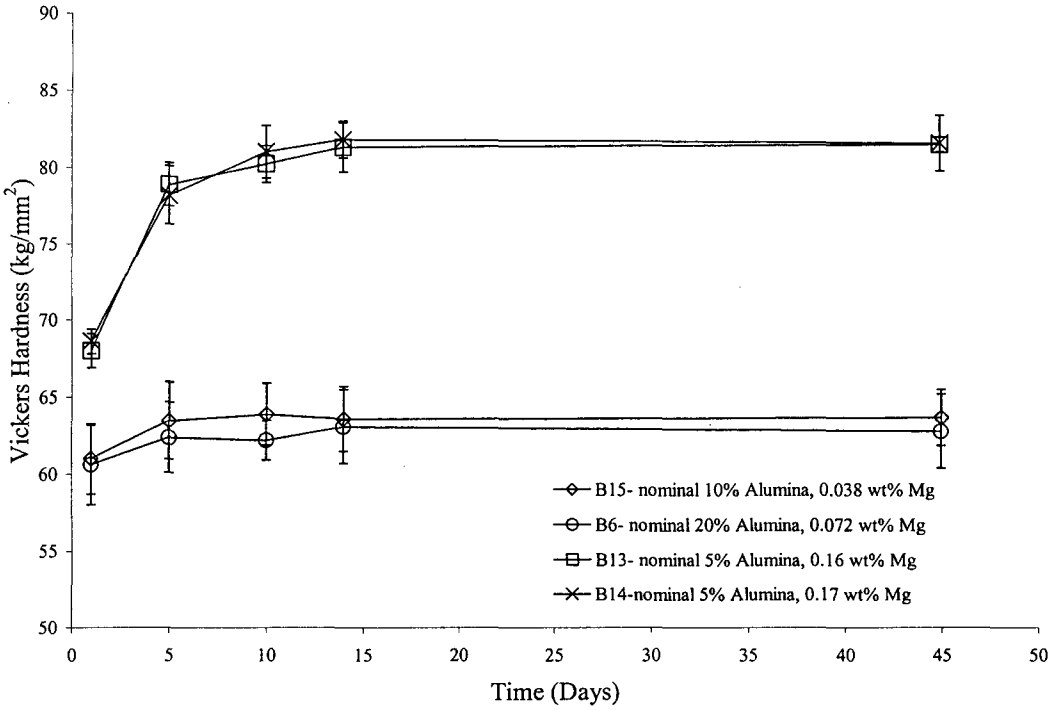

Figure 3.3. Vickers hardness measurement results versus aging time for four composites studied. Composite B15 was manufactured with a uniform distribution of granules produced on 010110 and possessed a 10% nominal volume fraction of Al_2O_3. Composite B6 was manufactured with composite granules produced on 010116 and possessed a 20% nominal volume fraction of Al_2O_3. Samples B13 and B14 each possessed nominal volume fractions of 5% Al_2O_3 and were manufactured on 001215 and 001207 respectively.

3.5 Transmission Electron Microscopy of the Composite Matrix

Matrix hardness versus time measurements on the composites with the most severe depletion of Mg suggested that little or no precipitation strengthening occurred during the natural aging process. As a confirmation of this hypothesis, a Transmission Electron Microscopy (TEM) investigation of the matrix was undertaken. A full TEM characterization of the matrix in each of the composites is beyond the scope of this work. The study was limited to investigating the presence of the β" and Q' precipitates in the matrix of two materials. The first investigated was the material atomized on 001201. This AA6111 material was impulse atomized without Al_2O_3 and possessed a measured 0.5 wt% of Mg. The second composite studied was atomized on 010129 and was processed with a nominal 10% volume fraction of Al_2O_3. Chemical analysis results of the Mg content in the matrix indicate that the matrix Mg content was 0.058 wt%.

Samples of each material were removed from the hot-pressed billets after hot pressing. The samples were grouped together, inserted into an air furnace and solutionized for 20 minutes at 560^0C. The samples were then removed from the furnace and water quenched to room temperature. Both samples were then aged for 14 days at room temperature. Transmission electron microscopy samples were produced by mechanically polishing down the sample thickness to approximately 100 μm. These thinned samples were then electron jet polished in a 10% perchloric acid and 90% methanol solution at around -35^0C. Transmission electron microscopy was carried out in a PHILIPS CM12 transmission electron microscope operating at 120 KeV.

Both bright field images and selected area diffraction patterns (SADP) taken along the <001> zone axis reveal clear differences in the matrix of each material. The bright field image of the high Mg, zero volume fraction Al_2O_3 material, shown in Figure 3.4(a), reveals the presence of the needle-shaped β" . The streaking in the SADP in Figure 3.4 (b) is indicative of the presence of β" precipitates.

The second matrix material from the low Mg (0.058 wt%) and nominal 10% volume fraction appears to be void of any precipitates as shown in the bright field image and SADP, Figures 3.5 (a) and (b). These results combined with both the chemical analysis and micro-hardness testing results indicate the absence of matrix precipitation strengthening in composites with nominal volume fractions exceeding 10%.

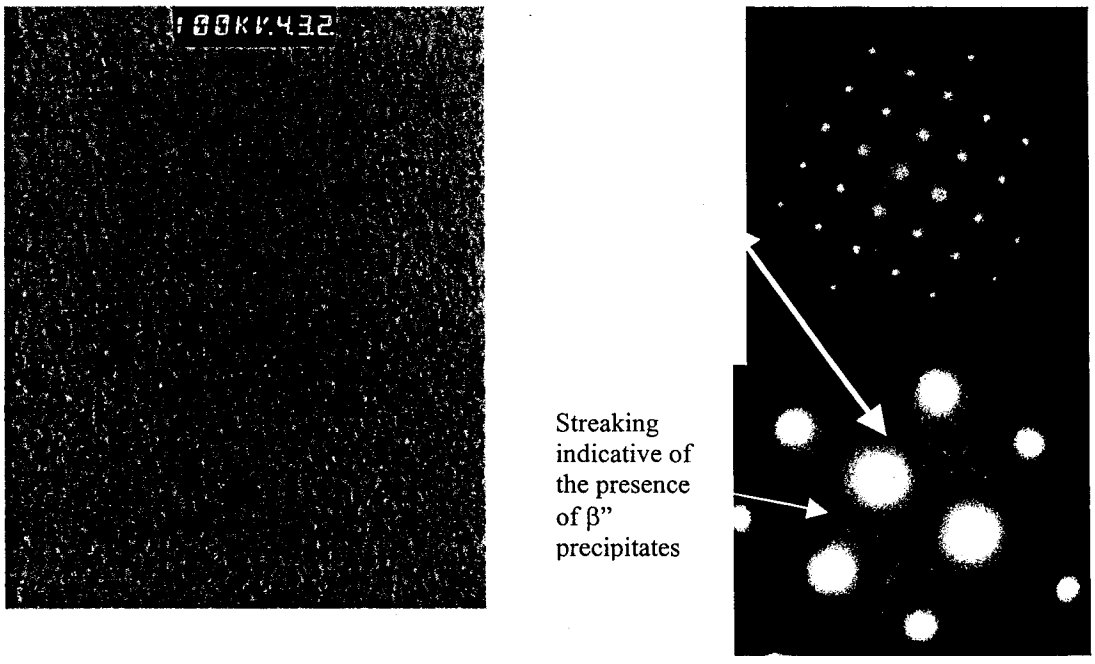

Figure 3.4 (a) Bright field and (b) selected area diffraction patterns taken along the <001> zone axis of a sample prepared from Al matrix containing 0.5 w% Mg. β" precipitates are visible in (a) and streaking in selected area diffraction pattern in (b) confirm the presence of β" precipitates in the matrix.

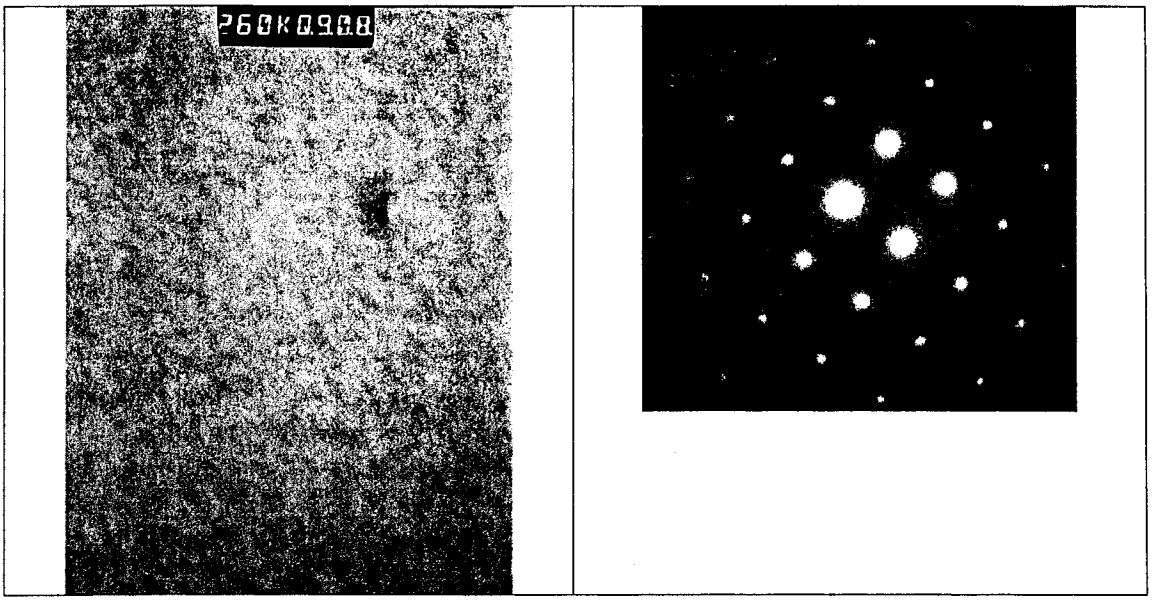

(a) (b)

Figure 3.5 (a) Bright field and (b) selected area diffraction pattern taken along the <001> zone axis of a sample removed from a matrix with 0.058 wt% Mg. Note the absence of precipitates in both the bright field image and the selected area diffraction pattern.

3.6 Post Processing Analysis of Al_2O_3 Particles

The chemical analysis, hardness measurements and the transmission electron microscopy investigation of the composite matrix indicated that the depletion in Mg did indeed result in a significant reduction in precipitation strengthening. Two questions related to the processing and Mg depletion remained. The first that will be addressed is an explanation as to what caused the Mg was depleted.

Precise measurement of the losses due to the Mg off gassing during the mixing phase of the atomization process or Mg consumed by reaction with the Al_2O_3 particles is beyond the scope of the thesis work. However, some general comments and basic explanations can be provided.

A nitrogen blanket covered the melt in the mixing phase for all the atomization runs. Based on an assumption that Mg depletion resulted from off-gassing into the inert atmosphere, all of the samples would be expected to have a similar amount of Mg depletion. Some Mg is likely lost due to off-gassing as indicated in Table 3.3 by comparing the Mg wt% of the original ingot and the 001201 atomized granules possessing no Al_2O_3. However Mg loss due to off-gassing alone does not seem to be a sufficient explanation for the severity of the loss in Mg for composite granules manufactured with higher volume fractions of Al_2O_3.

The deficiency in explaining the Mg depletion based on off-gasing alone is particularly evident when comparing the Mg analysis results for atomizing dates 001205 and 001207 in Table 3.3. The mixing temperature, time and atomizing temperature are nearly the same with the only exception being a difference in the nominal volume fraction of Al_2O_3. Increasing the volume fraction of Al_2O_3 while

Table 3.3. The matrix Mg content measured in wt% based on the atomization parameters and nominal Al_2O_3 volume fraction.

		Atomization Parameters			nominal alumina
Atomization Date	Mg wt%	Mix Temp (C)	Mix Time (min)	Atomizing Temp (C)	(vol%)
AA6111 ingot	0.6700				
001201	0.5000	770-780	not recorded	770-780	0
001205	0.4700	968	20	710	2
001207	0.1700	1000	20	710	5
001215	0.1600	1100	not recorded	950	5
010110	0.0380	1000	30	1000	10
010115	0.0890	1000	60	1000	20
010116	0.0720	1000	30	1000	20
010129	0.0580	1000	70	1050-1200	10

maintaining similar processing parameters during the atomization process appears to further deplete the Mg in the matrix.

A final question remaining was what effect did the atomization process have on the Al_2O_3 particles. Both optical and electron microscopy images, as shown in Figure 3.6 (a) and (b), reveal the presence of a layer coating the interface between some of the Al_2O_3 particles and the aluminum matrix. Different Al_2O_3 particles underwent varying degrees of interfacial reaction. Some particles possessed no reaction layer while others had a layer of reaction product up to 1μm thick as shown in Figure 3.6 (a). The formation of spinel or MgO layers on Al_2O_3 reinforced Mg containing aluminum alloys is not uncommon [Lloyd *et al.*(1994)], and severity of the Mg reaction with the Al_2O_3 to form either spinel ($MgAl_2O_4$) or MgO is dependent on

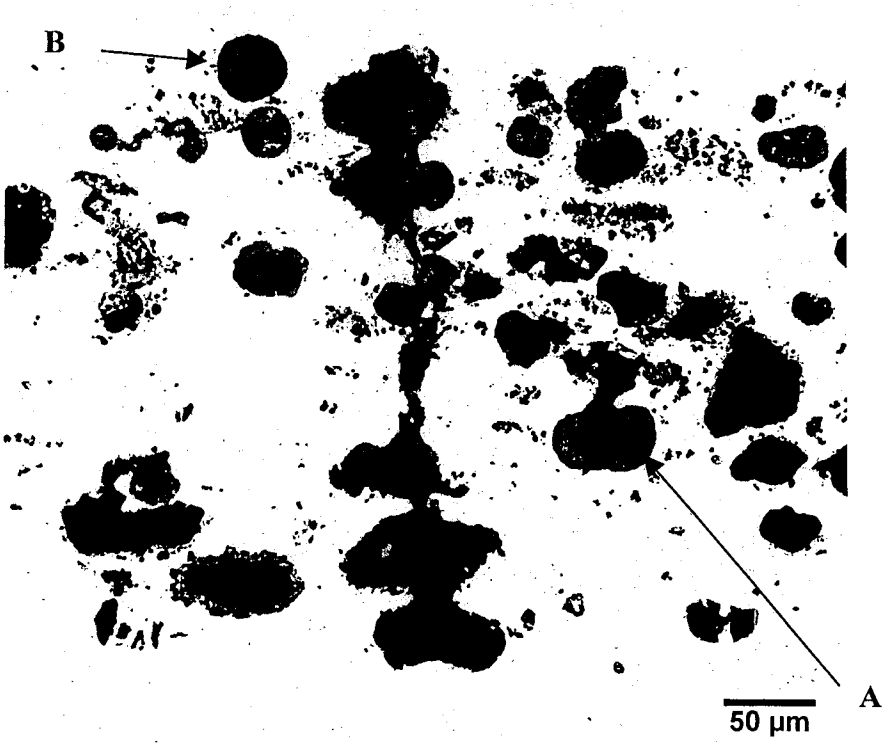

Figure 3.6 (a) Optical micrograph taken near the fracture surface of a composite with a measured 4% volume fraction of Al_2O_3 particles. Note that some particles have a thick layer of reaction product at the particle matrix interface (A). Others have very little or no reaction product surrounding the particles. (B)

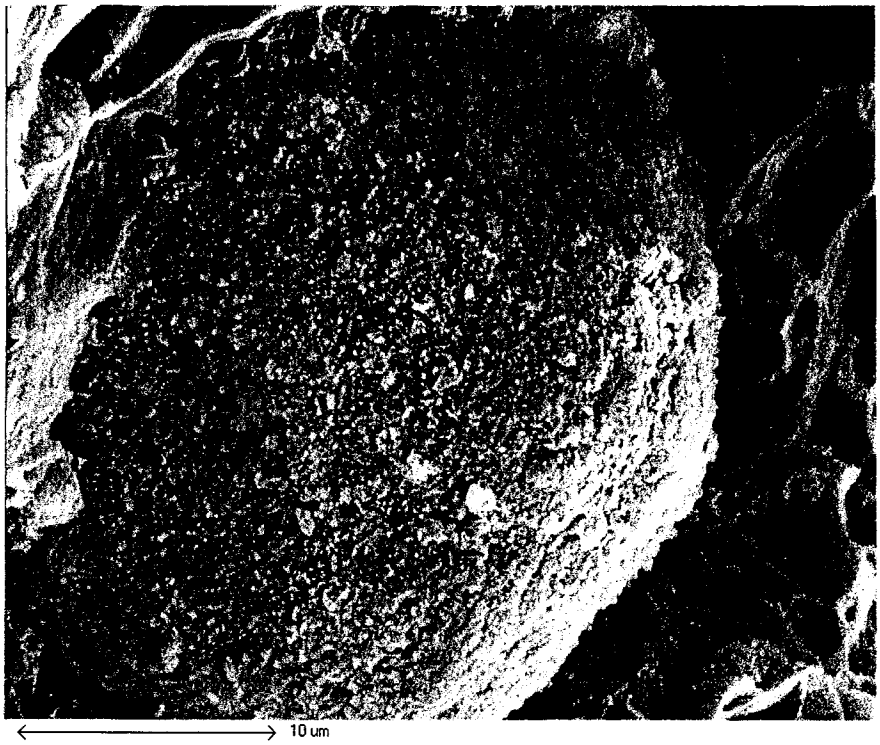

Figure 3.6 (b) Scanning electron microscope image of an Al_2O_3 particle coated with a layer of reaction product(s).

both temperature and the phase(s) of Al_2O_3 (Dudek *et al* (1993)). Formation of either phase requires the consumption of Mg, and in the case of the composite used in this work, the source of Mg for the reaction is within the AA6111 matrix.

Impulse atomization processing temperatures (>1000^{0}C) used to improve the wettability of the γ-Al_2O_3 not only increased the kinetics of the Mg interfacial reaction but also caused phase transformations in the particles. The phase transformation sequence of the spray dried Boehmite particles used to produce the γ-Al_2O_3 particle used in this thesis is presented in Figure 3.7. Three phase transformations, in the $\gamma \rightarrow \delta \rightarrow \theta \rightarrow \alpha$ sequence, can take place between the 650^{0}C calcination temperature used to produce the γ-Al_2O_3 and the 1000-1200^{0}C atomization temperatures.

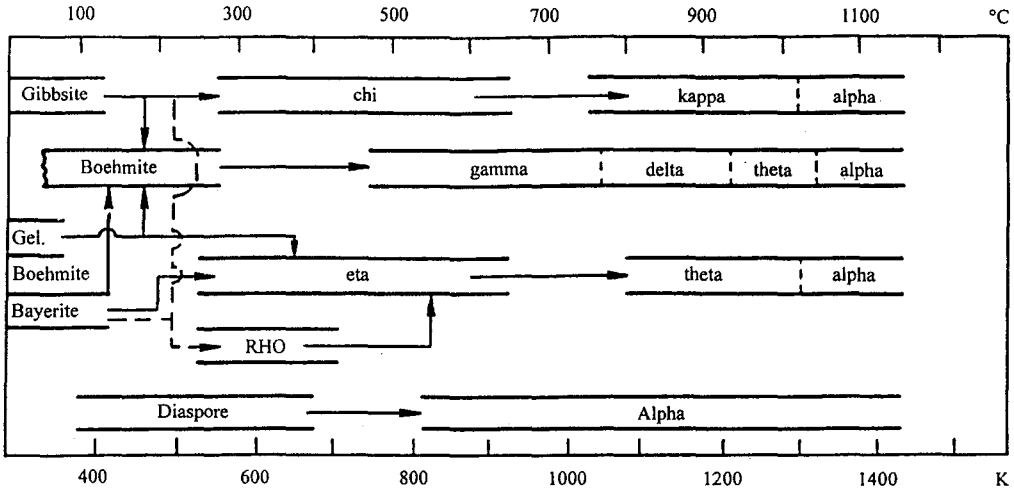

Figure 3.7 Thermal transformation sequence of alumina hydroxides (after Wefers and Misra (1987)). The Al_2O_3 particles used in this thesis started out as spray dried Boehmite as described in section 3.2.1.

X-ray diffraction on the Al_2O_3 particles received from CONDEA confirmed that the starting Al_2O_3 particles were all γ-phase, as indicated in the XRD results presented in Figure 3.8 (a). Results from particles extracted[2] from the impulse atomized composite granules (extracted from atomizing run 010116) presented in 3.8 (b), reveal that the α-Al_2O_3 phase exists. The magnitude of the α-Al_2O_3 peaks relative to the other peaks in the diffraction patter suggests that a majority of the Al_2O_3 particles transformed from γ to α-Al_2O_3 during the impulse atomization of the composite granules.

[2] Al_2O_3 particles were extracted from the composite courtesy Pierre Maroilis of Alcan Ltd. using a phenol solution to dissolve the aluminum matrix. XRD was performed by Doug Pfeiffer of Alcan Ltd. at Alcan's Kingston Research and Development Center.

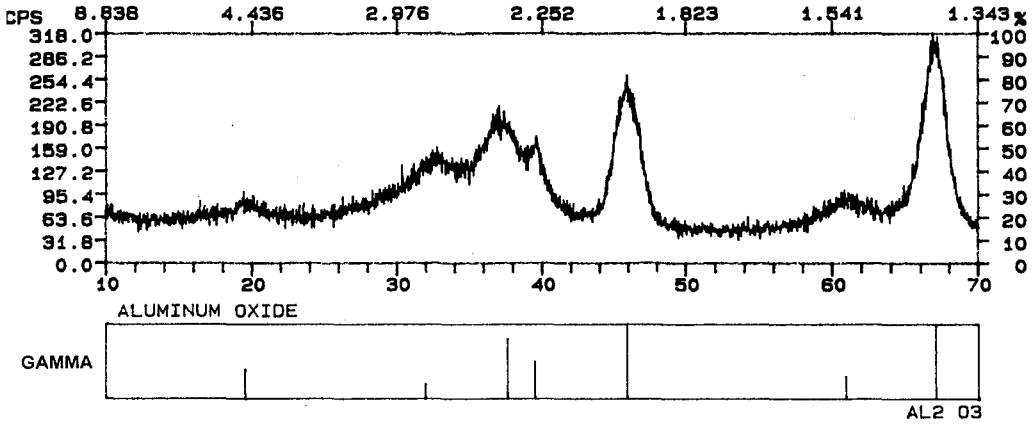

(a)

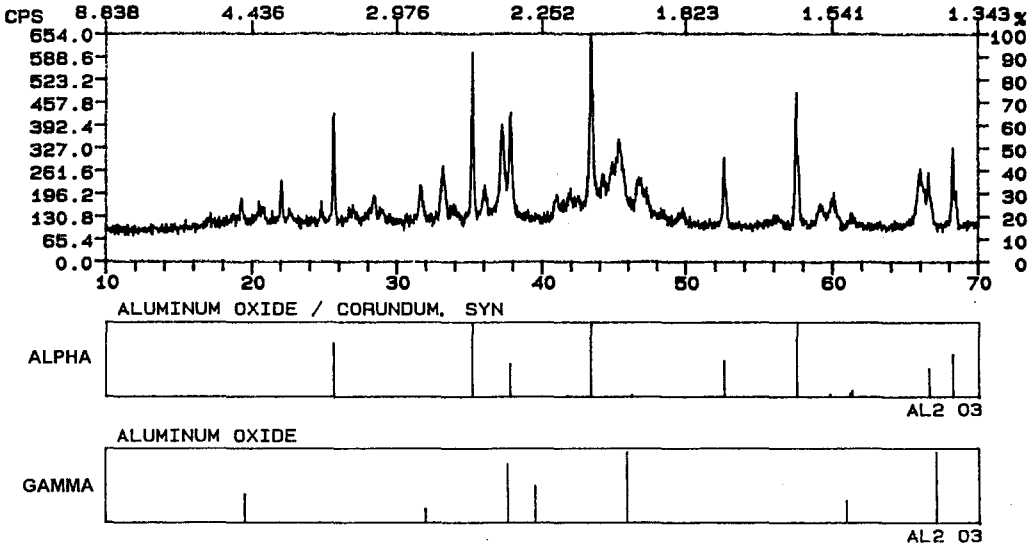

(b)

Figure 3.8 (a) X-ray diffraction results for the Al_2O_3 particles prior to processing. Result show that the Al_2O_3 particles are all gamma (γ) phase. (b) X-ray diffraction results for Al_2O_3 particles extracted from granules produced by the impulse atomization technique on run date 010116. The Al_2O_3 particles have primarily tranformed to the alpha (α) phase after processing.

3.7 Image Analysis of Al_2O_3 Volume Fraction

The fact that Al_2O_3 particles remained in the impulse atomization crucible suggested that the real volume fraction of Al_2O_3 in a given composite would differ from that of the nominal volume fraction. It is important at this point to clearly

differentiate the nominal volume fractions of Al_2O_3 discussed prior to this point of Al_2O_3. The nominal volume fractions are the target volume fractions of each atomization run. These "target" Al_2O_3 volume fractions were those resulting from mixing appropriate fractions of the raw AA6111 and Al_2O_3 particles in the atomizing crucible. As mentioned in section 3.2.2., following atomization unincorporated Al_2O_3 particles were always visible in the atomization crucible. It was therefore expected that the measured volume fraction would be less than that of the nominal volume fraction of Al_2O_3.

Two dimensional image analysis confirmed that the measured Al_2O_3 volume fraction in the composites following extrusion was indeed less than the measured nominal volume fractions. Two dimensional observation is limited to measuring the area fraction, and provided a given section is representative of the distribution and volume fraction of a given sample, this provides a measurement close or equal to that of the sample volume fraction. The estimated *average* volume fractions made by area fraction measurements using Image Tool 2.0, on polished sections of the composite extrusions are presented in Table 3.4.

Table 3.4. Comparison of nominal (estimated based on measured volumes mixed during the atomization process) and the measured average (based on 5 2-d sections per sample) volume fractions in composite billets used in this study.

Billet #	*Atomizing Date (s)*	*Mg wt %*	*Nominal Average Alumina Volume Fraction (%)*	*Measured Average Volume Fraction (%)*
6	010116	0.072	20	7.8
7	001207	0.17	5	0.6
8	010129	0.058	10	5.1
9	010115	0.089	20	0.58
11	001207	0.17	5	0.54
13	001207	0.17	5	0
14	001215	0.16	5	0.18
15	010110	0.038	10	3.78
16	010110/010116	0.0380/0.0720	10	5.96

Note: Billets 1 thru 5 were extruded at 400C and possessed a significant amount of processing damage they were therefore excluded from this study. Billets 10 and 12 were also excluded from the study.

Area fraction measurements were made on digital images acquired from an optical microscope. All measurements were made using digital images of the same magnification (50x) with thresholding performed so that the matrix was white and the Al_2O_3 particles were black. Thresholding tended to incorporate the reaction layer visible in the original micrographs into the white of the matrix background. The measured particle area fraction is therefore representative of the actual unreacted particle volume fraction and for the most part excludes the reaction layer.

The Al_2O_3 distribution in the composite samples with average volume fractions (or area fractions) of 4% or greater can be classified as being heterogeneous. Low magnification optical images of billet 6 (measured average volume fractions of 7.8) presented in Figure 3.9 that the composite can be subdivided into areas off high and low Al_2O_3 volume fraction. The area fractions of particles in regions of high and low Al_2O_3 particle fraction were independently measured. Local volume fraction of Al_2O_3 in the particle rich regions averaged 8.8% for the samples with an average composite volume fraction of 3.78% (sample B15). Composites with the highest average volume fractions (7.8% in sample B6) possessed regions of particles with volume fractions of up to 17.5%. The volume fractions of the particle poor regions of these composites typically averaged 0 to 2%. Two other higher volume fraction composites used in this thesis, B8 and B16, also possessed some heterogeneity in the distributions of the Al_2O_3 particles. In the B8 sample (measured 5.1% volume fraction), differences in the volume fraction for the high and low volume fraction regions were less severe. The low volume fraction regions averaged roughly 3% Al_2O_3 while the high volume fraction regions averaged 8% Al_2O_3. Sample B16 was

manufactured by combining the granules used to manufacture samples B6 and B15. The average volume fraction of the particle rich regions in the B16 composite was 13.4% (based on the measurement of three particle rich regions). It appeared however, that the ratio of particle rich to particle poor regions was approximately 1:2, meaning that the particle poor regions occupied more of the composite volume than particle rich regions.

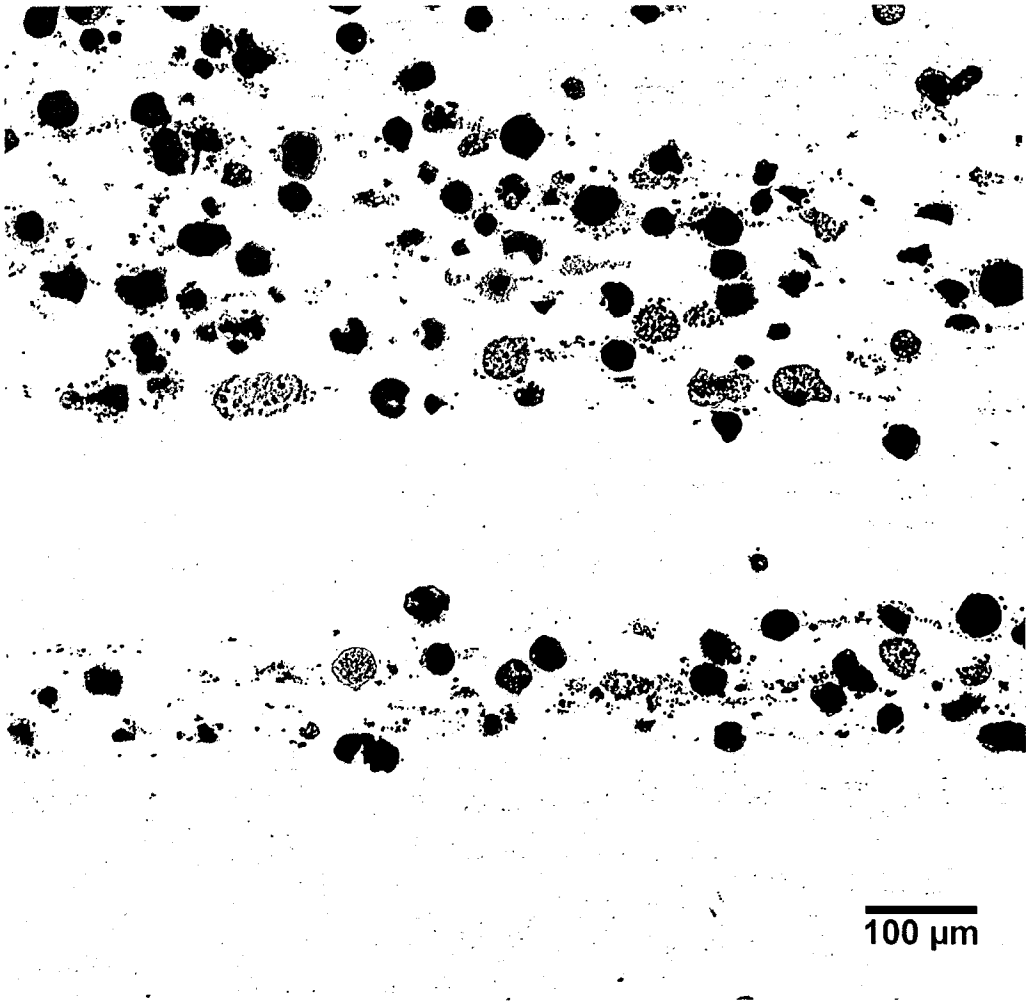

Figure 3.9 Optical micrograph of a sample with an average measured Al_2O_3 volume fraction of 7.8%. Note the bimodal nature of the spatial distribution of particles. A region of low volume fraction separates two high volume fraction regions.

3.8 Scanning Electron Microscopy of the Fracture Surface

A sample from each batch was loaded to fracture for scanning electron microscopic examination of the fracture surface. The fracture surfaces of all the composites can be classified into two groups: those with low measured volume fractions (<1%) and Mg levels greater than 1.6 wt% and the remaining composites possessing higher Al_2O_3 volume fractions and Mg levels of less than 1 wt%. In samples containing volume fractions of greater than 4% Al_2O_3 or greater the fracture surfaces reveal two length scales of void coalescence as shown in Figure 3.10. Large-scale void coalescence, with voids in the order of the particle diameter, occurs in the particle rich regions. In regions surrounding the particles rich regions the matrix is saturated with coalesced voids in the order of 1-5μm. Flat particle faces are typically visible in bottom of each void while the matrix between the particles appears to neck down to a knife like ridge. While the majority of the particles on the fracture surface are cracked, some particles that have decohered from the matrix are visible in regions of local high volume fraction as shown in Figure 3.11 and 3.12.

The fracture surface of samples with low volume fractions of Al_2O_3 and Mg wt % of roughly 0.17 wt% was much smoother in appearance as shown in Figure 3.13. In these samples the voiding occurred at only the 1-5 μm length scale similar to the particle poor regions of the higher volume fraction composites. The coalesced pores were strained along a plane of shear, which is indicative of a process of microvoid coalescence by shear [Gimple (2001)].

An estimate of the local strain at fracture was obtained by measuring the area of a sample's fracture surface using Image J. Examples of the fracture surfaces used

for the fracture surface area calculations are given in Figures 3.8 and 3.11. The results presented in Table 3.4 are written in terms of the reduction in area and the equivalent axial true strain at fracture. The reduction in area was calculated through

$$RA = \left[\frac{A_i - A_f}{A_i} \right] \times 100 \tag{3.1}$$

where A_i and A_f are the initial sample and the fracture surface areas respectively. The equivalent true strain at fracture was calculated through

$$\varepsilon_f = 2 \ln \left(\frac{A_i}{A_f} \right) \tag{3.2}$$

Error values for the reduction in area measurements were calculated by estimating the accuracy to which the image analysis could be done in terms of the correct selection of the fracture surface edge, which was typically 3 pixels in every direction. For a resolution of 200 pixels/mm this corresponds to an error of approximately 135 um^2. It is important to point out that while this does provide a value for the reduction in area, an exact value for the reduction in area requires that the void area be subtracted from the sample fracture surface area. The reduction in area values presented in Table 3.5 for samples that contain large-scale void coalescence (samples B15, B16 and B6) are therefore overestimates of the true reduction in area values.

These results indicate that the strain at fracture decreases with increased volume fractions of Al_2O_3. Increasing the volume fractions greater than a measured average of 3.8% had a minimal effect on further reducing the reduction in area at fracture.

Table 3.5 Reduction in Area and Equivalent True Axial Strain at Fracture for the composite materials studied in this thesis.

Al_2O_3 Volume Fraction	Sample ID	Reduction in Area (%)	Equivalent True Axial Strain at Fracture
0	B13	50.2 ± 2.1	1.48
0.18	B14	34.3 ± 1.8	0.84
3.78	B15	10.3 ± 2.1	0.19
5.96	B16	8.4 ± 2.1	0.17
7.8	B6	8.2 ± 2.1	0.17

Figure 3.10. Matching fracture surfaces of the 4% volume fraction composite. A sample manufactured from the same composite material is later used in the tomography work. The area of the fracture surface was calculated directly from the image on the left.

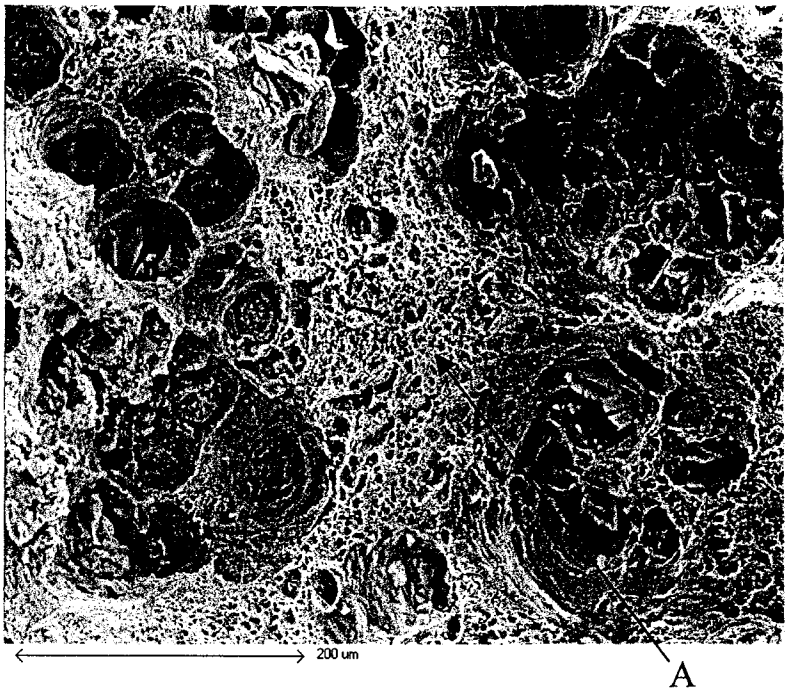

Figure 3.11 Scanning electron micrograph of fracture surface in a sample with an average 5.1% volume fraction of Al_2O_3, showing both the large and small scales of void coalescence (A).

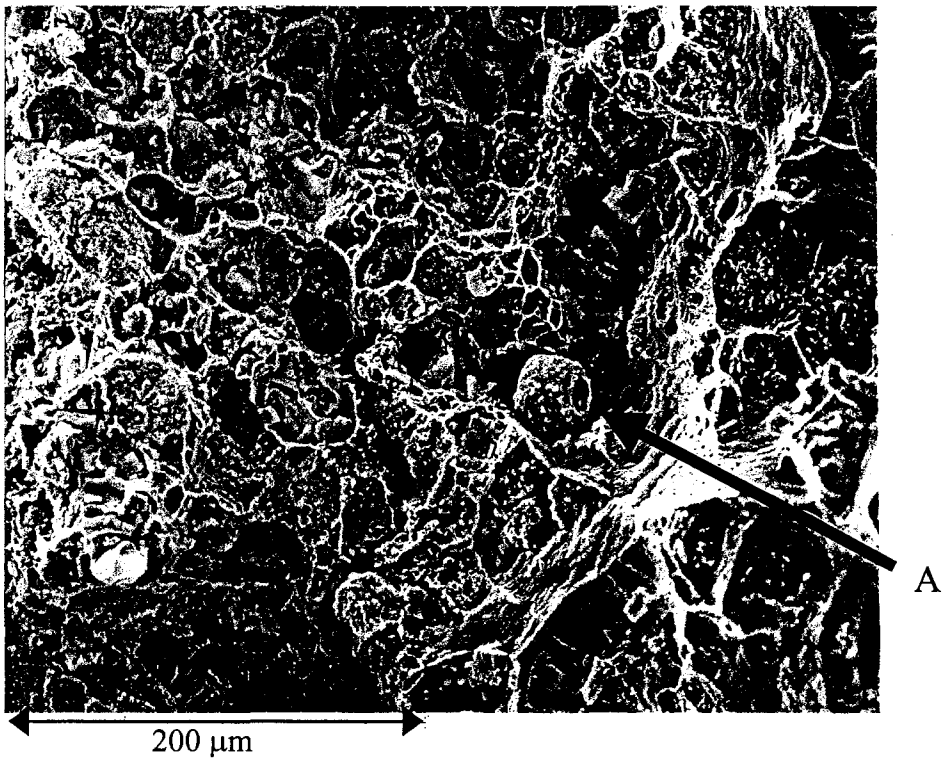

Figure 3.12 High magnification image of fracture surface in a region of high local volume fraction. While the majority of majority of particles in this region are fractured, some decohered particles are visible (A)

(a)

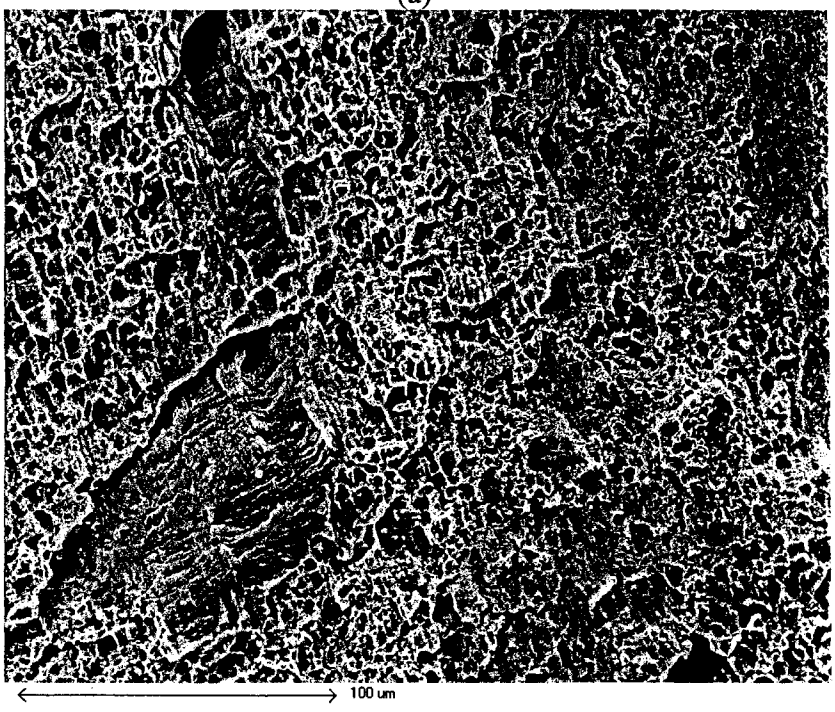

(b)

Figure 3.13 (a) Scanning electron micrograph of fracture surface on a sample with an average Al_2O_3 volume fraction of 0%. (b) Higher magnification image showing 1-5μm voiding.

3.9 Microscopy on Fracture Surface Cross-Sections

Each fractured sample was sectioned following electron microscopy of the fracture surface. Sample sections were prepared by first cold-mounting the fractured tensile sample in epoxy. The samples were then ground and polished until a section located approximately midway through the sample was obtained.

Metallography on the samples containing Al_2O_3 volume fractions of 4% or greater required a significant amount of patience and experimentation. Those interested in sectioning and polishing similar materials are encouraged to first follow the steps outlined in Appendix I. This procedure was the only one of the several attempted that provided a high-quality polish of the matrix without causing the particles to stand excessively proud of the polished matrix surface.

Optical images on the sectioned fracture surfaces of samples provided additional information, complimentary to the scanning electron images of the fracture surface, of the damage process. In areas of low volume fraction, including the entire cross-section of the low volume fraction composites as shown in Figure 3.14, the matrix failed along a line oriented approximately $45\text{-}55^0$ to the tensile axis. The sample with 4% volume fraction had no visible signs of micro-crack linkage between several cracked particles in the plane of the fracture surface investigated as shown in Figure 3.15. The connection of damage between two neighboring particles, is however, visible. In regions of high volume fraction, failure occurs by the linkage of damage between adjacent cracked particles, forming a fracture across the entire high volume fraction region approximately perpendicular to the tensile axis as illustrated in Figure 3.16. These fractures are then propagated through the low volume fraction

regions along an approximate 45^0 angle to the tensile axis. In composites with local high volume fraction regions, additional linkage across the high volume fraction regions occurs is limited to locations quite close to the fracture surface. At locations away from the rather diffuse neck little or no linkage was visible in any of the high volume fraction regions in the composites studied. Where linkage of the damage occurred, the distance between the cracked halves of a given particle was in the order of a particle diameter.

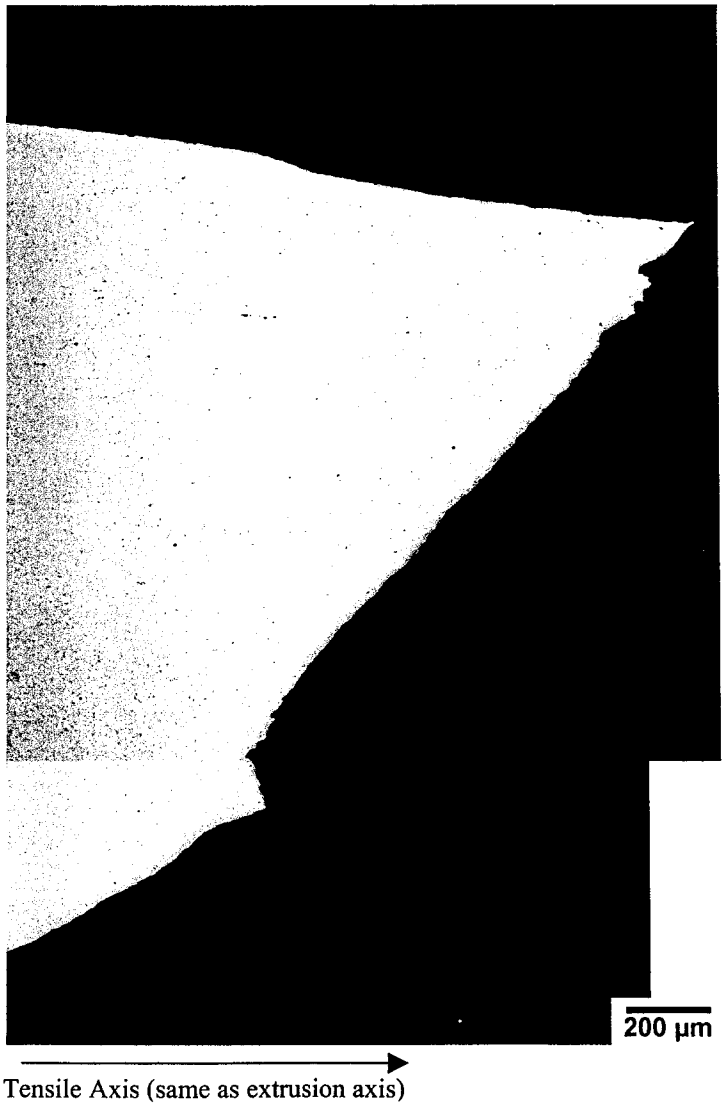

Figure 3.14. Optical micrograph of a fracture surface section for a composite possessing a measured 0% volume fraction of Al_2O_3.

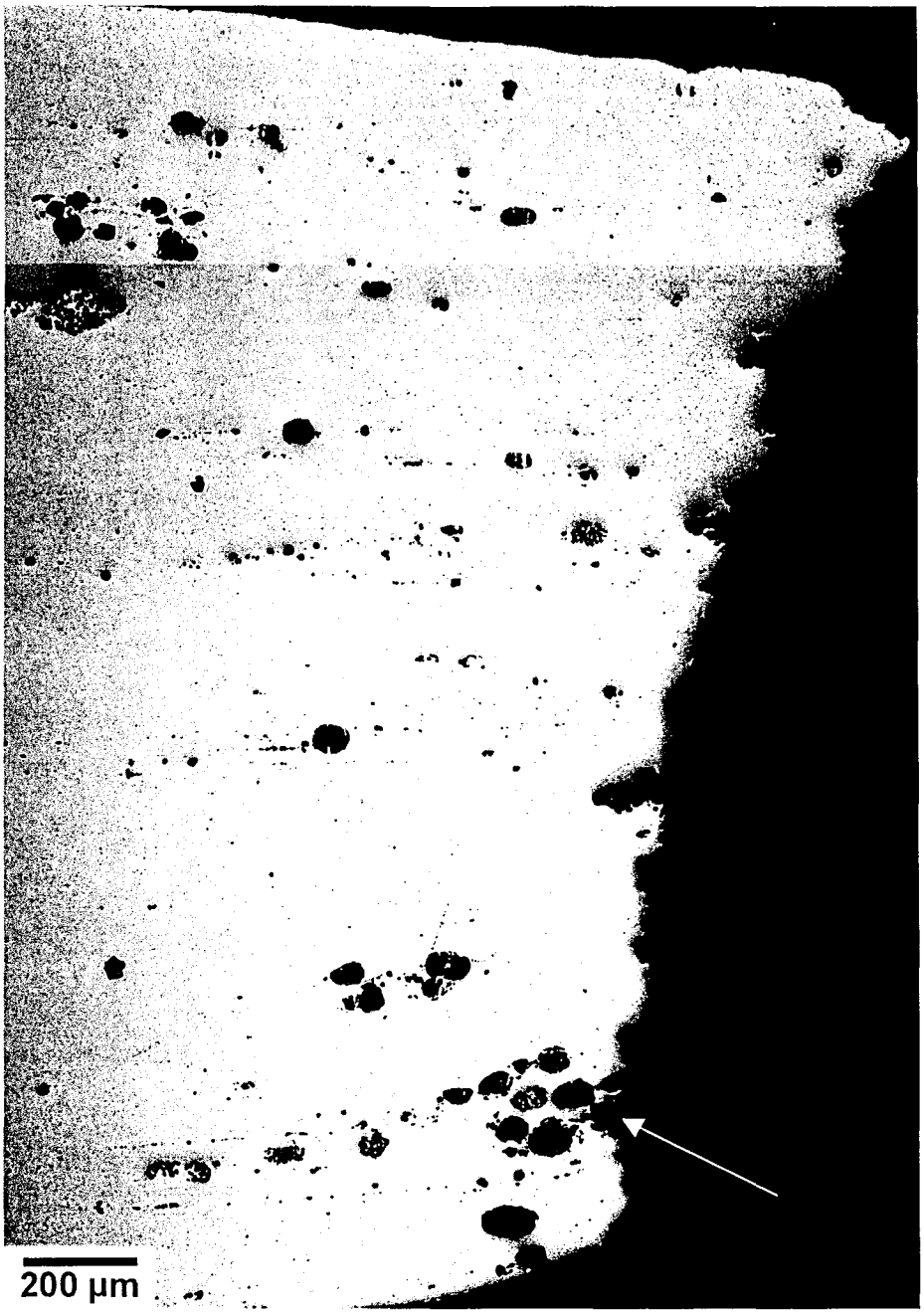

Figure 3.15. Optical micrograph of a fracture surface cross-section in a sample with an average 4.2% volume fraction. Note that the fracture surface intersects two cracked particles in a region of local higher volume fraction.

Figure 3.16. Optical micrograph of a fracture surface cross-section in a sample with an average 7.8% volume fraction. Note the linkage of damage between cracked particles visible in the high volume fraction region.

Damage in these composite materials was investigated in a more comprehensive manner through both mechanical testing and the use of x-ray

computed tomography. While this information provides a qualitative description of the fracture process complete understanding of the damage process can only be obtained with experimental work that allows for the direct observation of the damage process and the effect of damage in respect to the composite flow response as damage evolves with deformation. The x-ray computed tomography results, presented in Section 5, provided a unique opportunity to observe the damage process as it evolved in much greater detail than the introductory observations made in this section. Mechanical testing results, presented in the section that follows, allow for the investigation of the effects of damage on both composite stiffness loss and the composite flow response.

3.10 General Remarks

The process used to manufacture the composites used in this thesis yielded some unexpected results. Perhaps the most unexpected of these was the depletion of Mg from the matrix. While this initially appeared to complicate the quantification of the matrix flow response, it motivated the use of a new technique for the quantification of the matrix flow response. The use of instrumented sharp indentation to predict the flow response of an elasto-plastic material had previously only been attempted on monolithic aluminum alloys. The reasonably good results obtained in the work presented with in Section 4.6 of this thesis potentially opens up the door to a new approach of gaining an understanding of the flow response of individual phases in heterogeneous materials. This applies to metal matrix composites and potentially multiphase materials like dual phase steels.

CHAPTER 4

MECHANICAL TESTING RESULTS

4.1 Introduction

The deformation behavior of the Al/Al_2O_3 composites was investigated through a series of mechanical tests. One particular topic of interest was the way in which damage influences the tensile deformation behavior. This was first investigated by comparing the difference between the tensile and the compressive flow behavior. Compression testing tends to suppress damage and therefore provides data representative of the composite deformation in the absence of damage. The difference between the tensile and compressive flow curves therefore provides insight into how severely damage influences the deformation behavior.

The loss in stiffness with increased tensile deformation was monitored through tensile loading – unloading cycles. This loss in stiffness provides another means of characterizing how damage effected the composite response. Low strain Baushinger testing at two different volume fractions was employed to obtain quantitative information concerning the development of internal stress (mean matrix stress) as a function of Al_2O_3 content and the plastic prestrain.

A final series of mechanical tests are particularly interesting because they employ instrumented sharp indentation to determine the elasto-plastic response of the matrix in a rather unconventional manner. This provided the only known means of separately measuring the matrix flow properties of the Mg-depleted AA6111 matrixes. These results are of critical importance in this work since knowledge of the elasto-plastic matrix response is required in gaining an understanding of a composite's flow behavior.

4.2 Conventional Tensile Testing

Tensile testing was performed on two mechanical testing systems. The first system used was an Instron 4202/5500R Electro-Mechanical Test Frame with a 10 kN load cell using Series IX software. This system, with its low capacity load cell, was particularly attractive due to the small sample size and therefore relatively low loads (1-2 kN) required for deformation. An additional tensile test was performed on one sample from each on an Intron 100 kN servo-hydraulic loading system using Series IX software, to validate the results from the low capacity load cell. All tests were performed at room temperature at a constant strain rate of 0.0001 /second.

4.2.1 Results

To ensure that the experimental results from each of the sample batches were repeatable, a series of three tensile tests were performed on three different samples from each batch. These samples all underwent identical heat treatments and were of the same geometry. The results from tensile tests on each of the sample batches indicate that the flow response of samples removed from the same batch is very similar. Additionally, samples with the same composition but manufactured from different batches also had results similar to those of other batches with the same volume fraction. Representative tensile testing results for the Al_2O_3 volume fractions used in this thesis are included in Appendix II. The results presented in the Appendix are grouped based on volume fraction. Each plot for a particular volume fraction contains data for samples manufactured from the same and/or different sample batches of the same Al_2O_3 composition. The results were

found to be repeatable for all of the Al_2O_3 volume fractions and distributions examined in this thesis regardless of which batch the samples were manufactured from.

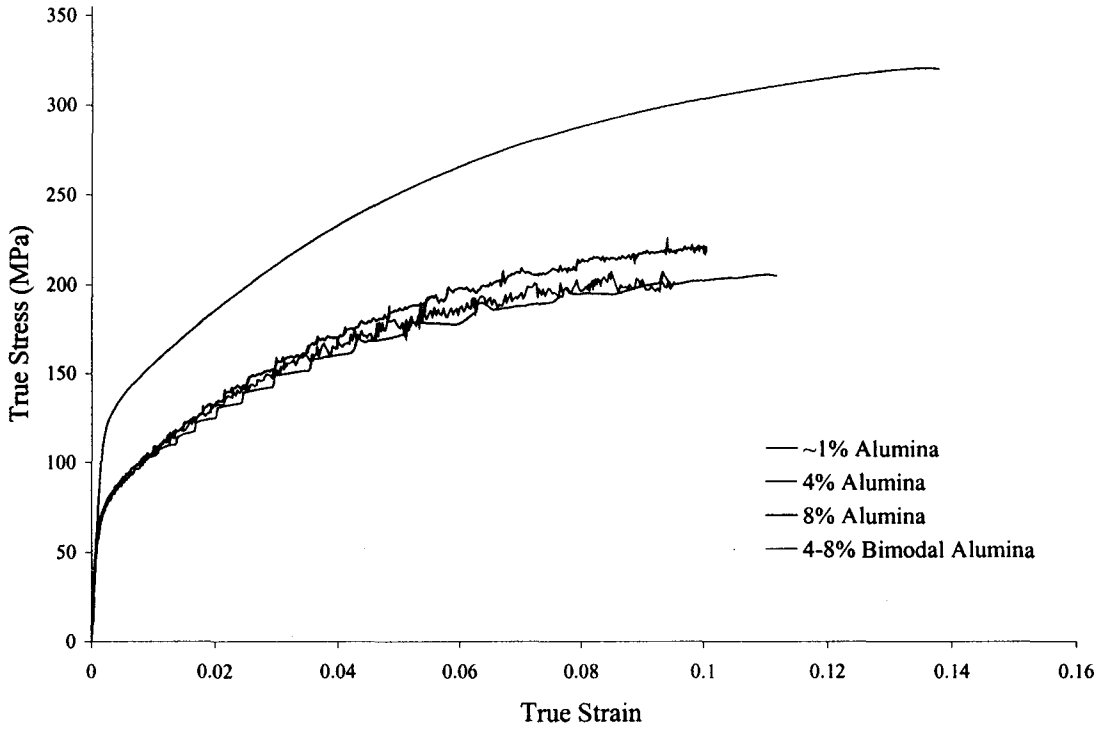

Figure 4.1. Room temperature tensile testing results for composites with different Al_2O_3 volume fractions and distributions. The matrix of the composites with ~1% Alumina had Mg concentrations of approximately 0.2 wt% whereas the matrix in the other composites had Mg concentrations of approximately 0.09 wt%.

Results representative of those for each Al_2O_3 volume fraction and/or distribution used in this thesis are presented in Figure 4.1. The difference in the flow curves of the 4%, 8% and the bimodal 4-8% Al_2O_3 composite are not significant in the low plastic strain regime. The spread in the average flow stress in the 4% to the 8% Al_2O_3 composites was at the most 40 MPa at a strain of roughly 8%. At low stains the flow stress values did not appreciably differ. This clearly was not the case for the low volume fraction composites with Al_2O_3 volume fractions of 1% or less. As explained previously, the stronger response

of these low volume fraction composites likely results from the much higher Mg content in the matrix that provides a significantly greater amount of precipitation strengthening.

Plotting the work hardening rate (θ) versus true tensile strain required smoothing of the experimental data due to the serrated nature of the loading curves. For each experimental tensile curve for a given composite, smoothing was performed using negative exponential 3rd order spline fit to the plastic deformation data with Sigma Plot 2000 software. The smoothed data was then numerically differentiated and plotted with the corresponding tensile loading curve. Results for each volume fraction are plotted in Figures 4.2 to 4.5. A comparative plot of the work hardening of all the samples studied versus tensile strain is presented in Figure 4.6.

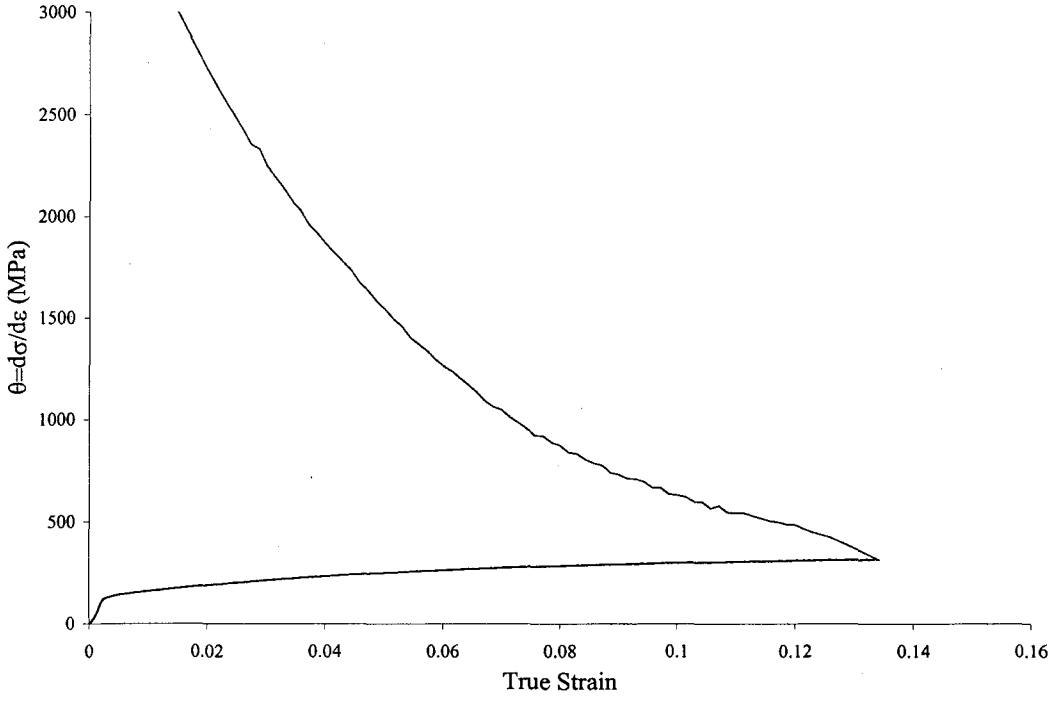

Figure 4.2 Effective work hardening rate (θ) versus true tensile strain for sample with ~1% Al_2O_3.

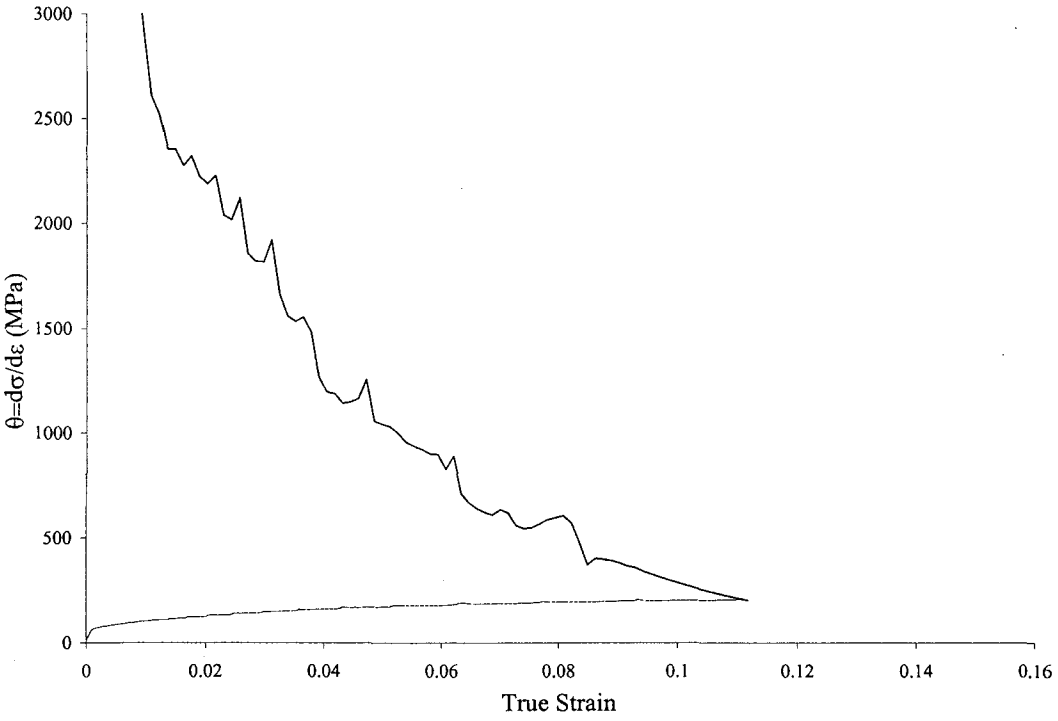

Figure 4.3 Effective work hardening rate (θ) versus true tensile strain for samples possesing 4% volume fraction Al_2O_3.

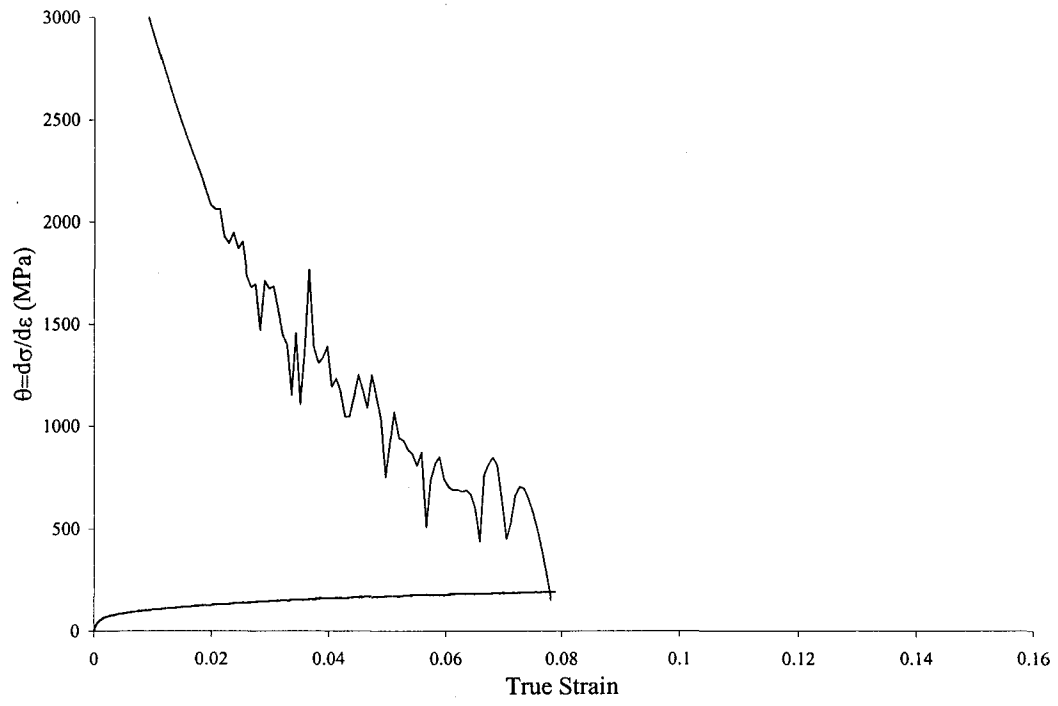

Figure 4.4 Effective work hardening rate (θ) versus true tensile strain for samples possessing 8% volume fraction Al_2O_3.

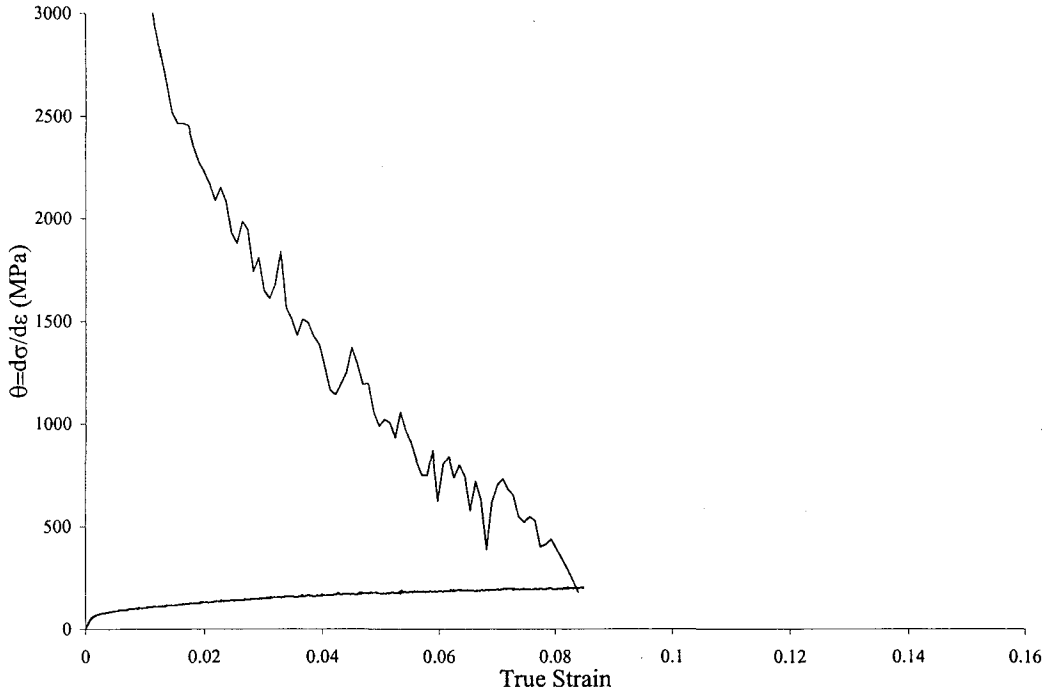

Figure 4.5. Effective work hardening rate (θ) versus true tensile strain for samples having a bimodal distribution of regions with 4 and 8% volume fractions of Al_2O_3

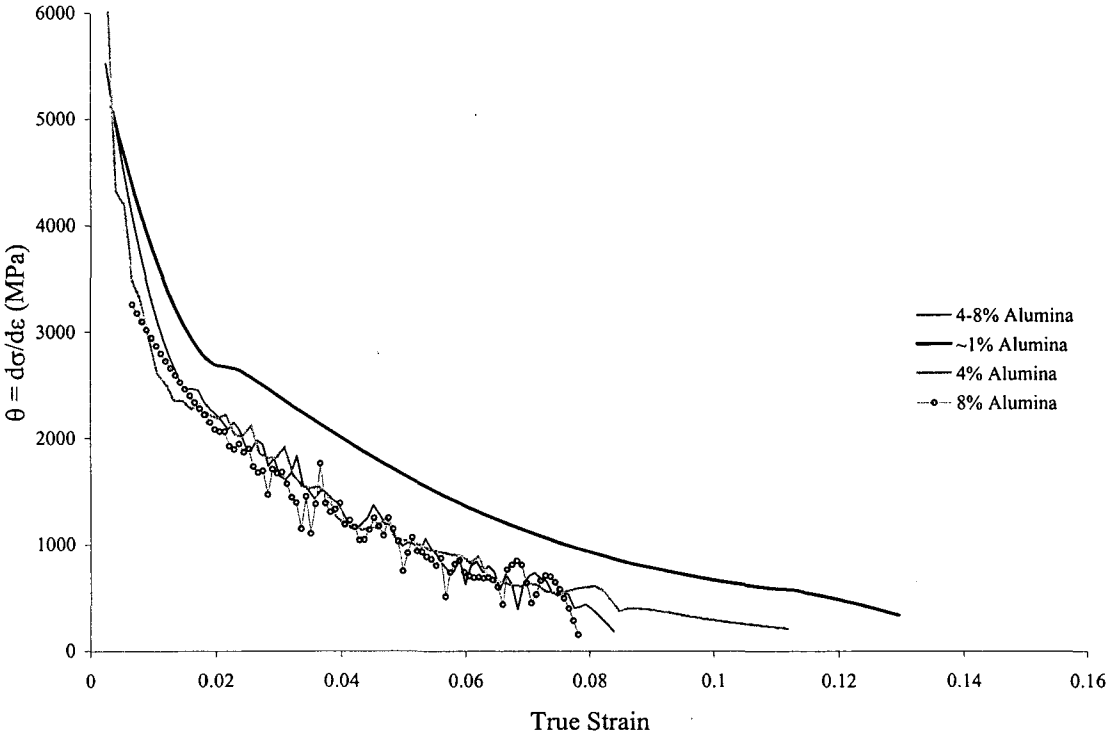

Figure 4.6 Comparison of the difference in the effective work hardening for composites possessing varying Al_2O_3 (Alumina) volume fractions and/or distributions.

At low strains the work hardening rates of all the composites were similar. At larger strains, however, the work hardening rate for the composite possessing less than 1% Al_2O_3 was greater than those for the higher volume fraction regions at a given value of strain. Differences between the work hardening rates of the 4%, 8% and the bimodal 4%-8% Al_2O_3 composites at low to moderate strains (up to ~8%) were difficult to distinguish. At higher strains however, the differences became discernible particularly at the locations where the work hardening rate quickly dropped too a value equal to the composite tensile stress. At this point the work hardening rate dropped most rapidly for the 8% Al_2O_3 composite and only slightly slower for the bimodal 4%-8% composite. The work hardening of the 4% Al_2O_3 volume fraction composite dropped off at a more gradual rate and the rapid drop occurring in the two composites with higher volume fraction was not observed.

4.3 Compression Testing

Compression testing was used to evaluate the deformation behavior of the composites in a state of stress that promotes the suppression of damage. Each compression sample was machined to the specifications detailed in Appendix II. All samples were carefully examined to ensure that the loading faces were parallel and the sample walls were perpendicular to the loading faces. Prior to testing, the compression platens were ground smooth with 1200 grit SiC paper and lubricated with a methanol/boron nitride paste. Additional lubrication was applied to each compression sample by painting the methanol/boron nitride paste onto each of the loading faces.

Sample geometry restrictions made it impossible to measure the compressive straining by direct mounting of the extensometer onto the sample surface. As an

alternative, a spring-loaded push rod, which functioned in the same way as a linear voltage displacement transducer without the electronics, was used to directly measure the platen displacement. Fixing one arm of an extensometer onto the base the push rod apparatus and fixing the other onto the moving shaft of the apparatus monitored the movement of the pushrod. An adaptor piece was added to the shaft of the pushrod so that when the extensometer was mounted the knife-edges would remain along the same vertical axis. A complete diagram of the compression testing apparatus is included in Appendix II.

4.3.1 Results

A summary of the compression testing results for the four composites studied in this thesis is presented in Figure 4.7. All compressive loading curves have been shifted along the strain axis so that a line drawn tangent to the upper section of the linear portion of the loading curve would intersect both the strain and stress axis at zero. This was required because the lubrication method resulted in varying thickness in the methanol/boron-nitride layer. These thickness differences caused a variation in the amount of initial loading required to "seat" the samples. In all cases the loading curves became linear at a stress of approximately 30 MPa. Lubrication was only applied prior to testing and visible barreling typically began to occur at strains of approximately 20%. To ensure that any effects resulting from barreling are excluded from the results, compressive loading curves are only plotted to a true strain of 12%.

The apparent soft elastic loading response made it difficult to directly compare the entire tensile and compressive loading curves. Since plastic deformation occurs over a larger strain regime, the sensitivity of the strain measurement to the presence of the lubricating layer is diminished. As a result, the tensile and compressive flow curves are

plotted versus true plastic strain. The zero plastic strain point for both the tensile and compressive flow curves was defined at the point of intersection of a line drawn parallel to the elastic portion of the each loading curve at a 0.2% offset. The resulting tensile and compressive loading curves for the composites studied are shown in Figure 4.8 (a-d).

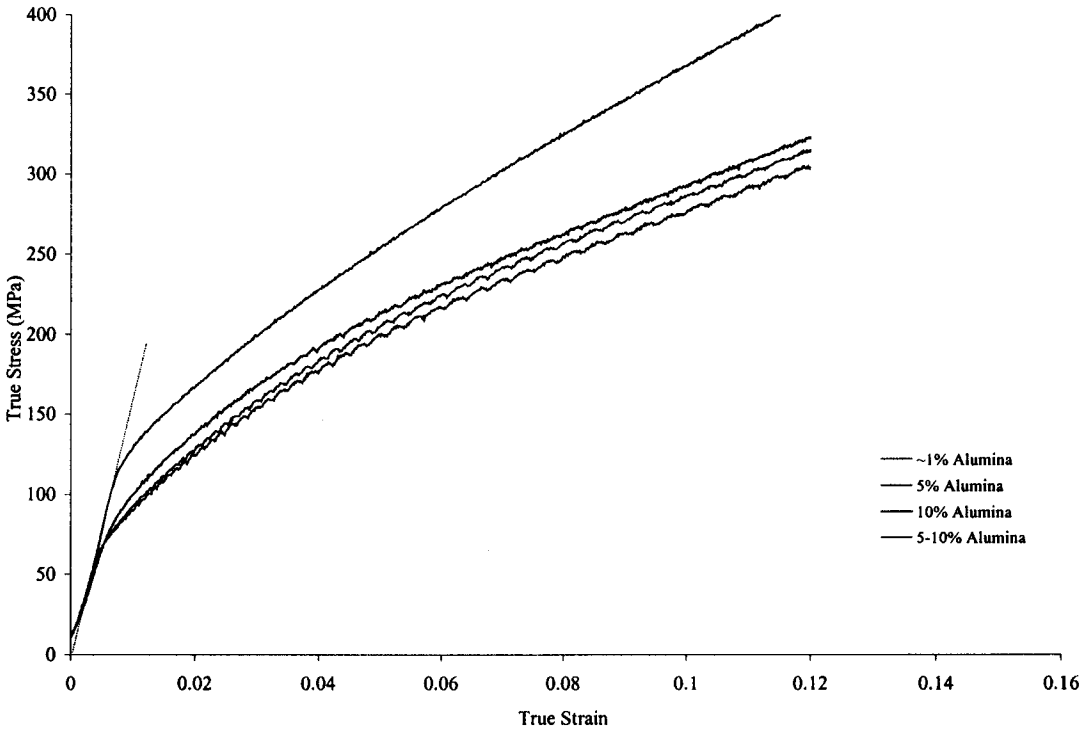

Figure 4.7. Summary of compression testing results for the four volume fractions studied in this thesis. Note that the compression testing curves have been shifted so that a tangent drawn along the linear portion of the loading curve intersects both the strain and stress axis at zero.

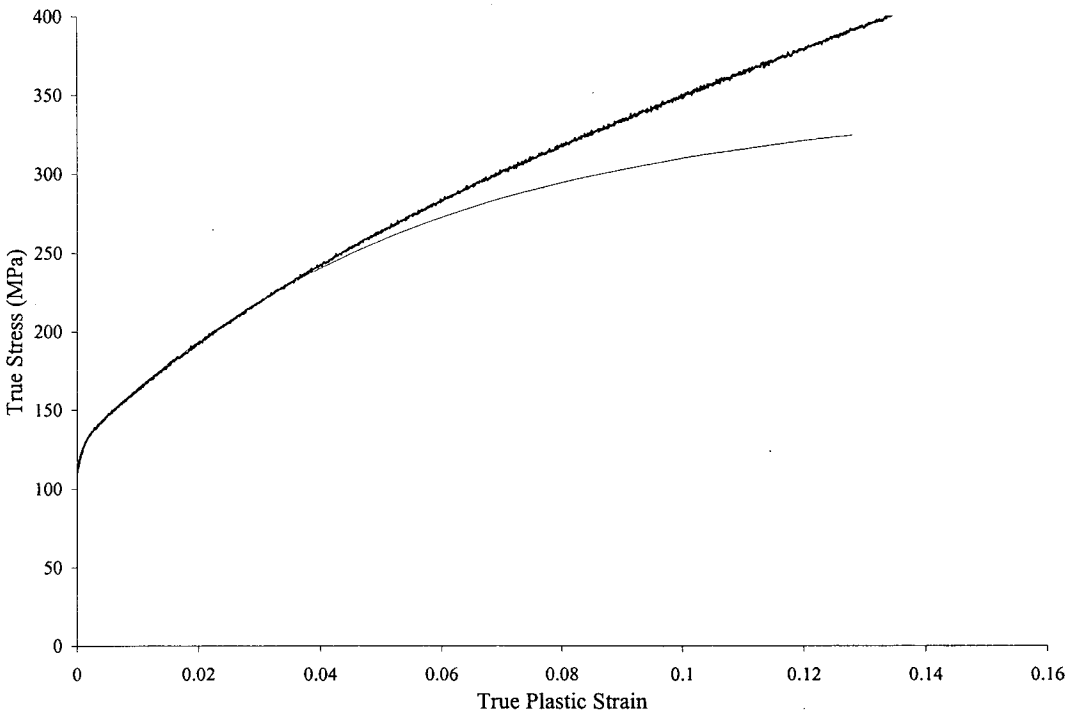
True Stress (MPa)
400
350
300
250
200
150
100
50
0
0
0.02
0.04
0.06
0.08
0.1
0.12
0.14
0.16
True Plastic Strain

(a)

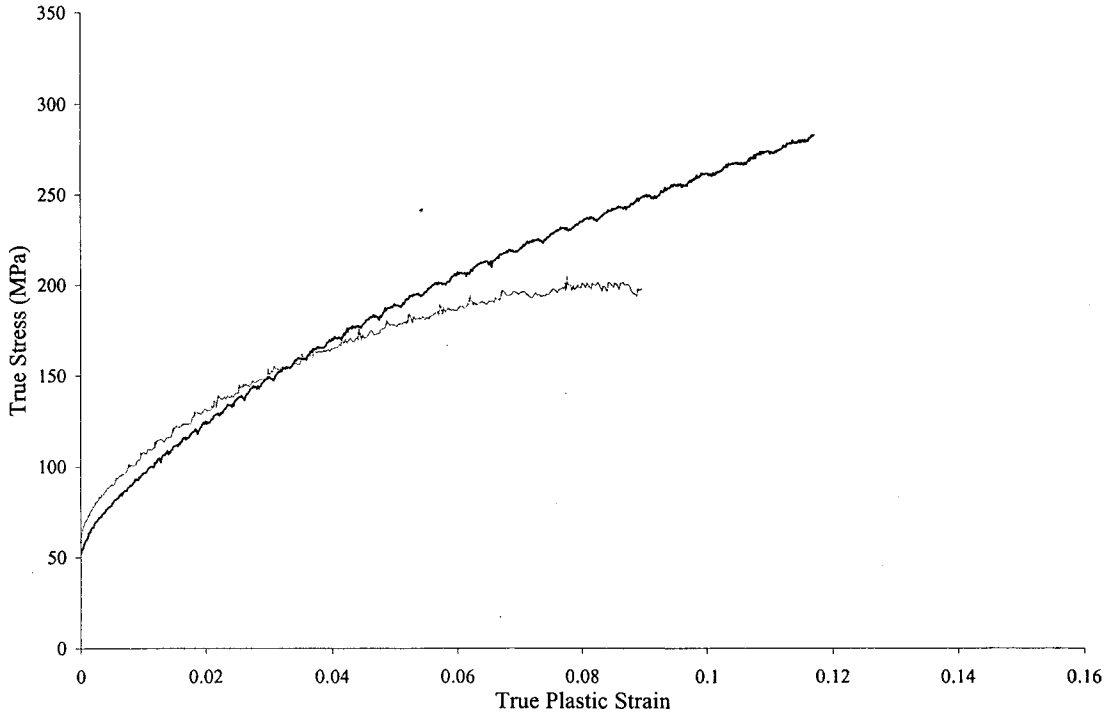
True Stress (MPa)
350
300
250
200
150
100
50
0
0
0.02
0.04
0.06
0.08
0.1
0.12
0.14
0.16
True Plastic Strain

(b)

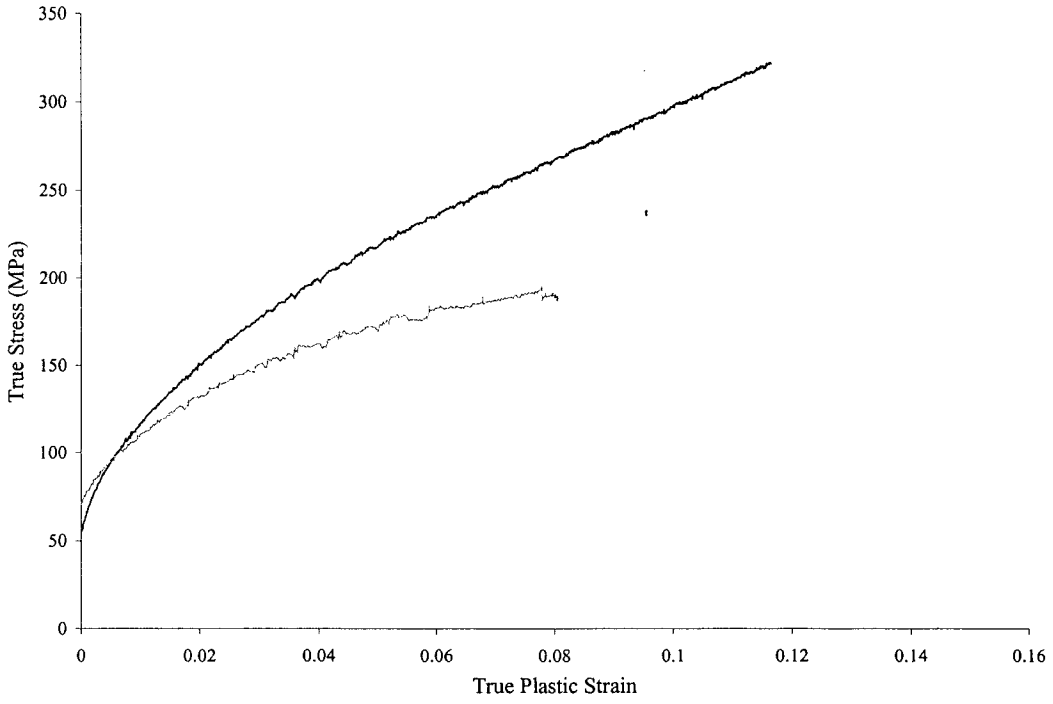

(c)

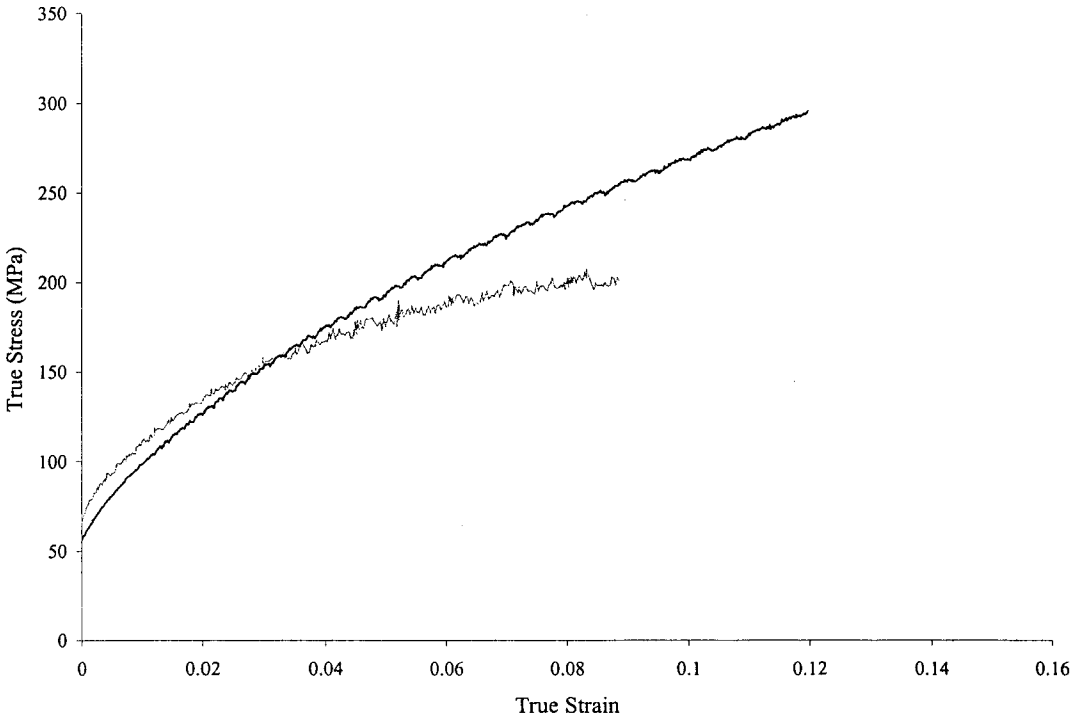

(d)

Figure 4.8 Comparison of compressive (black) and tensile (gray) loading curves for samples with (a) ~1% Alumina, (b) 4% Alumina, (c) 8% and (d) a bimodal mixture of 4% and 8% Alumina. Note that the scale for the stress axis in 4.12 (a) is different than the scale used in 4.12 (b) to (d).

The correlation between tensile and compressive behaviour scaled with the volume fraction. Composites with Al_2O_3 volume fractions of 4% or possessed flow curves of similar shape up to strains of roughly 4%, with the compressive flow curves of slightly lower magnitude than the tensile curves. At this point the tensile work hardening rate (the slope of the flow curve at a given value of strain) decreased at a considerably greater rate than the compressive work hardening rate. The composite with 8% Al_2O_3 possessed tensile and compressive flow curves which never appeared to be in agreement in any portion of the deformation. In these composites, the tensile work hardening rate was much less than that in compression almost immediately after plastic flow commenced.

All the composites with volume fractions of 4% or greater experienced a "crossing" of the compressive and tensile flow curves. This effect has been observed by both Maire *et al.* (2000) and Corbin (1992) and results in the compressive yield stress being smaller than in tension and the work hardening being higher in compression than in tension. The crossing of the curves occurs at much larger strains in the composites with volume fractions of 4% or less than in the 8% volume fraction composites. The crossing of the curves is delayed in the lower volume fraction composites because the differences in work hardening rate in tension and compression are small over a much larger strain range than the 8% volume fraction composites.

4.4 Tensile Load-Unload Cycles

The load and unloading testing cycles were performed to monitor the change in stiffness of the composites with loading. Tensile load and unload cycles were performed using the same experimental set-up and sample geometry as used in the tensile monotonic

loading. All samples were unloaded to approximately 10-20 MPa before the next loading cycle commenced. The strain rate for both the load and unload cycles was 0.0001 /s.

4.4.1 Results

The tensile load and unload testing results for each composite are presented in Figures 4.9 (a) to (d). Also included in these plots are the corresponding monotonic tensile loading curves. The match between the monotonic loading and cyclic loading was quite close particularly at low to moderate strains. At higher strains, near the failure point as defined by the Considère condition ($\frac{d\sigma}{d\varepsilon} = \sigma$), some deviations between the curves can be observed.

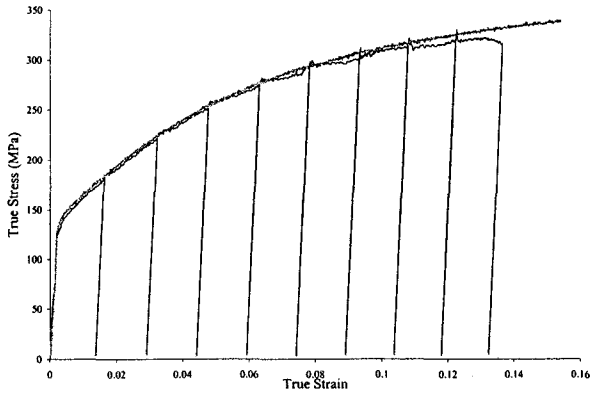

(a)

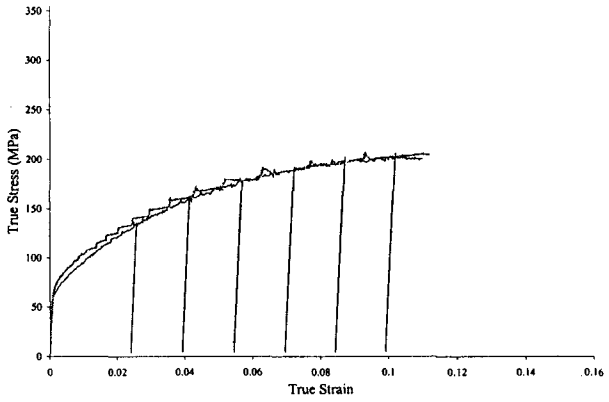

(b)

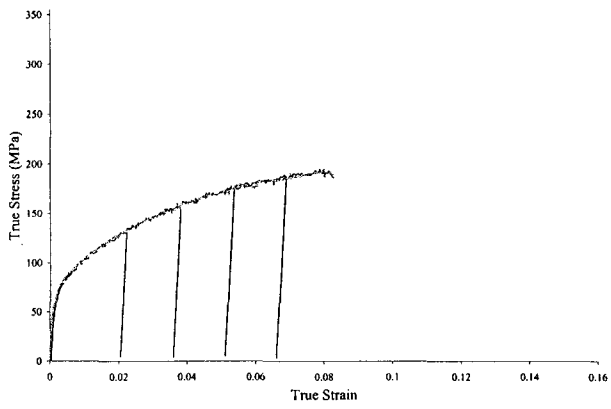

(c)

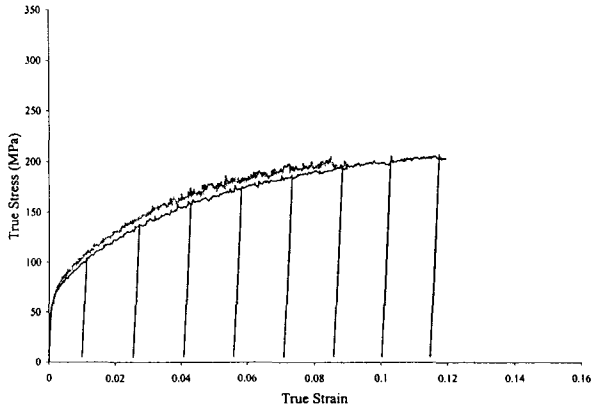

(d)

Figure 4.9 (a)-(d). Tensile load-unload curves (black) and the corresponding monotonic tensile loading curves (gray) for composites with (a) 1% alumina, (b) 4% alumina, (c) 8% alumina and (d) a bimodal 4% and 8% alumina.

The tensile load-unload curves were used to monitor the change in the composite elastic modulus. Measurement of the elastic modulus in particulate composites is often difficult and inaccurate through conventional mechanical tests [Clyne and Withers (1993)]. One reasonably accurate method (± 0.5-1.5 GPa) is to measure the slope of the tangent to the initial portion of the reloading curve from an the load-unload cyclic test.

A tangent line for each reloading sequence was created by extracting the first set of data points corresponding to a stress range of approximately 20-60 MPa and fitting them to a linear expression using Microsoft Excel. The slope of this line was taken as the value of the composite elastic modulus. When extracting the reloading data points, the first few data points of the initial reloading curves were removed to reduce the errors associated with machine backlash resulting from the cross-head loading direction change. With the backlash eliminated the reloading curves consistently appeared linear in the 20-60 MPa stress range. The measured values of elastic modulus are presented in Table 4.1. The

unloading – reloading loops possessed a small amount of hysteresis resulting from a limited amount of microplasticity. Therefore the measured values most likely slightly underestimate the measured values of stiffness (Clyne and Withers (1993)). A plot of the normalized elastic modulus (measured/modulus measured from first loop) versus tensile strain is presented in Figure 4.10. All composites, with the exception of the composite containing less that 1% Al_2O_3 experienced a measurable loss (greater than the measurement error) in stiffness with increased tensile loading.

Table 4.1 Measured values of elastic modulus at given values of true tensile strain at reloading for composites with ~1% Al_2O_3, 4% Al_2O_3, 8% Al_2O_3 and a bimodal 4%-8% Al_2O_3 volume fractions. The effective medium analysis predicted value of the initial composite elastic modulus is given in brackets.

~1% Alumina (71.1 GPa)		4% Alumina (73.6 GPa)		8% Alumina (80.0 GPa)		4-8% Alumina (76.8 GPa)	
True Strain	Measured Elastic Modulus (GPa)	True Strain	Measured Elastic Modulus (GPa)	True Strain	Measured Elastic Modulus (GPa)	True Strain	Measured Elastic Modulus (GPa)
0.0135	70.7	0.0237	72.9	0.0204	80.1	0.0125	74.1
0.029	71.1	0.039	69.3	0.0358	72.9	0.025	72.3
0.044	71.0	0.054	69.4	0.051	68.6	0.041	69.2
0.059	71.8	0.068	68.8	0.066	67.8	0.058	68.9
0.074	71.8	0.086	66.2			0.071	69.0

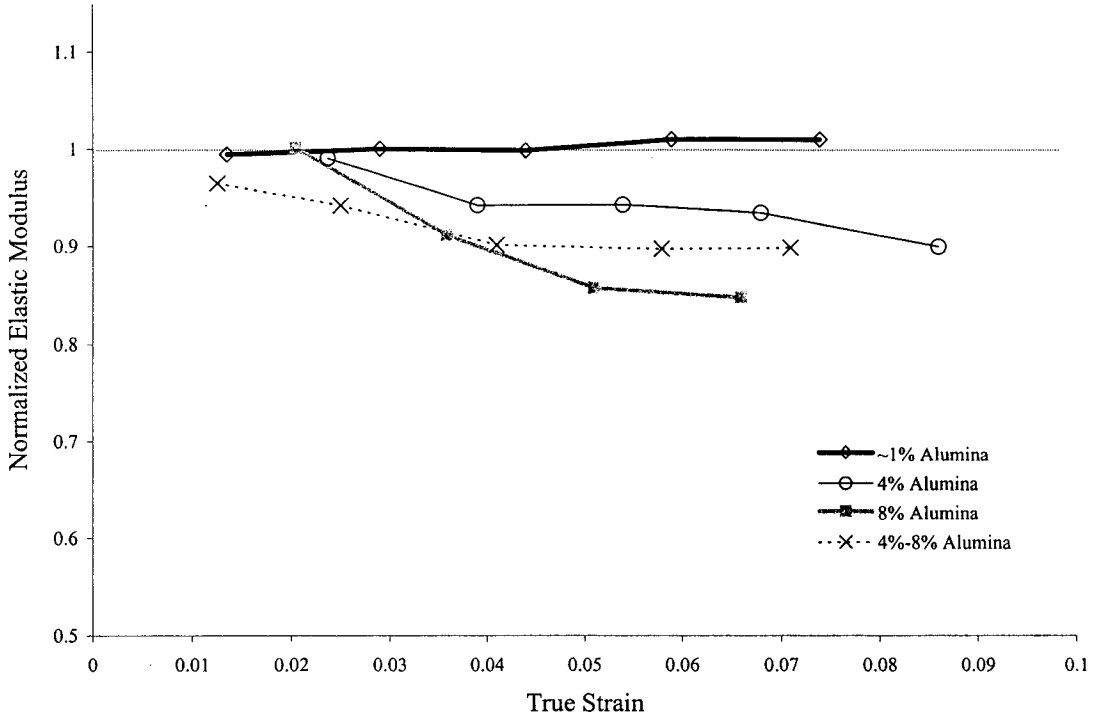

Figure 4.10 Plot of the normalized elastic modulus of each composite versus true tensile strain. The measured values of elastic modulus have been normalized with the modulus predicted by the effective medium analysis

4.5 Baushinger Tests

The Baushinger effect was studied on two composites with differing volume fraction. Two composites with an average volume fraction of 5% Al_2O_3 were examined along with three having a volume fraction of less than 1% Al_2O_3 so that the development of internal stresses at the two volume fractions could be probed. The loading sequence involved first straining each sample to a strain of ~1% in the tensile direction. Loading was then reversed so that straining occurred in compression until visible buckling of the samples was observed. Buckling typically occurred at compressive strains of approximately -0.5% (or equivalently cumulative strains of approximately 2.5%). As a result, data points at cumulative strains of 2% or greater were excluded to avoid the

inclusion of buckling effect in the data interpretation. Representative examples of the Baushinger loading loops acquired for each volume fraction are presented in Figure 4.11.

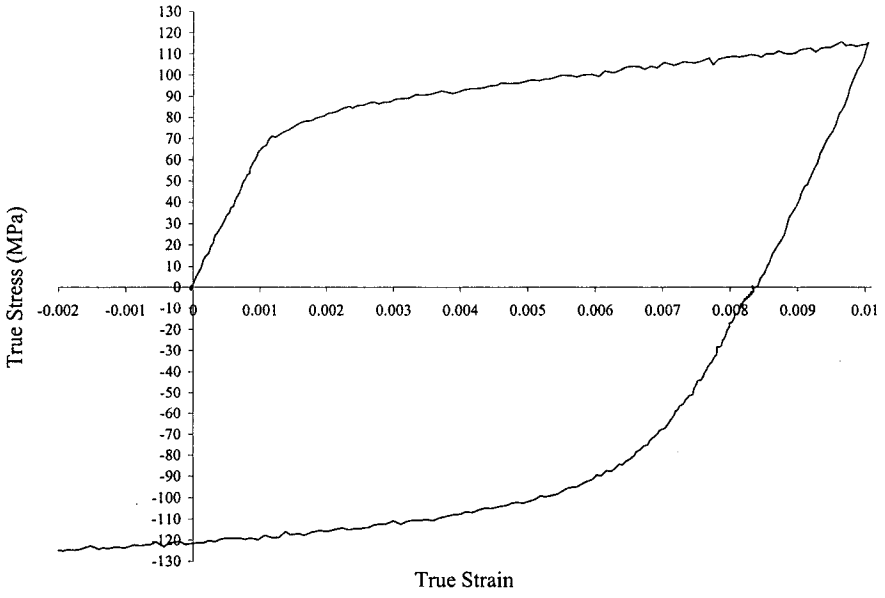

(a)

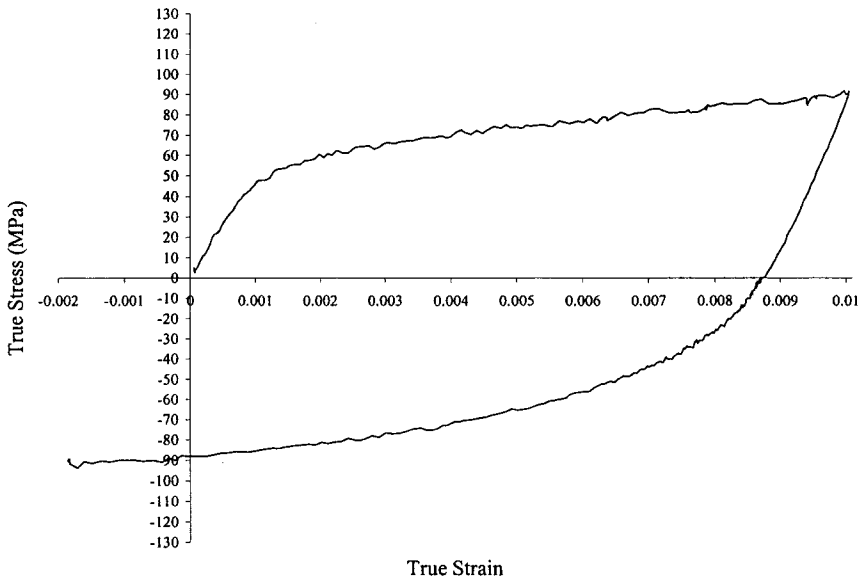

(b)

Figure 4.11. Examples of tensile followed by compressive loading Baushinger tests on samples with (a) ~1% Al_2O_3 and (b) 5% Al_2O_3.

Analysis of the Baushinger effect required reflection of the compressive flow curve onto the tensile axis and plotting the results as a function of cumulative strain. The plastic portion of the tensile loading curve was then fit to the Ramberg-Osgood power-law hardening equation (eq. 2.23)) so that the forward deformation curve could be reasonably estimated up to cumulative strains of 2%. Examples of the Ramberg-Osgood extrapolation to strains of 2% are plotted along with the absolute value of stress versus cumulative strain in Figure 4.12. Note that the yield stress in tension and compression measured at a 0.1% offset are virtually the same for both composites studied.

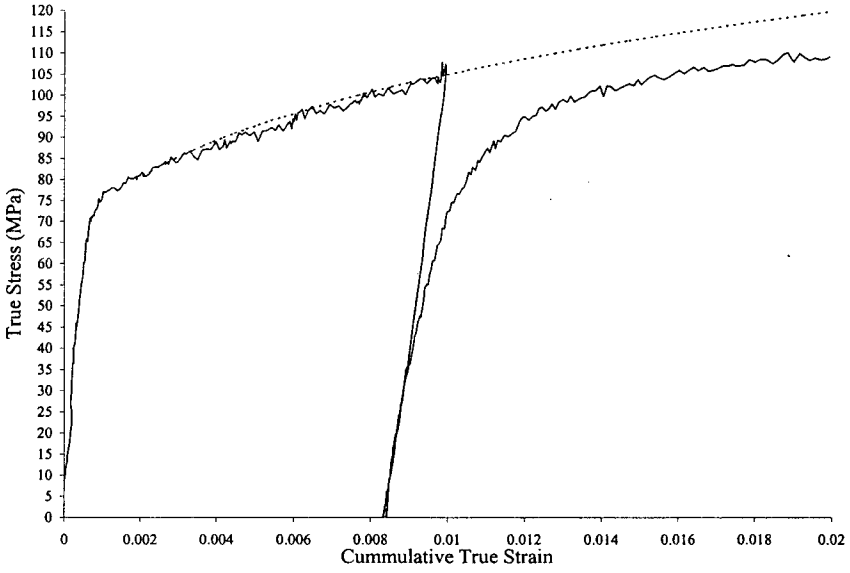

(a)

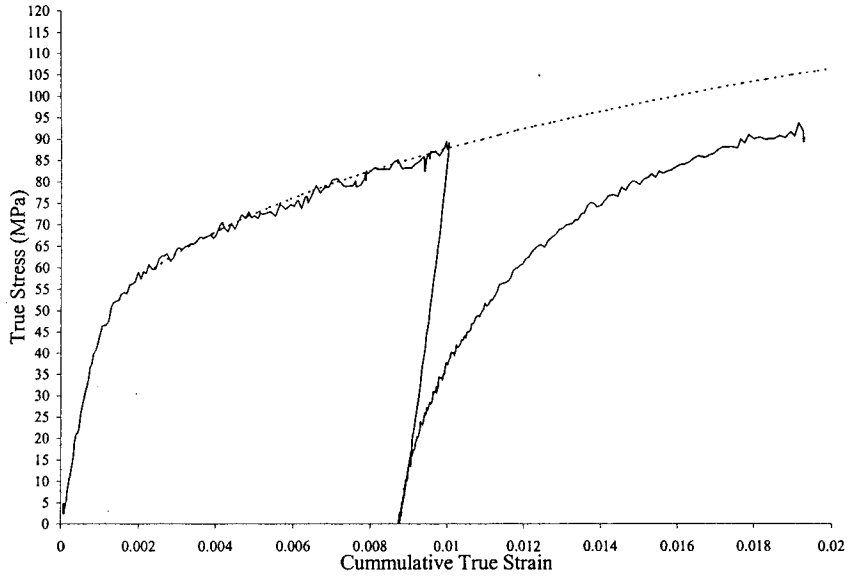

(b)

Figure 4.12 Plots of Ramberg-Osgood prediction of forward tensile deformation (dashed line) and the absolute value of stress versus cumulative strain for a tension first Baushinger test on composites with (a) 1% Al_2O_3 and (b) 5% Al_2O_3.

One of the more common approaches to investigating the Baushinger effect is to measure the value of the permanent softening associate with load reversal. This requires that the reverse loading curve be plotted until a tangent drawn along it would be parallel to one drawn along the forward loading curve. In this work, sample geometry constraints limited the maximum amount of reversed compressive deformation prior to buckling. This prevented the reversed compressive loading curves from ever becoming truly parallel at least for the composite samples. In order to enhance the comparison, the difference between the estimated forward deformation flow curve and magnitude of the compressive loading curve was evaluated at 0.1% reversed loading strain increments. Calculation results for the five composite samples studied composites studied (Three 1% and two 5% volume fraction Al_2O_3) are presented in Figure 4.13. The reverse true strain was calculated by simple subtraction of the value of cumulative strain where loading in the compressive

strain commenced from the given value of cumulative strain where the difference between the magnitude of the forward and reverse stress was evaluated.

Both volume fraction composites evaluated appeared to approach an asymptotic value of the difference between the forward and reverse loading curve. If parallel tangents could be drawn along the forward and reverse loading at the points corresponding to where the difference between the forward and reversed loading became asymptotic, the value of the asymptotic stress difference would be equivalent to the conventional definition of permanent softening. Conservative values of the asymptotic difference in the forward and reverse stress have therefore been taken as estimates of the permanent softening present in the two composites volume fractions studied. The estimated values of permanent softening were 4 MPa and 13 MPa for the ~1% Al_2O_3 and 5% Al_2O_3 volume fraction composites respectively, indicating that more internal stresses were developed in the composites of higher volume fraction.

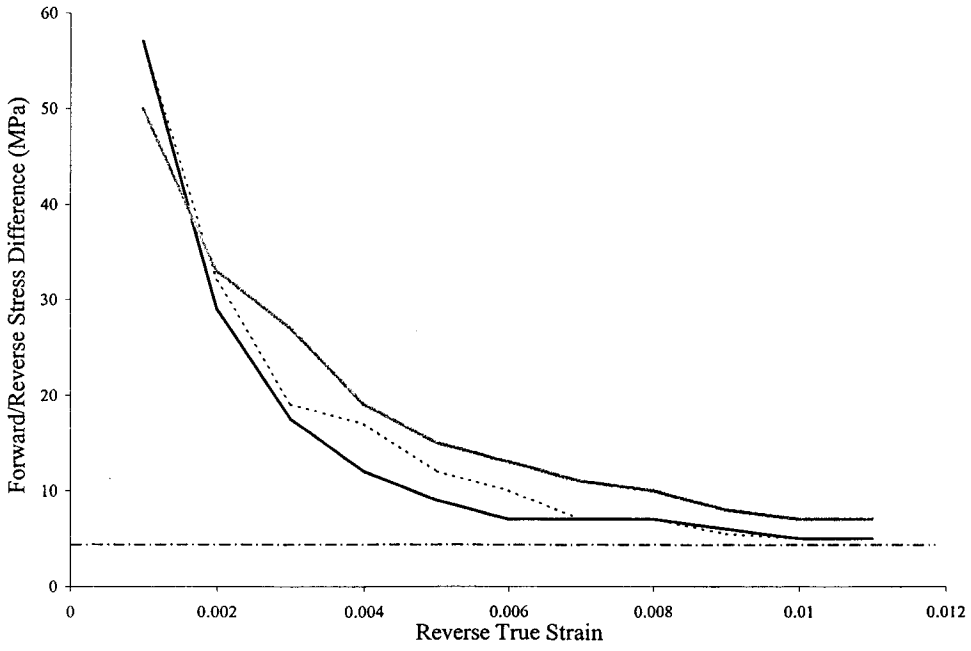

(a)

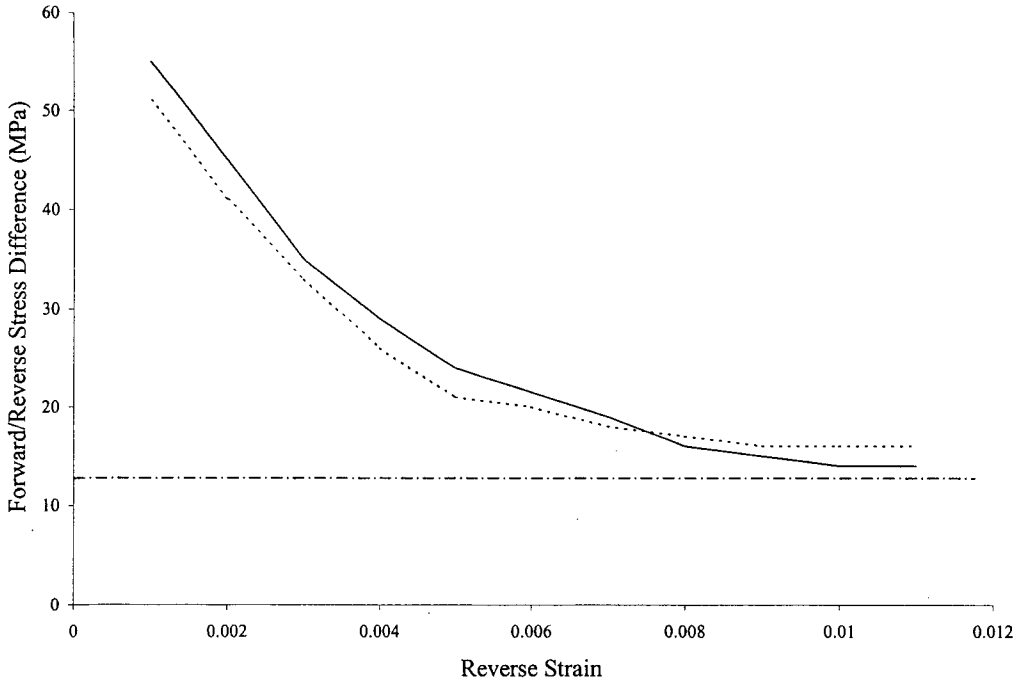

(b)

Figure 4.13 (a) & (b). Magnitude of the difference between the forward and reverse stress versus reversed loading strain for composites with (a) ~1% Al_2O_3 and (b) 5% Al_2O_3.

4.6 Instrumented Micro-hardness Estimates of the Matrix Flow Response

In section 3.5 the varying degree of Mg depletion from the AA6111 matrix was discussed. While transmission electron microscopy and micro-hardness measurements suggest that the matrix precipitation process, and therefore most likely the matrix flow response, differs from that of conventional AA6111 the two techniques do not allow for a quantitative measure of the resulting matrix flow response. Further, since all the matrixes, with varying degrees of Mg depletion, exist only in composites with differing Al_2O_3 volume fractions, direct measurement of the matrix flow response was not possible through standard mechanical tests. Reasonable estimates of the matrix flow response were clearly necessary, particularly for the modelling work that follows in Section 6.3.

One relatively new approach to estimating the flow properties of elasto-plastic materials utilizes the results from instrumented micro-hardness measurements [Doener and Nix (1986) and Dao *et al.* (2001)]. Recently Dao et al (2001) have developed an approach that requires only properties extracted directly from the load, P, versus displacement, h, indentation curves. Using their approach it is possible to gain a reasonable estimate of a material's elastic modulus[1], yield strength and work hardening exponent.

A schematic illustration of a typical load, P, versus displacement, h, of an elasto-plastic material to instrumented indentation is presented in Figure 4.18. The information essential to the calculation of a material's elastic modulus, work hardening exponent and yield strength are included on Figure 4.14. The value of loading slope, C, the initial unloading slope, $\left.\frac{dP_u}{dh}\right|_{hm}$, and $\frac{h_r}{h_m}$ are three independent quantities that can be directly obtained from a single P-h curve (Dao *et al.*(2001)). Seventy six large deformation finite element simulations on materials with differing elasto-plastic responses were used by Dao *et al.*(2001) to develop a series of five dimensionless equations (equations and solution order described in detail within Appendix III) that use these three independent quantities to uniquely determine a material's elastic modulus, yield strength and work hardening exponent. These values are then used to predict the material's flow curve through

$$\sigma = \begin{cases} E\varepsilon & \text{for } \sigma_y \geq \sigma \\ \sigma_y\left(1+\frac{E}{\sigma_y}\varepsilon_p\right)^n & \text{for } \sigma \geq \sigma_y \end{cases} \qquad (4.1)$$

[1] Accurate elastic modulus measurements require that the stiffness of the loading apparatus be well characterized so that the machine stiffness effects can be subtracted from the measured values.

Using this approach Dao *et al.* (2001) report reasonable agreement between the predicted and experimental elasto-plastic response of Al 6061-T6511 and Al 7075-T651 using an indentation load of 100 grams force. In their results the prediction of the elastic modulus had the least variability while the estimated work hardening exponent and yield stress had a higher degree of scatter.

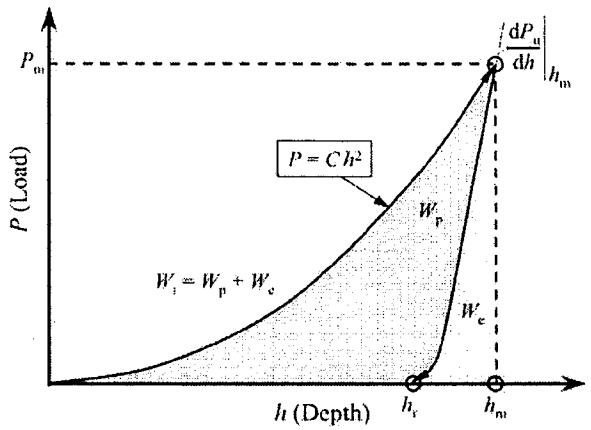

Figure 4.14. The features of the P versus h curve necessary for extraction of the elasto-plastic response. (after Dao *et al.* (2001))

4.6.1 Results

The approach outlined by Dao *et al.* (2001) was used to predict the elasto-plastic response of the matrix in four composite materials. Details of the composite Mg and Al_2O_3 fractions in each of these composites are provided in section 3.6. Essentially the composites B13 and B14 possess less than ~1% volume fraction Al_2O_3 and a Mg weight percent of approximately 1/3 (roughly 0.2 wt%) that of commercial AA611 (~0.6-0.68 wt%). The other two composites studied possessed similar levels of Mg (roughly 1/10 that of AA6111) and two different Al_2O_3 volume fractions (B6 = 8% and B15 = 4% volume fraction Al_2O_3).

Instrumented sharp-indentation was performed on a Shimadzu Ultra-micro Hardness testing machine using a high quality (sub micron tolerances) Vickers indentor. Both loading and unloading occurred at a rate of 2.5 grams/sec with a 2 second dwell time at 25 gram maximum force. All samples were polished following the steps outlined in Appendix I. Flatness of the indented piece was ensured by first maintaning surface flatness during metallographic preparation. The samples were then mounted on a stage using a device that ensured a high degree of horizontal alignment. The focal length of the viewing apparatus on the indenting machine was short and therefore any unevenness of the surface prior to indentation could be easily checked by ensuring the polished plane remained well focused while moving the sample 500 μm in any direction.

Prior to presenting the experimental results some general observations should be noted. Two factors appeared to be equally important in ensuring reasonably repeatable estimates of the elasto-plastic properties. The first was the shape of the indent left in the material. If the sides of the indented impression were not symmetrical the calculated results fell well outside the range of the repeatable results generated from indents of symmetrical shape. The irregularly shaped indents were more common in the higher volume fraction composites than those with low volume fraction. This was most likely cause by indentation occurring too close to Al_2O_3 particles situated just under the surface indented, thereby constraining the plastic flow of the matrix. Examples of these irregularly shaped indents are presented in Figure 4.15 and a load-unload curve is presented in Figure 4.16.

A second factor that appeared to effect the results was the magnitude of the indentation load. A series of experiments were performed at 10 grams force. Results

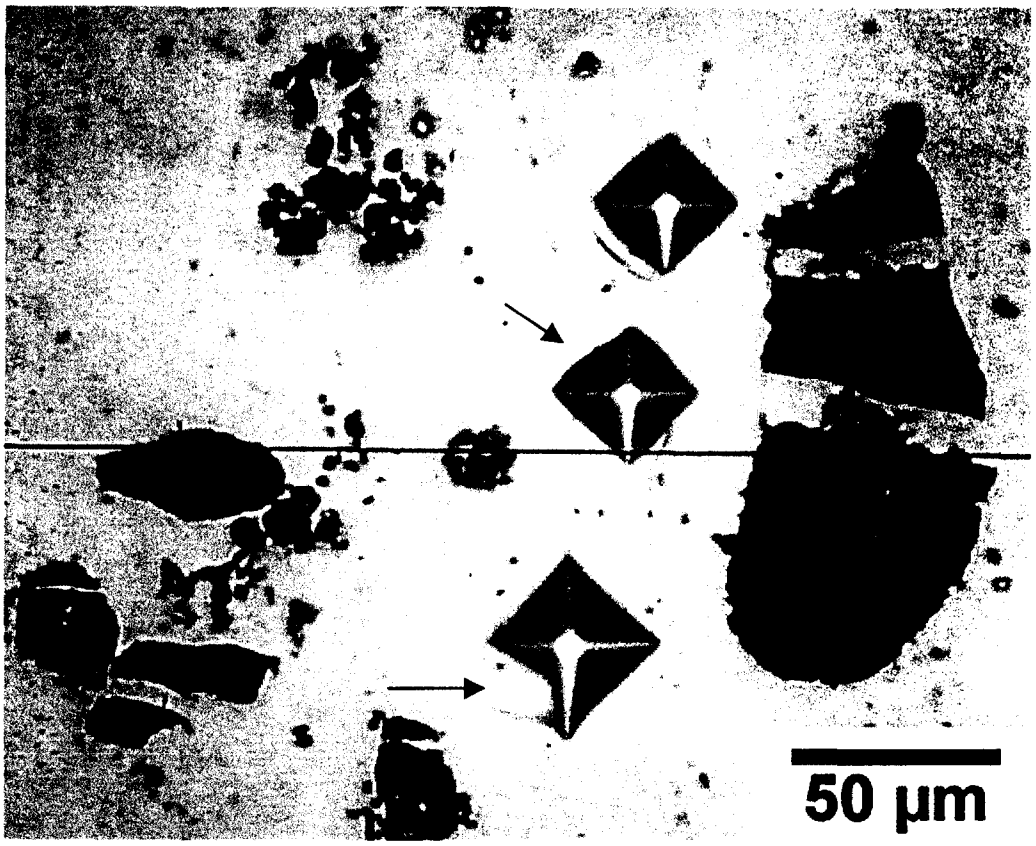

Figure 4.15. Examples of irregularly shaped indents in the matrix of the 8% volume fraction composite studied. Ideally shaped indents would be perfectly symmetrical. Calculations of the elasto-plastic loading curves from instrumented indentation data from indents that left irregular shapes such as these always predicted elasto-plastic properties outside of the range of rather repeatable predictions obtained from data associated with indents of regular shape.

generated from the load versus displacement curves at this loading had a high degree of scatter and generated what appeared to be unreasonable values of yield stress (~18 MPa) and work hardening exponent (~0.46). In many cases the load versus displacement curves themselves possessed some very irregular features (unusual jumps in load or displacement) for both the loading and unloading portions of the curve. Increasing the load to 25grams force as will be shown in what follows, produced much more reasonable and fairly repeatable measures of the elastic modulus, yield strength and work hardening exponent.

The predicted values of the elastic modulus, the yield strength and the work hardening exponent for the four composites studied are presented in Table 4.2. Four indents for each of the low volume fraction composites were used to calculate the mean and standard deviation values. Five indents were used in the calculation for both the 4% and 8% composite materials.

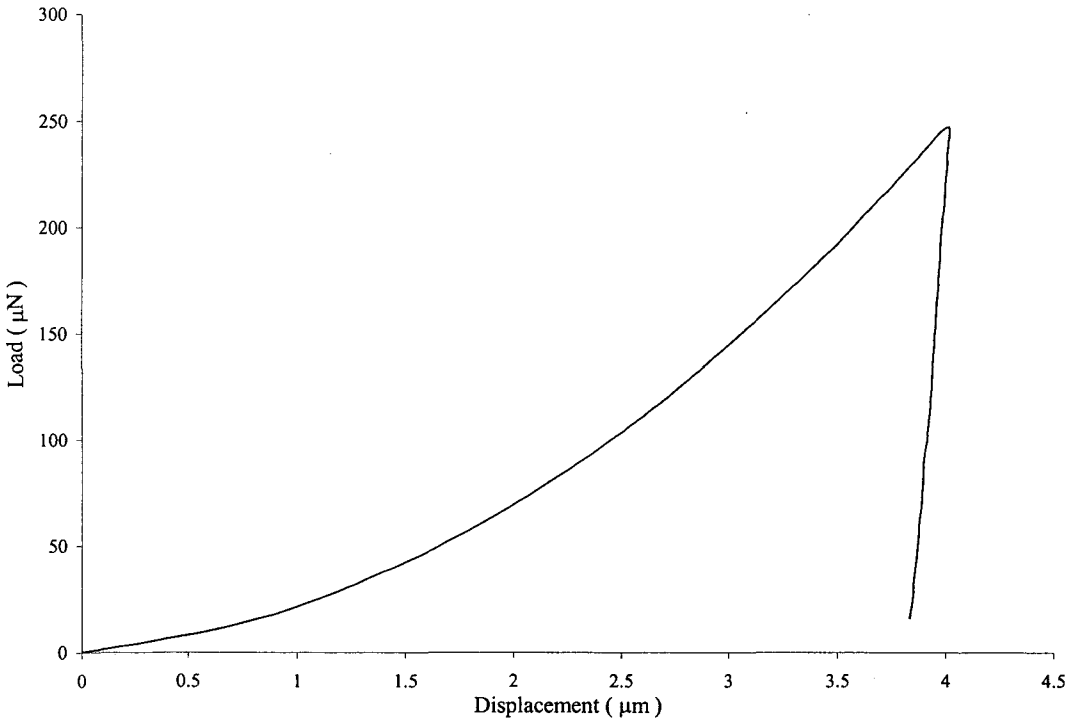

Figure 4.16 A typical load versus depth instrumented indentation curve for the matrix in the composite sample possessing and average 4% volume fraction of Al_2O_3.

The accuracy of the instrumented sharp indentation predictions was compared with the experimentally determined tensile flow curve of sample B14 and B13 using the average values calculated from the indentation of sample B14. This was the best comparison that could be made with the experimentally determined tensile flow curves since this composite material was the closest to a monolithic matrix of all the material studied (the composite possessed a volume fraction of less than 0.8% Al_2O_3). The measured tensile composite

response should therefore be expected to be only very slightly higher than that of that resulting from a test conducted on the monolithic matrix. The results of the predicted flow curve and the experimental comparison are presented in Figure 4.17. Comparison between the predicted elasto-plastic and the experimentally determined elasto-plastic response appeared to be reasonably good, with the values calculated for B14 slightly overestimating the experimentally determined response and that for B13 slightly underestimating it. The agreement between the predicted and experimental flow curve for samples B13 and B14 suggested that the values estimated for samples B15 and B6 are likely satisfactorily close. This is particularly true when the maximum difference between the predicted and experimental behavior for B13 and B14 is well within variability in the flow response observed in the experimental data for the 4% and 8% composites as illustrated in Figure 4.18 and 4.19.

Table 4.2 Elasto-plastic properties of matrix estimated from instrumented sharp indentation.

Composite	Elastic Modulus*[2]	Yield Stress	n
B13~ 1%Al_2O_3	55.4 ± 1.3 GPa	95.4 ± 5.0 MPa	0.247 ± 0.005
B14~ 1%Al_2O_3	52.8 ± 1.7 GPa	101.8 ± 1.9 MPa	0.257 ± 0.007
B15~ 4%Al_2O_3	51.1 ± 3.7 GPa	48.8 ± 2.1 MPa	0.307 ± 0.008
B6~ 8%Al_2O_3	49.0 ± 3.7 GPa	51.1 ± 3.0 MPa	0.301 ± 0.009

[2] This is the effective elastic modulus that includes the effects of both the indented material and the machine stiffness in the calculated value.

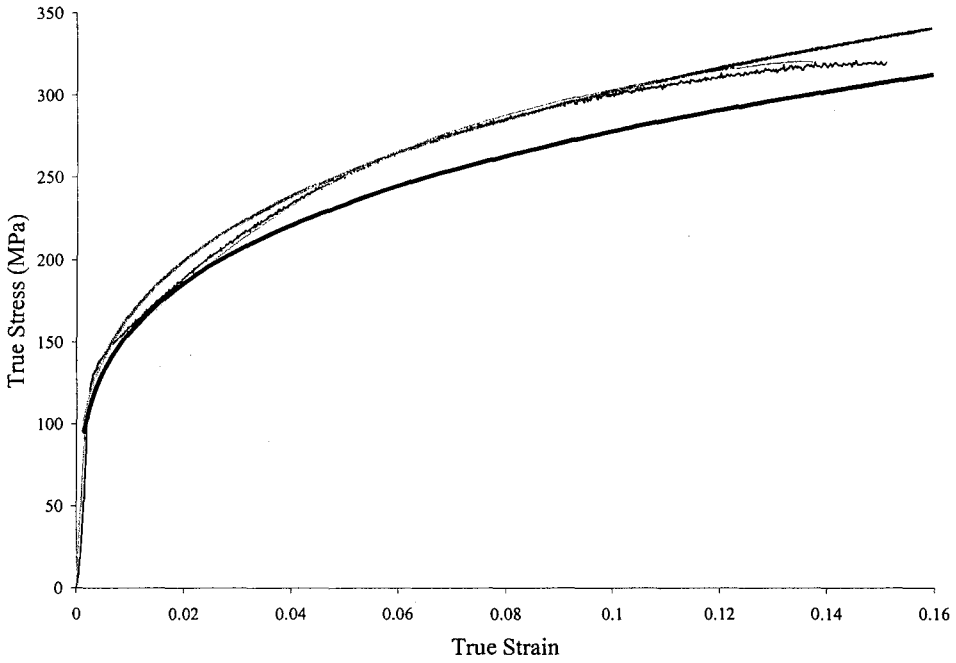

Figure 4.17 Comparison of the experimental and instrumented sharp indentation predictions matrix flow response for composites possessing ~1% Al_2O_3. Gray curves B14 (thick predicted-thin experimental). Black lines B13 (thick predicted- thin experimental).

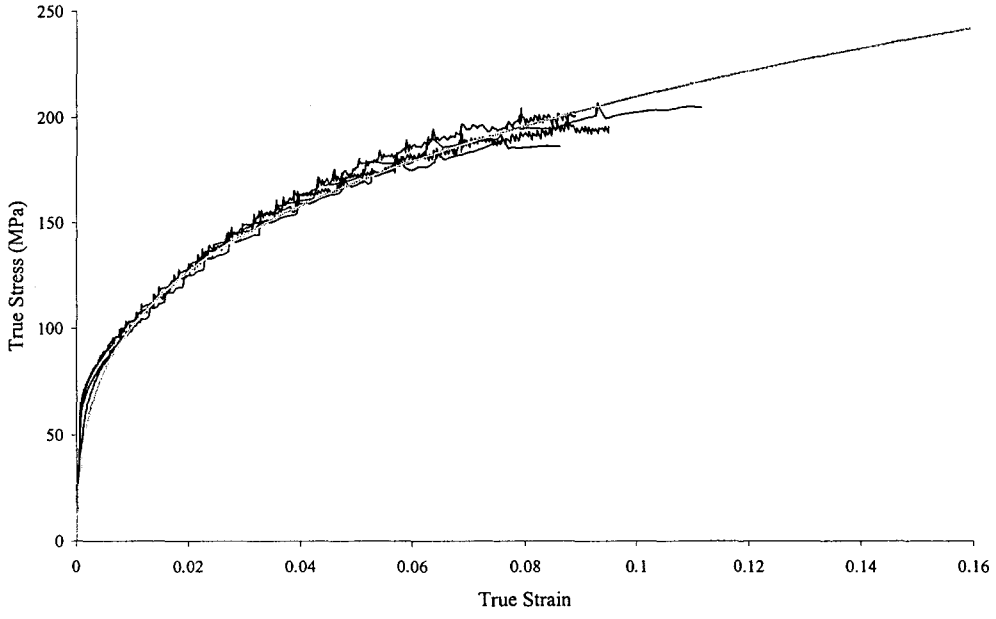

Figure 4.18. Predicted matrix response for B15 (grey line). Plotted along with four different experimental composite flow curves measured on B15 samples(dark lines).

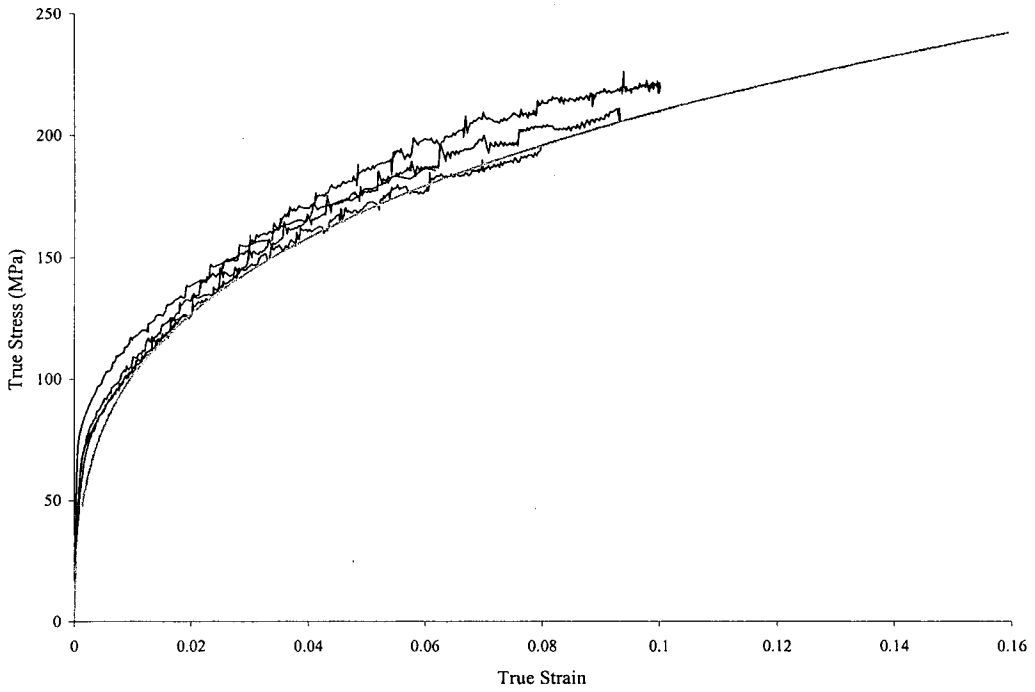

Figure 4.19. Predicted matrix response for B6 (grey line). Plotted along with three different experimental composite flow curves measured on B6 samples(dark lines).

4.7 Summary of General Observations

1. Composites possessing the lowest volume fraction of Al_2O_3 provided the strongest response in both tensile and compressive loading. This likely results from the higher Mg wt % in the matrix that provides a higher flow stress than those observed in matrix of the composites with higher volume fractions Al_2O_3 and lower Mg wt%.
2. The 4%, 8% and bimodal 4%-8% Al_2O_3 volume fraction composites had strength levels that scaled with the volume fraction. The samples with ~8% Al_2O_3 had a stronger response than the 4%-8% Al_2O_3 volume fraction composites. These bimodal composites in turn were stronger than those with 4% Al_2O_3.
3. The flow response in compression was higher than the tensile flow response.

4. A measurable loss in stiffness with increased tensile strain was observed in the cyclic loading-unloading tests for composites with volume fractions of 4% or higher. No measurable loss in stiffness was observed in the composite possessing less than 1% volume fraction Al_2O_3. The loss in stiffness was greatest for the 8% volume fraction composite and lowest for the 4% volume fraction composite suggesting that the mechanical response of the higher volume fraction composite is more sensitive to the damage process.
5. The reverse-loading tests revealed that a Baushinger effect, measured in terms of an estimated value of permanent softening, exists. The magnitude of the permanent softening was greatest for the sample with 5% volume fraction Al_2O_3. The ~1% Al_2O_3 samples has a smaller amount of permanent softening. The flow stress in tension and compression measured at 0.1% offset were virtually the same.
6. The instrumented microhardness measurements provided reasonable predictions of the matrix flow response in the composites possessing ~1% Al_2O_3. The elasto-plastic properties predicted by the instrumented sharp indentation measurements were generally repeatable. The range in the predicted effecitive stiffness had the greatest variability of the parameters extracted. In all cases the predicted effective stiffness was a minimum of 15 GPa less than the assumed value of 70 GPa for aluminum. The estimate of the work hardening exponent and the yield stress appeared to be reasonably consistent with the values observed on the experimental flow curves. The predictions for the higher volume fraction composites are likely well within the experimentally observed scatter in the tensile flow curves and can therefore be considered as estimates reasonable for use in modelling predictions of the composite flow response.

CHAPTER 5

X-RAY TOMOGRAPHY

5.1. Introduction

This chapter describes x-ray tomography experiments performed on Beamline ID19 at the European Synchrotron Radiation Facility (ESRF) in Grenoble, France. A significant amount of data has been generated through the experimental work at the ESRF and, as will be shown, X-ray tomography has proven to be very powerful tool for both qualitative and quantitative characterization of damage in heterogeneous material system used in this work.

High resolution X-ray tomography was described in Section 2.8. A detailed description of the experimental technique specific to beamline ID 19 at the ESRF is located in Appendix III. Image resolution levels achieved in the following experiments, 1.9μm, require a high energy and highly collaminated x-ray beam. The ESRF provides the high energy, hard x-rays through the synchrotron radiation source and beamline ID19 at the ESRF ensures high beam collamination through its large (150 m) source-to-sample distance.

X-ray tomography, particularly when performed with the high-resolution levels possible at the ESRF, is a particularly attractive alternative to other conventional damage measurement techniques. The clear advantage of these experiments is that they allow for three-dimensional viewing of the damage process as it occurs with tensile deformation. Unlike density change or acoustic emission measurements, measuring damage using tomography coupled with in-situ loading allows for not only quantification of the amount of damage but also allows for equally

important observations of the damage process, how the heterogeneity of the particle distribution affects damage, the effect of second phase geometry and size and finally comparison of the differences in damage based on the location within the sample (surface or in the bulk).

Observations using conventional metallography, whether it be a process of serial sectioning a sample to reconstruct a three dimensional volume or surface observation of the damage process using in-situ loading within a scanning electron microscope, provides some of the damage observations described in the previous paragraph. However, the observations and the accuracy of the measurements using these techniques are quite limited when compared to x-ray tomography.

Serial sectioning has a number of disadvantages, including the obvious difficulty in carefully sectioning and imaging multiple planes through a sample. The process of polishing sample sections itself is prone to smearing the damage, particularly when the matrix material is soft. This coupled with the elastic unloading that occurs on the unloaded samples tends to either close or conceal cracks or pores existing within the sample.

Surface observation with in-situ tensile loading in a scanning electron microscope is limited to surface observation. It has been experimentally confirmed, by directly comparing the damage measurements obtained by the surface observation approach with those from x-ray tomography [Babout et al (2001), Maire (2001)], that damage existing on the surface can be different than that of the bulk. The differences can be significant, particularly when the experimental observations are being used to develop models of the damage process.

The advantages of observing damage, occurring at length scales greater than 2 μm, using x-ray tomography are clear. Experiments conducted for this research allowed for quantification of the effects of particle size, shape and distribution on the damage occurring throughout the composite. Additionally the experiments reduced or eliminated the damage measurement errors associated with either surface observation or serial sectioning. These experiments have provided an uncommon opportunity to provide a comprehensive description of the damage process that would have otherwise difficult to obtain through conventional means.

The results presented in the sections that follow in this chapter required a significant amount of data processing. This data processing, in particular the reconstruction of the radiographs to form the tomographic volumes on which all work is based on and the segmentation of images for automated data processing, was made possible through a collaborative effort with E.Maire at INSA de Lyon, France. All the calculations whether manual or through semi-automatic techniques, using calculating software, were made using two freeware programs, AI3D created by Luc Salvo and Charles Josserond (GPM2, Grenoble, France) for image processing and Image J a three dimensional volume viewer.

5.2. Tomography Results

This section describes both the data analysis methods and results. Initially, the true strain and stress calculations are described. Tomography results that follow are grouped in two sections. The first section presents both the qualitative and quantitative data generated through image processing software. The second section

details results generated through manual measurements using Image J, a three dimensional commercial viewing and measuring software.

5.2.1. Determination of True Stress and Strain

The calculation of true stress and true strain required coupling data from the tensile loading controller and the tomography images. The cross-sectional area of each sample was physically measured at five locations along the gauge length of the sample prior to testing. The deviation from the mean of the measurements on the undeformed sample was less than 2 μm. To ensure the accuracy of the cross-sectional area measurements made using the three-dimensional images generated

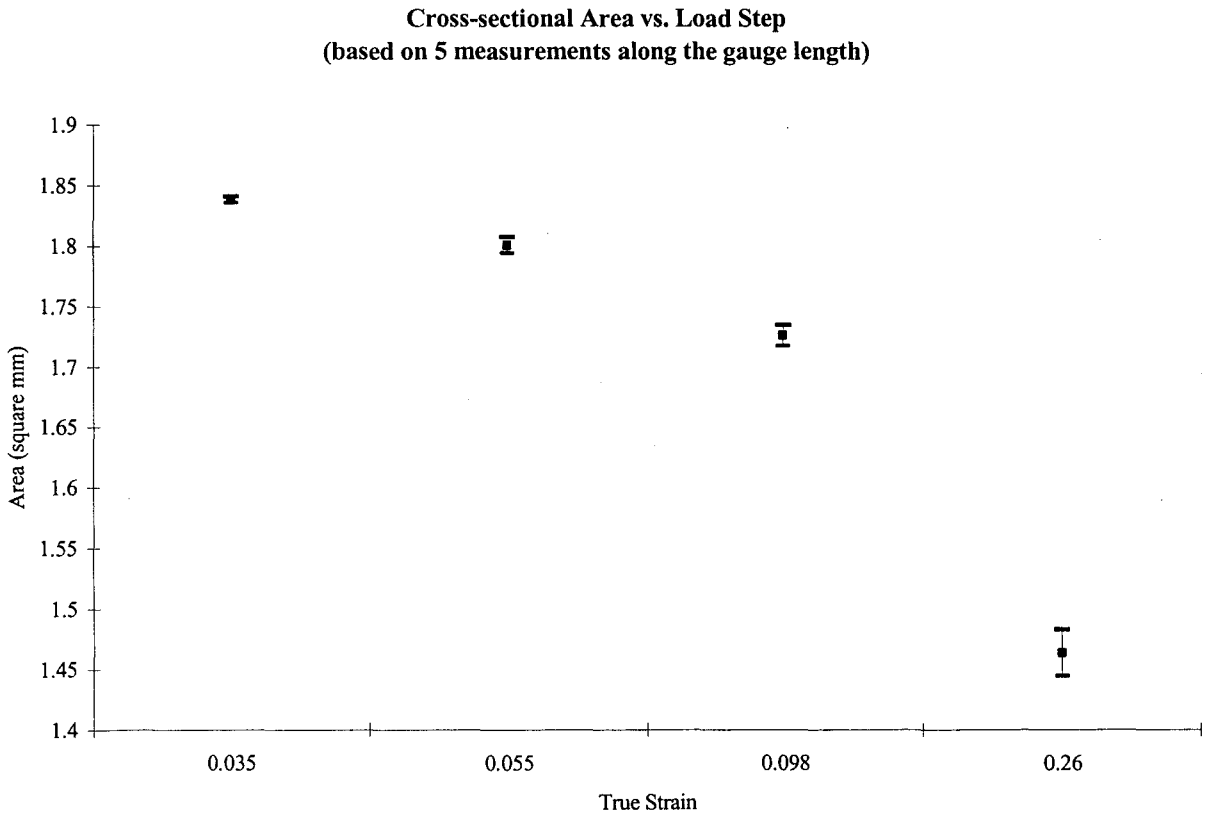

Figure 5.1. The cross-sectional area variation versus true tensile strain in 4% volume fraction Al_2O_3 tomography sample.

through x-ray tomography were the same as those made by physically measuring the dimensions, the results of each measurement technique were compared. The cross-sectional areas were found to be virtually identical at the undeformed state. At all the subsequent loading increments, the cross-sectional area was directly measured from the tomography images. As in the measurements made prior to deforming the sample, five measurements were made at each load increment. The calculated average and standard deviation of these measurements are provided in Figure 5.1. Initially the standard deviation of the cross-sectional area measurement was quite small. As loading progressed however, the standard deviation increased, reaching a maximum at the largest plastic deformation where sample necking became significant. However the uncertainty never exceeded ±0.3 mm.

The true strain at each load increment was calculated using the average measured cross-sectional area for the given loading increment and the average measured initial cross-sectional area. True stress was calculated by taking the maximum load recorded at a given loading increment and dividing that load by the corresponding cross-sectional area measured on the tomography images. The value of the particle stress at a given loading increment was estimated using results from the FEM calculations of Brockenbrough and Zok (1995). They estimate that the particle stress for a uniform distribution of reinforcing particles is approximately 2 to 2.18 times the composite stress. In their work they found that this particle stress was only slightly sensitive to volume fraction and fairly sensitive to the work hardening exponent, with high values of n corresponding to a higher multiplication factor for the particle stress. In this work the particle stress was estimated as being 2.18 times the

composite stress because the matrix material has a high hardening exponent (n~0.3) and the particle distribution was not uniform. The heterogeneity in the distribution would most likely increase the stress partitioning to the particles in the particle rich regions. This in turn would increase the stress acting in the particles at a given increment of strain suggesting that $\sigma_p = 2.18\sigma_c$ is a reasonable estimate of the particle stress.

5.2.2. Data Generated Through Image Processing

Both qualitative and quantitative data was produced using data processing software. Thresholding techniques[1], in this case a region-growing algorithm used in the image processing software VgStudiomax, allowed for segmenting the particles from the matrix in the uniform 4% volume fraction of Al_2O_3 sample. The experiments for the 8% Al_2O_3 sample were conducted with too large a sample-detector distance. As a result, the reconstructed volumes had too high a level of phase contrast for segmentation. The 0-8% sample was not deformed to a sufficiently high strain to cause significant damage in the composite and the 0-4% sample had too few particles to provide a statistically significant description of damage. These results will therefore describe the data generated on the 4% volume fraction Al_2O_3 sample.

[1] A complete description of the image processing required to generate both the qualitative and quantitative data is provided in Appendix III.

5.2.2.1. Qualitative Results

VgStudiomax was used on the binary images to assign different colours to those particles that had fractured than those that had not. Using the software it was possible to make the matrix transparent allowing for viewing of the particles in 3 dimensional space. This generated qualitative descriptions of the damage process where both the effects of distribution and the damage rate could be investigated.

Images presented in Figures 5.2 and 5.3 show the sample perpendicular to the loading axis and looking down the tensile axis respectively. The heterogeneity in the particle distribution is quite clear, particularly in Figure 5.3. By looking down in tensile axis, the clustering of particles is clearly visible. The particle clusters are highly elongated in the direction of extrusion (parallel to the tensile axis) forming stringers of particle-rich regions.

Qualitatively, these series of images indicate that clustering does influence the damage process. For the most part, particles located within the particle rich regions tend to fracture at lower strains than isolated particles. By following the damage in Figures 5.2 (a)-(e) and 5.3 (a)-(e) it is apparent that more particles within a particle rich region fracture than the isolated particles at any given increment of strain. Further, these series of images suggest that damage occurs at low strains and evolves quite rapidly with strain.

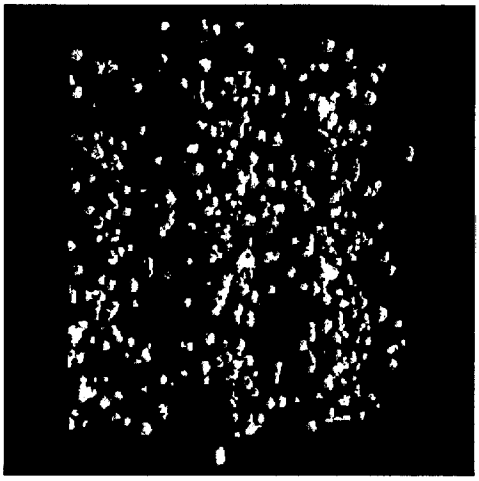

Figure 5.2(a) ε=0

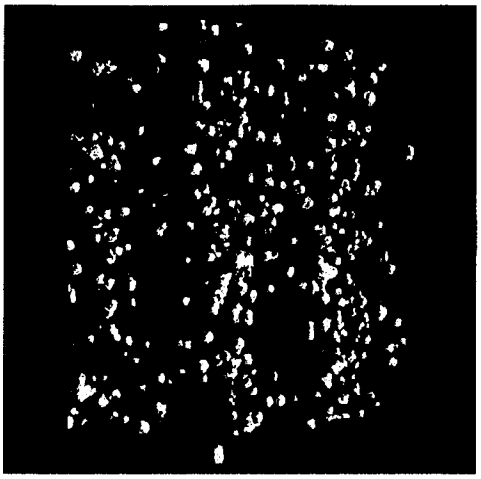

Figure 5.2(b) ε=0.035

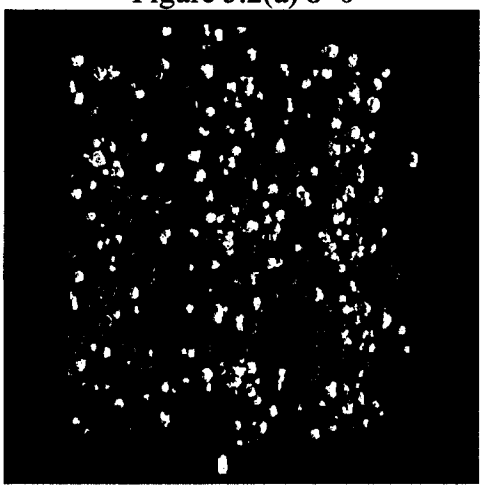

Figure 5.2(c) ε=0.055

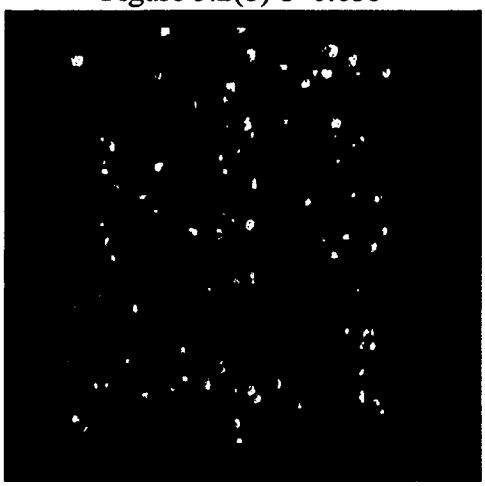

Figure 5.2(d) ε=0.098

Figure 5.2(e) ε=0.26

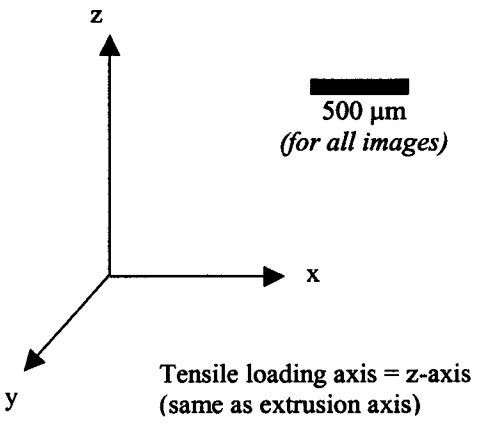

Figure 5.2. Three dimensional illustration of damage evolution with tensile strain. Undamage particles are shaded yellow, those fractured are shaded red. Looking at the tensile axis.

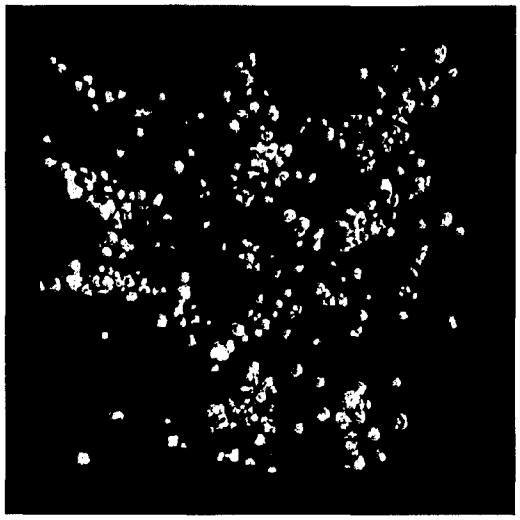

Figure 5.3(a) ε=0

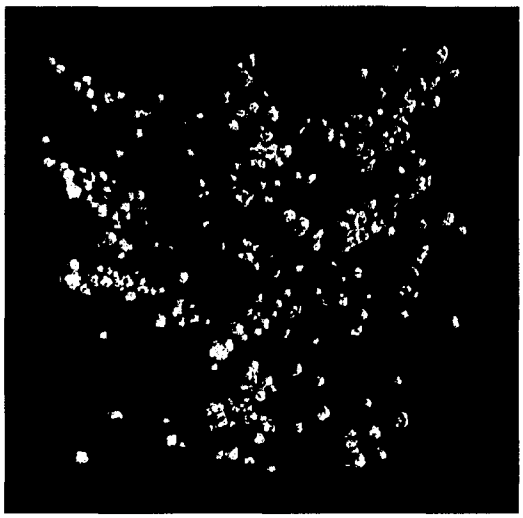

Figure 5.3(b) ε=0.035

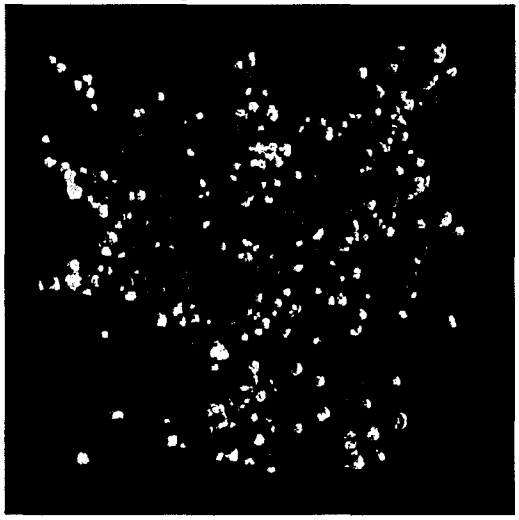

Figure 5.3(c) ε=0.055

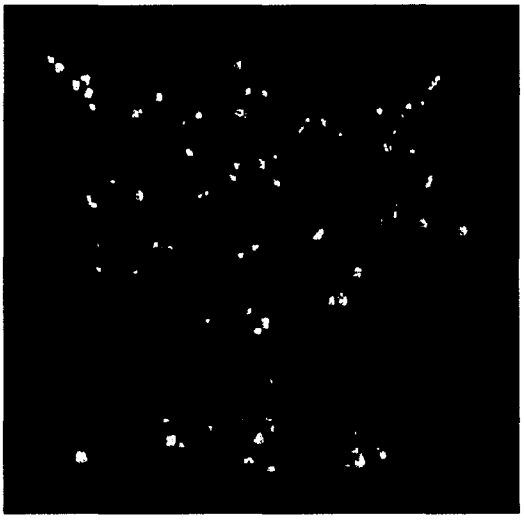

Figure 5.3(d) ε=0.098

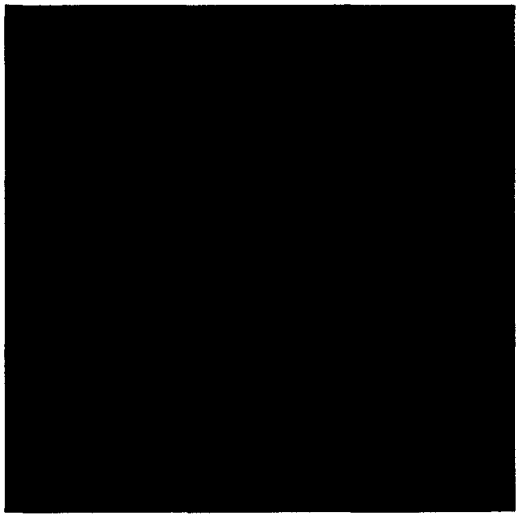

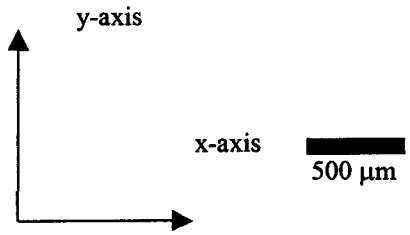

Figure 5.3(e) ε=0.26

Figure 5.3. Same as Figure 5.2 except looking down tensile axis.

5.2.2.2 AI3D Calculations

AI3D was employed to perform calculations on the binary files created for each of the load increments. The AI3D image processing software performs the calculations on the voxels of the three dimensional volume rather than the pixel-based calculations used in conventional two-dimensional image processing software. Calculations are essentially the same as those on two-dimensional images in that they are based on the differences in contrast between the voxels present in the images.

The dependence of fracture on particle size was investigated using the AI3D calculation results. Results are illustrated in Figure 5.4 through plotting the average fractured particle diameter versus the estimated particle stress. An open circle represents the average diameter of the entire particle distribution prior to loading. The remaining data points on the graph represent the average and standard deviations of the fractured particles only; undamaged particles within the particle distribution are not included in the calculation. At the lowest stress increment, the average fractured particle diameter value is highest. As the loading increases the average values approach that of the measured values of the entire particle distribution (the data point for the unloaded material). Since the values of fractured particle diameter are the highest at the lowest stress level it is clear that size dependence does exist. Initially the largest particles fracture, resulting in the highest average in fractured particle diameter. The largest standard deviation value is most likely attributed to the flaw size sensitivity of brittle fracture, where those particles that are weakest due to their flaws fracture first. As loading increases, an increasing number of the smaller particles in the particle distribution fracture until at the final loading point, where all

particles are fractured, the average and standard deviation of the fractured particle diameter equals that of the undamaged particle distribution prior to loading.

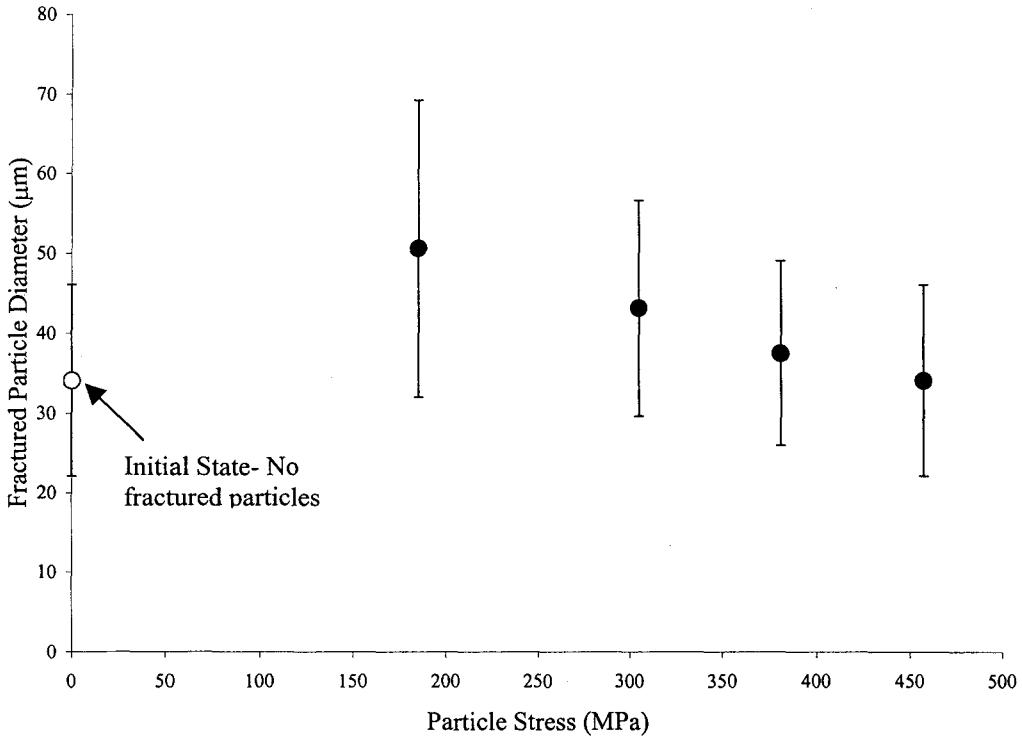

Figure 5.4 Average and standard deviation of the diameter of fractured particles versus particle stress. Note that at the first loading increment the larger particles fracture first resulting in the highest average cracked particle diameter. As loading continues an increasing number of smaller particles fracture lowering the average cracked particle diameter until it approaches the average diameter of the particles in the distribution.

The effect of particle shape on fracture was also investigated by examining the spherodicity. The spherodicity is roughly the inverse of the aspect ratio and was used in place of the aspect ratio because AI3D does not provide a measure of the largest dimensions in the principle directions required to calculate the aspect ratio. The program provides a calculation of the surface area and volume so that the spherodicity can be calculated as an alternative to the aspect ratio. It should be emphasized that the spherodicity of the particles was determined on the sample prior

to deformation. The change in spherodicity resulting from the particles elongating along the tensile axis is therefore not included in the calculation. This is therefore limited to providing a measure of the sensitivity of particle fracture relative to the initial particle shape. As in Figure 5.4, the data point for the entire particle distribution prior to loading is included on the spherodicity vs particle stress plot in Figure 5.5. The average value of the spherodicity of the particle distribution prior to damage is approximately 0.75, less than the value of 1 that would represent a perfectly spherical particle. Particle fracture is slightly sensitive to the particle shape with the least spherical particles fracturing earlier than those with higher sphericity. This is in agreement with a number of experimental observations that indicate that less spherical particles, in particular angular shaped particles, fracture more easily than spherical particles [Clyne and Withers (1993), Lorca (2000)].

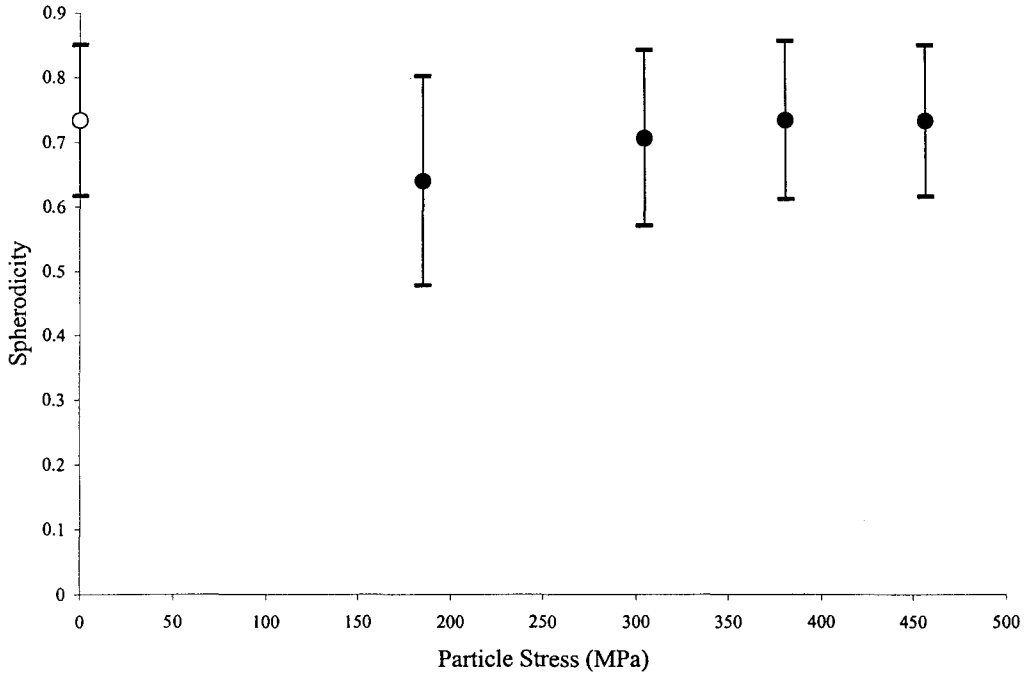

Figure 5.5. Average spherodicity of fractured particles versus particle stress. Perfectly spherical particles would have and spherodicity of 1. Note that the least spherical particles fracture first and that the spherodicity of fractured particles approaches that of the entire particle distribution (the data point at zero stress) as loading increases.

Perhaps one of the most useful quantitative measurements from AI3D is the measurement of the fraction of cracked particles at a given value of load. These results combined with the estimate of the particle stress at a given loading increment provide the data required to estimate the Wiebull properties of the reinforcing particles. The fraction of cracked particles versus the particle stress is plotted with a Wiebull fit to the data in Figure 5.6.

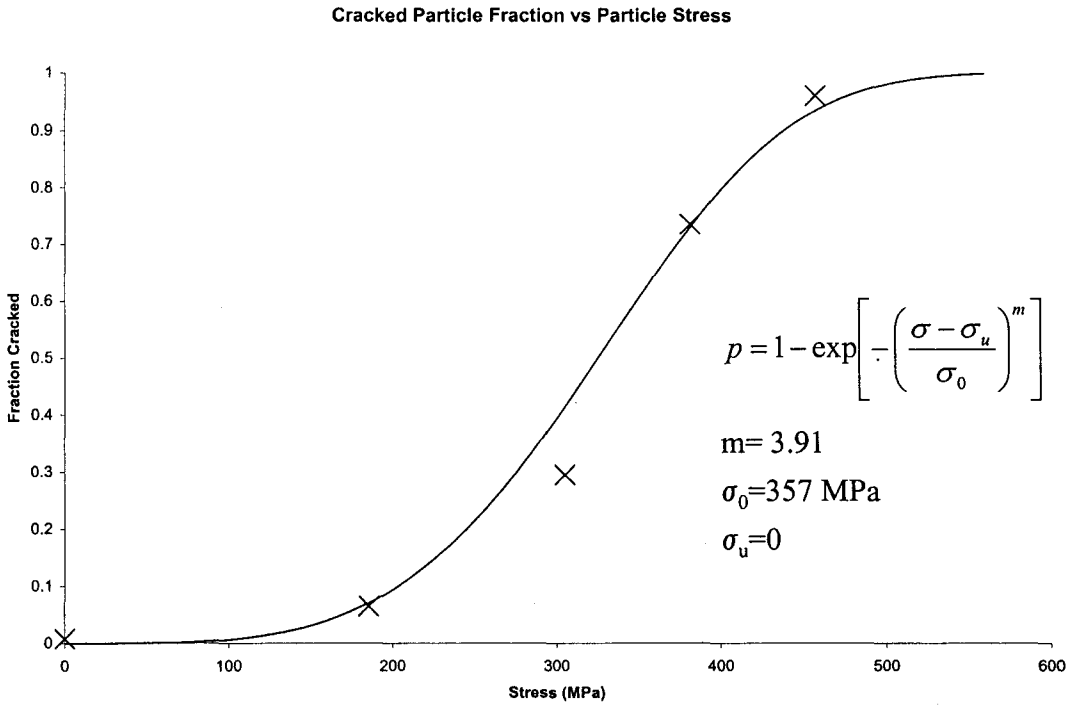

Figure 5.6. Fraction of cracked particles versus particle stress. Data fit to the Wiebull function for determination of the Wiebull modulus(m), the characteristic stress (σ_O) and the threshold stress (σ_u).

Estimating the Wiebull properties is of particular use because it provides a good description of the strength properties of the ceramic Al_2O_3 particles. Experimentally it is difficult to measure the particle strength through conventional testing methods due to both the small size (40-50 μm) and shape of the particles. X-

ray tomography also has the added benefit of measurements made on material in the loaded state and throughout the bulk. Tomography results generated with in-situ tensile loading reduce crack closure effects resulting from elastic unloading of the sample. Effects from plugging the cracks via mechanical polishing and surface effects are eliminated since the particles are examined in the bulk volume of the sample. These results would therefore be expected to provide more accurate estimates of the particle fracture properties than conventional observations methods. Results from these measurements provide a Wiebull modulus value of 3.91, a relatively moderate value of the variability in the fracture strength. A higher Wiebull modulus suggests higher certainty in the strength, and a value of 3.91 is in good experimental agreement of the values $3<m<6$ reported in literature for Al_2O_3 (Mochida *et al.* (1991)) and SiC reinforced (Brechet *et al.* (1991), Llorca (1995)) Al-matrix composites. This low value of Wiebull modulus is often attributed partially due the polycrystalline nature of the reinforcement and the manufacturing methods (attrition or spray drying) that present a wide distribution in internal defect size. The characteristic strength, a value near the mean fracture strength of the particles, was 357 MPa, a relatively low value of fracture strength. The best fit to the experimental measurements was achieved by setting the threshold strength equal to zero.

5.3.3 The Role of Particle Distribution on Damage

A number of features of the damage process were investigated using a 3 dimensional volume viewer on the raw reconstructed volumes. This approach allowed for following a specific set of the same particles through all the loading

increments. By doing this effects of neighboring particles on damage could be quantified.

One of the first interesting observations was the damage mechanism itself. While damage through particle cracking as observed in this composite system is well documented for a number of metal matrix composite systems [Llorca (2001)], the particles studied here were unusual in that they underwent multiple fracture as shown in Figure 5.7 (a)-(c). This suggests that the particles still effectively reinforce the matrix to the extent that a sufficient level of stress partitioning can take place on the cracked particles so that they are reloaded up to a new fracture stress. This is contrary to a number of fracture models that neglect the possibility of particles reloading up to a fracture stress, to cause multiple fractures in the particles, after the initial cracking takes place [Derby et al (1999), Brockenbrough and Zok(1994)]. While Derby et al. describes the loss of composite stiffness through particle shattering, it is assumed that particle shattering occurs instantaneously, not progressively as in the damage process in this composite system.

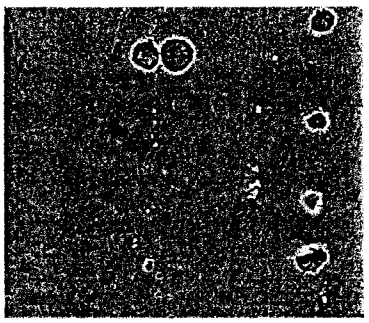

Figure 5.7 (a)

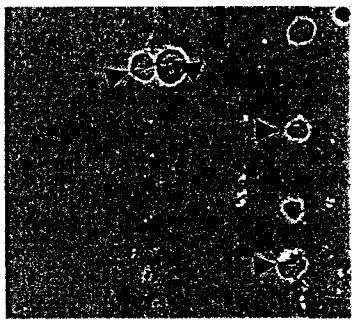

Figure 5.7 (b)

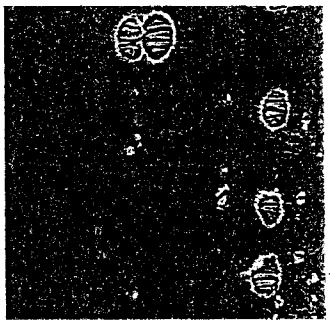

Figure 5.7 (c)

Figure 5.7 (a-c) Two-dimensional slices of the three dimensional volume generated by x-ray tomography. The slice was extracted near the center of the three dimensional volume. (a) The slice of the material prior to deformation, (b) The same slice at ε=0.098 and c) taken at the final strain of ε=0.26. Arrows in (b) point to the cracks in the particles. Multi-stage cracking is clearly visible in (c).

The effect of particle heterogeneity was studied using a multi-stage process. Initially, a set of 37 particles were selected and identified within the composite volume on the unloaded .raw tomography volume. Each of the selected particles were then classified based on the number of neighboring particles surrounding them. Isolated particles were defined as those having no particles spaced less than one particle diameter away from them in three dimensions. This distance was determined by finite element method [Guilemere *et al* (200) and Watt *et al.*(1997)] to be the distance at which stress fields from neighboring particles begin to significantly influence each other. The non-isolated particles were classified as having 1 or more neighboring particles spaced less than or equal to one particle diameter away in any direction, assumed to represent a "region of interest". These particles were then further subdivided as having one, two, three or four or more neighboring particles within this region.

Once the initial sets of particles were identified, these same particles were followed through all of the subsequent loading increments. Those that had decohered rather than fracture, were removed from the data set. This reduced the total number of sampled particles by 3, so the total number of particles monitored and measured through all the load increments was 34. At each of the loading increments the maximum length and width of the particle were measured. Additionally the number of cracks in each of the particles and the corresponding crack opening displacement of each crack in all the 34 particles was measured at each load increment. All measurements were made by directly counting the number of pixels across the dimension of interest. Counting the pixels was accurate with negligible error (it was

possible to increase the magnification sufficient so that the individual pixels were distinctly visible). Measurement errors reported in the following data are limited to the image resolution, ie. 1.9 μm. The maximum dimensional measurement error is therefore 1.9 μm. in all the data that follows.

A total of 22 non-isolated and 12 isolated particles were followed at each load increment. By entering the measurement data in a database it was possible to compare the differences in damage between the isolated and non-isolated particles. Perhaps the most obvious measure of damage is a comparison of particle cracking versus the composite tensile strain. In this composite system, it was possible to take this one step further by plotting the average number of cracks in the reinforcing particles versus composite tensile strain and plotting the results for both the isolated and non-isolated particles as shown in Figure 5.8. Initially the mean number of cracks for the isolated and non-isolated particles is not significantly different. However, as tensile loading proceeds, it is clear that the mean values do differ, suggesting that the non-isolated particles damage more quickly than the isolated particles.

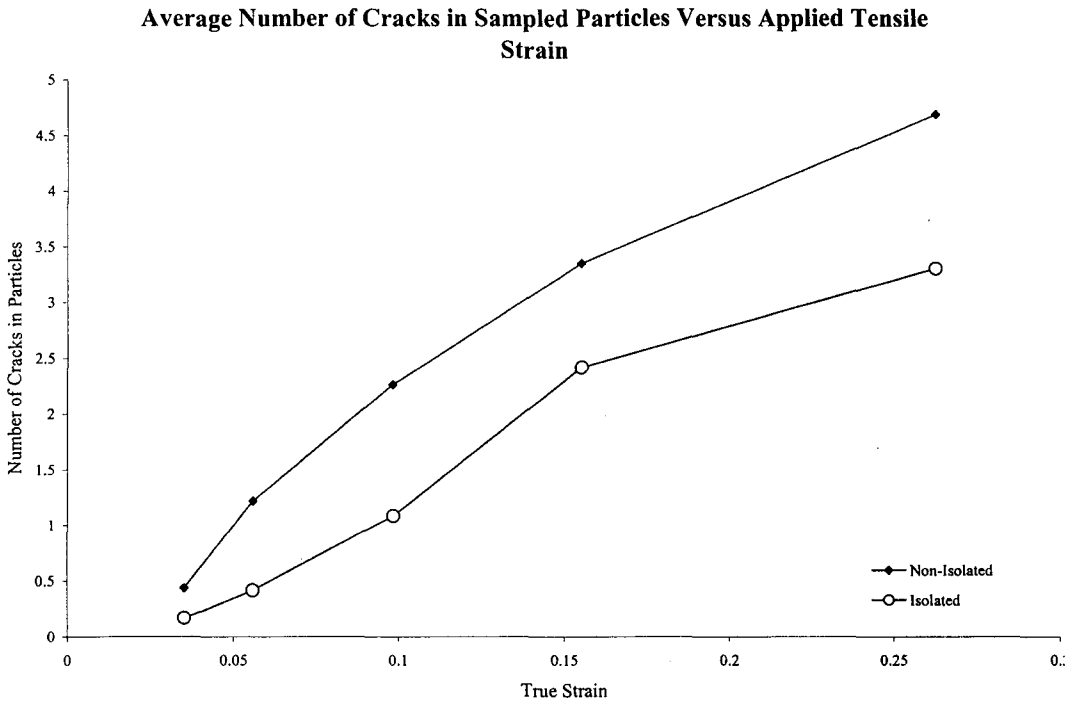

Figure 5.8. Comparison of the average number of cracks in both isolated and non-isolated particles.

A true test of the significance of heterogeneity on damage is to test the difference statistically. One such test is the T-test, a statistical test that measures the significance of the difference between two data sets based on both the mean and standard deviation values of each of the particle sets. The T-test for two data sets with unequal numbers of data entries is defined as

$$T = \frac{(\bar{X}_1 - \bar{X}_2) - D_o}{\sqrt{\frac{S_1^2}{n_1} + \frac{S_2^2}{n_2}}} \tag{5.1}$$

where X_1 and X_2 are the mean of the isolated particle and non-isolated particle data set respectively. S_1 and S_2 are the standard deviations of each data set and n_1 and n_2 are the number of particles in each set, in this case 12 and 22 respectively. D_0 is the value of the testing hypothesis, where the hypothesis is H_0: $\mu_1-\mu_0=0=D_0$ is used in this work. In this form, the hypothesis states that no difference exists in the mean values of each data set. This hypothesis is rejected, ie. the differences are statistically significant, if the calculated T is greater than T_α, where α is the significance level. The T tests described in this chapter use a 5% significance level, or a 95% confidence interval, at each load increment to determine if, statistically, isolated particles damaged less readily than particles with neighbors. The results of the statistical analysis (where T-data is the calculated value and T-0.05 is the 5% significance T-test value) for the significance of the difference for the number of cracks in the isolated and non-isolated data sets are presented in Table 5.1.

Table 5.1. Comparison of the statistical significance of the difference in the number of cracks in isolated and non-isolated particles at each tensile strain increment

Average Number of Cracks

Strain	*T-Data*	*T-0.05*	*Difference Significant?*
0.044022	1.28422	2.92	No
0.063027	2.93841	2.4	Yes
0.106295	3.57662	1.943	Yes
0.154764	2.57592	1.98	Yes
0.279314	2.01274	1.77	Yes

Results of the analysis indicate that the differences between the mean number of cracks in the non-isolated particles and the isolated particles are statistically different at all but the first increment of strain. This statistical evaluation confirms

that the increase in damage rate in the non-isolated particles, as measured by the number of cracks in the particles at a given strain increment, present if Figure 5.8 is statistically significant. The non-isolated particles have less damage at a given increment of strain than the non-isolated particles.

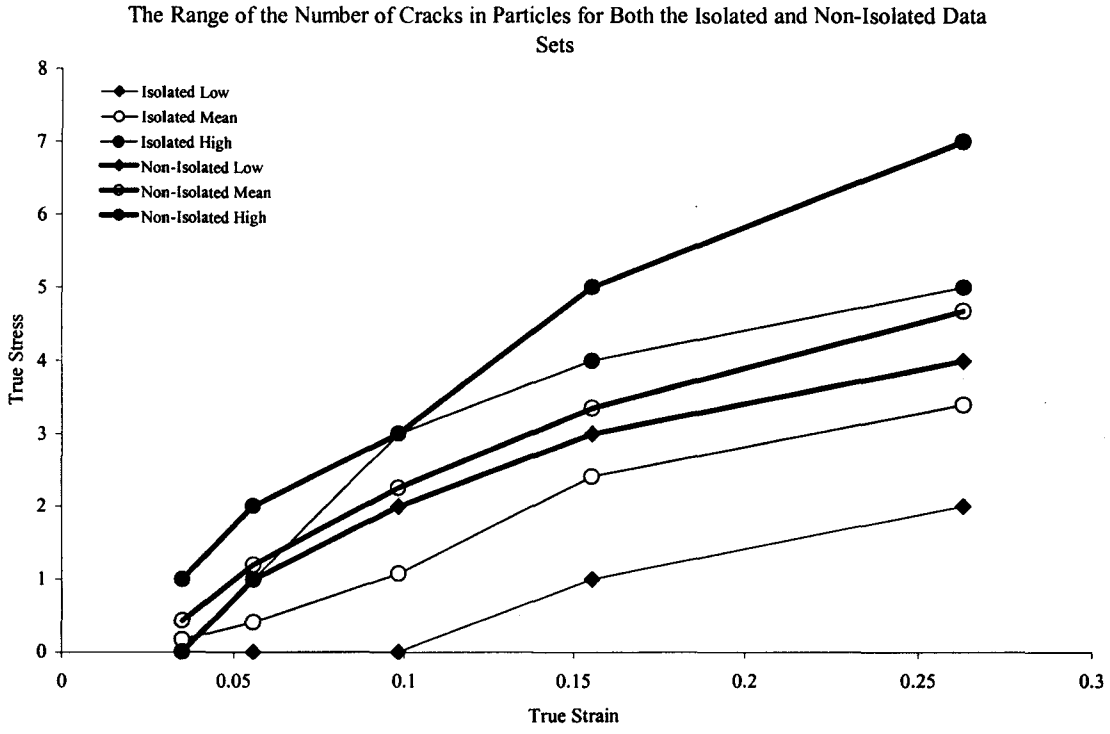

Figure 5.9. Comparison of the extreme values of the number of cracks in particles for the isolated and non-isolated data sets.

Data points for particles with the maximum and minimum number of cracks in both the isolated and non-isolated data sets at each strain increment are presented in Figure 5.9. These results suggest that while the curve that represents the particle with the maximum number of cracks in the isolated data set overlaps the mean curve for the isolated particles, a clear difference in the minimum curves for each data set exists. Perhaps most significantly, plotting the curves for the minimum data points in

each set suggests that the fracture in the isolated particles can be delayed for a significant amount of tensile loading over their non-isolated counterparts.

As previously mentioned, the non-isolated particles were further subdivided into four separate classes. The number of cracks versus true tensile strain was compared with particles having only one neighbor, those with two, those with three and finally those with four or more neighbors. Each of these subdivided classes only consisted of 5 particles and therefore while the results provides some insight into the effect of the degree of clustering; the accuracy is limited by the sample size. Based on comparison with the mean of the entire non-isolated distribution, particles with a higher number of neighboring particles do not seem to contain more cracks than those with fewer neighbors as shown in Figure 5.10. The effect of higher order clustering

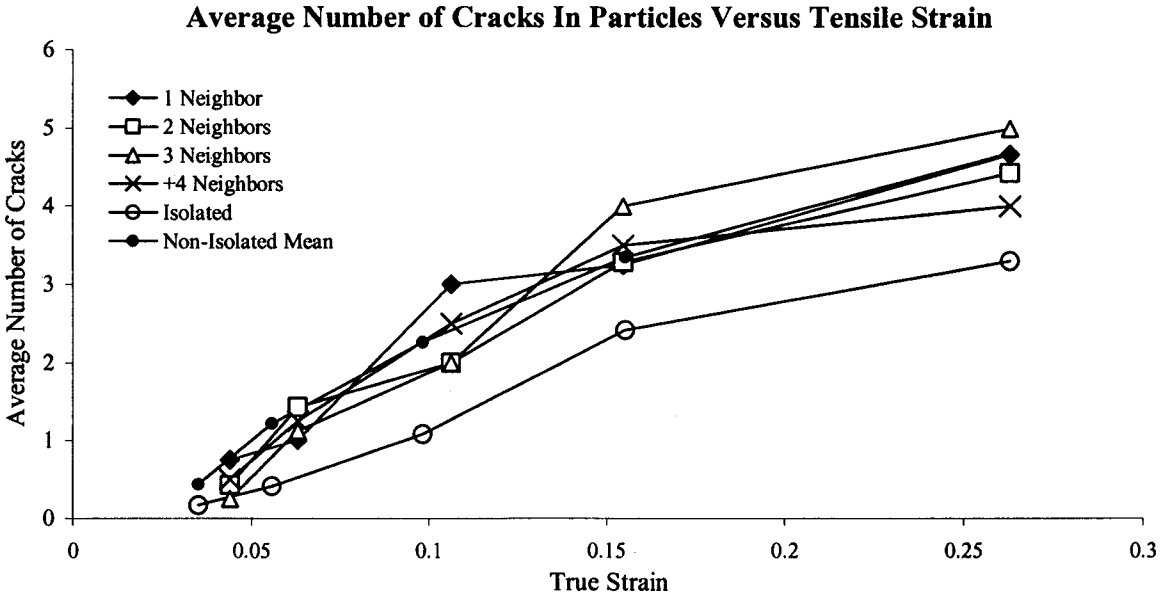

Figure 5.10. Comparison of the average number of cracks in particles versus tensile strain for particles with 1 neighbor, 2 neighbors, 3 neighbors and 4 or more neighbors. Mean values for the number of cracks in particles for the isolated particles and the entire non-isolated data set are include for comparison.

does not appear to have any effect on the damage when measured based on the average number of cracks in a given particle set at each increment of tensile loading as illustrated in Figure 5.10.

As expected the only measured change in particle dimensions with tensile strain occurred along the length of the particles (the length was parallel to the tensile axis). Since the particles deform elastically only, the length change occurred through particle cracking. Once particles initially cracked, the additional length change occurred through further separation of the cracked portions as the crack opening displacement of the original cracks increased, or, by further cracking of the particles. Figure 11 (a)-(f) illustrates the combined effect of length change resulting from the opening of the original crack and by multiple cracking. Almost all the particles sampled in this study elongated with the combination of these two mechanisms. By studying a given particle at the final deformation state, it was quite easy to see which crack formed first. As seems intuitively correct, the earliest formed cracks in a particle always had the largest value of crack opening displacement (the distance between two cracked portions of uncracked material) at the final deformation stage. The cracks that formed later in the deformation were typically finer than those that formed in the earlier deformation stages of the composite.

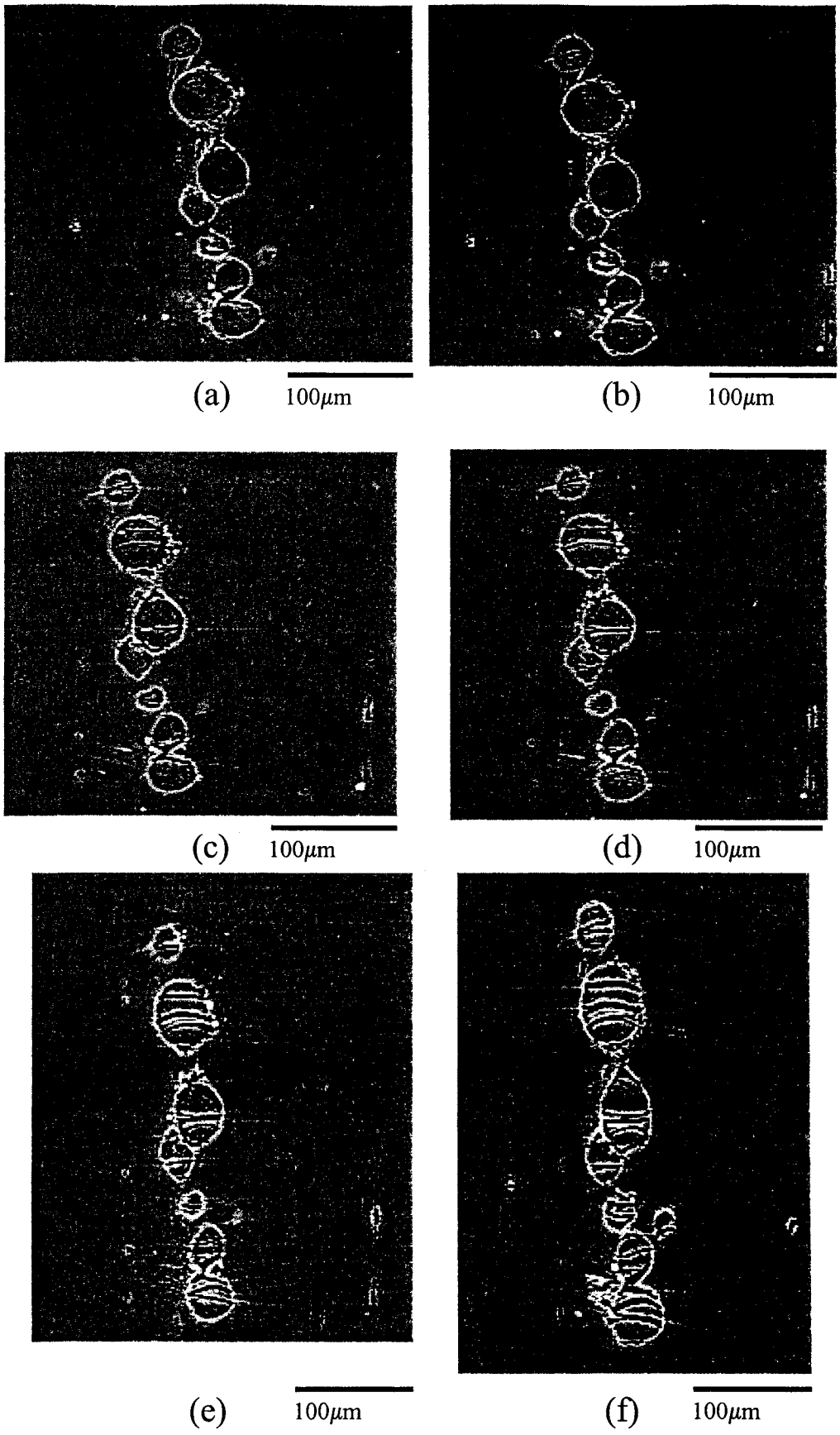

Figure 5.11(a)-(f). Illustration of the evolution of damage with tensile loading. Damage occurs through the multiple cracking of the particles. As a result the particles elongate in the direction of tensile loading. (a) $\varepsilon = 0$, (b) $\varepsilon = 0.044$, (c) $\varepsilon = 0.063$, (d) $\varepsilon = 0.106$, (e) $\varepsilon = 0.154$ and (f) $\varepsilon = 0.279$.

The average change in particle length versus true tensile composite strain for the isolated and non-isolated particle data sets is presented in Figure 5.12. Results from this plot follow a trend that would be expected following those presented in Figure 5.8. The change in length at a given level of true composite tensile strain was larger for particles with neighbors than isolated particles. Statistically the differences are significant at all the tensile loading increments except the initial load as presented in Table 5.2. These results are expected since the non-isolated particles contain more cracks at a given strain increment and as previously discussed, the elongation of the particles require particle cracking to occur.

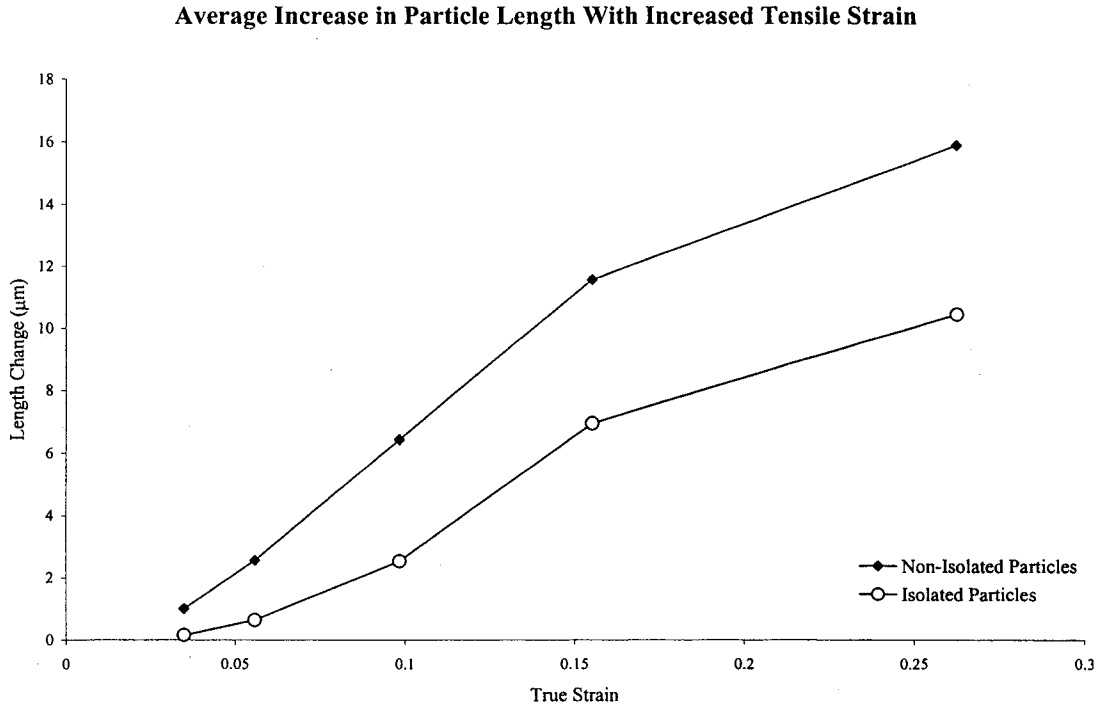

Figure 5.12. The average increase in particle length through particle cracking and crack opening during tensile straining for the sample with a 4% volume fraction of Al_2O_3.

Table 5.2. Comparison of the statistical significance of the difference in the length change between isolated and non-isolated particle data sets at each tensile strain increment.

Average Length Change

Strain	*T-Data*	*T-0.05*	*Statistical Difference*
0.044022	2.20688	6.314	No
0.063027	3.40378	2.8	Yes
0.106295	4.34478	1.86	Yes
0.154764	2.84775	1.74	Yes
0.279314	2.81104	1.71	Yes

An interesting trend was observed when the Average Crack Opening Displacement (COD) versus true tensile strain was plotted. The average crack opening displacement was calculated by dividing the length change of each particle by the number of cracks in the particle. The difference in the crack opening displacement between the isolated and non-isolated particles is largest at the lowest values of strain. The non-isolated particles have the highest average crack opening displacement, however, at higher strains, the average crack opening displacement of the isolated particles approaches an apparent plateau in the value for the non-isolated particles. Statistically, the mean values of the crack opening displacement for each data set are only significantly different at one of the intermediate strain increments.

Another interesting note is that the isolated particles approach the plateau experience by the non-isolated particles. The isolated particle curve seems to be shifted to the right of the non-isolated curve. The shape of both curves is similar, suggesting the clustering does not affect the maximum crack opening displacement, it only accelerates the attainment of the maximum plateau value. This seems intuitively

reasonable since the particle clusters have higher local volume fractions of particles, therefore higher stress partitioning, which in turn accelerates the damage.

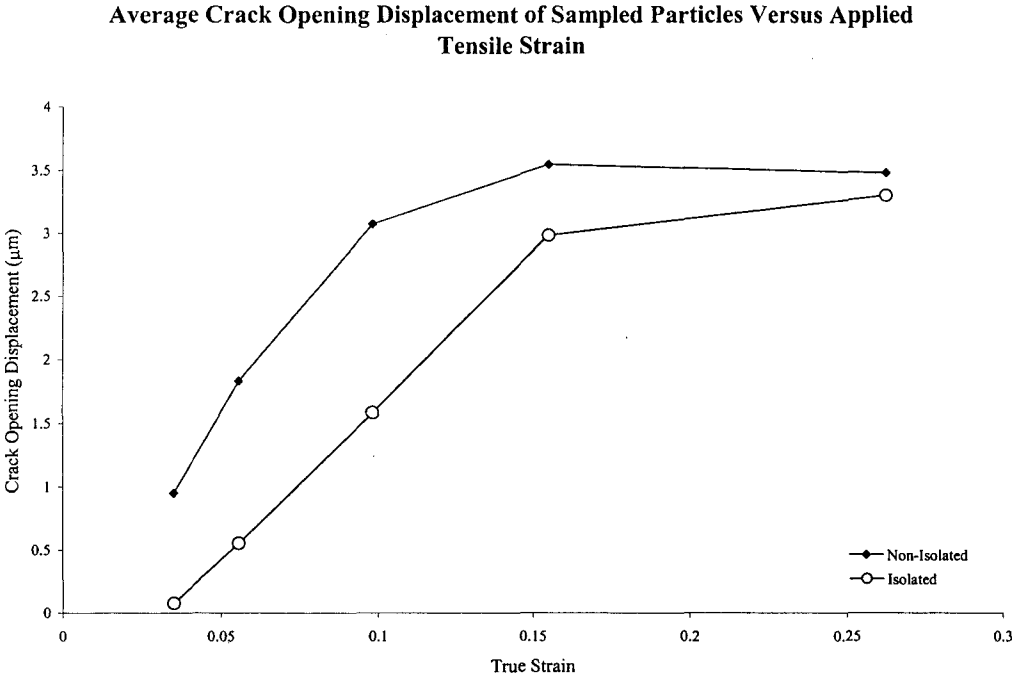

Figure 5.13. The average crack opening displacement of the isolated and non-isolated particle versus true tensile strain.

Table 5.3. Comparison of the statistical significance of the difference in the crack opening displacement between isolated and non-isolated particles data sets at each tensile strain increment.

Average Crack Opening Displacement

Strain	*T-Data*	*T-0.05*	*Statistical Difference*
0.044022	2.49445	6.314	No
0.063027	2.79688	4	No
0.106295	2.99104	2.353	Yes
0.154764	0.99735	2.132	No
0.279314	0.3159	2.1	No

5.4 Summary of General Observations

1. X-ray computed tomography has proven to be a powerful tool to observe damage processes occurring at length scales higher than the resolution limits of the technique (~2μm). The technique has provided a vast amount of both qualitative and quantitative information on the damage processes occurring during the tensile deformation of the aluminum/Al_2O_3 composite studied in this thesis.
2. Both the largest particles and the least spherical particles fractured before the smaller and more spherical particles in the distribution.
3. The particle spatial distribution was heterogeneous. Clusters of high volume fraction of Al_2O_3 particles were aligned in stringers oriented in the direction of extrusion and tensile deformation.
4. The damage process initiated through particle cracking. Upon further deformation the particles underwent a multi-stage cracking process suggesting the particles could be reloaded to a value of stress as great, if not greater, than the original fracture stress of the particles.
5. Isolated particles tended to fracture later in the tensile deformation process than particles having one or more neighbor.
6. At all stages of deformation studied the non-isolated particles underwent more multi-cracking, and therefore more elongation in the direction of tensile deformation, than isolated particles.
7. The average crack opening displacement of the non-isolated particles appeared to saturate and the crack-opening displacement for the isolated particles approached the plateau of the non-isolated particles.

CHAPTER 6

ANALYTICAL DAMAGE MODELLING

6.1 Introduction

Two damage models are described in this chapter. The first damage model described extends the earlier work of Maire and Wilkinson (1997) by adding a calculation of the damage linkage processes occurring in the same class of composite materials that their original modelling work was based on. The second model describes the damage process observed in the AA6111/Al_2O_3 system studied in this thesis.

These two materials differ primarily by the damage process; the material investigated by Maire and Wilkinson failed at low plastic strains while the system studied in this thesis failed at higher strains. Both systems had a significant modulus mismatch ($E_{particles}$~ (5-6) x E_{matrix}) and damaged through particle cracking. The main difference between the two systems was that the damage process in the AA6111/Al_2O_3 system allowed for multiple cracking of the particles.

A number of analytical models exist for damage processes in composites, or other multi-phase systems, that involve microvoid nucleation, growth and coalescence (Christmensen et al. (1989), Brown and Embury (1973)). While this damage process is fairly well understood and modelled, models that deal specifically with damage occurring through particle cracking are lacking. Few models exist and those that do fail to capture the processes limiting the maximum uniform elongation (also referred to as ductility in the discussion that follows).

Describing the damage processes occurring in the high and low ductility systems through analytical modelling is particularly useful because the two systems reside on the upper and lower limits of ductility typically observed in this class of composite materials. It is therefore expected that the composites that damage through particle cracking will have both work-hardening behavior and maximum uniform elongation values that fall somewhere between the two boundary values offered by the systems presented here.

The only input parameters required in the models that follow are all experimentally determined. Prior to modelling a given system the matrix mechanical response must be first determined through experimental measurement. Similarily, the particle fracture behaviour must be experimentally determined through some form of metallographic observation so both the damage mechanism and the fracture properties of the particles can be determined.

6.2 The SCEMA-Damage Model

This model employs the tangent modulus self-consistent effective medium approximation (SCEMA) used in the work of Maire and Wilkinson (1997). The model was first developed by Corbin and Wilkinson(1994a,b,c) to study the effects of the second phase volume fraction and distribution on the mechanical response of a metal matrix composite. It was later updated in the work of Maire and co-workers(1997 etc.) to included the effects of damage, in the form of stiffness loss through particle cracking, on the mechanical response. This model, which will be now referred to as the SCEMA-Damage model, served as an ideal starting platform for the development of comprehensive models for damage in both of the low and higher ductility composite

systems described in the following sections of the chapter. The model was particularly useful because it allows for the treatment of heterogeneity in the particle distribution, which has been experimentally shown to have a significant influence on the damage process.

The SCEMA-Damage model is described in detail in Appendix I and in the work of Wilkinson et *al.* (1997, 1998, 1999) and will only be outlined here for clarity. Modelling the mechanical response of a composite material requires two steps. In the first step, the SCEMA model as described in Section 2.1.6 is used to develop the constitutive relations for materials of uniform composition containing different particle volume fractions. This model is similar to the Eshelby equivalent inclusion model in that it calculates the stress partitioning resulting from the experimentally determined differences in the modulus of the matrix and the reinforcing particles.

Plasticity is treated by assuming that all plastic deformation takes place in the matrix while the particles remain elastic. The deformation of the matrix is assumed to obey the Ramberg-Osgood description for a power-law hardening material. Prior to modelling, the mechanical response of the matrix is experimentally determined. The experimental flow curves are then fit to the Ramberg-Osgood formulation for input into the model. At each increment of strain, the tangent modulus is calculated directly from the Ramberg-Osgood expression. This value of the matrix tangent modulus is then used in place of the matrix elastic modulus in the effective medium calculation. By knowing both the elastic modulus of the reinforcing particles, E_p, and the tangent modulus of the matrix, E_m, at a given strain increment, the modulus of the composite can be determined through the

SCEMA formulation. This solution of the composite modulus, E_c, essentially simplifies down to solving a quadratic equation of the form

$$AE_c^2 + (BE_p + CE_m)E_c + DE_pE_m = 0 \qquad (6.1)$$

where A, B, C and D are constants that are dependent on both the reinforcement shape, volume fraction and Poisson's ratio. Using this approach, it is possible to relate the composite stress to the composite strain by multiplying the calculated composite modulus with the value of strain at a particular strain increment. With knowledge of the composite stress and the corresponding composite strain it is possible to plot the entire predicted flow curve of the undamaged composite. The flow curve is then fit to the Ramberg-Osgood equation. This process is repeated for each uniform volume fraction of composite material required for the second stage of the modelling process.

Heterogeneity in the particle distribution is treated using the same approach as described for a uniform distribution. As an example consider a composite containing a bimodal distribution of regions of 5% and 20% volume fraction. Each region is treated as a separate phase embedded in the composite. In this case the 5% region would be treated as one phase with power-law hardening properties determined by fitting the data generated for a uniform 5% region. The 20% volume fraction phase would be treated in the same way. At each increment of strain the composite modulus would be calculated using the SCEMA formulation and the tangent modulus values generated from the Ramberg-Osgood descriptions of both the 5% and 20% regions. The main difference between this and the approach described for a composite with a uniform distribution of a second reinforcing phase is that the particle elastic modulus and the matrix tangent

modulus are replaced with the tangent modulus of each phase, in this case the 5% and 20% regions, within the bimodal composite.

The SCEMA-Damage model of Maire et *al.*(1997) extends this model one step further by treating the effects of damage occurring through particle cracking. Since particle fracture results in a local loss of stiffness, the properties of the regions containing damaged particles possess different mechanical properties than that of the undamaged material. The damaged material is distinguished from the undamaged material by treating it as an additional phase with properties defined through the results of finite element calculations by Brockenbrough and Zok(1995). Through a number of FEM calculations with cracked particles embedded in matrices with differing flow properties and differing levels of particle/matrix stiffness mismatch they were able to develop an expression relating the flow stress of the damaged material, $\sigma_{yield}^{damaged}$, to that of the unreinforced matrix, σ_{yield}^{matrix}, through a relationship of the form:

$$\sigma_{yield}^{damaged} = g^{damage}\sigma_{yield}^{matrix} \tag{6.2}$$

where g^{damage} is a function of the work hardening exponent only and both $\sigma_{yield}^{damaged}$ and σ_{yield}^{matrix} are evaluated at the same strain.

Treating each phase as having both damaged and undamaged regions dictates that the original SCEMA formulation be modified so that it can support a greater number of phases. This is accomplished by incorporating the self-consistent formulation of Kreher and Pompe (1989) into the model:

$$\left\langle \frac{E_i^{tangent} - E_{composite}^{new}}{E_i^{tangent} + \frac{3}{2}E_{composite}^{new}} \right\rangle = 0 \tag{6.3}$$

where $E_i^{\tan gent}$ us the tangent modulus calculated for each phase, $E_{composite}^{new}$ is the composite tangent modulus and the angle brackets represent an average, weighted by the volume fraction, over all phases, including both damaged and undamaged regions, of the composite.

Once the composite tangent modulus is established, the stress in the composite and each of the participating phases is calculated as described in detail in Appendix I. The value of stress in a given undamaged region of a phase is used to directly determine the stress acting on the undamaged particles within the phase. This particle stress is then used to determine the fraction of reinforcing particles that have cracked based on the classical form of the Wiebull function:

$$W(\sigma_p, a) = 1 - \exp\left[-\left(\frac{a}{a_1}\right)^3\left(\frac{\sigma_p - \sigma_u}{\sigma_o}\right)^m\right] \tag{6.4}$$

Where a is the average particle diameter, a_1 is a scaling parameter and σ_p is the stress acting on the particle at a given strain. The threshold stress, σ_u, for rupture, the characteristic stress, σ_o and the Weibull modulus, m, are all experimentally determined properties of the ceramic reinforcement.

The volume fraction of damaged material is directly estimated [see Wilkinson et. *al*(1998) or Appendix I for derivation] through:

$$D_i(\sigma_p) = \int_o^\infty \xi(a) \cdot W(\sigma_p, a) da \tag{6.5}$$

where $\xi(a)$ is the volume distribution function of particle sizes and $D_i(\sigma_p)$ is the damage parameter equivalent to the volume fraction of damaged material, $f_{damaged}$, in a given

phase. It is intuitively clear that as the composite is loaded and more particles crack, that the volume fraction of damaged material increases. Since the total volume fraction of both the damaged and undamaged regions of a phase must equal 1, ie. ($f_{undamaged} + f_{damaged} = 1$), a greater portion of the material within a phase is damaged with each increment in damage defined in eq. (6.5) This is illustrated conceptually in Figure 6.1.

The increment in damage is assumed to occur instantaneously at constant strain. Since the elastic modulus of the damaged region is much lower than that of the same region without damage, the composite modulus and as a result the composite stress is reduced. This stress reduction in each phase and the composite is calculated following the formulation of Wilkinson *et al.* (1998) through a process of elastically unloading the composite at constant strain and stress redistribution. Once the stress is redistributed between the phases, it is important to reload each phase elastically up to its former flow

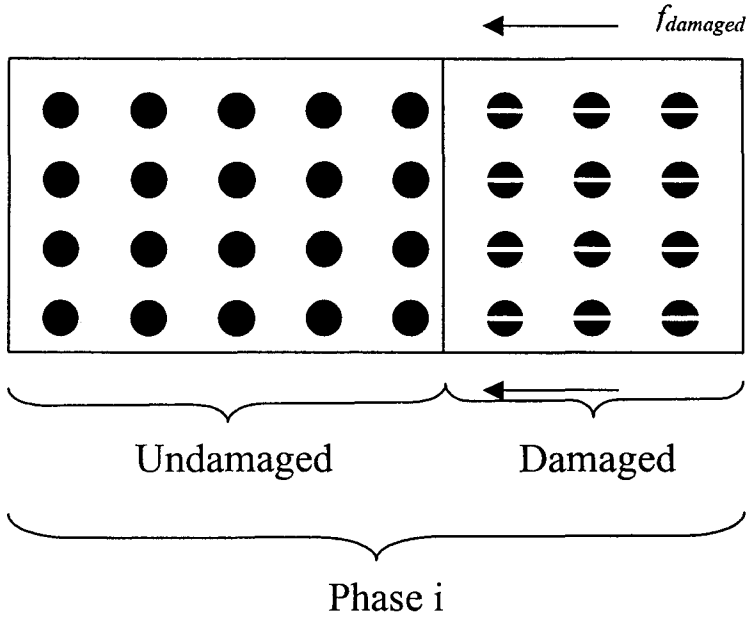

Figure 6.1 Conceptual illustration of damaged and undamaged regions within a single phase of composite material. As the composite is strained, increasingly more particles fracture causing the damaged region to grow at the expense of undamaged material.

stress before plastic deformation recommences. To prevent overshooting the previous flow stress, the composite is reloaded at strain increments much smaller than those used prior to unloading.

The comprehensive treatment of the damage in the SCEMA-Damage model results in predictions that provide a good fit to the experimental data of a number of experimental systems [Maire *et al.*,(1997), Conlon (1998), Poruks (1998)]. In some cases (Maire *et al.*,(1997), the model prediction is so close to the experimental data, that the flow curves are virtually indistinguishable.

Although the original model provides a good fit to the experimentally determined flow curves at low to moderate strains (up to approximately 5~10%), the ductility of the experimental material is significantly overestimated as later illustrated in Figures 6.7 and 6.8. This suggests that at low plastic strains, consideration of the loss of stiffness solely through particle cracking is sufficient. However, examination of experimental data at higher plastic strains, particularly when the volume fraction of reinforcement is high, suggests that the drop in work hardening rate is more severe than predicted through particle cracking. Thus at higher strains additional damage mechanisms, including the loss of plastic constraint at high reinforcement volume fractions, must be present.

6.3 Low Ductility Composite Materials

Insight into damage mechanisms present in fractured materials can be gained through examination of micrographs parallel to the loading direction (Figure 6.2). These suggest that composite fracture initiates by a micro-crack linkage process through the region of high volume fraction region. In Figure 6.2 a micro-crack linking damage between

adjacent cracked particles is visible in the high volume fraction region. The mechanism resulting in the linkage of damage between adjacent cracked is not clearly understood. However, the additional drop in the work hardening rate present in experimental data [Maire et al. (1997)] at higher plastic strains suggests that linkage occurs rather rapidly. This suggests that the damage process controlling ductility is the unstable linkage of

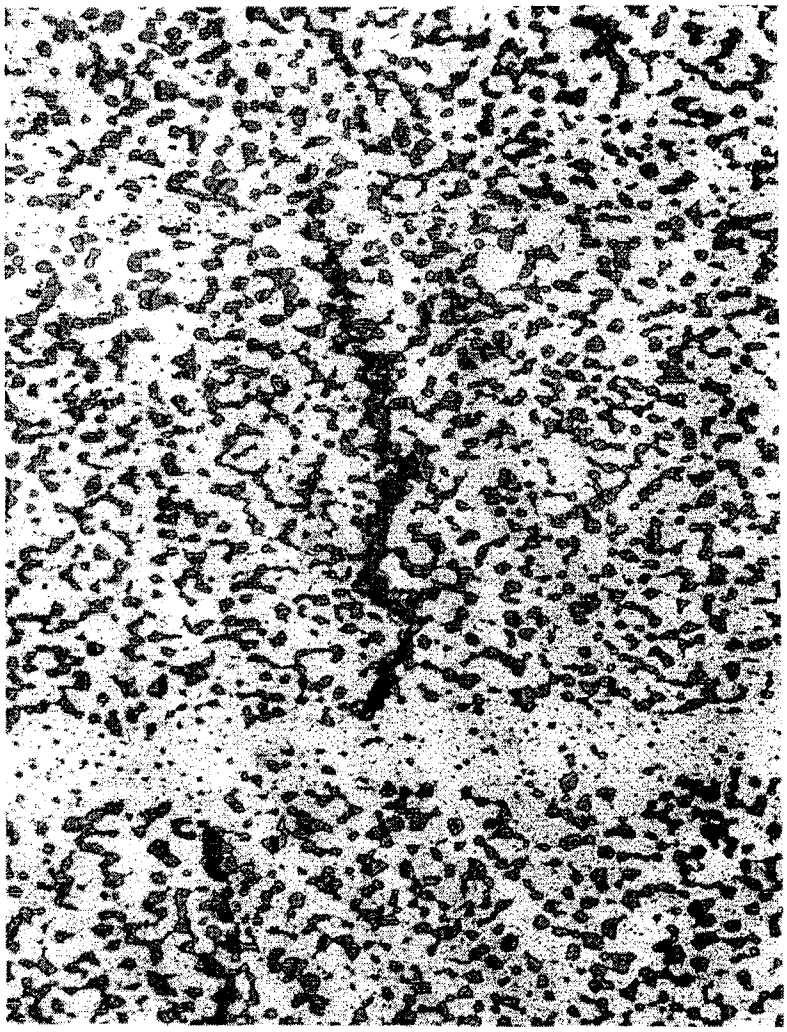

Figure 6.2 - SEM micrograph of crack transversing through particle rich region of a $CuAl_2$ reinforced Al 356 composite with a bimodal distribution of second phase particles [Wilkinson et al.(1997)]. Notice that both cracked $CuAl_2$ particles and a macro-crack formed by damage linkage are present.

Micro-crack linkage may be envisioned to occur through two general mechanisms. The first involves the linkage of cracks through a form of the Griffith criterion. To use this approach, an estimate of the effective composite fracture toughness, K_I, must be made. The composite fracture toughness can be approximated through a rule of mixtures calculation using both the volume fraction and fracture toughness of each phase. The variation of fracture stress with cracked particle spacing can then be modeled by replacing the cracked particles with two equivalent penny shaped cracks in an infinite matrix. The crack size, a, is equal to the average diameter of the cracked particles and it is assumed that once the particles crack, no load transfer between the matrix and particles takes place. At volume fractions of the order of 30% and assuming that the particles are uniformly distributed, the Griffith approach predicts that crack linkage would occur at a far field stress of 1 GPa if the spacing, λ, between cracked particles was 0.05a (spacing equal to 5% the particle diameter). Based on experimental results, this significantly over estimates the point at which linkage occurs. This can be attributed to the dominance of the fracture toughness value of the aluminum matrix, when compared to that for SiC, in the rule of mixtures calculation. In addition this fracture model is based on linear elastic fracture mechanics which fails to account for the large amount of energy, in the form of plastic energy, consumed by a crack as it propagates through the aluminum matrix.

A further consideration is the distribution of second phase particles in a real material. When the volume fractions are high, the local stress triaxility that develops between closely spaced particles inhibits plastic flow, increasing the energy required for deformation. As the particle spacing decreases it becomes increasingly energetically favorable to cleave rather than plastically deform, significantly decreasing the local value

of K_I in the matrix. As is clear in Figure 6.2, particle spacing can vary from several particle diameters apart down to distances at which particles almost touch one another where the effect of local stress triaxility may be of significance.

Ashby's experiments [Bannister and Ashby(1991)] discussed in section 2.6.4, reveal the strong dependence of the flow behavior on stress triaxality of ductile materials. When the triaxality is high, typically soft and ductile materials can reach stress values up to 8 times that of unconstrained material and fail at much lower strains [Bannister and Ashby(1991)]. When the particle spacing is small, in the order of particle diameter (volume fractions of 20% for the AA6111/Al_2O_3 and the AA2618/SiC systems discussed in this chapter) the level of stress triaxality becomes significant as described in the finite element calculations of Watt *et al.*(1997) and Guilliemer-Neel *et al.*(2000). Composite materials, particularly those possessing high volume fractions of stiff reinforcing particles can be expected to have regions of high local stress triaxality. In these regions of high stress triaxality it seems therefore reasonable to assume that the matrix flow behavior significantly differs from that of the equivalent unconstrained matrix.

Based on the above argument, it is clear that when considering an appropriate model to describe the linkage process, one involving the local stress-state between adjacent cracked particles would be appropriate. Of those described in section 2.6, both the modified versions of the Brown and Embury model that incorporate stress triaxality [Brown and Embury (1973)] or Thomason's Limit Load failure[Thomason (1990)] model appear to be appropriate. However, as described previously, these models assume a coalescence criterion based on a uniform average particle spatial distribution. In this class of materials this assumption is clearly invalid. Even when the average volume

fractions is low, the local spacing of adjacent particles can fall below the critical separation distance required for the development of strong stress triaxility.

Another factor controlling the fracture behavior is the work hardening, or the resistance to plastic flow, of the matrix. When the reinforcing particle size is well within the continuum range, the work hardening of the composite is governed by both dislocation mechanics and more significantly, by the apparent work hardening resulting from the stress partitioning between the ductile matrix and the rigid reinforcement. When the particle spacing is below a critical distance in which high stress triaxality can develop, the work hardening of the matrix locally is further enhanced through elevated plastic constraint. However, when the reinforcement fractures, the additional work hardening capability of the matrix between particles resulting from the stress partitioning and plastic constraint is significantly diminished.

6.3.1. Low Ductility Fracture Model for Uniform Second Phase Distributions

An alternative to Thomason's limit load failure model for uniform particle distributions incorporates his concept of a localization mechanism involving the unstable failure of the inter-particle matrix, either through localized shear or load limit failure. In this case, internal necking or localized instability may be rationalized by considering the plastic constraint that the reinforcing particles impose on the matrix. Once the particles fracture this plastic constraint is lost and the stress acting on the matrix between the two cracked particles can exceed the fracture stress of the matrix. This can be approximated by setting the far field work hardening rate, WHR, equal to the stress acting between two penny shaped cracks separated a distance, λ, apart:

$$WHR = \sigma_a \left[1 + \alpha \sqrt{\frac{a}{\lambda}} \right] \tag{6.6}$$

The value of a is equal to the average particle diameter as it is assumed, and experimentally observed [Maire *et al.* (1997)], that particles in these composites fracture across their entire diameter. The term α is a stress concentration of the order 2 and σ_a is the far field applied stress of the participating phase. In this model it is assumed that cracked particles can be replaced by penny shaped cracks of equivalent diameter and that no stress partitioning takes place between the two cracked halves of the particles and the matrix. Rearrangement of eq. (6.6) yields an expression for the critical point at which linkage of damage between cracked particles occurs.

$$\frac{\lambda}{a} = \frac{4}{\left[\frac{WHR}{\sigma_a} - 1 \right]^2} \tag{6.7}$$

At this point it is useful to consider that the work hardening rate, WHR, the far field applied stress, σ_a, and the spacing between cracked particles, λ, are all functions of the applied strain. The cracked particle spacing for a uniform distribution of particles within a phase can be written in terms of the average particle diameter, a, the fraction of cracked particles and the total particle volume fraction of the phase:

$$\lambda(\varepsilon) = \left(\frac{a^3}{f_{cracked} \cdot f_{particles}} \right)^{1/3} - a \tag{6.8}$$

where $f_{cracked}$ and $f_{particles}$ are the fraction of cracked particles at a given strain and the total particle volume fraction of particles respectively.

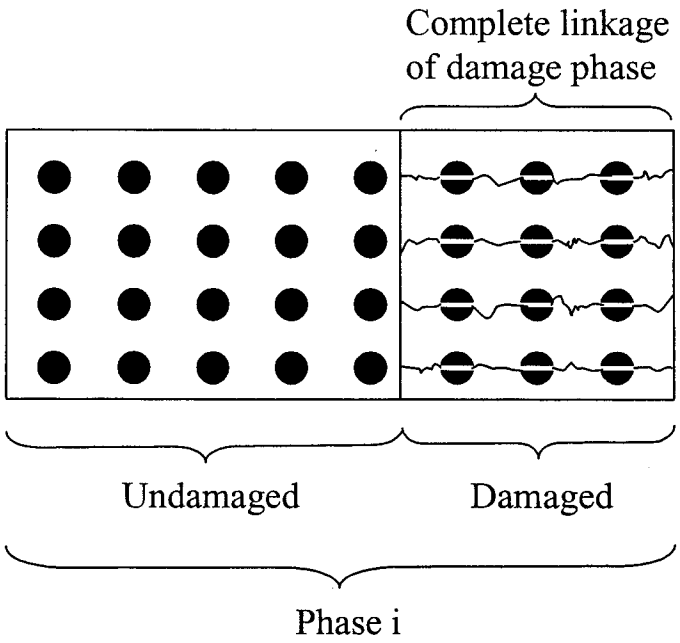

Figure 6.3 Conceptual illustration of a phase within a composite following the complete linkage of the damaged phase. It is assumed that the damaged phase now possesses zero stiffness and provides no mechanical contribution to the composite.

In this model, it is assumed that the condition for coalescence occurs when the mean cracked particle spacing in one of the participating regions reaches the critical value that satisfies the linkage criterion. Once this occurs, the region completely fails and all mechanical contributions of this region to the composite microstructure are lost as conceptually illustrated in Figure 6.3. This therefore serves as an upper bound of the composite ductility. A better model, developed in the following section, samples a distribution function describing the distribution of the cracked particle spacing. By doing

this, a better estimate of ductility is gained because the coalescence criterion is met earlier for some cracked particles spaced closer together in a given phase than others.

6.3.2 Low Ductility Fracture Model for Heterogeneous Second Phase Distributions

In many dispersion strengthened and composite systems, the distribution of the second phase particles is rarely uniform. Even for materials that can be characterized as having regions of different average volume fractions, for example those classed as being bimodal, the distribution of particles in each of these regions is also heterogeneous. Tessellation calculations [Pilkey *et al.*(1998)] of particle distributions indicate that the distribution of particle spacing may be modelled to follow a form of the Poisson distribution.

$$F(\lambda) = 2\pi\rho\lambda\exp(-\pi\rho\lambda^2) \tag{6.9}$$

where ρ is the cracked particle density and λ is the spacing between cracked particles. A Poisson distribution function that varies with strain is developed by writing the density of cracked particles in terms of the area fraction of cracked particles at each strain increment.

$$\rho(\varepsilon) = \frac{V_f(\varepsilon)}{\pi r^2} \tag{6.10}$$

Where r is the particle radius and V_f is the volume fraction of cracked particles. Substituting (6.10) into (6.9), yields the distribution function for spacing between cracked particles at each increment of strain.

$$F(\lambda,\varepsilon)=\frac{2V_f(\varepsilon)\lambda}{r^2}\exp\left(-\frac{V_f(\varepsilon)\lambda^2}{r^2}\right) \tag{6.11}$$

The variation of the distribution function with increased strain is illustrated graphically in Figure 6.4. As strain is increased, the volume fraction of cracked particles increases and the Poisson distribution progressively narrows while the mean cracked particle spacing decreases.

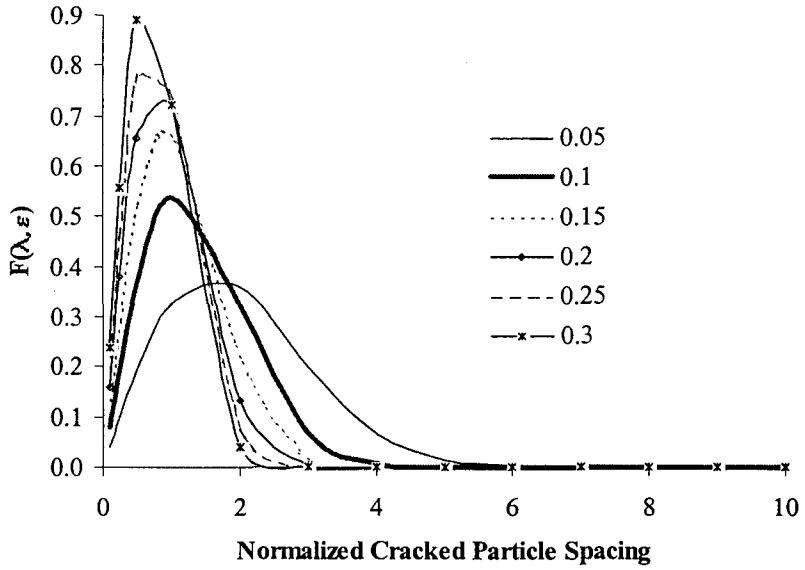

Figure 6.4. Graphical illustration of the Poisson distribution of cracked particle spacing variation as a function of the volume fraction of cracked particles. The lines 0.05, 0.1, 0.15, 0.2, 0.25 and 0.3 represent 5 vol%, 10 vol%, 15 vol%, 20 vol%, 25 vol% and 30 vol% of cracked particles, respectively. The cracked particle spacing has been normalized by the particle diameter and the cracked particle spacing is based on the edge to edge separation of particles.

Since the cracked particle spacing is non-uniform one would expect that the critical conditions for linkage as defined in eq. 6.7 would be reached at lower values of stress for more closely space particles. Incorporating this concept into the crack linkage model is readily achieved by combining the Poisson distribution of cracked particle spacing with the critical condition for linkage between two cracked particles. This is

accomplished by first determining the critical crack spacing, λ_c, at a particular level of strain by rearranging eq. 6.7 so it has the form:

$$\lambda_c = \frac{4a}{\left[\frac{WHR}{\sigma_a} - 1\right]^2} \tag{6.12}$$

The fraction of linkage events that occur at a given level of strain can be directly estimated by determining the number of cracked particles spaced the critical crack spacing for linkage and dividing this by all the cracked particles in the phase. This is evaluated directly from the Poisson distribution function (or any other cracked particle spacing distribution function) by:

$$f_{linked} = \frac{\int_0^{\lambda_c} F(\lambda,\varepsilon)d\lambda}{\int_0^{\infty} F(\lambda,\varepsilon)d\lambda} \tag{6.13}$$

This is illustrated schematically in Figure 6.5. With each increment of load and damage, the Poisson distribution shifts left and narrows while the fraction of linked particles sweeps to the right. To set a lower bound, it is assumed that once linkage between two particles occurs, the particles and the matrix between them can no longer sustain loading and possess zero stiffness. This is incorporated into the SCEMA-Damage model by

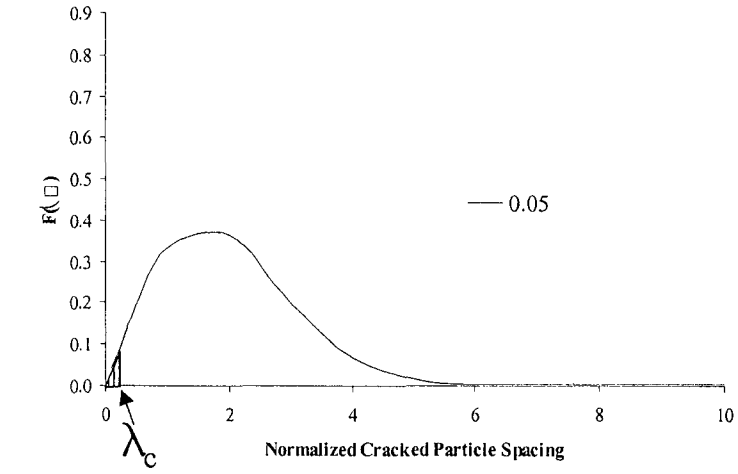

(a)

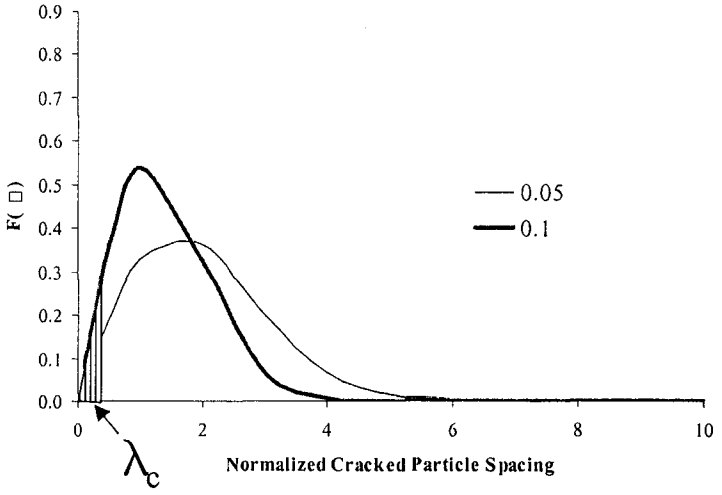

(b)

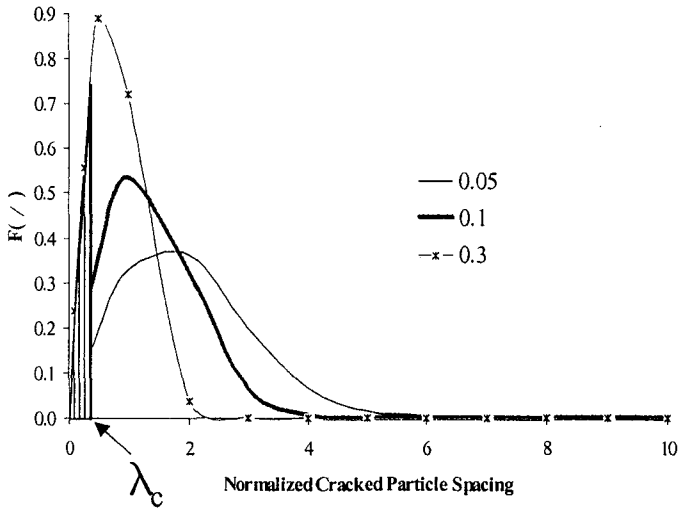

(c)

Figure 6.5 (a)-(c). Schematic illustration of the interaction between the fraction of particles that have linked and the Poisson distribution of cracked particle spacing. As deformation and damage proceeds, the Poisson distribution shifts left and the fraction of linked particles sweeps across the distribution to the right.

reducing the stiffness of the damaged region in proportion the linkage events that have occurred at a given strain:

$$E_{effective}^{damaged} = E^{damaged}(1 - f_{linked}) \tag{6.14}$$

Using this approach a phase is essentially treated as being composed of three regions. The undamaged region and a damage region possessing damage in the form of cracked particles and linked cracked particles as illustrated in Figure 6.6

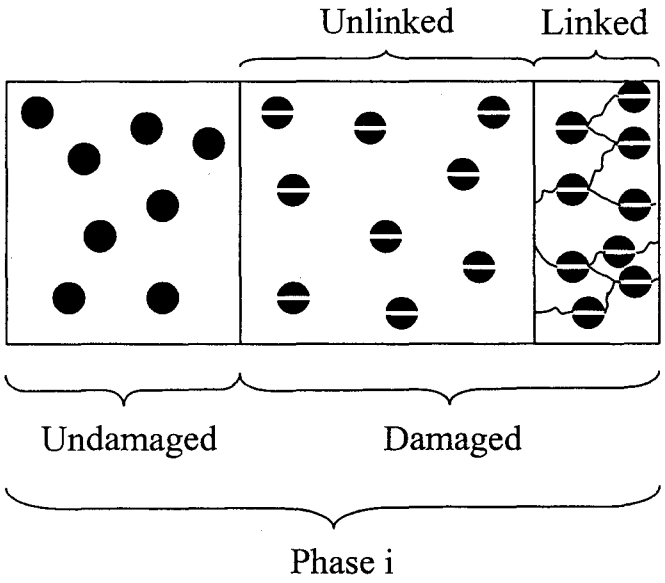

Figure 6.6 Conceptual illustration of the progressive linkage of cracks in the damaged region of the concept as described by the micro-crack linkage model.

6.3.3 Modelling Results for an AA2618/SiC Composite

As a preliminary validation to the modified damage models, the experimentally measured mechanical response of the AA2618/SiC system with two different volume fractions of SiC, 10% and 18%, were compared to the modelling predictions. Three models were used; the original version of the SCEMA-damage model, a modified SCEMA-Damage model with a uniform distribution of cracked particles within each phase and the SCEMA-Damage Crack Percolation model developed in the previous section.

6.3.3.1 Modelling Approach

The modelling approach follows that of Maire *et al.* (1997) exactly. By doing this it is possible to repeat their calculation to ensure that the original SCEMA-Damage model fits the experimental data in the same way as in the published literature. The SCEMA-Damage model was then revised to incorporate both micro-crack linkage models developed in the previous section. Values of the work hardening rate and the applied stress of all the phases at a given strain are readily extracted from the SCEMA-damage model. The properties extracted for the damaged phase are used directly with the two models of micro-crack linkage.

All initial material parameters followed those of Maire *et al.*(1997). The modelling input values of the modulus, reference stress and the hardening exponent are 74.5 GPa, 200 MPa and 0.15 respectively. The elastically deforming particulate reinforcement was defined as being spherical with a mean diameter of 11.5 μm and a Young's modulus of 450 GPa. The Wiebull parameters used to describe particle fracture

were σ_0=1700 MPa, σ_u=580 MPa and a Wiebull modulus (m) of 3.8, indicating that the variability in the reinforcement strength is high. The experimental flow curves used for this work have been extracted by digitizing a scanned image of the published experimental flow curves [Maire *et al.*(1997)] The digitized graph is then traced using Microcal Origin 5. Tracing of the graph is somewhat prone to error. However, in this case the error in the composite stress at a given strain is estimated as being less than 2~3MPa.

6.3.3.2 Results

It is useful to initially compare all the results from all the models: the original SCEMA-damage model, the SCEMA-damage model assuming sudden catastrophic linkage across the entire damage phase and the SCEMA-damage model incorporating the micro-crack percolation model. The results are also useful because as will be illustrated later, they serve to signify the effect of spatial heterogeneity within a phase of a bimodal distribution on damage development. The experimental results and predicted flow curves for an AA2618T4/SiC composite are presented for 10% and 18% volume fractions in Figures 6.7 and 6.8 respectively. Additionally, comparisons of the work hardening rates of each composition are provided in Figures 6.9 and 6.10.

One of the first things of note is the good fit with experimental data all three models provide at low strains. However, as previously mentioned, it is clear that the original SCEMA-damage model, labelled "Original Model" on the Figures 6.8-6.10, significantly overestimates the ductility of the experimental material at both volume fractions of SiC. The model incorporating micro-crack linkage through sudden, complete linkage of the damage region (Uniform Crack) provides a better prediction of composite

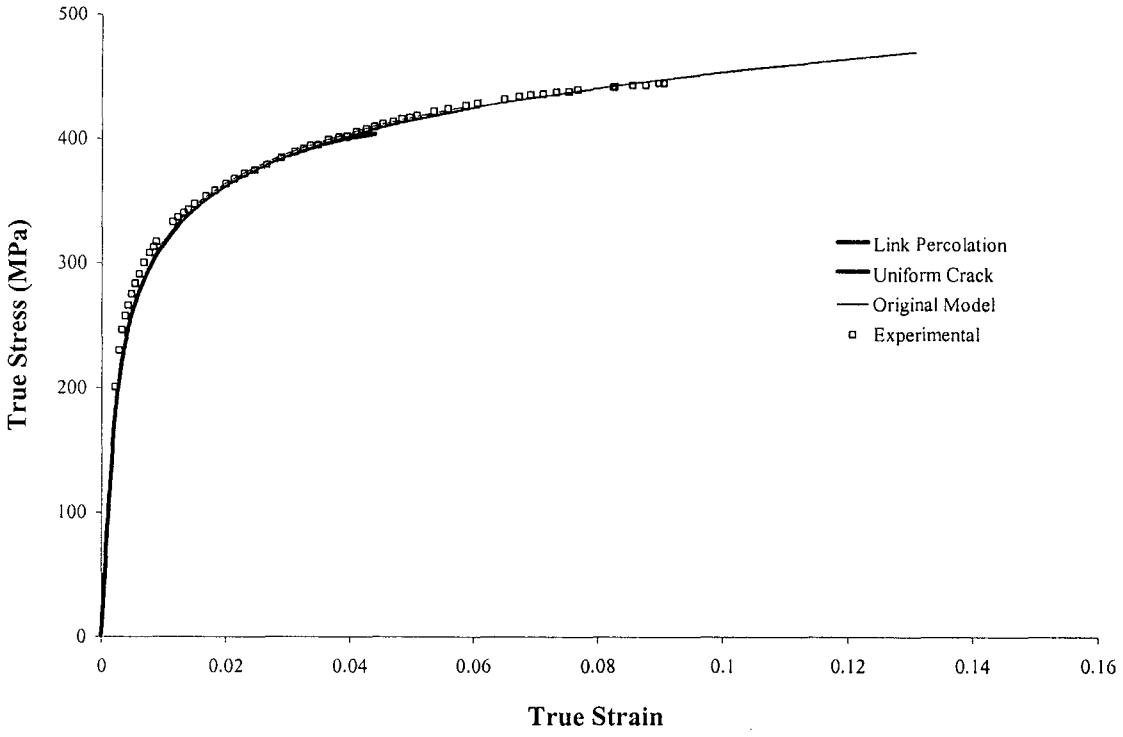

Figure 6.7 Comparison of the modelled flow curves and the experimental results for a AA2618T4 and 10 vol% SiC composite.

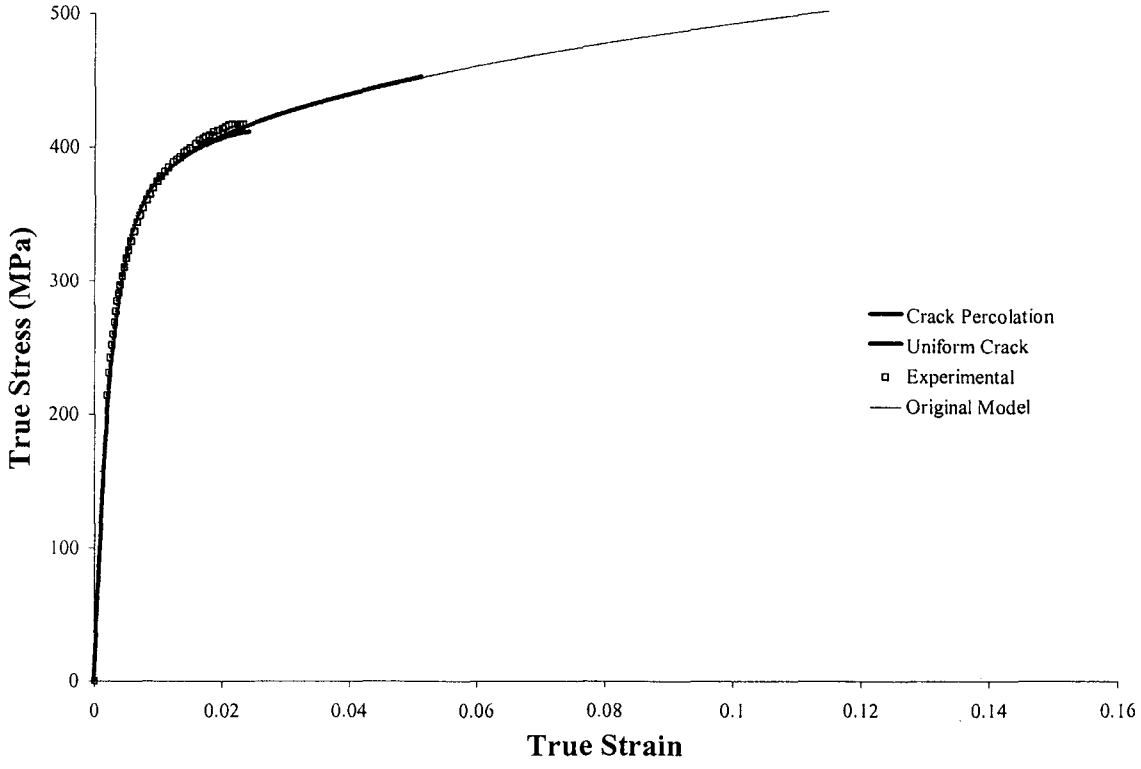

Figure 6.8. Comparison of the modelled flow curves and the experimental results for a AA2618T4 and 18 vol% SiC composite.

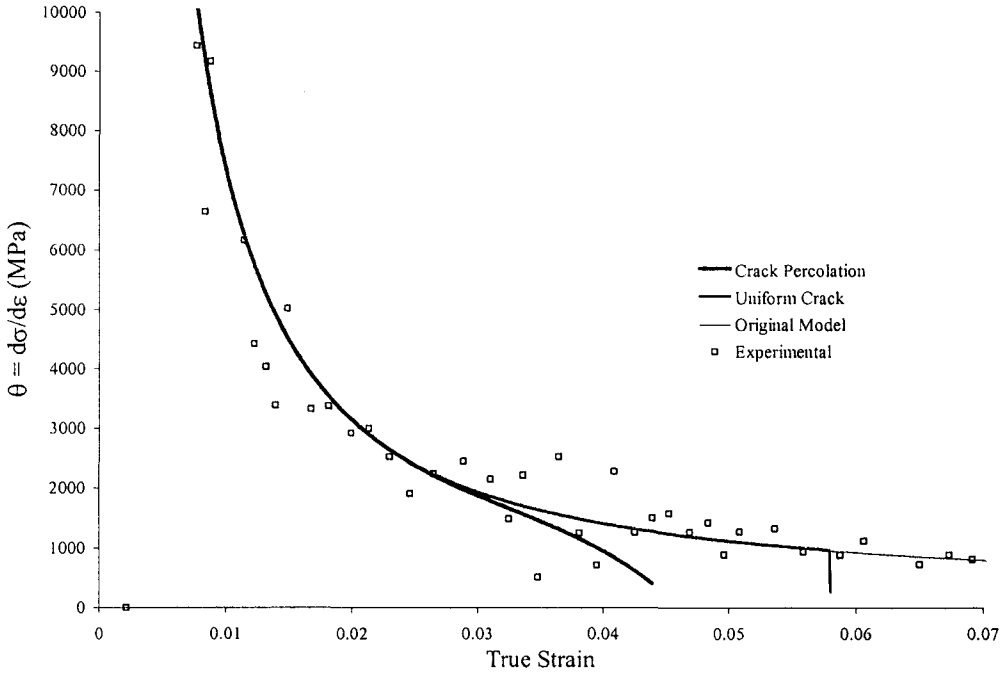

Figure 6.9. Comparison of the work hardening rates from the experimental data and those predicted by the three models for the 10vol% SiC material.

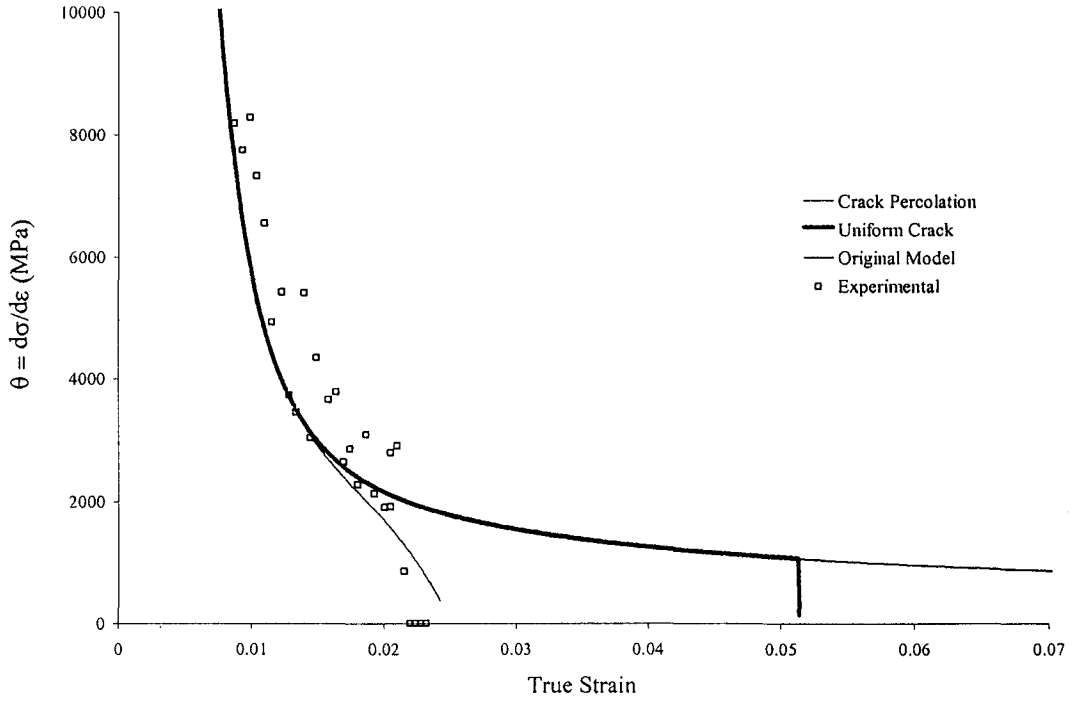

Figure 6.10. Comparison of the work hardening rates from the experimental data and those predicted by the three models for the 18vol% SiC material.

failure than the original model. However, the overestimation of ductility is still large for the composite with 18% volume fraction. The micro-crack percolation model (Crack Percolation) provides the best fit to the 18% volume fraction composite data. The modelling results for the 10% volume fraction composite is not quite as good. In both linkage models the estimate in the ductility is less than experimentally observed.

Interesting observations can be made when examining the predicted work hardening behavior. For both volume fractions of composite material, the work hardening rates in the crack-percolation model progressively drop from those predicted by the original model at strains less than those of the uniform crack linkage model. The work hardening rates predicted for the uniform crack linkage model drop at a larger strain and fall off suddenly while the drop in the work hardening rates in the original SCEMA-damage model fall off more gradually. While the crack percolation model underestimates the strain at which failure occurs in the 10% volume fraction composite, it provides the best prediction of the work hardening characteristics of all the models for both volume fractions of experimental material.

It is interesting to compare the damage as a function of strain for each of the models. In Figure 6.11, 2618 with 10% volume fraction, the damage evolution with strain remains identical for all models up until the strain at which the Considère criterion is reached for each model. In all cases both the uniform and the progressive percolation linkage models fail at damage levels less than 1, a value at which all particles have fractured. These models indicate that, depending on the strength characteristics of the particles and the flow properties of the matrix, failure of the composite can occur before all particles within it are fractured.

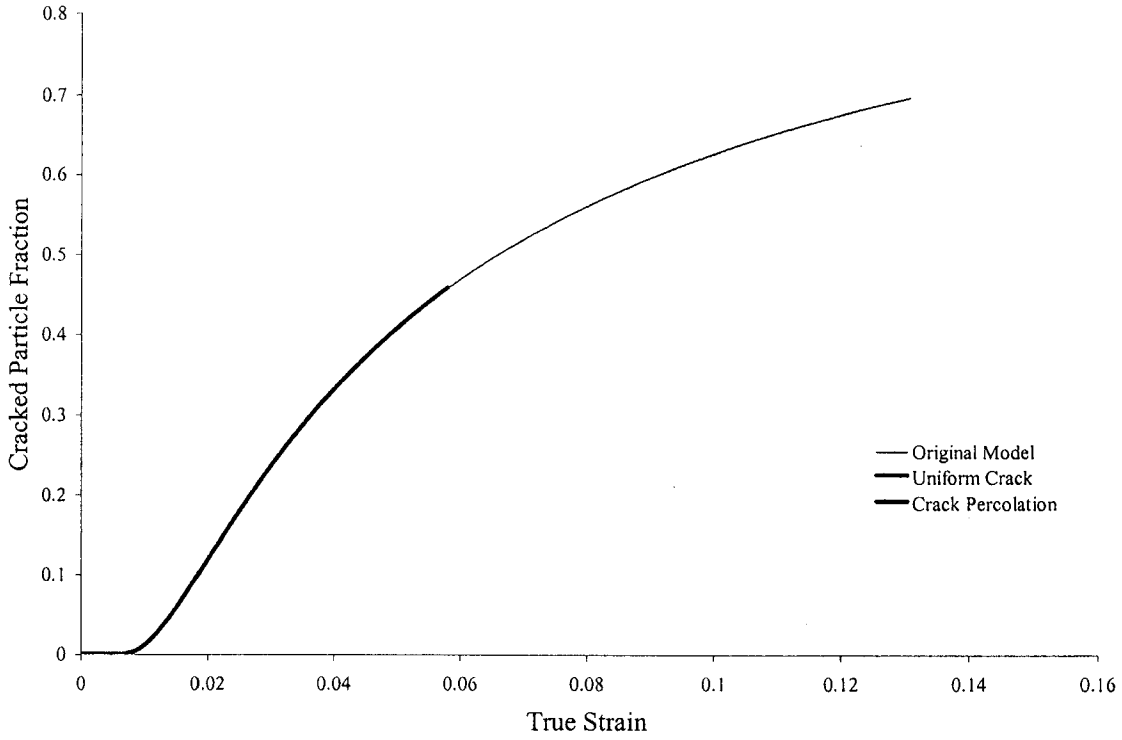

Figure 6.11 Composite damage predictions as a function of strain in an AA2618T4 and 10 vol% SiC composite.

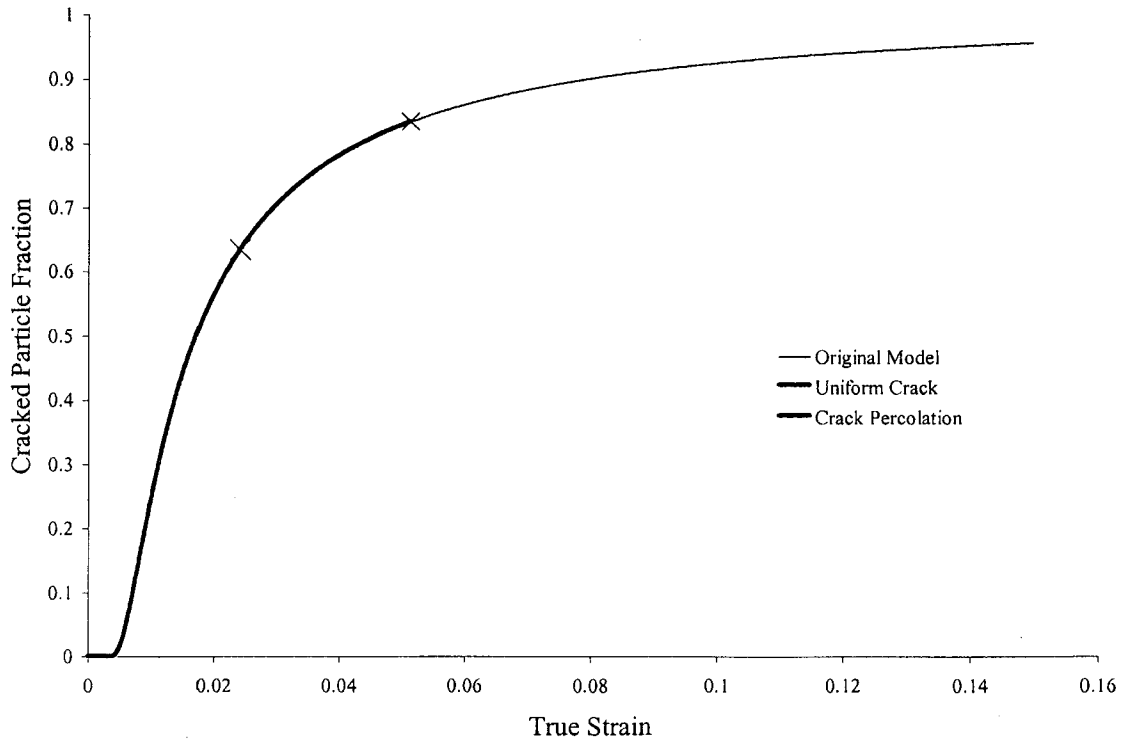

Figure 6.12 Composite damage predictions as a function of strain in an AA2618T4 and 18 vol% SiC composite.

6.4 Composites with Particles that undergo Multiple Cracking

The micro-crack linkage model described in the previous section provided results in good agreement with the experimental results of Maire et *al.* (1997). In that particular system, the description of the damage process present in the model fits well with the experimentally observed process. Damage occurred first through a process of particle cracking followed by the linkage of damage between cracked particles. While the damage process in the AA6111/Al_2O_3 system does involve particle cracking, and at some later stage damage coalescence, experimental observations reveal the presence of an additional damage process; multiple cracking of the cracked particles.

In this AA6111/Al_2O_3 system, a system with relatively large (40-50μm) Al_2O_3 particles, damage occurs through a mechanism that includes multiple cracking of the particles. The fact that the particles undergo multiple fracture with increased tensile strain suggests that while the particles unload with particle cracking, they can be reloaded up to a new level of fracture stress. Based on the flaw size sensitivity of fracture in the ceramic particles, the stress required to produce another crack in the particles must be at least as great, if not greater, than the stress required to cause the first cracking event. This has significant implications on the damage process.

Multiple cracking suggests that the stiffness loss resulting from particle cracking may be more than that suggested by Brockenbrough and Zok's (1995) FEM calculation. A description of the multi-cracking process should include the results from their FEM calculation since it does provided a good description of the effect of the loss in particle stiffness when particles fracture. However, the damage parameter derived in Brockenbrough and Zok's work resulted from FEM calculations at fairly low strains

(~1%) since it was found that strength ratio of the composite flow stress to the matrix flow stress reached an asymptote fairly early in deformation. If the particles are sufficiently strong, reloading the particles up to a new fracture point would be difficult. In this case, the damage parameter derived by Brockenbrough and Zok would be sufficient to describe the loss of stiffness resulting from particle cracking throughout the entire deformation process (excluding the final stage of micro-crack linkage). However, when the particle strengths are low, and the modulus mismatch remains high as in the composite material used in the experimental work presented in this thesis, it is clear that at some distance away from the crack interface the particles can be reloaded so that they undergo multiple fracture. It seems reasonable to expect that this additional fracturing of the particles will further reduce the stiffness of the previously fractured particles. The model that follows couples the results of Brockenbrough and Zok's FEM calculation with a process that incorporates the additional loss in stiffness resulting from multiple fracture of the reinforcing particles.

6.4.1 Model Development

The starting point for such a model would be the determination of an expression relating the average number of cracks in the particles to the tensile strain. The tomography experiments described in Chapter 5 provide this information. Using the tomography data it is possible to plot the average number of cracks in particles versus true tensile strain as shown in Figure 6.13. A linear expression can be used to approximate the average number of cracks, n, in the particles to the composite tensile strain, ε_c, through

$$n = 19.2\varepsilon_c \tag{6.15}$$

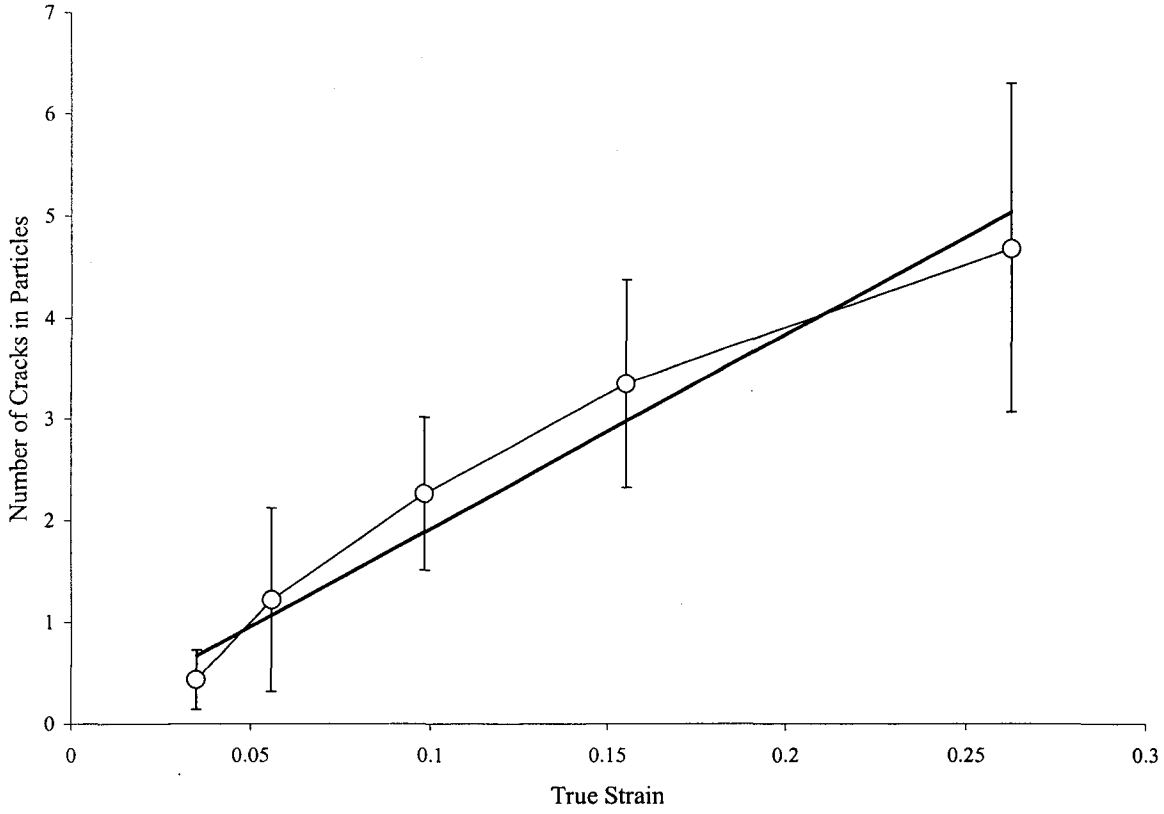

Figure 6.13. Plot of the average number of cracks in cracked particles versus composite true tensile strain shown with error bars. A linear relationship was used to describe the number of cracks in particles with tensile strain. A best fit was found by plotting a line with a slope of 19.2 passing through the origin.

Once the relationship between the average number of cracks in the cracked particles and composite strain was established, the next step was to determine the fraction of particle volume that was completely unloaded with each additional cracking event in the particles. It was assumed that the remainder of the particle volume away from a crack unload zone followed the behavior predicted by the work of Brockenbrough and Zok (1995). The thought process employed to develop the model is outlined schematically in Figure 6.14.

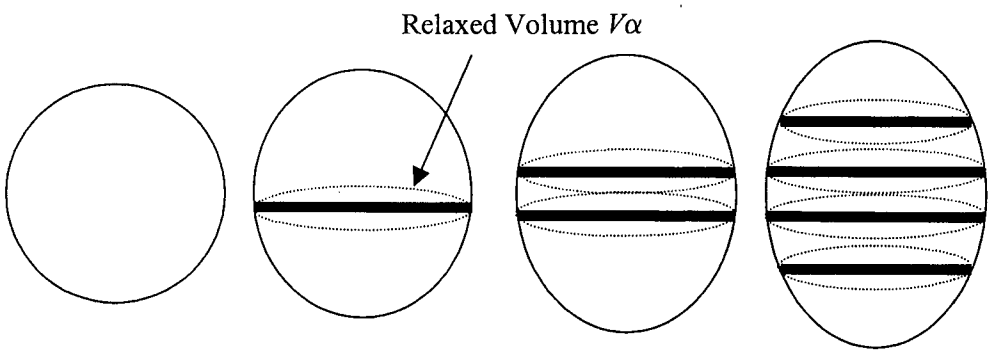

B & Z	V	$V(1-\alpha)$	$V(\frac{2}{3}-\alpha)$	$V(1-2-\frac{n-1}{n+1})$
Unloaded	0	$V\alpha$	$V(\alpha+\frac{1}{3})$	$V(\alpha+\frac{n-1}{n+1})$

Figure 6.14. Schematic illustration of thought process used to develop model of particle multiple cracking. B & Z refers to the volume of material following the damage behavior described by the FEM calculation of Brockenbrough and Zok (1995). Unloaded refers to the volume of fraction of each particle that is completely relaxed with each fracture event.

Each crack in the particle unloads an amount of material equal to $V\alpha$. In the model, this unloaded fraction of the damaged particles is assumed to have zero stiffness. The remaining material within the damaged volume follows the loading behavior described by Brockenbrough and Zok (1995). Expressions for the fraction of Unloaded material and Damaged material, defined as "B & Z" in Figure 6.14, for n cracks can be written as

$$V(\alpha+\frac{n-1}{n+1}) \rightarrow \text{Unloaded Material} \tag{6.16}$$

$$V(\frac{2}{n+1}-\alpha) \rightarrow \text{B \& Z Material} \tag{6.17}$$

where α is a parameter describing the fraction of the particle volume unloaded with each additional crack in the particle.

6.4.2 Modelling Results

The model for composites with particles that undergo multiple fracture was evaluated to determine the sensitivity to the value of the unload parameter, α and the fit to the experimental data. Modelling followed the same steps outlined in section 6.2. The matrix behaviour was assumed to follow the Ramberg-Osgood relationship for a power-law hardening solid

$$\varepsilon = \frac{\sigma}{E} + \alpha \frac{\sigma_o}{E}\left(\frac{\sigma}{\sigma_o}\right)^{1/n} \tag{6.18}$$

where σ_o is a "reference stress", α is a proportionality constant and n is the hardening exponent. These initial models used with arbitrary values for the modulus, reference stress and hardening exponent of 70 GPa, 29 MPa and 0.28 respectively. The value of α was 3/7.

Reinforcing particles were assumed to be spherical possessing a stiffness of 390 GPa. The fracture properties of the Al_2O_3 particles were assumed to follow those determined in section determined in section 5.2.2.2 and fit to the Wiebull function with a reference stress, σ_o, threshold stress, σ_u, and Wiebull modulus, m, of 357 MPa, 0 MPa and 3.8 respectively. The values used in these fracture strength parameters describe relatively weak particles with a large uncertainty in the stress at which fracture occurs (m=3.8).

Prior to running the particle multiple cracking damage model, the mechanical response of the undamaged composites had to be determined. The flow response of two Al_2O_3 volume fractions, 5% and 10%, were evaluated. Undamaged model predictions for

the composites were fit to the Ramberg-Osgood relationship. The parameter values that provided the best fit are presented in Table 6.1.

Table 6.1 Ramberg-Osgood Parameters used in modelling work presented in section 6.4

Material	E	σ_o	n	κ
Matrix	70 GPa	29 MPa	0.28	3/7
Matrix + 4% Al_2O_3	73.5 GPa	31.1 MPa	0.311	3/7
Matrix +8% Al_2O_3	82.9 GPa	32.8 MPa	0.325	3/7

The effect of the unload parameter on the predicted tensile flow curve is illustrated in Figures 6.15 and 6.16 for 5% and 10% volume fraction composites. Each increment in the amount of material unloaded, described by the α parameter, progressively reduces the magnitude of the composite flow stress once strains of approximately 5% are exceeded. Using the current function (eq. 6.13) used to relate the average number of cracks in cracked particles to the composite strain, this strain corresponds to an average value of 1 crack per cracked particle. This is the point at which the multi-stage cracking model effectively begins to influence the mechanical response of the composite.

Examination of both Figure 6.15 and 6.16 suggests that the composite flow response is slightly more sensitive to the value of the α parameter at higher volume fractions. This is illustrated more clearly in by plotting the composite work hardening

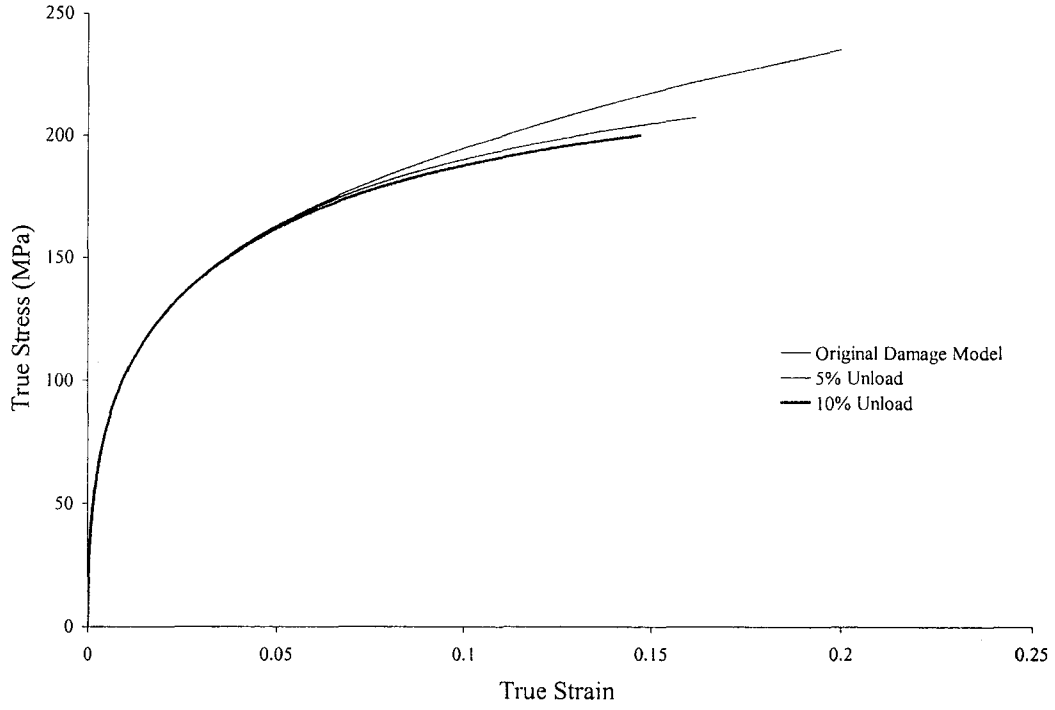

Figure 6.15. The effect of varying the degree of the α parameter (described by #% Unload on plot) on the tensile flow response for the 4% volume fraction Al_2O_3 composite studied in this thesis.

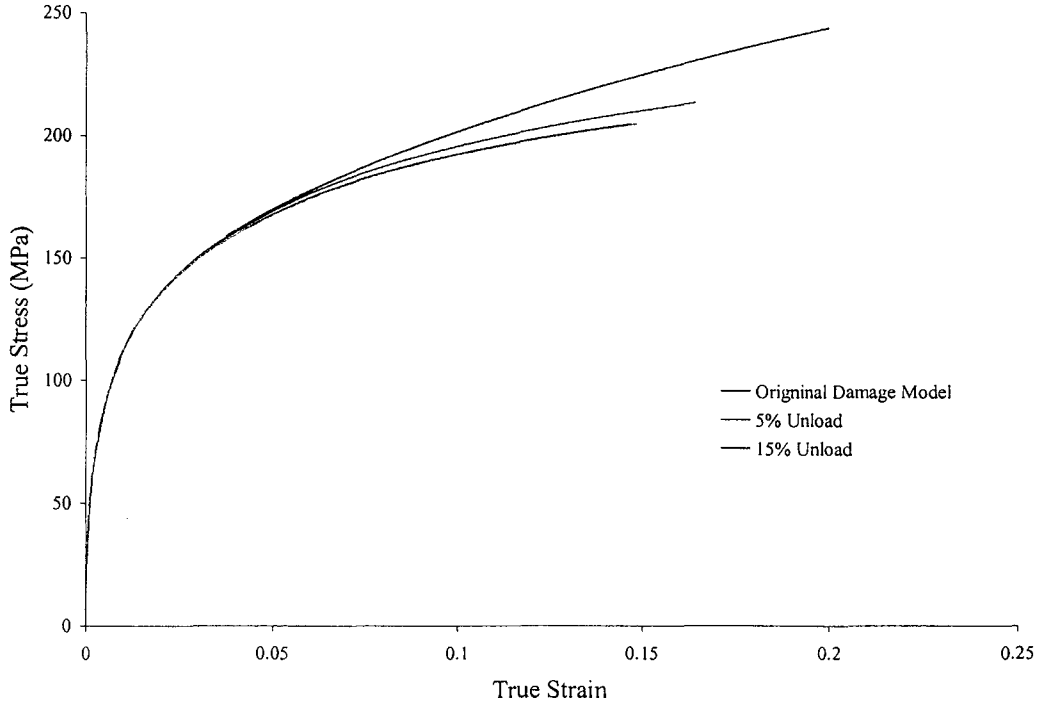

Figure 6.16. The effect of varying the degree of the α parameter (described by #% Unload on plot) on the tensile flow response for the 8% volume fraction Al_2O_3 composite studied in this thesis.

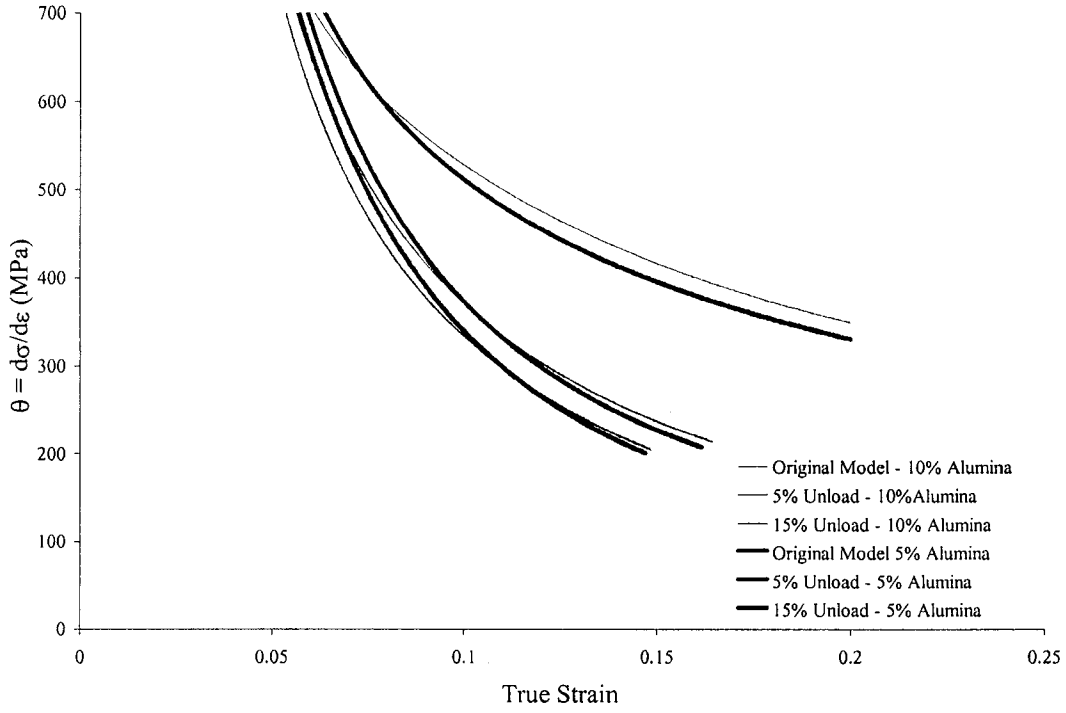

Figure 6.17. Comparison of the composite work hardening rates for composites with 4% and 8% volume fraction Al_2O_3. The effect of changing the unload parameter α (described by #% Unload) on the work hardening rate for each composite is illustrated.

The model for particle multi cracking, and its suitability to modelling the composite response observed in the composite system used in this thesis will be examined in greater detail in the discussion that follows. In particular, comparisons with the predicted flow response in terms of both the predicted flow curve and work-hardening and that experimentally observed will be discussed. Finally, the model will be combined with the micro-crack linkage model developed in 6.3.1 to provide a model describing the complete deformation behaviour from initial loading to failure defined by the Considere criterion.

6.5 Summary of General Observations

1. The overall shape of the tensile loading curves for the low ductility composite systems discussed in the first section of this thesis were well predicted by the original SCEMA-damage model employed in the earlier work of Wilkinson et al (1997). This original SCEMA-damage model however significantly over-predicted the maximum uniform elongation defined as the point of plastic instability based on the Considere criterion.
2. Incorporation of the low ductility fracture model for heterogeneous second phase distributions developed in this chapter greatly improved the prediction of the composite ductility. This model also appears to have captured the additional loss of composite work hardening rate observed at strains approaching the instability point in the experimental material.
3. Incorporating a progressive micro-crack linkage model based on sampling a heterogeneous distribution function, in this case a Poisson distribution function, provided a better prediction than the model that assumed a uniform distribution of second phase particles. This suggests that the particles that have the greatest influence on the ductility are those spaced distances less than the average particle spacing. These local regions of higher volume fraction appear to have the greatest control on the final damage process limiting the ductility.
4. A model for particle mutli-cracking has been developed to incorporate both the loss of stiffness associated with particle cracking as defined by the FEM work of Brokenbrough and Zok and an additional loss of stiffness resulting from particle

multi-cracking. The modelling results indicated that higher volume fraction composites are slightly more sensitive to the value of the unload parameter α than lower volume fraction composites.

5. Incorporating the particle multi-cracking model reduces the composite stress at a given strain and provides more significant reduction in the composite work hardening rate and over that of the original SCEMA-damage model. Increasing the value of the unloading parameter further reduced both the magnitude of composite stress at a given strain and the work hardening rate.

CHAPTER 7

DISCUSSION

7.1 Introduction

The effect of damage on the deformation behavior of a heterogeneous material is illustrated in Figure 7.1. Damage evolution can lead to a reduction of the following parameters; stiffness, work hardening rate and the strain at which instability in the deformation occurs. The degree to which these are degraded is largely controlled by both global and local properties as illustrated in Figure 7.2. These properties include the degree of stress partitioning, the fracture behavior of the particles, heterogeneity in the particle distribution and local properties that may influence the damage coalescence such as the matrix work hardening behavior and strain distribution.

X-ray tomography proved to be an effective technique in providing for a 3-dimensional investigation of both global and local effects. Global effects investigated in these new sample bulk observations included the rate at which particles fractured with increased tensile strain and the sensitivity of damage to the size and shape of particles. Important effects, studied in detail for the first time in three dimensions, included both the effect of local particle volume fraction on damage and the coalescence of damage. This information was complimented with 2-dimensional observations on fractured samples so that the evolution of damage could be followed from the point at which it initiated to the point of sample fracture.

Mechanical tests were employed to determine the influence of damage on the mechanical response, in terms of the parameters listed in Figure 7.1. Comparisons between tensile and compressive curves and load-unload testing cycles allowed for

examination of the global reduction in work hardening rate and composite stiffness resulting from damage. The presence of internal stresses, resulting from stress partitioning between the particles and the matrix, were probed through load-reversal experiments.

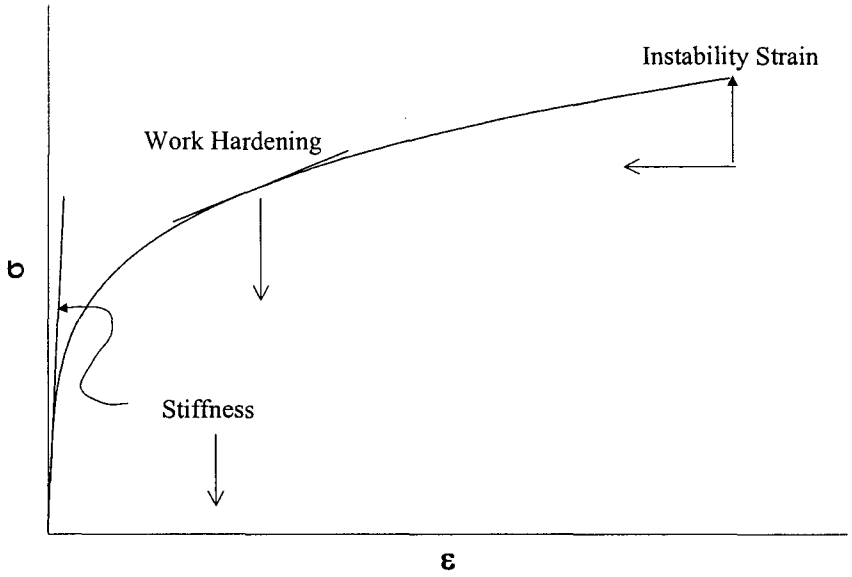

Figure 7.1. Some ways in which damage can influence the mechanical response of a heterogeneous material.

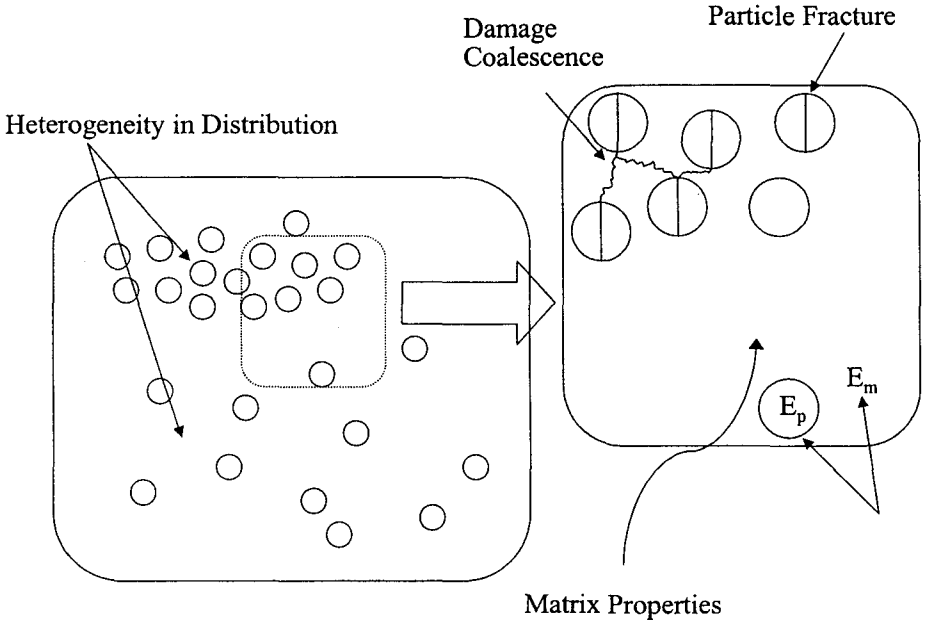

Figure 7.2. Microstructural properties that can influence the degree to which damage influences the mechanical response.

Instrumented indentation tests were used to measure the elasto-plastic properties of the local matrix. This non-destructive technique had previously only been applied to estimating the global elasto-plastic response of monolithic materials. The new application to multi-phase materials allowed for an estimate of the local matrix flow response separate from the global response of the composite. Data generated through instrumented sharp indentation was of significant importance as it, combined with the data generated through x-ray computed tomography and other mechanical tests, was used to develop new comprehensive and complete models of the damage process and the resulting composite mechanical response.

Two models were developed to describe both the experimentally observed damage process occurring within the material studied in this thesis and the well documented low ductility common to particulate reinforced composites. Both models use experimentally determined input parameters, obtained through the work performed in this thesis and published literature. As will be shown, the combination of the novel experiments conducted in this thesis with the new models developed to describe experimentally observed behaviour provide a good description of damage and the resulting effects on the deformation behavior of heterogeneous materials.

7.2 Quantification of Damage Through X-ray Tomography

The advantages of damage observation based on x-ray tomography with in-situ tensile loading were described in section 2.8. The technique is relatively new and affords the opportunity to characterize the damage mechanisms from the global scale down to the level of a single particle. These include determination of the rate of

damage evolution and the sensitivity of damage to local volume fraction, reinforcement size and shape. In this work, x-ray tomography was applied to investigate these parameters in a material that damages by particle cracking during tensile loading.

7.2.1 Damage as a Function of Tensile Deformation

The evolution of damage, measured in terms of the fraction of particles containing one crack or more, provided one method of quantifying the rate of damage accumulation in the composite. This is a general measure of damage evolution and considers the fraction of cracked particles, of those sampled in the tomography volume investigated, at a given deformation increment. These results were plotted in terms of the fraction of cracked particles versus both the predicted particle stress and strain.

The plot for the fraction of cracked particles versus particle stress can be fitted by the Wiebull function describing the probability of fracture based on a given particle stress. The parameters used to fit the Wiebull function (σ_o=357 MPa, σ_u=0 and m=3.91) suggest that the reinforcing particles were relatively weak and had a rather high variability in strength (m=3.91). While this high variability in strength indicates that a large flaw size distribution within the particles exists, it is important to note that a large variability in the stress acting on particles existed due to the heterogeneous nature of their spatial distribution. This apparent high variability in strength therefore incorporates both the variability in the particle flaw size and variability in local particle stress. It should be emphasized that three dimensional

bulk measurement of the damage evolution, defined by the fraction of cracked particles for a given value of deformation, confirms that the Wiebull function provides a good model for the damage process in composites that damage through particle fracture.

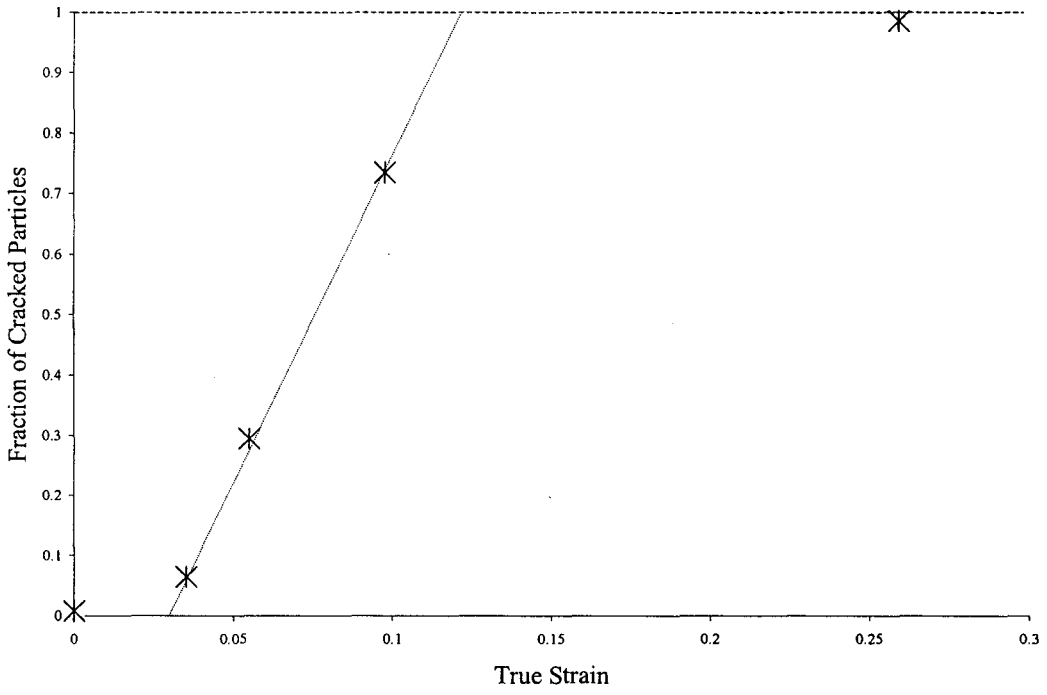

Figure 7.3 Tomography data illustrating the linear increase in damage, defined as the fraction of cracked particles, versus tensile strain.

As an alternative to plotting fraction of cracked particles versus stress, the fraction of cracked particles versus tensile strain can be plotted as shown in Figure 7.3. These results reveal that damage in the composites studied in this thesis evolves linearly and quite rapidly with tensile strain.

This is in agreement with a number of experimental measurements on several Al-matrix based composites (Llorca *et al.*(1993), Llorca and Poza (1995)) that indicate that particle fracture rate increases in an approximately linear fashion with

the applied strain, as shown in Figure 7.4. The particles investigated in these experiments were of angular shape and much smaller than the 40-50μm diameter spherically shaped particles used in the experimental work presented in this thesis. These results suggest the observed trend that damage increases linearly with tensile deformation is insensitive to both particle shape and aspect ratio. It must be emphasized that, as discussed section 7.2.4, while the observed linear trend is present regardless of particle size or shape, this does not mean that the rate at which the damage increases linearly is not size or shape dependent.

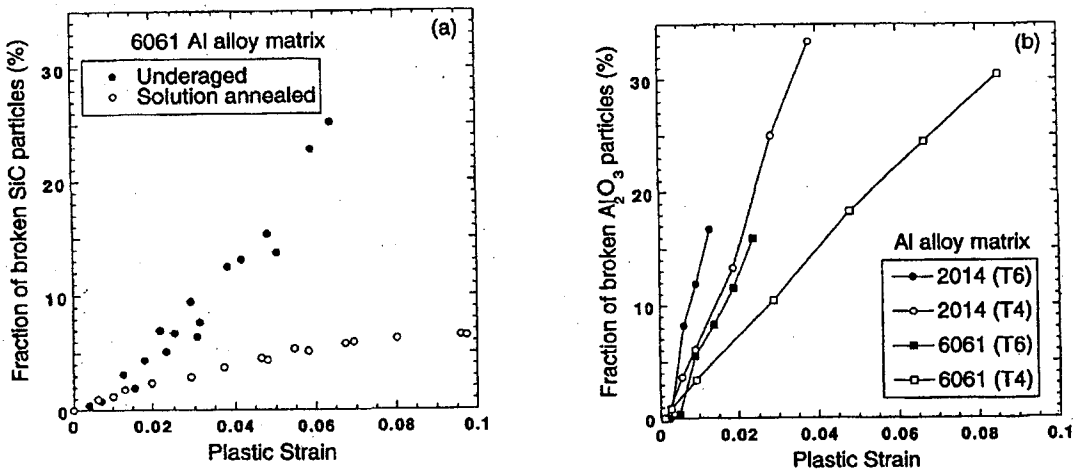

Figure 7.4 Fraction of cracked particles versus the applied plastic tensile strain. (a) 6061 alloy reinforced with 15 vol% SiC. Measurements were made with *in-situ* optical and reinforcement size was 15 μm (after Llorca *et al.*(1993) (b) 6061 and 2014 Al alloys reinforced with 15 vol% Al_2O_3. The fraction of cracked particles was estimated from the degradation of the elastic modulus during deformation. The average particle diameter was 12 μm (after Llorca and Poza (1995)).

7.2.2 Damage as a Function of Local Volume Fraction

The progressive multiple cracking of the reinforcing particles provided a means of assessing the effect of particle distribution on the damage rate. In contrast to using an approach based on the fraction of cracked particles which is sensitive over

a fairly narrow strain range, using the evolution of damage as a function of the number of multiple cracking events allowed for comparison over a much larger strain range.

The results provide a clear indication of the sensitivity of damage to the particle distribution. Particles with one or more neighbors, with a neighbor being defined as a particle located within a one particle diameter distance, started to crack at lower strains than the isolated particles. Thereafter, the rate of damage, assessed as the slope of the average number of cracks per particle, was roughly equal for both the isolated and non-isolated particles. These results reveal that while damage initiation in isolated particles requires a longer incubation period, the rate of growth is roughly equal for both the isolated and non-isolated particle populations once damage commences in each.

Comparing the non-isolated particles with different numbers of neighbors indicates that particles interacting with more than one neighbor behave in a similar manner to those with just one neighbor at any increment of strain. This reveals that the interaction of two particles spaced less than one particle diameter apart introduces a level of constraint in the matrix between the particles sufficient to accelerate the damage. It also indicates that the presence of more particles within the same one particle diameter zone of interaction, as is the case in particle clusters, does not provide a significant enhancement of the magnitude of the matrix plastic constraint. This observation is new and somewhat surprising since it was expected that a cluster of several particles was required to enhance stress partitioning so that damage would be accelerated (Llorca (1995)).

7.2.3 Coalescene

One of the most surprising results was that no linkage of damage between the multi-cracked particles occurred up to a local strain of 26% in the tomography volume observed. At this strain the deformation within the sample became non-uniform as illustrated in Figure 7.5. The fact that no linkage occurred may have resulted from the composite possessing a low average Al_2O_3 volume fraction (only 4%). As a result the stress partitioning required to cause particle fracture occurred at larger strains, possibly exhausting the work hardening of the matrix before particle damage could significantly influence the fracture process. Examination of the fracture surface for a sample manufactured from the same composite material, but pulled to fracture in uniaxial tension, indicates that while some local coalescence between particles occurred, fracture in general did not require the coalescence of damage between cracked particles.

It was clear in the tomography images presented in Chapter 5 that locally high volume fraction regions of Al_2O_3 existed within the 4% volume fraction sample investigated. While damage coalescence between fractured particles was not observed at this low volume fraction, it is clear that at higher volume fractions the linkage of damage between cracked particles did contribute to the fracture process. This suggests that a threshold volume fraction may exist for widespread damage coalescence. Below this volume fraction micro-crack linkage, if it occurs, may be the result and not the cause of global instability.

One additional point of interest is the fact that in all of the sections of fracture surfaces linkage of damage in particle rich regions only occurred in areas in close

proximity to the fracture surface. This further indicates that a few linkage events at a local scale, can rapidly result in global instability. In the case of this composite, this instability was in the form of localized shear in the matrix connecting the micro-crack linked regions leading to macroscopic failure.

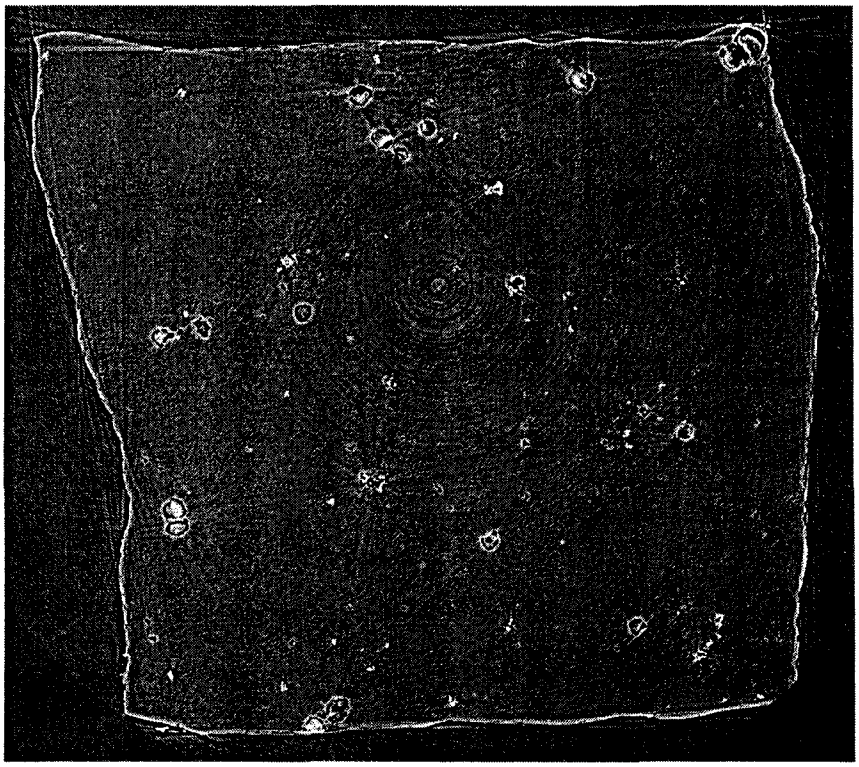

Figure 7.5 Sample cross-section of the necked sample generated through x-ray tomography at a local true strain of 26%. Prior to deformation the cross-section was almost perfectly square. Note that at this location along the gauge length the deformation is no longer uniform. No coalescence occurred between the particles, including those in groups of four or more, in this sample even after localization to this degree was visible.

7.2.4 The Effects of Particle Size and Shape

The tomography work also provided a 3 dimensional verification of the effects of both particle size and shape on damage (Brechet *et al.*(1991)). Particles of the largest size and those with a less spherical shape (or of higher aspect ratio) tended to fracture first. Based on the size sensitivity (probability of fracture $\sim 1-\exp(-d^3)$) of fracture in brittle solids, like the Al_2O_3 particles used in this work, this size sensitivity was not unexpected. Higher aspect ratio particles were also expected to fracture first based on earlier experimental observations (Brechet *et al.*,(1991)) and the theoretical prediction (Clyne and Withers (1993)) of a more inhomogeneous stress field existing in particles with aspect ratios greater than 1, the aspect ratio for a spherical particle which has a homogeneous stress field.

7.3 The Influence of Damage on the Mechanical Response

Evidence of damage accumulation occurring before final fracture has been well documented both in the tomography work described in this thesis and from the published literature (Lloyd,(1991), Maire *et al.*,(1997)). Mechanical testing results provide complimentary measures of the way in which these damage processes influence the composite flow response. In this work the influence of damage accumulation on the mechanical response was investigated through comparing differences in composite flow in tension and compression and the loss of composite stiffness with increased tensile deformation.

7.3.1 Differences in the Mechanical Resistance in Tension and Compression

Comparison of the compressive with the tensile flow curves can provide information of the effect of damage on the flow response. Compressive loading tends to suppress damage such that the rate of damage accumulation is lower than that in tension (Tao (1991), Zok (1988)). As a result, differences in the compressive and tensile loading flow curves can provide insight into how severely the flow response is influenced by damage. Caution, however, must be exercised when comparisons between the compressive and tensile flow curves are made. In particular factors such as experimental errors associated with performing compression tests and residual stresses remaining from material production process may influence the response in either compression or tension.

7.3.1.1 Experimentally Introduced Asymmetries

An effect more likely to cause asymmetries when a sample is compressed between platens is related to break down of the lubrication layer between the loading faces of the compression samples and the compression platens. The added friction between the surfaces will constrain plastic flow and give rise to an apparent increase in the work hardening rate. While no barrelling was evident, which would indicate a severe amount of plastic constraint at the surfaces, a small amount of frictional constraint would be sufficient to cause the divergence between the tensile and compressive flow curves. Additionally, in the low plastic strain regime slight sample mis-alignment has been shown to significantly effect the flow response near the elastic plastic transition (Clyne and Withers (1993))

7.3.1.2 Difference in Stress Partitioning Resulting from Processing

In metal matrix composites strain incompatibilities can arise from the thermo-elasto-plastic loading associated with the production process (for example extrusion and heat treatment). An example of this would be the thermal residual stresses resulting from the coefficient of thermal expansion mismatch between the matrix and the reinforcing particles. While this stress field can be relaxed by plastic deformation of the matrix around the particles, unrelaxed elastic stresses can influence the initial plastic deformation.

Yield asymmetries in tension and compression are well documented (Arsenault and Wu (1987)) for Al matrix based composites reinforced with SiC and Al_2O_3. This behaviour, with the flow stress higher in compression than in tension, is generally described on the continuum length scale by the mean field theory (Clyne and Withers (1993). Based on the coefficient of thermal expansion (CTE) of the Al matrix being much greater than the reinforcement ($CTE_{matrix} >> CTE_{reinforcement}$) the effect of cooling the composite from processing to room temperature results in a residual mean tensile stress in the matrix. This residual tensile stress may tend to aid flow in the tensile direction and hinder it compression.

Others (Corbin(1993), Prangnell (1994)) have reported the opposite effect at strains near the elasto-plastic transition, with the compressive flow stress being lower than that in tension. Buffiere *et al.* (1999) suggest that based on mean field modelling this can be attributed to local micro-yielding resulting from the presence of residual stresses remaining from the thermo-mechanical treatment.

While asymmetries have been experimentally observed, the flow behaviour particularly in compression is very sensitive to sample alignment and plastic constraint effects. In addition, under high deformation conditions, the stress field associated with equiaxed particulate reinforcement can be assumed to be homogeneous. At strains beyond the elastic-plastic transition it is expected that the contributions from thermal residual stresses would only result in a shift of the tensile and compressive flow curves along the stress axis and have little or no effect on the work hardening.

7.3.1.3 The Influence of Damage on Work Hardening

The Al_2O_3 composites possessing volume fractions of $<<1\%$ Al_2O_3, were used as a reference because effects resulting from difference in the coefficient of thermal expansion and the loss in work hardening resulting from particle fracture were likely negligible. As a result, comparison of the tensile and compressive flow curves would provide an indication of the strain range at which experimentally introduced asymmetries would be negligible. Both the compressive and tensile flow curves were in good agreement up to a plastic strain of roughly 5% at which point the work hardening rate in tension falls off more rapidly than in compression.

Divergence in the flow curves at this point may occur for two possible reasons. The first is the presence of a damage process involving matrix microvoid nucleation and growth during tensile deformation. This process would require that a reduction in composite stiffness accompany the loss in work hardening because of the resulting formation of porosity. Since no stiffness loss with increased tensile strain

was observed in this material, as described in the section that follows, an explanation of the divergence in the tensile and compressive flow curves based on microvoid nucleation and growth does not appear to be appropriate. The second more likely cause of the divergence of the tensile and compressive flow curves at this 5% plastic strain results mainly from the breakdown of the lubrication layer and as a consequence added plastic constraint. The discussion that follows is therefore limited to comparing differences between the composite flow curves at strains less than this 5% plastic strain. This is based on the assumption that machine introduced asymmetries would begin to become significant at roughly the same strains for all the composite samples studied.

If the compressive flow curves can be considered to provide a work hardening response representative of that in tension without damage, these results indicate that the composite flow response is quite sensitive to damage. This is particularly true in the composite with the highest volume fraction that showed the greatest divergence in the compressive and tensile flow curves in the 1%-5% plastic strain range. The work hardening rate was significantly higher in compression for the entire strain range and the tensile flow curves diverged from the compressive curves quite rapidly. The point at which divergence between the tensile and compressive flow curves occurred scaled with the volume fraction, with the 4% Al_2O_3 volume fraction curves diverging at the largest strain (of those with volume fractions of 4% or greater). The curves for the 4%-8% bimodal composite diverged at slightly smaller strains.

These results suggest the initial particle fracture process occurring in these composites does influence the composite flow response. Damage accumulation has

the largest impact in samples with the highest volume fraction and scales with the volume fraction of reinforcement. These results are in agreement with previous modelling work (Brockenbrough and Zok (1994), Wilkinson *et al.* (1999)) that predict a significant reduction in work hardening, with the effects being most severe at higher volume fractions, with second phase damage.

One limitation in the comparison between the compressive and tensile flow curves was that the comparisons were restricted to plastic strains of less than 5%. Observations of the influence of damage on the mechanical response was therefore limited to investigating the effects of only the first portion of the damage accumulation process observed in the tomography work. Multiple cracking of the particles did not occur to a large extent until strains of greater than 5% and therefore the above results only provide a quantification of the effects of damage accumulation in terms of the initial cracking of the particles within the particle population.

7.3.2 **Loss in Stiffness**

Tensile load-unload cycles provided an indication of the influence of damage on the mechanical resistance, in terms of the loss in composite stiffness, throughout the entire tensile deformation history. The samples with less than 1% Al_2O_3 experienced no measurable loss in the normalized (normalized with the modulus predicted by the effective medium approximation) stiffness with increased tensile deformation. All composites with Al_2O_3 volume fraction of 4% or higher experienced a measurable loss in stiffness with tensile deformation, with the loss in stiffness scaling with the volume fraction. The highest volume fraction composite

experienced the greatest stiffness loss, loosing approximately 20% of the original stiffness. The reduction in stiffness at the same strain for the 4% composite was approximately half of that experienced by the 8% volume fraction composite.

Stiffness loss associated with the fracture of reinforcing particles with increased deformation has been previously used to characterize damage accumulation (Lloyd (1991)). These results are in agreement with Lloyd (1991) and indicate that the loss in stiffness is directly related to the process of particle damage. This point is more evident when comparing the flatt nature of the normalized stiffness loss in the composites possessing volume fractions of $<<1\%$ Al_2O_3. In these composites the volume fraction of reinforcement is so low that particle damage would have little or no influence on stiffness loss with increased strain. The results also suggest that no measurable dilatational damage, in terms of microvoid growth, occurred in these low volume fraction composites up to the tensile strains investigated. If dilatational damage had occurred to a significant degree, the sample density, and therefore the measured modulus values would have decreased.

In the 4% volume fraction sample observed in the tomography work, many particles within the sample studied contained at least one crack by a tensile strain of 5%. At strains greater than 5% many of the particles underwent multiple fracture. It is clear that the normalized composite stiffness continues to fall at strains exceeding 5%, however, these results fail to provide a means of distinguishing the contributions of particle multiple fracture to the additional loss in stiffness. A question remaining is whether or not the stiffness loss is properly accounted for through the use of a model that treats the fractured particles as possessing a single crack (Brokenbrough

and Zok (1995)) or if particle multiple cracking appreciably influences the loss in stiffness. This topic will be revisited in the modelling portion of the discussion that follows.

7.4 Experimental Investigation of the Local Properties

The local properties of the composite material were investigated by a novel application of instrumented sharp indentation to investigate the local matrix properties and load-reversal experiments to investigate the presence of internal stresses.

7.4.1 Instrumented Indentation

The application of instrumented sharp indentation as a non-destructive means of predicting the elasto-plastic response had been previously limited to monolithic materials (Dao *et al.*(2001)). Application of the technique to measure local properties in multi-phase materials is a new and potentially powerful approach to characterize the local response of all participating phases within a heterogeneous material.

In this work, it was possible to compare the predictions generated from the instrumented sharp-indentation results with those obtained through uniaxial tensile tests on a virtually monolithic material. The predicted values of the yield stress appeared to be in good agreement with those observed in the uniaxial tensile testing results. Yield stress predictions were also reproducible with the maximum standard deviation from the mean of 5%. Based on comparisons with the experimental tensile deformation curves, predictions of the value of the work hardening exponents, n, appeared to be reasonable and repeatable at the indentation loads used to generate the

results presented in this thesis. The values of the elastic modulus predictions were significantly less than those expected for Al but were similar for each material tested.

The predicted elastic modulus values resulting from instrumented indentation on each Al matrix were approximately 15-20 GPa less than the value typically quoted for Al (70 GPa, Cambridge Engineering Selector V4. (2000)). The fact that similar values were predicted for each Al matrix suggests that the approach outlined by Dao *et al.* (2001) produces repeatable measures of the modulus and that the error is likely related to machine effects. Elastic modulus predictions are the most sensitive of all the predicted elasto-plastic values to machine effects. This is because the elastic modulus is calculated directly from the slope of the unloading curve at maximum load. The slope of this line is very sensitive to the machine stiffness effects because the displacement associated with unloading is quite small. Small errors associated in the measured values of displacement upon unloading can therefore lead to fairly significant errors in the unloading slope. In comparison, the loading portion of the curve occurs over a much larger displacement and therefore errors in the displacement measurement are much less significant when calculating the loading curvature, a parameter used to estimate both the work hardening exponent and the flow stress. Precise measurements of the elastic modulus therefore require that each instrumented sharp indentation machine be carefully calibrated to correct for machine stiffness effects.

Results generated from instrumented indentation have proven to be quite useful in providing an estimate of the composite matrix flow response. The predictions generated for the two low volume fraction composites bounded the results

generated from the uniaxial tensile tests. At low strains the microhardness predictions for both composites overestimated the hardening occurring immediately after yielding. At strains of roughly 2-5%, the predicted drop in hardening was more than that observed in the uniaxial tensile tests. However, at strains greater than 5% the overall shape of the predicted flow curves were similar to those generated from tensile testing. The predictions for the higher volume fraction composite matrixes (Al_2O_3 volume fractions of $\geq$ 4%) appeared reasonable in terms of the overall prediction to that of the actual composite flow response. As described in section 3.4, material processing constraints limited a direct comparison of the predicted composite matrix flow response to that determined through uniaxial tensile tests.

It was also clear that the estimated elasto-plastic values were sensitive to both the indentation load used and the resulting shape of the indented impression left in the material. Sensitivity to the indentation load used may result solely from the introduction of surface deformation during the metallographic preparation of samples. At low loads this small amount of surface deformation may be sufficient to influence the results because the indent may not penetrate far enough through the surface deformation layer to sample the true properties of the matrix lying below the deformed surface layer. At larger indentation loads, the indentation depth is much greater and, if the depth is sufficiently greater than that of the layer of surface deformation, contributions from the deformed surface layer will become negligible. When estimating the elasto-plastic response with small indentation loads great care should therefore be taken to ensure that no deformation is introduced on the sample surface during the metallographic preparation.

The errors associated with utilizing the load and unloading curves from indentations that left irregularly shaped indents are not surprising. The irregular shapes, particularly when one side of the indented impression is much different than the others, likely results from some form of flow restraint existing within the sample in an area local to the indentation location. In multi-phase particles, this constraint generally results from a neighboring second phase influencing the plastic flow of the elasto-plastic phase studied. In these cases, each indent should be visually inspected before using the resulting load-unloading curve to predict the phase's response. In this work, data generated from irregularly shaped indents was discarded because it likely would not have provided results representative of the individual phase studied.

The results generated through instrumented indentation within this thesis were used primarily to determine the matrix flow response for modelling purposes. It is clear, however, that the technique is not limited to this. Based on these preliminary results it is apparent that this technique offers the opportunity to precisely probe the mechanical response of individual phases within a broad array of multi-phase materials.

7.4.2 Probing the Presence of Internal Stresses Through Load Reversal

Analysis of the Bauschinger effect and its relationship to the internal stresses generated at given values of prestrain is not straightforward in continuum-scale particulate metal matrix composites (Clyne and Withers (1993), Llorca *et al.* (1990)). In ductile materials that are either precipitate or dispersion hardened, the Bauschinger effect is often rationalized in terms of the interaction between dislocations and

particles. From a continuum standpoint however, existence of the Bauschinger effect resulting from microplasticity is difficult to explain using the isotropic hardening models typically employed to describe the matrix flow response.

In this work, both transient and permanent softening was observed to a larger degree in the 5% Al_2O_3 volume fraction composite than the composite possessing less that 1% Al_2O_3. This combined with the TEM work revealing the absence of the precipitates typically found in an AA6111 alloy, suggests that the observed Bauschinger effect results from long range internal stresses generated through stress partitioning between the continuum scale reinforcing particles and the matrix, not dislocation-precipitate interactions.

Analysis of the Bauschinger effect and its relationship to the development of internal stresses is limited to the above volume fraction largely due to experimental limitations. An amount of experimental material sufficient to characterize the Bauschinger effect both at varying volume fractions and varying values of forward prestrain was not available at the time of writing. It is therefore difficult to quantify the relationship between observed Bauschinger effect to the reinforcement volume fraction. This discussion is therefore limited to suggesting that a strain path dependent effect is introduced by the presence of 5 vol% Al_2O_3.

7.5 Analytical Modelling

Two analytical damage models were developed in chapter 6. The first was developed to describe the behaviour generally observed in composites that typically fail at low values of tensile deformation (Maire et al (1997), Corbin and

Wilkinson(1993)). A second model was developed to describe the particle multiple cracking observed in the system used in this study.

7.5.1 **Low Strain Composite Fracture**

The basis of the low-strain composite fracture model was described in detail within section 6.2. In summary, this new model was developed to describe the low strain fracture behaviour observed in many particulate reinforcement composite systems, particularly when the reinforcement volume fraction is high. In these particulate reinforcement composites, the coalescence of damage between adjacent cracked particles is very rapid and failure often fails immediately after coalescence begins (Llorca (2000)).

Incorporation of the micro-crack linkage model developed in section 6.3 greatly improved upon the predicted flow response provided by the original SCEMA damage model. In particular, when comparing the predicted flow response with the experimental material used in the original study of Maire *et al.*(1997) the agreement was exceptionally good, particularly with the composite of the highest volume fraction.

This new description of the micro-crack linkage process suggests that linkage of damage results when the stress acting in the matrix between two adjacent cracked particles exceeds the work hardening capacity of the matrix. It is again emphasized that this provides a lower bound to composite ductility since it is assumed that once particles fracture the work hardening rate of the matrix material between the two cracked particles is equal to that of the unreinforced matrix.

The model also reveals the significance of the spatial distribution of particles on the damage process. Models that assumed a uniform particle distribution, utilizing the same micro-crack linkage model, provided results that failed to capture the experimentally observed sensitivity to volume fraction (Maire et al (1997)) and as a result significantly over-predicted the strain at which failure occurred for the composite with 18% volume fraction. Incorporating a distribution function to describe the spatial distribution of particles provided excellent predictions in terms of the point of composite failure in the observed in the high volume fraction composite. It also captured the additional loss in work hardening experimentally observed in composites of both 10% and 18% volume fraction at strains near failure.

7.5.2 Comparison With Published Values of Failure Strains

The micro-crack linkage model developed to deal with the experimentally observed low values of ductility provided good predictions of those observed by Maire *et al* (1997). To ensure that the model reasonably describes the behaviour of other systems, the ductility predicted by the model was compared to the published data provided by Clyne and Withers (1993). The results are presented in Figure 7.6 as a function of the volume fraction of the particulate, either angular or spherical, reinforcement. In addition to plotting the results based on the model input parameters determined by Maire *et al.* (1997), the effects of changing the matrix work hardening exponent on the predicted ductility were also investigated. The effects of changing the work hardening exponent were evaluated using the same input values described

by Maire *et al.* (1997) with the only exception being increasing or decreasing their experimentally determined matrix work hardening exponent by ±0.05.

These results are in good agreement with the experimentally observed values of failure strain, particularly at volume fractions of 20% and 30%. Based on the modeling work the linkage process appears to be sensitive to variations in the work hardening rate, with increased values of work hardening exponent delaying failure at all volume fractions and decreased values accelerating failure. The sensitivity to variation in the work hardening exponent also appears to be greatest at higher volume fractions. The results in Figure 7.6 also suggest that the experimentally observed

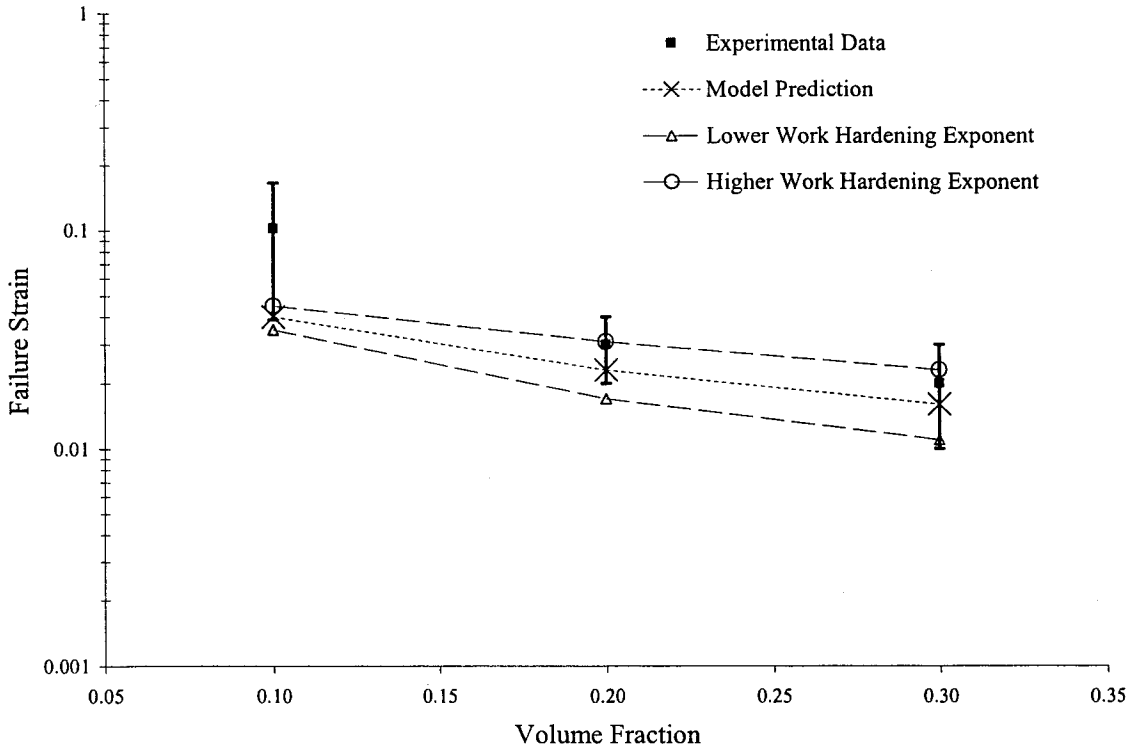

Figure 7.6 The variation in failure strain with increased volume fractions of particulate reinforcement. The average experimentally observed values (shown with error bars) was was extracted from data published by Clyne and Withers (1993). The curve labelled "Model Prediction" is based on modelling input parameters determined by Maire *et al.* (1997). Also shown is the effect of increasing or decreasing the matrix work hardening exponent, while keeping all other input parameters constant, on the predicted failure strain.

difference in the failure strains may be attributed to differences in the matrix work hardening properties between the various composite systems studied.

7.5.3 The Model for Particle Multiple Cracking

A model to describe particle multiple cracking was developed in addition to the low strain composite fracture model used to describe the experimentally observed low ductility behaviour observed in many composite systems presented throughout the published literature. The model, and its basis, is fully described in section 6.4. The model can be summarized as an extension of the Brockenbrough and Zok (1995) model describing the softening behavior associated with the existence of a single crack within a reinforcing particle. In the particle multiple cracking model, it is assumed that a small volume of material in the immediate vicinity of the crack is completely unloaded with each cracking event. The remaining material follows the behaviour described by Brockenbrough and Zok.

The modelling results have been compared to the experimental tensile testing data for each composite Al_2O_3 volume fraction. The modelling predictions are based on experimentally measured properties of both the Al matrix and Al_2O_3 reinforcement. The Al_2O_3 particles were assumed to have a modulus of 390 GPa with the fracture behaviour, as defined by the Wiebull function, following that determined from the x-ray tomography in section 5.2.2.2. These measurements provided a predicted Wiebull modulus, m, of 3.91 and a characteristic stress, σ_o of 357 MPa. The best fit of the experimental data to the Wiebull function was achieved by setting the threshold stress equal to 0.

The matrix elasto-plastic response used as input into the model for each composite was determined directly from the instrumented sharp indentation results presented in 4.6. The values for the work hardening exponent and the flow stress were used in conjunction with an estimated matrix elastic modulus of 70 GPa to predict the elasto-plastic flow curve through the method proposed by Dao (2001).

$$\sigma = \begin{cases} E\varepsilon & \text{for } \sigma_y \geq \sigma \\ \sigma_y \left(1 + \dfrac{E}{\sigma_y}\varepsilon_p\right)^n & \text{for } \sigma \geq \sigma_y \end{cases} \tag{7.1}$$

These predicted matrix flow curves where then fit to the Ramberg-Osgood power law hardening equation

$$\varepsilon = \frac{\sigma}{E} + \alpha \frac{\sigma_o}{E}\left(\frac{\sigma}{\sigma_o}\right)^{1/n} \tag{7.2}$$

for determination of the reference stress,σ_o, and work hardening exponent, n. The value of the scaling parameter, α, and elastic modulus, E, were held constant at 3/7 and 70 GPa respectively. The values of the work hardening exponent determined by fitting the flow curve predicted by the instrumented sharp indentation to the Ramberg-Osgood description of a power-law hardening solid were virtually identical to those measured by the indentation, while the values of reference stress were approximately 30 MPa. This step was necessary because the SCEMA model employed the tangent modulus construction based on the Ramberg-Osgood description of a power-law hardening solid. This power law description is useful because it allows for a better description of the entire elasto-plastic response through

the incorporation of both the elastic, $\frac{\sigma}{E}$, and plastic, $\alpha\frac{\sigma_o}{E}\left(\frac{\sigma}{\sigma_o}\right)^{1/n}$, contributions in the description.

Since the matrix flow properties are used directly in all modelling work, the accuracy of the predicted composite response is sensitive to how closely the instrumented micro-hardness measurements match the flow response of the matrix. The modelling results used in the comparisons that follow should therefore be treated as estimates used to predict the general trends observed in the experimental composite material.

The modelling results, presented in Figures 7.7 and 7.8, predict a slightly stronger response than experimentally observed for both the 4% and 8% volume fraction. This is not entirely unexpected since the flow properties of the matrix are likely slightly overestimated, particularly at low strains, by the instrumented micro-hardness measurements (see section 7.5). Comparison of the predicted and experimental work hardening rates in Figures 7.9 and 7.10 provides a better picture of the role of particle multi-cracking and the significance of the unload parameter α on the composite loading response. At low strains all the models under-predict the drop in the work hardening rate. At higher plastic strains, however, the work hardening rate predictions of the multiple cracking models are closer to the experimental data then those of the original damage model. Qualitatively, higher values of the unload parameter appear to provide better predictions of the composite work hardening rates at high tensile strains. Accounting for the additional loss in work hardening

associated with particle multiple cracking however still fails to capture the point at which failure, as defined by Considère, occurs in the experimental material.

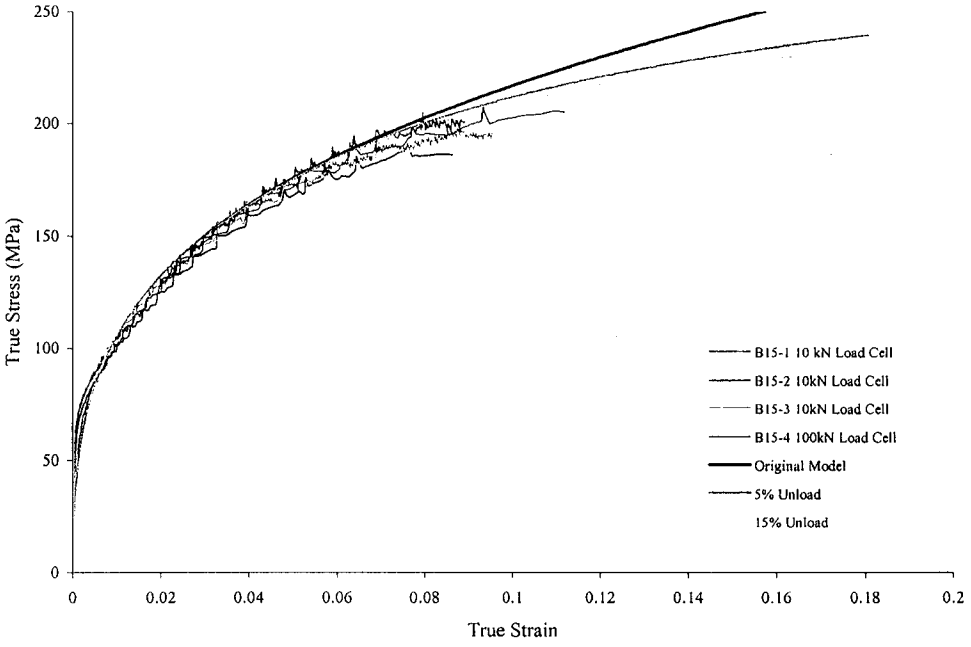

Figure 7.7. Comparison of experimental and predicted flow curves for the composite containing 4% volume fraction Al_2O_3.

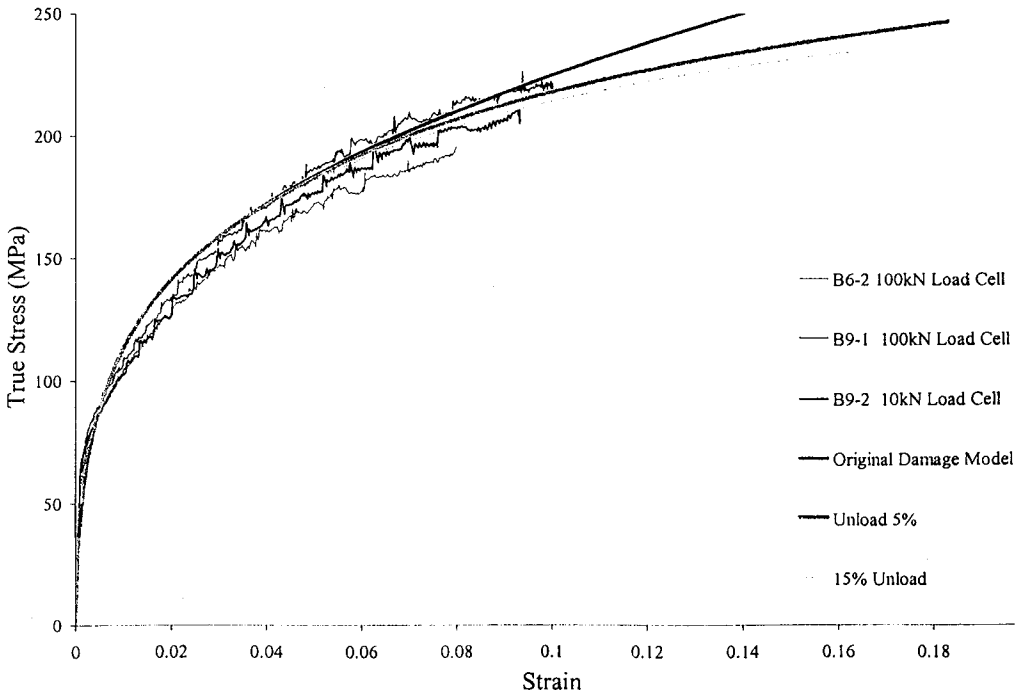

Figure 7.8. Comparison of experimental and predicted flow curves for the composite containing 8% volume fraction Al_2O_3.

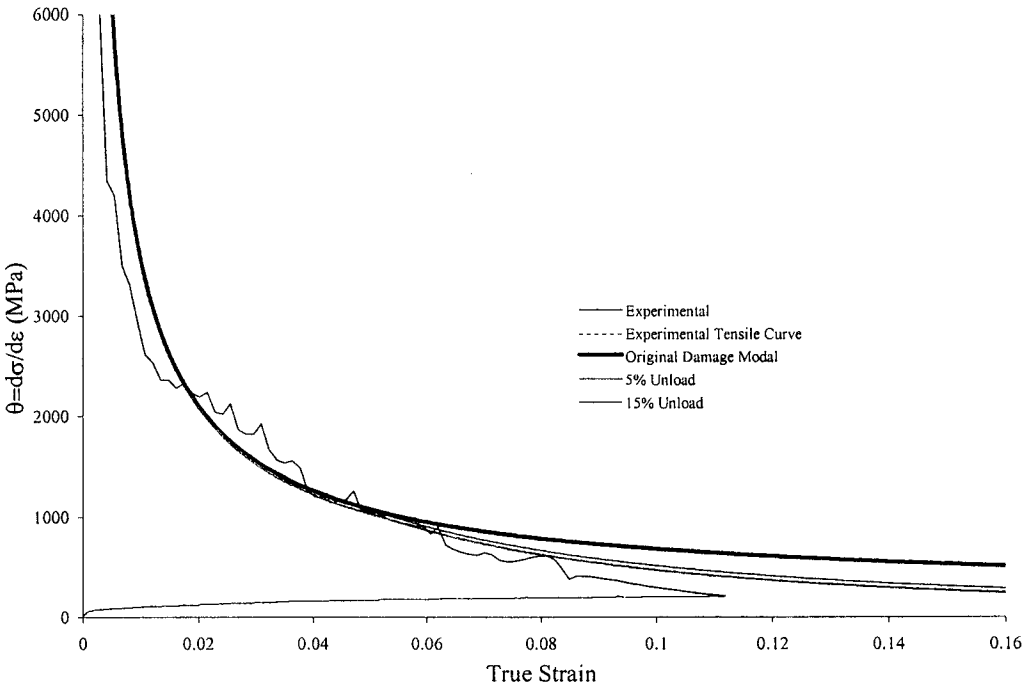

Figure 7.9. Comparison of the experimental and predicted work hardening rates ($\theta = d\sigma/d\varepsilon$) for the 4% volume fraction Al_2O_3 composite.

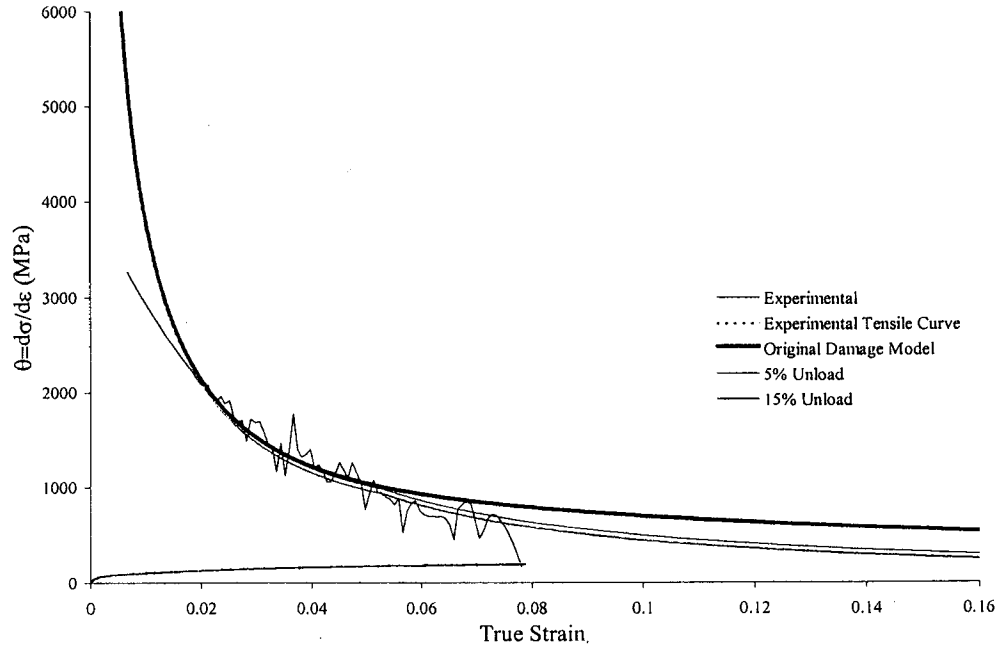

Figure 7.10. Comparison of the experimental and predicted work hardening rates ($\theta = d\sigma/d\varepsilon$) for the 8% volume fraction Al_2O_3 composite

7.5.4 A Final Model for the Experimentally Observed Behavior

The particle multiple cracking model appeared to provided a better prediction of the experimentally observed deformation behavior than the original SCEMA damage model. While accounting for the softening resulting from the multiple cracking of the particles did improve upon the predictions provided by the original SCEMA damage model, like the SCEMA damage model, the ductility was significantly overestimated. This suggests that the softening, or loss in work hardening, resulting from the particles undergoing multiple fracture alone is not sufficient to cause the localization resulting in failure.

To improve the prediction of composite ductility, the model for composites that with particles that undergo multiple fracture (described in the previous section and section 6.4) was combined with the micro-crack linkage model for low ductility fracture model (see section 6.3.2). The same input parameters described in the previous section were employed with the only difference between the particle multiple cracking model and this combined model being the incorporation of a description for the localization process leading to failure. As will be shown, this combined model provides a better prediction of the composite ductility and the experimentally observed loss in stiffness with tensile deformation.

The models predict failure at strains much less than those at which the particle multiple cracking model alone. At these strains the softening attributed to the particle multiple cracking is small and differences in the predicted flow response for varying values of the unload parameter, α, are negligible. In Figure 7.11 and 7.12, it is clear that the predictions of the point at which failure occurs as defined by Considère are

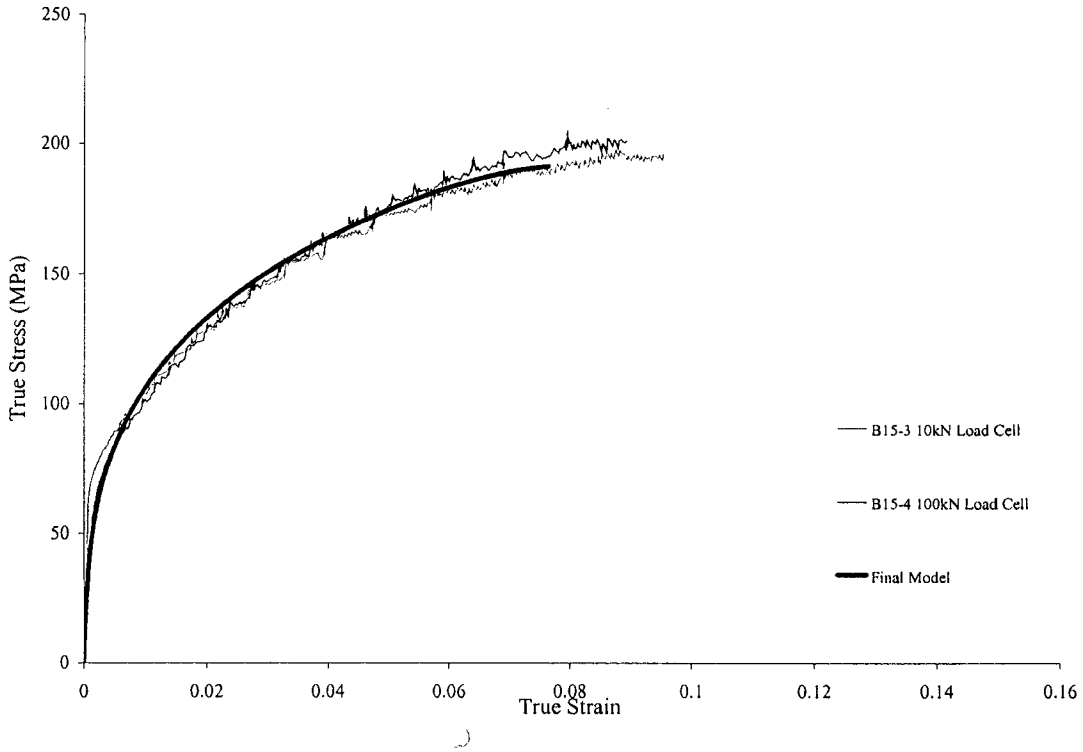

Figure 7.11 Comparison of experimental and predicted flow curves resulting from the combined particle multiple cracking and micro-crack linkage models for the composite containing 4% volume fraction Al_2O_3.

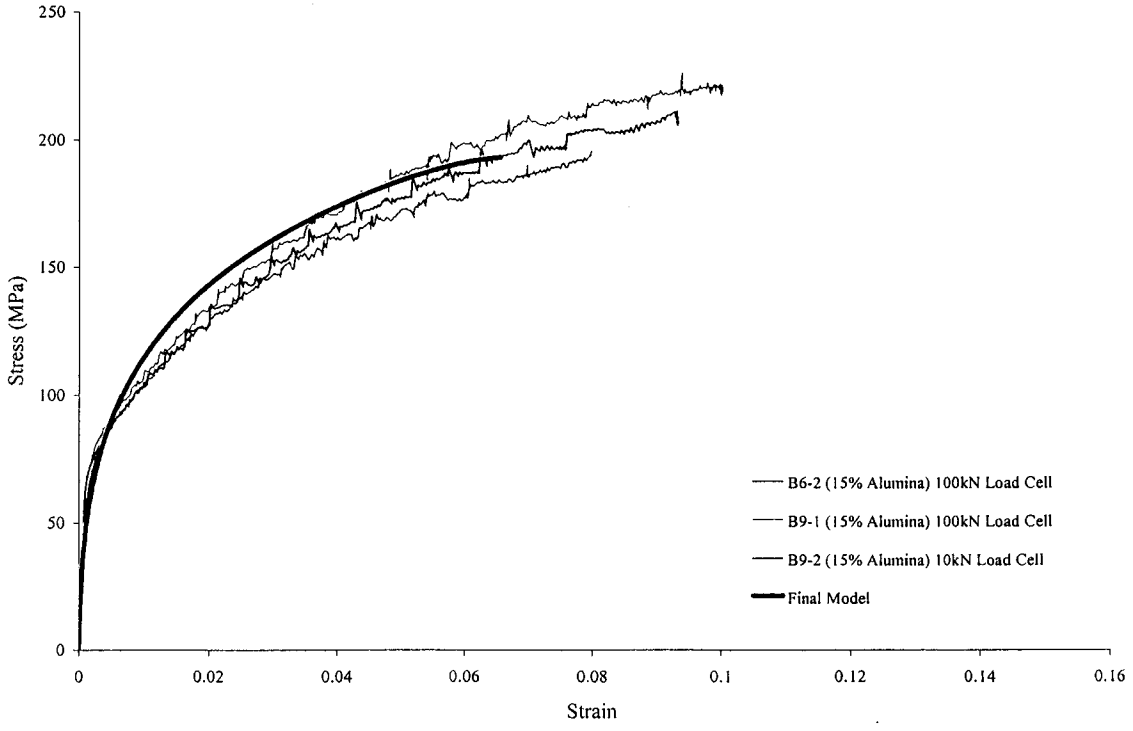

Figure 7.12 Comparison of experimental and predicted flow curves resulting from the combined particle multiple cracking and micro-crack linkage models for the composite containing 4% volume fraction Al_2O_3.

The predicted work hardening response of the particle multiple cracking model improved with the incorporation of the multi-crack linkage model as shown for the 4% and 8% composites in Figures 7.13 and 7.14. This was especially true when the experimental scatter in the flow response is considered as was done for the 4% volume fraction as shown in Figure 7.13. These results suggest that while particle multiple cracking may reduce the composite work hardening at high plastic strains, the softening associated with particle multiple cracking, at the strain levels the experimental materials failed, is not sufficient to cause the observed reduction in work hardening in the experimental material.

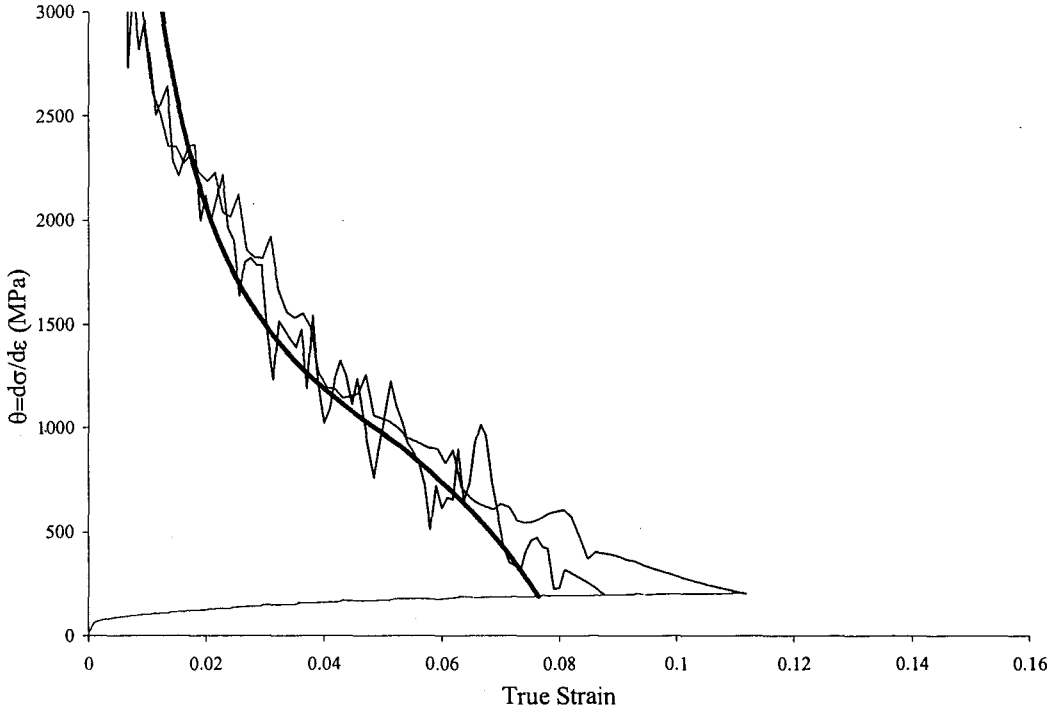

Figure 7.13. Combined model prediction of the 4% Al_2O_3 composite work hardening rate (thick line) compared with two experimentally measured work hardening rates on the 4% composites (thin jagged lines). The experimentally measured tensile loading curve for one of the 4% volume fraction samples is included (thin line on the bottom of the plot)

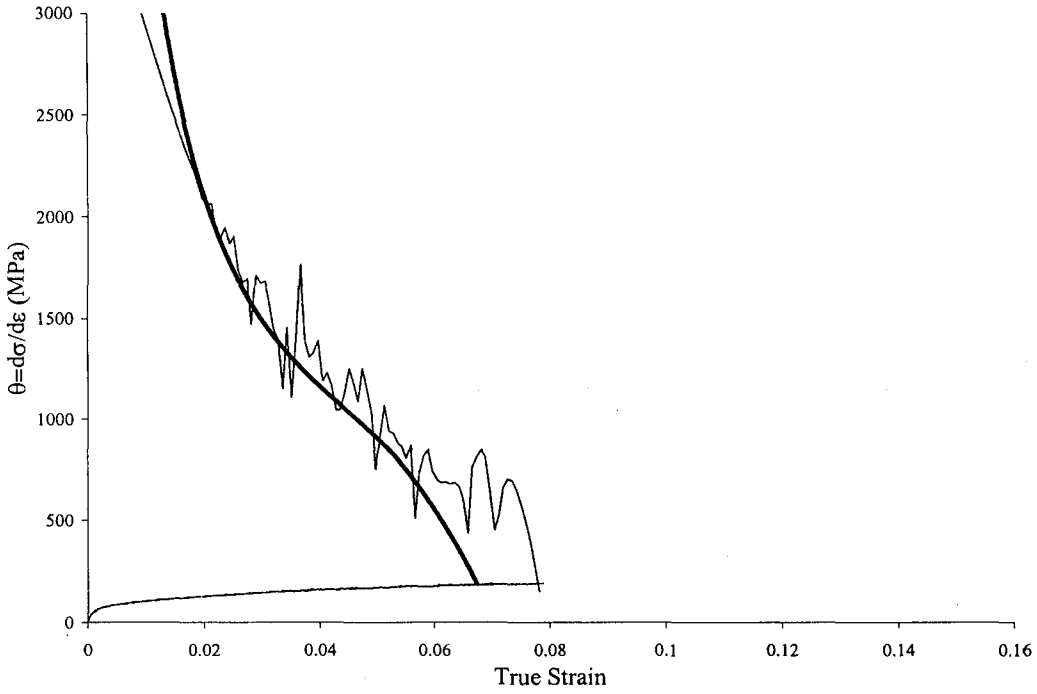

Figure 7.14. Combined model prediction of the 8% Al_2O_3 composite work hardening rate (thick line) compared with the experimentally measured work hardening rate on a 8% composites sample (thin jagged line). The experimentally measured tensile loading curve for one of the 8% volume fraction samples is included (thin line on the bottom of the plot)

The loss in stiffness predicted by the combined particle multiple cracking and multi-crack linkage model was in reasonably good agreement with experimentally measured values as shown in Figures 7.15 and 7.16. The model predicted a loss in stiffness more representative of that observed experimentally than that provided by the original SCEMA-Damage model. It is important to once again emphasize that experimental measurement of the stiffness is difficult through mechanical tests, particularly on particulate metal matrix composites are prone to error, as discussed in section 4.4, so the experimental data points are more representative of trends than precise values.

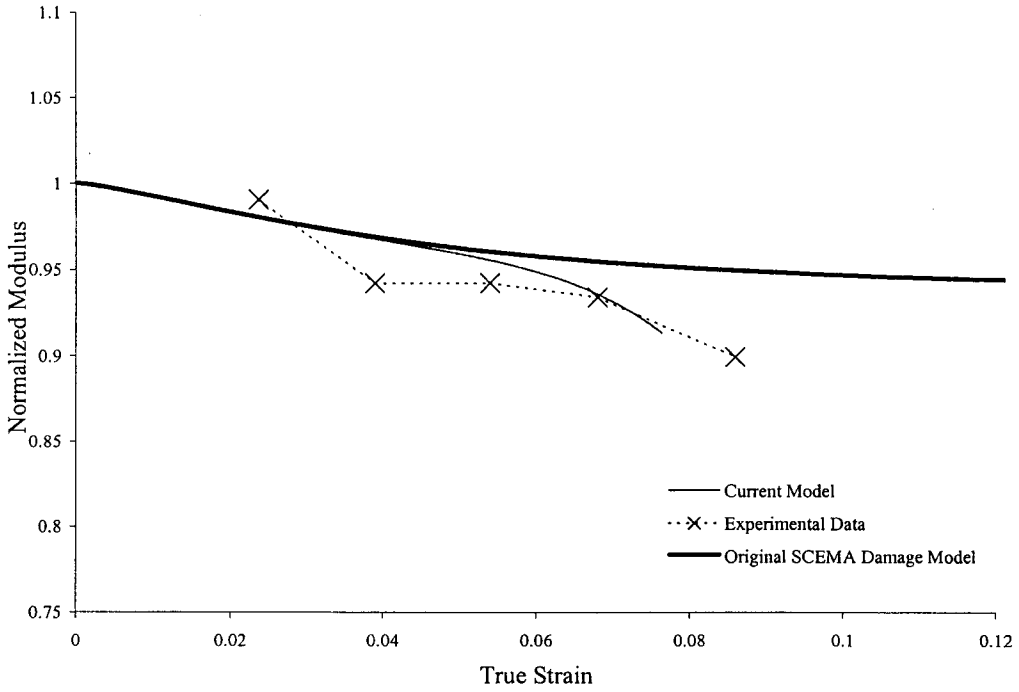

Figure 7.15. Modelling comparisons of the reduction in composite stiffness with the trends observed in experimental measurements for a composite with 4% volume fraction of Al_2O_3 particles. Note that the current model, which combines both particle multiple cracking and multi-crack linkage provides a much better representation of the observed trends than the original SCEMA damage model.

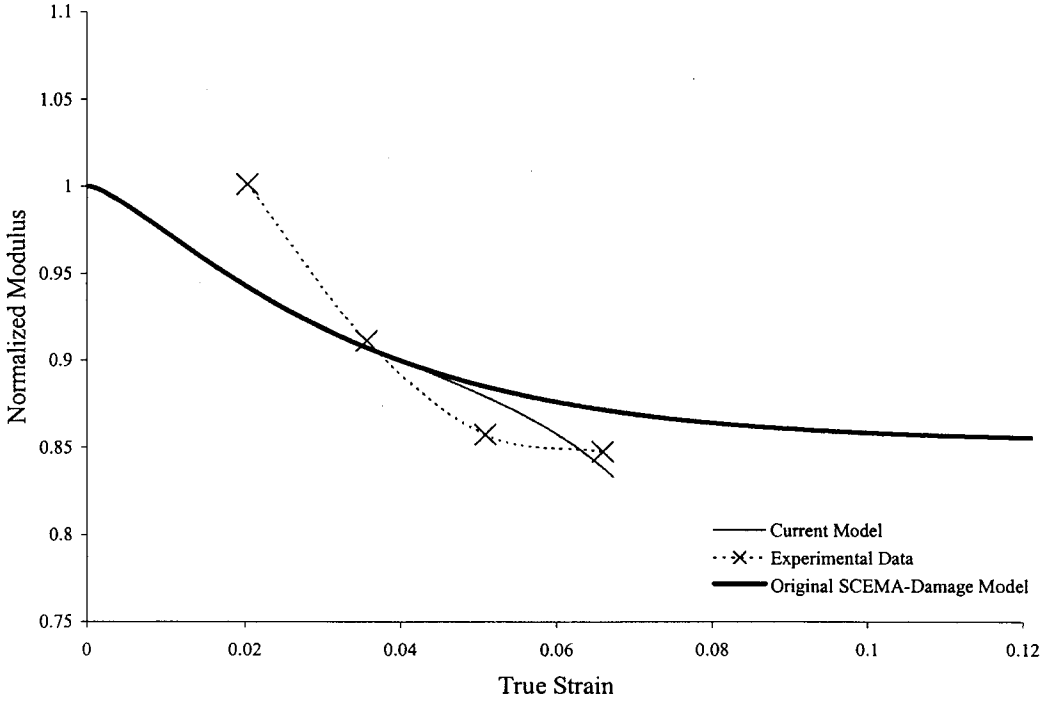

Figure 7.16. Modelling comparisons of the reduction in composite stiffness with the trends observed in experimental measurements for a composite with 8% volume fraction of Al_2O_3 particles. Note that as in the case of the 4% composite the predictions from the current model are better than those of the original SCEMA damage model

7.5.5 Summary of Modelling Work

The results generated through the modelling work suggest that the damage localization process plays a significant role in the deformation behaviour in particulate metal matrix composites. The micro-crack linkage that occurs at the local scale between adjacent cracked particles, rapidly propagates through the region of high volume fraction and as a result leads to a rapid decrease in the work hardening of the composite. This causes the work hardening rate to fall below that of the composite stress at strains much lower than those predicted by considering the reduction in work hardening resulting from particle fracture alone. Incorporation of this new model describing the linkage of damage though the inter-particle matrix improved the SCEMA-damage modelling predictions for both composites studied. The agreement with the experimental data was particularly good for the 18% SiC volume fraction composite described by Maire *et al.*(1997).

While the modelling work does suggest that at large strains the multiple fracture of the particles does significantly influence the composite response, damage localization effectively over-powers these contributions. Based on the modelling results, it is expected that once damage evolution, measured in terms of the fraction of cracked particles, becomes significant the linkage of damage through the matrix between adjacent cracked particles will dominate other factors influencing the composite response.

7.6 Extensions for Future Work

The tomographic work presented in this thesis yielded new information on the evolution of damage within a composite undergoing tensile deformation. One important observation lacking, however, is the damage coalescence process occurring prior to fracture. The experimental tomography work carried out in this thesis may have failed to capture the final linkage process for two main reasons.

- The composites studied did not possess a sufficient volume fraction of particles for the localization process to occur.
- The samples were not strained to a level sufficient to cause the localization of damage. Future work, currently being carried out in collaboration with Eric Maire (INSA de Lyon, Lyon, FR) will involve deformation of a sample to larger strains with a sample of higher volume fraction containing a notch. These large strains and high triaxality introduced by the presence of a notch should ensure that localization of damage occurs between the cracked particles.

One difficulty encountered in the tomography work carried out in this thesis was the thresholding of the tomographic images so that the particles and matrix could be separately analyzed. This resulted from rather small differences in the x-ray attenuation coefficient between the Al_2O_3 and Al and the presence of the interfacial reaction layer on some of the particles. Future tomography work should utilize a processing route that prevents the formation of this reaction layer and/or use particles of similar stiffness and strength but possessing attenuation coefficients of a greater difference than the matrix. This is particularly true when quantitative image analysis is part of the experimental objective.

Quantitative image analysis of the spatial 3-dimension particle distribution in the tomographic volume would allow for a 3-dimensional extension of the tessallation techniques currently used to characterize the second phase distribution in two dimensions. The techniques are currently under development and require experimental three-dimensional validation. Calculations on the 3-dimensional tomography volume could also be used to validate, or define, a function defining the three-dimension distribution of the particles within a microstructure. These descriptions are currently limited to 2-dimensions.

The strain-path dependence of the flow response in continuum scale heterogeneous materials has been limited to observations on the Bauschinger effect (Corbin (1992)). No investigation on the effect of changing the strain path to another loading axis has yet been performed. Strain path change experiments- for example tension, followed by compression on a perpendicular axis- may provide valuable information on the strain path sensitivity of particulate metal matrix composites. In addition if deformations are carried out to sufficient levels of strain, the effects of damage on strain path sensitivity to be further characterized.

The instrumented sharp-indentation test results provided reasonably good descriptions of the flow response. They did however significantly underestimate the material stiffness. Precise measurements on individual phases within a multi-phase material would therefore require that each indentation machine be properly calibrated to account for machine stiffness effects. One approach to doing this is to indent high purity samples of different material with known modulus, and then correlate the errors to the experimental stiffness. Through this approach it should be possible to

account for machine stiffness effects and therefore develop an expression to correct the measurements made on different materials.

One final topic of interest is the sensitivity of damage localization to the matrix work hardening rate. The micro-crack linkage model describing the damage localization process suggests that this process is sensitive to the matrix work hardening. Manufacturing a composite material, with matrix flow properties that could be modified through heat treatment, and combining this with tomography work with a sample at two matrix strength levels may yield a confirmation of this hypothesized matrix work hardening sensitivity.

CHAPTER 8

CONCLUSIONS

The primary focus of this study was to investigate damage processes occurring within a continuum scale heterogeneous material and relate these to the deformation behavior of the material. This was accomplished by employing x-ray tomography so that damage could be observed within the bulk of the material as it evolved with tensile deformation. This along with information extracted at both the local and global scale through the other experimental work contained within this thesis was used to develop models that predict the flow response of heterogeneous materials. From this work a number of conclusions can be made.

Both the work hardening rate and the stiffness of a heterogeneous material are decreased as damage evolves. This can be clearly seen from a comparison of the work hardening rates of the composites in tension and compression. Compressive loading curves (which tends to suppress damage) exhibited higher work hardening rates than comparative tensile curves at plastic strains of 3% or less. The differences in work hardening scaled with volume fraction, with the compressive and tensile flow behavior diverging earlier in the deformation for the samples of higher volume fraction. The loss in stiffness with increased tensile deformation also scaled with volume fraction, with the highest volume fraction samples having the greatest loss in stiffness. In all composites studied, the stiffness of the composites fell below that estimated for the aluminum matrix at the final deformation strains studied.

The elasto-plastic properties of the matrix were reasonably well estimated through results generated through instrumented indentation tests. The effective

modulus was roughly 20 GPa lower than would be expected for the aluminum matrix. This results from the fact that the effective modulus includes both the machine and sample stiffness effects. The estimates of the yield strength and work-hardening exponent, however, are reasonably accurate. When the machine stiffness effects are corrected for, the technique shows promise as a useful approach for probing the mechanical response of small volumes of individual phases.

The tomography work revealed that damage evolves approximately linearly with strain within the bulk when measured in terms of the fraction of cracked particles or the number of cracks within the multiply cracked particles. Both the largest particles and those with the highest aspect ratio fractured earliest in the deformation. The results also show that damage development within the bulk during tensile deformation is well described by the Weibull function.

The effect of having one or more neighbors within a one-particle diameter interaction region is limited to reducing the level of tensile deformation required to initiate damage. Isolated particles require more global deformation for damage to initiate than the non-isolated particles, but once they begin to damage, damage evolves at roughly the same rate. More importantly the results show that the damage in non-isolated particles is influenced primarily by the ratio of particle spacing to particle diameter and not the number of particles contained within the cluster.

Models developed to describe the deformation of continuum scale heterogeneous materials provide predictions in good agreement with the experimental results. Incorporation of the model describing the micro-crack linkage process that leads to global instability provided results in excellent agreement with the

experimental results of a AA2618 alloy reinforced with 18% volume fraction SiC. This model when combined with the SCEMA-damage model provides predictions of ductility as a function of volume fraction which are in good agreement with the values published in literature. The predicted ductility was sensitive to variation of the matrix work hardening exponent. Increasing the matrix work hardening exponent increases the ductility while lowering the work hardening exponent lowers the ductility. Modelling these variations in work hardening exponent, particularly at volume fraction of 20% or more captured the variation of the values of ductility reported in the literature.

The model for particle multiple cracking process observed in the experimental work within this study indicates that the process leads to a reduction in the work hardening rate over that predicted based on particles undergoing only a single cracking event. This reduction in work hardening, however, was not significant at the values of strains the experimental material used in this work failed at. Combining this model with the micro-crack linkage model yielded predictions of the experimentally observed behavior in much better agreement than the model accounting for particle multiple cracking alone. Once damage, measured in terms of the fraction of cracked particles, becomes significant the linkage of damage through the matrix between adjacent cracked particles will dominate other processes influencing the mechanical response of the composite.

REFERENCES

Ashby, M.F., Blunt, F.J and Bannister, M. (1989), Acta Metall. 37, 1847-1857

Argon, A. S., Im, J. and Safoglu, R. (1975), *Metall. Trans.* A., 6A, 825.

Arsenault, R.J. and Wu, S.B., (1987), *Mater Sci Eng.* 96, 77.

Auriault, J.L., (1991), *Int. J. Engng. Sci.*, 29, 785-795.

Babout, L., Maire, E. Buffiere, J.Y. and Fougeres, R. (2001), *Acta. Mater.* 49, 2055-2063.

Banister, M. and Ashby, M.F. (1991), *Acta. Metall. Mater.*, 39, 2575-2582

Bao, G., (1992), *Acta. Metall. Mater.,* 40, 2547-2555.

Brechet, Y., Embury, J.D., Tao, S. and Lou, L., (1991), *Acta. Metall. Mater.,* 39, 1781-1784

Brown, L.M. and Embury, J.D., (1973), *Proc ICSMA III*, 164-168

Brown, L.M. and Stobbs, (1976), *Phil. Mag.,* 34, 351-372.

Brockenbrough, J.R. and Zok, F.W., (1995), *Acta. Metall. Mater.*, 43, 11-20.

Budianski, B., (1959), *J.Appl. Mech.*, 27, 261.

Buffiere, J-Y., Maire, E., Cloetens, P., Lormand, G., Fougers., R., (1999), *Acta. Metall.,* 47, 1613-1625.

Dudek, H.J., Kleino, A. and Borath, R., (1993), *Mater. Sci & Eng.*, A167, 129-137.

Koken, E., Chandrasekaran, N, Embury, J.D., Burger, G, (1988), *Mater Sci and Eng A.,* V A104, 163-168.

Christmensen, R. and Lo, K.H., (1979), *J.Mech. Phys. Solids*, 27, 315.

Christmensen, R., (1990), *J. Mech. Phys. Solids*, 38, 379.

Christmensen, T., Needleman, A., Suresh, S., (1989), *Acta. Metall.*, 37, 3024.

Chu, C.C. and Needleman, A., (1980), *J. Engng. Mater. Tech.*, 102, 249.

Clyne, T.W. and Withers, P.J., (1993), An Introduction to Metal Matrix Composites, Cambridge Press, 45-56.

Conlon, K.T., (1998), Ph.D. Thesis disertation, McMaster University.

Corbin, S.F. and Wilkinson, D.S., (1994), *Acta. Metall. Mater.*, 42, 1311.

Dao, M., Chollacoop, N., Van Vliet, K.J., Venkatesh, T.A., Suresh, S., (2001), *Acta Mater*, 49, 3899-3918

Dong, M. and Schmauder, S., (1996), *Acta. Mater.*, 44, 2465-2478.

Dong, M., LeBle, P., Weber, U. and Schmauder, S., (1999), *Materials Science Forum*, 308-311, 1000-1005.

Embury, J.D. , (1985) *Metallurgical Transactions* A, 16A, 2191-2200.

Eshelby, J.D., (1957), *Proc. Roy. Soc. London*, (A), 376.

Felkamp, L.A., Davis, L.C., Kress, J.W., (1984), *J. Opt. Soc. Am.*, 1 No 6., 612-619.

Fleck, N.A., Mueller, G.M., Ashby, M.F., Hutchinson, J.W., (1993), *Acta. Metall. Mater.*, 42, 475-487.

Fougères, R., Maire, E., Lormand, G. and Vincent, A., (1996), IUTAM Symposium on micromechanics of plasticity and damage of multiphase materials. A. Pineau et A. Zaoui (eds.) Kluwer academic publishers, 59-66.

Goods, S.H. and Brown, L.M., (1979), *Acta Metall. Mater.*, 27, 1-15.

Guillemer-Neel, C., Feauges, X. and Clavel, M., (2000), *Metall. Mat. Trans. A,* Vol 31, No. 12, 3075-3085.

Hashim, S. and Strickman, S., (1963), *J. Mech. Phys. Solids*, 11, 127-140.

Hershey, A.V., (1954), *J.Appl. Mech.*, 21, 236-241.

Hill, R., (1965), *J.Mech. Phys. Solids*, 13, 213.

Hirano, T., Usami, K., Tanaka, Y. and Masuda, C. (1995), *J. Mater.Res.*, Vol 10, No 2, 381-386.

Hutchinson, J.W., (1970), *Proc. Roy. Soc. London*, 319 (A), 247.

Hutchinson, J.W., (1998), Harvard University Press, MECH. 342.

Kelly, A. and Nicholson, R.B., (1971), Strengthening Methods in Crystals, Ch. 1, 2, 3, and 8.

Kiser, M.T., Zok, F.W. and Wilkinson, D.S., (1996), *Acta. Mater.*, **44**, 3465-3476.

Kinney, J.H., Stock, S.R., Nichols, M.C., Bonse, U., Breunig, T.M., Saroyan, R.A., Nusshardt, R., Johnson, Q.C., Busch, F., Antolovich, S.D., (1990), *J.Mater. Res.*, **Vol. 5**, No. 5., 1123-1129.

Lépinoux, J. and Estrin, Y., (2000), *Acta Mater.*, **48**, 4337-4347.

Lipkin, D.M., Clarke, D.R. and Beltz, G.E., (1996), *Acta Mater.*, **44**, 4051-4058.

Llorca, J., Martin A., Ruiz, J. and Elices, M., (1993), *Metall. Trans*, **24A**, 1575-1588.

Llorca, J. and Poza, P. (1995), *Acta Metall. Mater.*, **43**, 3959-3969.

Llorca, J., (1995), *Acta Metall. Mater.*, **43**, 181-182.

Llorca, J., (2000), "Void Formation in Metal Matrix Composites" in Comprehensive Composite Materials, Ed. T.W. Clyne pp 91-115.

Llorca, J. and Gonzalez, C., (1998), *J. Mech. Phys. Solids*, **46**, 1-28.

Lloyd, D.J. (1991), *Acta Metall. Mater.*, 39, 57-91.

Lloyd, D.J., Jin, I and Weatherly, G.C., (1994), *Scripta Metall et Ma*ter. 31, 393-396.

Maire, E., Wilkinson, D.S., Embury, J.D. and Fourges, R., (1997), *Acta Mater.*, **45**, 5261.

Maire, E., Buffiere, J.Y., Salvo, L., Blandin, J.J., Ludwig, W. and Letang, J.M. (2002)

Maire,E., Buffière, J-Y., Salvo, L., Blandin, J.J., Ludwig, W. and Létang, J.M. (2001), Advanced Engineering Materials, 3 No 8, 539 - 546

Mavriplis, D.J. (1997)), NASA CR-201675 ICASE Report No. 97-20, 21.

McLeod, A.D. and Gabreyl, C.M., (1992), *Metall.Trans.* **23A**, 1279-1283.

Mochida, T., Taya, M., Lloyd, D.J., (1991), *Mater. Trans.*, JIM, **32**, 931.

Molinari, A., Ahzi, S., and Kouddane, R., (1997), *Mech. of Mater.*, **26**, 43-62.

Nan, C.W., and Clarke, D.R., (1996), *Acta, Met. Mater.*, **44**, 3801-3812.

Needleman, C.A., Nutt, S. and Suresh, S., (1989), *Mater. Sci. Engng.*, **A107**, 49

Pilkey, A.K. and Worswick, M.J. (1998), Advances in Industrial Materials, D.S. Wilkinson,W.J. Poole and A. Alpas eds., The Metallurgical Society of CIM, 105-122

Prangell, P.B., Downes, T., Stobbs, W.M., Withers, P.J., (1994), *Acta Metall Mater*, 42, 3425-3436.

Rice, J.R. and Tracy, D.M., (1969), *J. Mech. Phys. Solids*, **17**, 201.

Srivastan, S., (1996), *J. Mater. Sci.*, **31**, 1375-1388.

Talbot, D.R.S. and Willis, J.R., (1985), *J. Appl. Math.*, **35**, 39-54.

Tanaka, K., Mori, T., Nakamura, T., (1970), *Phil. Mag.*, 21, 267-279.

Tao, S., (1991), *M.Eng Thesis*, McMaster University, Hamilton, Ontario.

Taya, M. and Chou, T-W., *Int. J. Solid, Structures*, 17, 553-563.

Thomason, P.F., (1990), Ductile Fracture of Materials, Permagon Press.

Thomason, P.F., (1985), *Acta Met.*, 33, 1029, 1987

Thomson, C.I.A., Worswick, M.J., Pilkey, A.K., Lloyd, D.S., Burger, G.C., (1998), *Mech. Phys. Solids*, 47, 1-26.

Watt, D.F., Xu, X.Q. and Lloyd, D.J., (1996), *Acta. Mater.*, 44, 789-799.

Watt, J.P., Davies, G.F. and O'Connel, R.J., (1976), *Rev. Geophys. And Space Phys.*, 14, 541.

Wefers, K. and Mirsa, C. (1987), *Oxides and Hydroxides of Aluminum;* ALCOA Laboratories, 20.

Whitehouse, A.F. and Clyne, T.W., (1992), *Acta. Metall. Mater.*, 41, 1701-1711.

Wilkinson, D.S., Maire, E., Embury, J.D., (1997), *Mater. Sci. and Engng.*, A233, 145-154.

Wilkinson, D.S., Marie, E., Fougeres, R., (1999), *Mater. Sci. and Engng.*, A262, 264-270.

Withers, P.J., Stobbs, W.M., Pederson, O.B., *Acta. Metall.*, 37, 3061-3084.

Worswick, M.J., Pilkey, A.K., Lloyd, D.J. and Court, S., (1999), *Proc ICM8*

Worswick, M.J., Pilkey, A.K., Lloyd, D.J. and Court, S., (2000), *SAE World Congress*, 2000-01-0773.

Worwick, M.J., Pilkey, A.K., Thomson, C.I.A., Lloyd, D.J. and Burger, G. (1998), ASM Microstructural Science, 26, 26-29.

Wray, P.J., Richmond, O. and Morrison, H.L., (1983), *Metallography*, 16, 39-58.

Zok, F., (1998), *Ph.D. Thesis*, McMaster University, Hamilton, Ontario.

Zong, B.Y., Guo, X.H. and Derby, (1999), *Mater. Sci. and Tech.*, 4167, 827-832.

APPENDIX I

POLISHING PROCEDURE

All grinding steps require a repeated rotation sequence of 0-180^0–90^0-180^0-90^0-repeat with rotations every 4 seconds to ensure surface flatness.

Grinding Steps

Grind on 240 grit SiC paper to the approximate surface depth desired.

Rinse and grind on 600 grit SiC paper for about 1 minute.

Rinse samples carefully

Polishing Steps

Polish sample for 4 minutes on Buehler Metcloth with 15μm diamond paste and Norpar as lubricant.

Carefully rinse and dry sample.

Polish sample for 4 minutes on Pan-W* cloth with Microid Diamond Compound Extender.

Carefully rinse and dry sample.

Polish 2 minutes on "fresh"** colloidal Si on Microcloth.

Quickly remove and completely rinse sample so no colloidal Si dries on sample surface.

---

* Pan-W cloth (#810-529) and Microid Diamond Compound Extender (#811-004) can be obtained from Leco Instruments Ltd. 6185 Danville Road, Mississauga, Ontario, L5T 2H7.

**Samples polished with old colloidal Si always tended to "over-etch" which resulted in the particles standing taller than the matrix. As a result, it was impossible to obtain good quality optical micrographs. Follow all times posted in polishing steps closely, exceeding these times usually degrades the surface finish quality.

APPENDIX II

MECHANICAL TESTING SAMPLES

AND

INSTRUMENTED MICRO-HARDESS CALCULATIONS

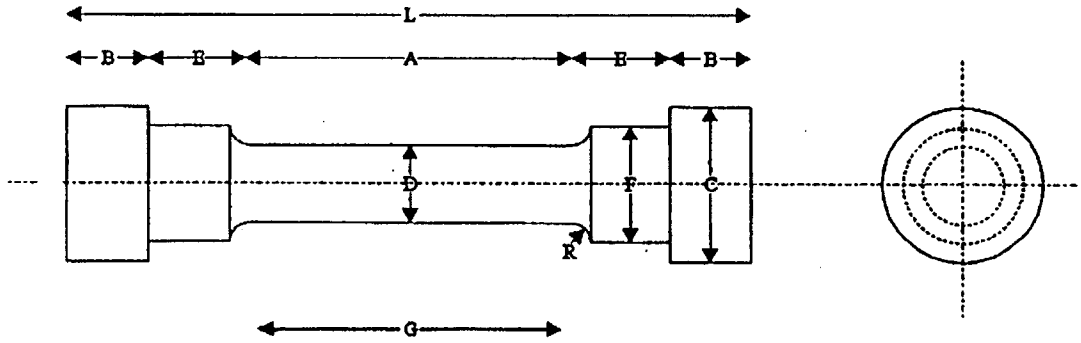

DIMENSIONS

A - LENGTH OF REDUCED SECTION - 0.625 + 0.005 in.
B - LENGTH OF END SECTION - 0.139 +/- 0.005 in.
C - DIAMETER OF END SECTION - 0.198 +/- 0.002 in.
D - DIAMETER - 0.113 +/- 0.002 in.
E - LENGTH OF SHOULDER AND FILLET - 0.208 +/- 0.005 in.
F - DIAMETER OF SHOULDER - 0.141 +/- 0.002 in.
G - GAGE LENGTH - 0.650 +/- 0.005 in.
L - OVERALL LENGTH - 1.519 +/- 0.005 in.
R - RADIUS OF FILLET - 3/32 in.

End section threaded on all load-unload and reverse loading samples

Figure AII.1 Geometry of tensile, load-unload and reverse loading samples. The end section was threaded on all samples with the exception of those used in conventional tensile testing.

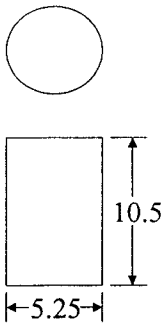

Cylindrical Compression Samples.
All Dimensions in mm

(a)

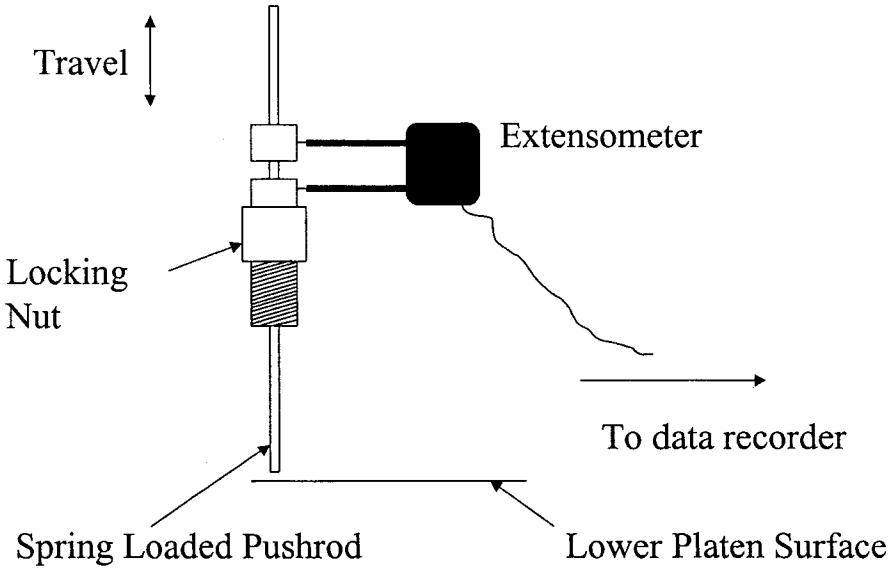

(b)

Figure AII.2 (a) Compression testing samples and (b) spring loaded pushrod mechanism coupled with extensometer to measure compressive strains.

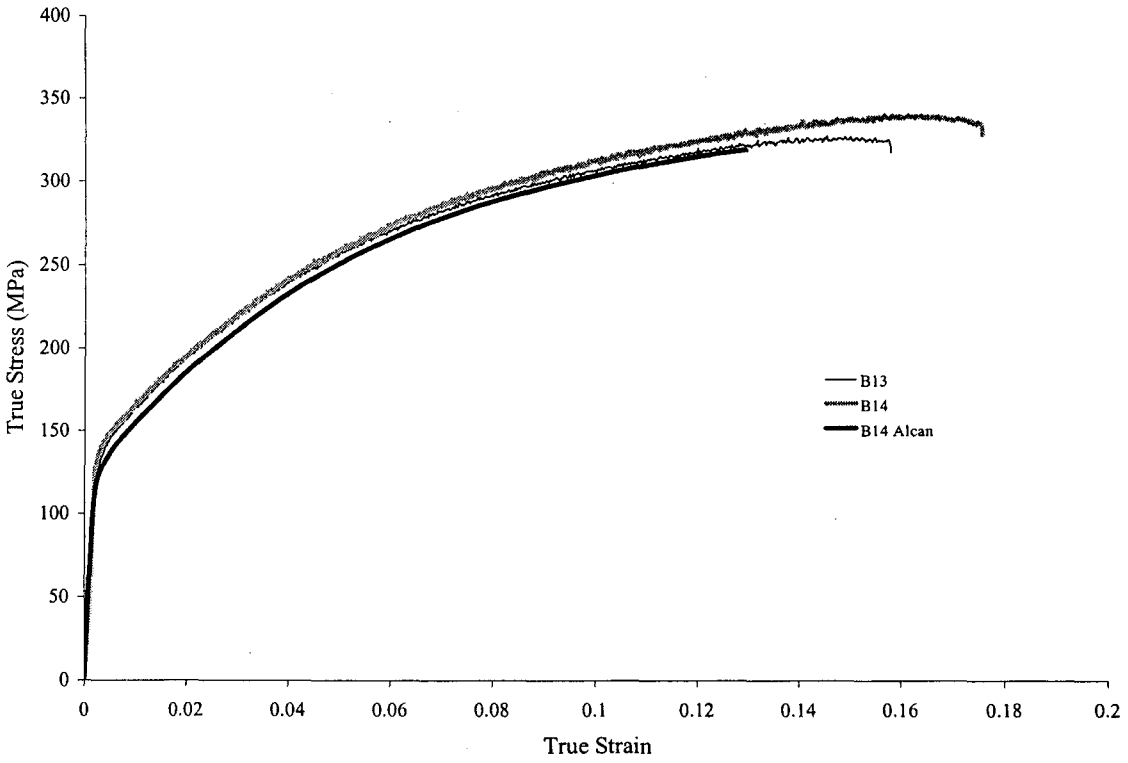

Figure AII.3 Representative tensile loading curves for samples with <<1% Al_2O_3

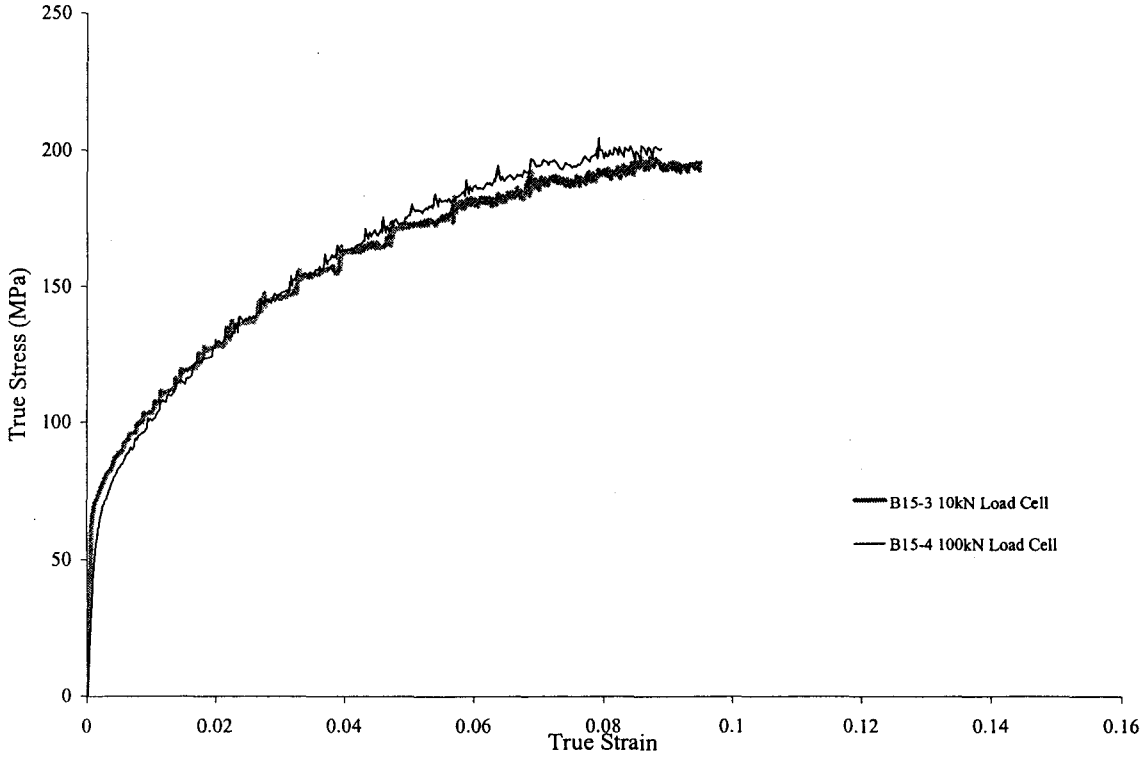

Figure AII.4 Representative tensile loading curves for samples with 4% Al_2O_3

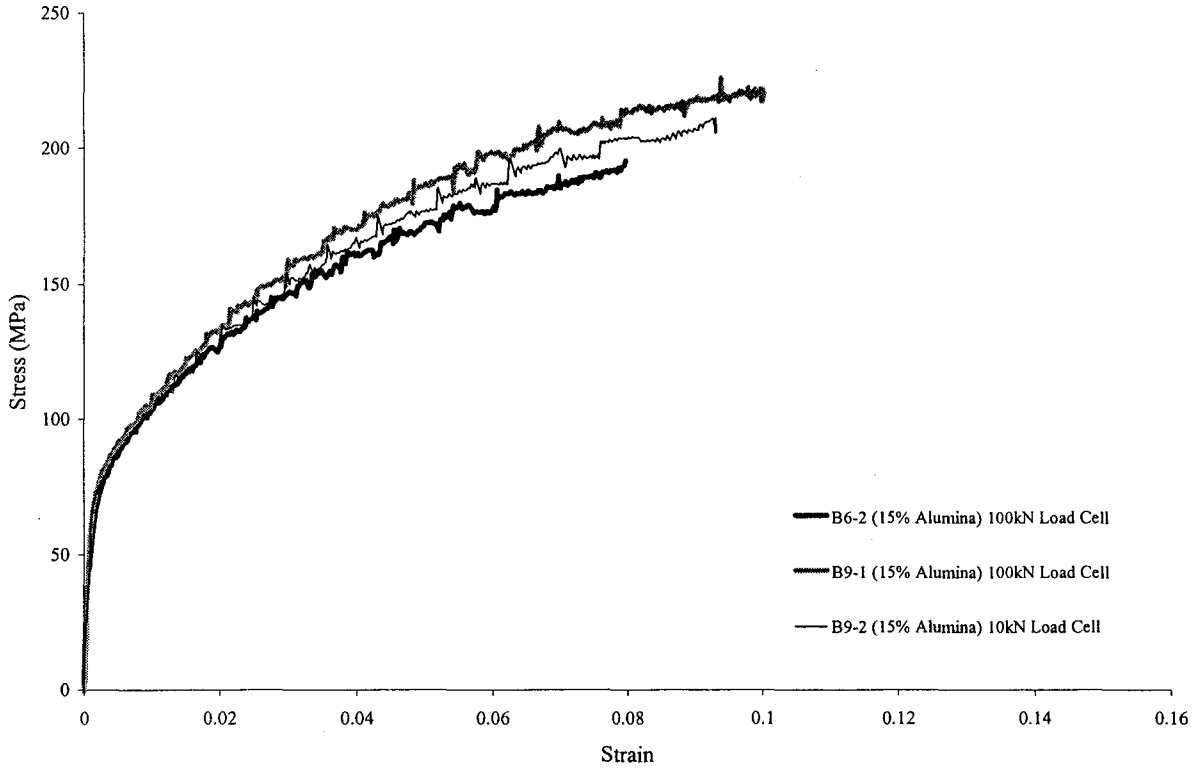

Figure AII.5 Representative tensile loading curves for samples with 8% Al_2O_3.

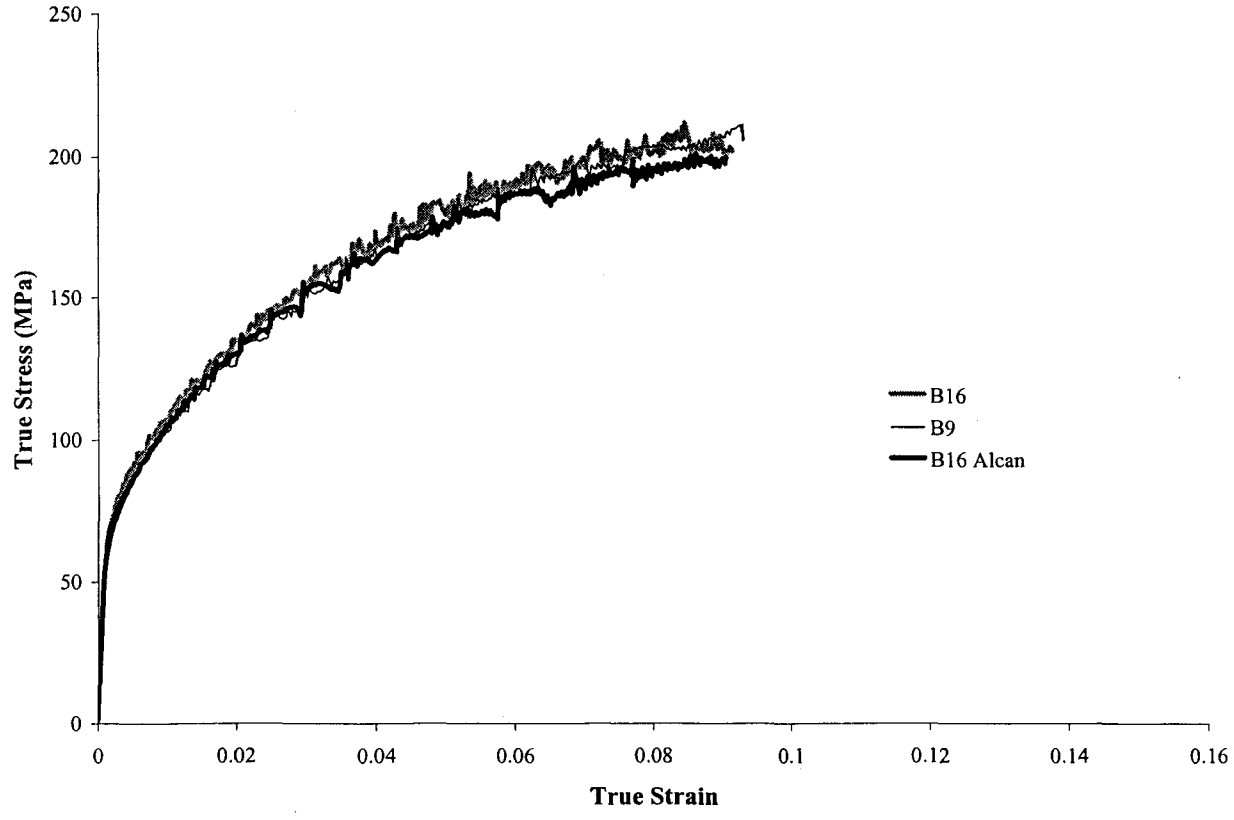

Figure AII.6. Representative tensile loading curves for samples with bimodal 4-8% distributions of Al_2O_3.

INSTRUMENTED SHARP INDENTATION CALCULATIONS

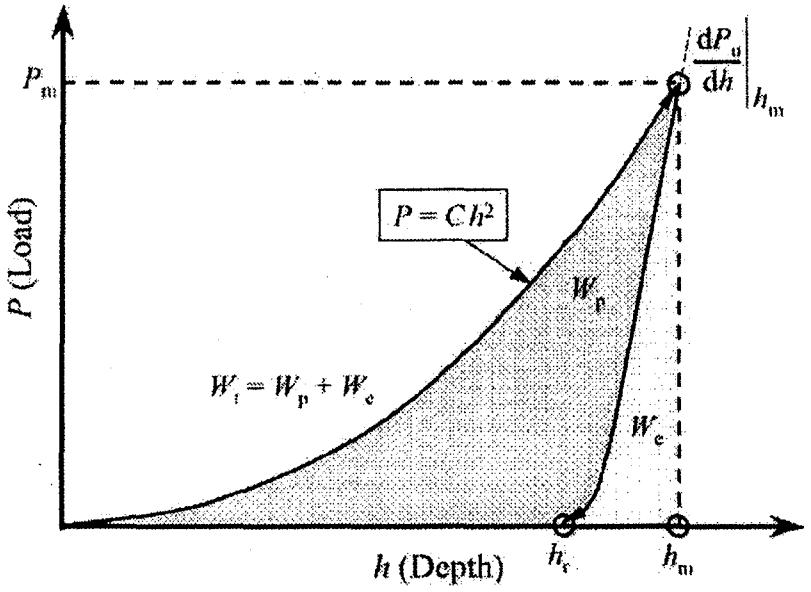

Figure AII.7 Parameters extracted from instrumented sharp-indentation loading curves. After Dao *et al* (2001).

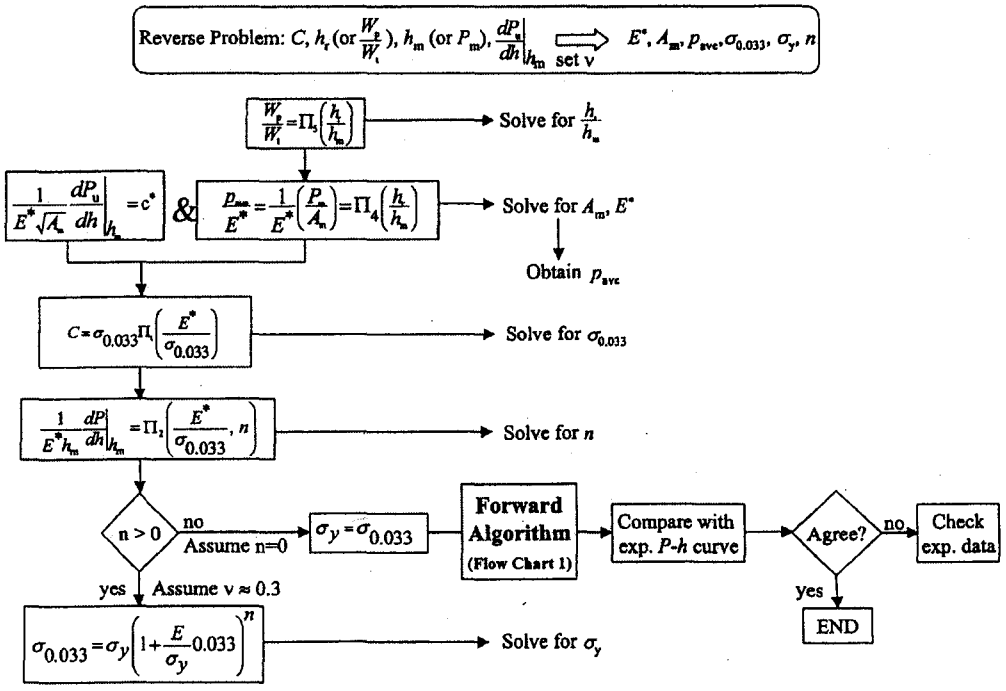

Figure AII.8 Algorithm for solving the elasto-plastic properties of the indented material. After Dao *et al.* (2001)

Table A1. Elasto-plastic parameters used in the present study

	E (GPa)	σ_y (MPa)	σ_y/E
19 combinations of E and σ_y*	10	30	0.003
	10	100	0.01
	10	300	0.03
	50	200	0.004
	50	600	0.012
	50	1000	0.02
	50	2000	0.04
	90	500	0.005556
	90	1500	0.016667
	90	3000	0.033333
	130	1000	0.007692
	130	2000	0.015385
	130	3000	0.023077
	170	300	0.001765
	170	1500	0.008824
	170	3000	0.017647
	210	300	0.001429
	210	1800	0.008571
	210	3000	0.014286

* For each one of the 19 cases listed above, strain-hardening exponent n is varied from 0, 0.1, 0.3 to 0.5, resulting a total of 76 different cases

$$\Pi_1 = \frac{C}{\sigma_{0.033}} = -1.131\left[\ln\left(\frac{E^*}{\sigma_{0.033}}\right)\right]^3 + 13.635\left[\ln\left(\frac{E^*}{\sigma_{0.033}}\right)\right]^2 - 30.594\left[\ln\left(\frac{E^*}{\sigma_{0.033}}\right)\right] + 29.267 \quad \text{(B1)}$$

$$\Pi_2\left(\frac{E^*}{\sigma_r}, n\right) = \frac{1}{E^* h_m}\frac{dP_u}{dh}\bigg|_{h_m} = (-1.40557n^3 + 0.77526n^2 + 0.15830n - 0.06831)\left[\ln\left(\frac{E^*}{\sigma_{0.033}}\right)\right]^3 + (17.93006n^3 - 9.22091n^2 - 2.37733n + 0.86295)\left[\ln\left(\frac{E^*}{\sigma_{0.033}}\right)\right]^2 + (-79.99715n^3 + 40.55620n^2 + 9.00157n - 2.54543)\left[\ln\left(\frac{E^*}{\sigma_{0.033}}\right)\right] + (122.65069n^3 - 63.88418n^2 - 9.58936n + 6.20045) \quad \text{(B2)}$$

$$\Pi_3\left(\frac{\sigma_r}{E^*}, n\right) = \frac{h_r}{h_m} = (0.010100n^2 + 0.0017639n - 0.0040837)\left[\ln\left(\frac{\sigma_{0.033}}{E^*}\right)\right]^3 + (0.14386n^2 + 0.018153n - 0.088198)\left[\ln\left(\frac{\sigma_{0.033}}{E^*}\right)\right]^2 + (0.59505n^2 + 0.034074n - 0.65417)\left[\ln\left(\frac{\sigma_{0.033}}{E^*}\right)\right] + (0.58180n^2 - 0.088460n - 0.67290) \quad \text{(B3)}$$

$$\Pi_4 = \frac{p_{ave}}{E^*} \approx 0.268536\left(0.9952495 - \frac{h_r}{h_m}\right)^{1.1142735} \quad \text{(B4)}$$

$$\Pi_5 = \frac{W_p}{W_t} = 1.61217\left\{1.13111 - 1.74756\left[-1.49291\left(\frac{h_r}{h_m}\right)^{2.535334}\right] - 0.075187\left(\frac{h_r}{h_m}\right)^{1.135826}\right\} \quad \text{(B5)}$$

$$\Pi_6 = \frac{1}{E^*\sqrt{A_m}}\frac{dP_u}{dh}\bigg|_{h_m} = c^* \quad \text{(B6)}$$

Figure AII.9 Dimensionless equations derived through the work of Dao *et al* (2001). The 19 cases solved to develop these dimensionless equations are shown in Table AI within Figure AII.9. Adapted directly from Dao *et al.* (2001).

$c^* = 1.2105$ for Vickers indentor (1.1957 and 1.2370 for Conical and Berkovich respectively).

$A_m = 24.50\ h^2$ where h is at taken at maximum indentation depth.

APPENDIX III

TOMOGRAPHY EXPERIMENTAL METHOD

A.III.1 Tensile Samples

Experiments were conducted on the same AA6111/Al_2O_3 composite system used throughout the research presented in this thesis. Tensile samples were machined from extruded material to the specifications in Figure AIII.1. Four different Al_2O_3 volume fractions and distributions were investigated; a bimodal 0-8%, a uniform 4%, a uniform 8% and a bimodal 0-4% volume fraction samples were used. To ensure repeatability, the samples were then grouped with the tensile samples employed in experiments described in Section 5.1 and heat-treated to a T4 state (Solutionizing at 560^{0}C for 20 min followed by quenching and room temperature aging). The samples were further manually reduced in thickness from 2 mm to approximately 1.4 mm by grinding on 600, 1200 and finally 4000 grit SiC grinding paper. Surface flatness was

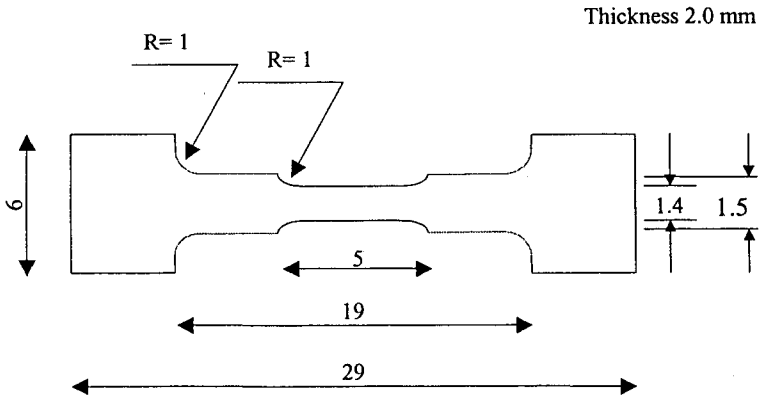

Figure AII.1. Tensile sample geometry used for tomography experiments.

maintained by first bonding one side of the sample to a SiC polishing jig and removing 300 μm followed by flipping the sample and removing the same amount of material from the other side.

AIII.2 X-Ray Tomography Experimental Set-up

The tomography experiments were performed with an x-ray beam energy of 22 keV. Radiographs were taken at 0.5^0 rotational increments with a 0.8 second collection time. A cooled CCD detector position of approximately 25 cm away from the sample provided the best balance between attenuation and phase contrast. A total of 360 radiographs were taken for a complete scan of a sample at each of the desired loading increments. A complete scan took approximately 20 minutes to complete.

AII.3 In-situ Tensile Loading

In-situ tensile loading was accomplished by using a testing system, develop by researcher at INSA, Lyon Fr. The loading is accomplished via a high precision screw driven loading frame that transmits load from the top portion of the loading machine to the bottom through a polymer tube. This tube is essentially invisible to the x-ray beam and allows for complete, obstruction free rotation of the sample through 360^0. The testing machine is affixed to a high precision 4-axis positioning platform in the experimental hutch of beamline ID19. Prior to running any of the samples, positional adjustments are made to ensure that the samples are properly centered and are accurately positioned at the center of rotation so the sample is always centered in the beam at any angle of rotation.

A controller that collects both displacement and load data controls loading. Once the sample is loaded to a predescribed load or displacement, the loading sequence is paused at constant displacement so that the tomography scan can be completed. Prior to starting the scan, the vertical position of the entire loading apparatus is re-adjusted so that the centered position of the sample can be corrected for the straining of the sample. By constantly vertically repositioning the loading apparatus, the same features of the microstructure remain within the same field of view. A complete tomography scan requires approximately 20 minutes. In this time, because the position of the sample is fixed, some sample unloading takes place due to

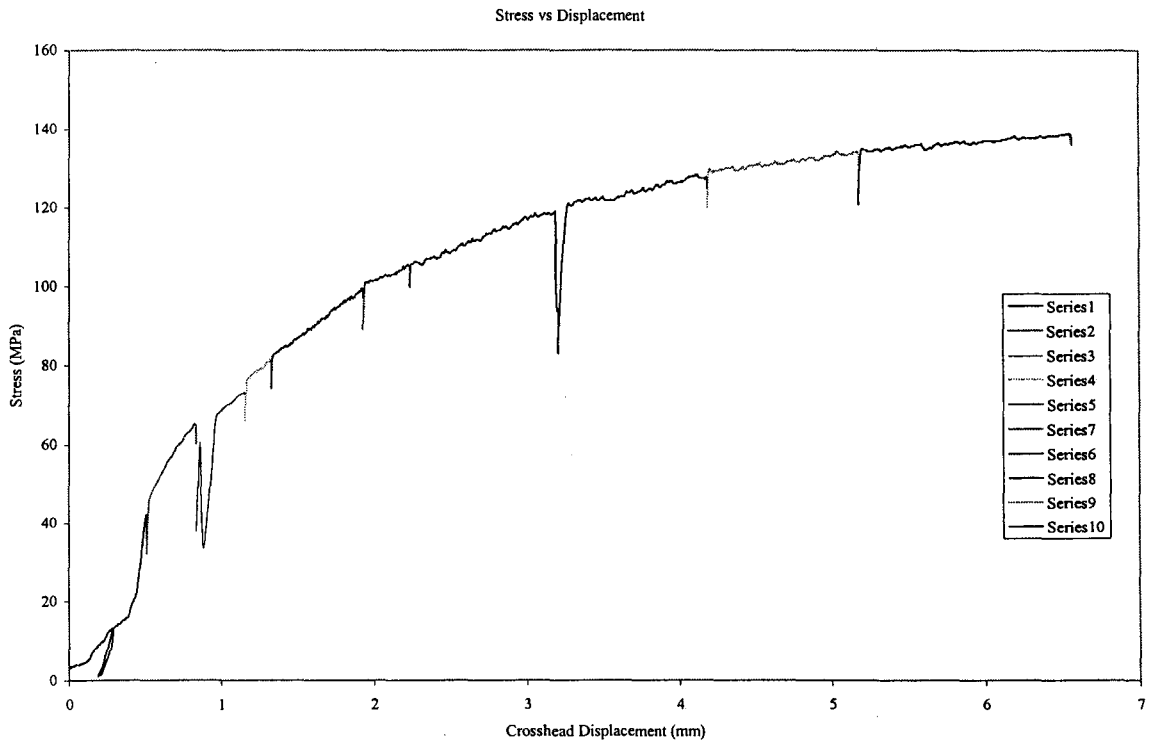

Figure AIII.2. In-situ stress vs. displacement tensile loading curve for uniform 4% volume fraction Al_2O_3 sample used for the generation of tomography data. Each colour represents a different loading increment.

the combined relaxation of the sample and the polymer tube. The loading curve for the 10% volume fraction sample is presented in Figure AIII.2.

AII.4 Reconstruction of Radiographs to Form Tomographic Volumes

Each of the tomography scans, consisting of a series of 360 radiographs, were recontructed using a back filter project algorithm employed at the ESRF computation facilities. The reconstructed images were saved in the .raw format after the gray levels were manually adjusted to ensure good contrast between the particles and the matrix.

AIII.5 Data Analysis

AIII.5.1 Determination of True Stress and Strain

The calculation of true stress and true strain required coupling data from the tensile loading controller and the tomography images. The cross-sectional area of each sample was physically measured at five locations along the gauge length of the sample prior to testing. The deviation from the mean of the measurements on the undeformed sample was small. The physical measurements were compared to measurements taken directly from the tomography data and were found to be virtually identical at the undeformed state. At all the subsequent loading increments, the cross-sectional area was directly measured from the tomography images using Image J. As in the measurements made prior to deforming the sample, five measurements were made at each load increment. Initially the standard deviation of the cross-sectional

area measurement was quite small. As loading progressed however, the standard deviation increased, reaching a maximum at the largest plastic deformation.

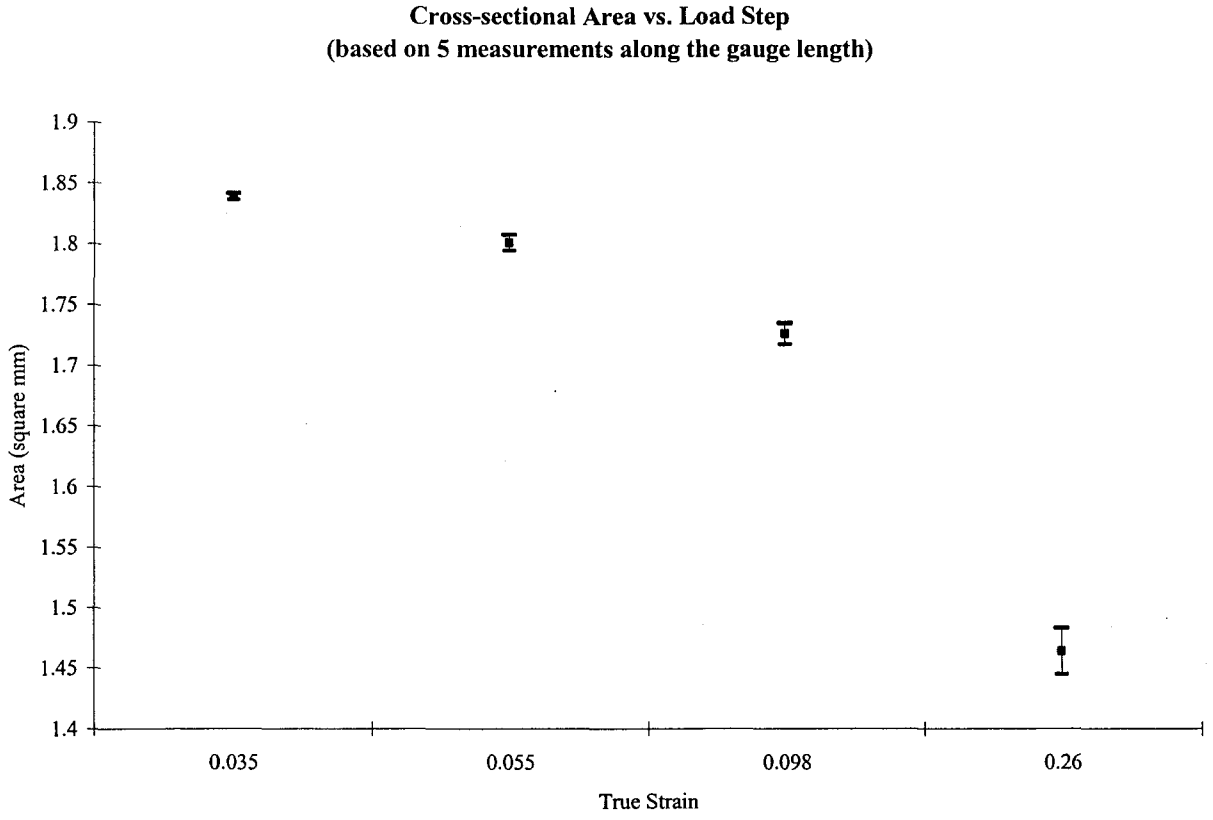

Figure AIII.3. The cross-sectional area variation versus true tensile strain in 4% volume fraction Al_2O_3 tomography sample.

The true strain at each load increment was calculated by using the measured cross-sectional area for the given increment and the measured initial cross-sectional area. True stress was calculated by taking the maximum load recorded at a given loading increment and dividing that load by the instantaneous area. The value of the particle stress at a given loading increment was estimated using results from the FEM calculations of Brokenbrough and Zok (1995). They estimate that the particle stress for a uniform distribution of reinforcing particles is approximately 2 to 2.18 times the

composite stress. In their work they found that this particle stress was only slightly sensitive to volume fraction and fairly sensitive to the work hardening exponent, with high values of n corresponding to a higher multiplication factor for the particle stress. In this work the particle stress was estimated as being 2.18 times the composite stress because the matrix material has a high hardening exponent (n~0.3) and the particle distribution is not uniform. The heterogeneity in the distribution would most likely increase the stress partitioning to the particles in the particle rich regions. This in turn would increase the stress acting in the particles for at a given increment of strain suggesting that $\sigma_p = 2.18\sigma_c$ is a reasonable estimate of the particle stress.

AIII.5.2 Image Processing Data

Both qualitative and quantitative data was produced using data processing software. Thresholding techniques, in this case a region growing algorithm used in the image processing software VgStudiomax, allowed for segmenting the particles from the matrix in the uniform 4% volume fraction of Al_2O_3 sample. A binary image was created from the segmented raw data of the sample prior deformation using AI3D.

This baseline binary file created on the unloaded sample was used as the working file for the processing of each of the following load increments. A new binary data file pertaining to a given load increment was created for each tomographic scan on the uniform 4% volume fraction Al_2O_3 composite sample. This was accomplished by opening the baseline binary file and the raw data file simultaneously. By having both images visible on the screen it was possible to

identify each of the particles that had visibly fractured in the raw data file with those in the binary file. When a particle was identified as being fractured in the raw data file, the corresponding particle in the binary file was segmented using the VgStudiomax region-growing algorithm. Once the binary file was segmented to differentiate the particles that had fractured at the particular strain increment, the binary file was saved under a new filename relating it to the strain increment investigated. These new segmented binary files could them be reopened in AI3D where thresholding techniques were used to differentiate between those particles that had fractured with those that had not. This segmented binary file could then be used to develop qualitative images of the samples using Vgstudiomax or for calculation using the computation features of AI3D.

APPENDIX IV

SCEMA-DAMAGE MODEL ALGORITHM

The following contains a complete outline of the computational algorithm used in the prediction of mechanical response of both the AA6111/Al_2O_3 and AA2614/SiC systems described in this thesis. Both the original Self Consistent Effective Medium Approximation (SCEMA) originally developed by Corbin and Wilkinson and the damage model developed in Chapter 5 of this thesis are included in this description.

Program Initiation

Input base material parameters including;

- Parameters of each of the participating phases (hardening exponents, initial flow stress, reinforcing particle Weibull parameters, volume fractions and elastic modulus of each phase)
- Output file configuration
- Initiation of array variables

Calculation of the initial composite modulus by solving the root of the SCEMA equation. If more than two phases are present the formulation developed by Kreher and Pompe(1989) is used.

$$\left\langle \frac{E_i^{Tan} - E_{composite}^{Tan}}{E_i^{Tan} + \frac{3}{2}E_{composite}^{Tan}} \right\rangle = 0 \qquad (1)$$

where E_i^{Tan} is the tangent modulus calculated for each phase, $E_{composite}^{Tan}$ is the composite modulus and the angle brackets represent an average, weighted by the volume fraction, over all phases, including both damaged and undamaged, of the solid.

Begin Main Calculation (Continuous loop until failure condition is met)

1. Increment composite strain ($d\varepsilon_{composite}$)
2. Derive Tangent Modulus of unreinforced matrix using the Ramberg-Osgood flow law. (hardening exponent and yield stress preset during program initiation)
   a. Calculate the tangent modulus of the unreinforced region

$$\frac{1}{E_i^{Tan}} = \frac{1}{E_i} + \frac{\alpha}{E_i n} e^{\left(\frac{1}{n-1}\ln\frac{s}{s_o}\right)} \qquad (2)$$

where:

E_i^{Tan} is the tangent modulus of phase *i*, in this case the unreinforced region
E_i is the elastic modulus
n is the hardening exponent
s is the current stress
s_0 is the original yield stress
α is a scaling parameter in the order of 3/7

b. Calculate stress increment in unreinforced region = $E^{Tan}_{unreinforced}$ * strain increment.
c. Stress in unreinforced region = stress from previous step + stress increment.

3. Increment yield stress of the unreinforced matrix in each the damaged phases based on contributions from dislocation/particle interactions.
   a. Increment of yield stress equal to:

$$d_{yield} = \sqrt{\left(d^{orowaon}_{yield} + d^{kinematic}_{yield}\right)^2 + \left(d^{isometic}_{yield}\right)^2 + \left(d^{CTE}_{yield}\right)^2} \qquad (3)$$

   where CTE is the coefficient of the thermal expansion. A full description of these contributions can be found in Nan and Clark (1993).

   b. The new unreinforced matrix yield stress in each damaged phase is the sum of the yield stress from the previous loop calculation and d_{yield}.

$$\sigma^{yield}_{unreinforced} = \sigma^{yield}_{old} + d^{yield} \qquad (4)$$

No Unloading

4. If the level of damage increment calculated in the previous global strain increment does not require the unloading of any participating phases, calculate the tangent modulus of both the damaged and undamaged phases using the equation in 2 a.
   a. A new value of the tangent modulus is calculated for each of the undamaged phases. In this calculation the values of the yield stress, elastic modulus and hardening exponent remain constant at the values assigned for each phase during program initiation. The value of tangent modulus for each phase is dictated by the stress in each phase at a global increment of strain.
   b. In the damaged regions, the calculation of the tangent modulus is based on the work of Brokenbrough and Zok(1995). Equation 2a is still employed to calculate the tangent modulus of each of the damaged phases. However, the values of the elastic modulus and yield stress used in the tangent modulus calculation are based on Brokenbrough and Zok's(1995) FEM calculation. The results of the FEM calculation indicated that both the elastic modulus, $E^{damaged}$, and the $\sigma^{damaged}_{yield}$ scale with a damage

parameter, g^{damage}, that is dependent on the work hardening exponent only.

$$g^{damage} = 1 - \gamma f - \beta(f)^2 \quad (5)$$

$$\gamma = 0.916n \quad (6)$$

$$\beta = 0.01 + 0.828n \quad (7)$$

where f and n are the volume fraction of particles in a given damaged phase and the work hardening exponent of the unreinforced matrix respectively. The elastic modulus and the yield stress of the each damaged phase can now be written as;

$$\sigma_{damage}^{yield} = g^{damage}\sigma_{unreinforced}^{yield} \quad (8)$$

$$E_{damage} = g^{damage}E_{unreinforced} \quad (9)$$

where $E_{unreinforced}$ is the modulus of the undamaged, unreinforced matrix and $\sigma_{unreinforced}^{yield}$ is the value of the unreinforced matrix yield stress obtained in 3b.

5. The new composite modulus is calculated based on the values of the tangent modulii for each of the participating phases using the effective medium approximation of equation (1). The value of the composite stress increment can now be calculated using the new value of the composite modulus, $E_{composite}^{new}$ and the global strain increment.

$$d\sigma_{composite} = E_{composite}^{new} d\varepsilon_{composite} \quad (10)$$

The composite stress and strain can now be written as

$$\sigma_{composite} = \sigma_{composite}^{old} + d\sigma_{composite} \quad (11)$$

$$\varepsilon_{composite} = \varepsilon_{composite}^{old} + d\varepsilon_{composite} \quad (12)$$

where $d\varepsilon_{composite}$ is the global composite strain increment.

6. The stress and strain increments in each of the participating phases are determined through

$$d\sigma_i = \left\langle \frac{5E_i^{\tan}}{3E_{composite}^{new} + 2E_i^{\tan}} \right\rangle d\sigma_{composite} \quad (13)$$

$$d\varepsilon_i = \frac{d\sigma_i}{E_i^{\tan}} \quad (14)$$

where $E_i^{\tan}$ is the tangent modulus calculated in step 4a for the ith phase. The stress and strain in each of the phases, damaged and undamaged, are then calculated through summation of the previous values and the increments.

$$\sigma_i = \sigma_i^{old} + d\sigma_i \quad (15)$$

$$\varepsilon_i = \varepsilon_i^{old} + d\varepsilon_i \quad (16)$$